UNIVERSITY OF CALIFORNIA SAN DIEGO

Protein-Protein Interactions and Substrate Processing in *E. coli* Type II Fatty Acid Biosynthesis

A dissertation submitted in partial satisfaction of the requirements for the degree
Doctor of Philosophy

in

Chemistry

by

Jeffrey Todd Mindrebo

Committee in charge:

Professor Michael D. Burkart, Chair
Professor Joseph P. Noel, Co-Chair
Professor William Fenical
Professor Elizabeth Komives
Professor Tadeusz F. Molinski
Professor Navtej Toor

2020

This dissertation of Jeffrey Todd Mindrebo is approved, and it is acceptable in quality and form for publication on microfilm and electronically:

_____

_____

_____

_____

_____

Co-Chair

_____

Chair

University of California San Diego

2020

DEDICATION

To my family, friends, and loved ones who have supported me during this journey, especially my wife, whom I found along the way.

EPIGRAPH

Do unto others twenty percent greater than you expect them to do unto you,

to correct for subjective error.

— Linus Pauling

.

TABLE OF CONTENTS

LIST OF ABBREVIATIONS

α/β Hydrolase domain	ABH
Acyl Carrier Protein	ACP
Acyltransferase	AT
Adenosine triphosphate	ATP
Center of gravity	COG
Chain length factor	CLF
Chemical shift perturbation	CSP
Coenzyme A	CoA
Dehydratase	DH
Enoyl reductase	ER
Fatty acid	FA
Fast protein liquid chromatography	FPLC
Fatty acid synthase	FAS
Fatty acid biosynthesis	FAB
Fatty acid methyl ester	FAME
Ferredoxin-like domain	FL
Gas Chromatography-Mass Spectroscopy	GCMS
High pressure liquid chromatography	HPLC
Ketoreductase	KR
Ketosynthase	KS
Malonyl-CoA ACP transacylase	MAT
Molecular Dynamics	MD

Nuclear magnetic resonance ..... NMR

Partner enzyme ..... PE

Partner protein ..... PP

Prinicple component analysis ..... PCA

4'-Phosphopantetheine ..... PPant

4'-Phosphopantetheinyl transferase ..... PPtase

Polyketide biosynthesis ..... PKB

Polyketide synthase ..... PKS

Protein Data Bank ..... PDB

Protein protein interactions ..... PPIs

Unsaturated fatty acids ..... UFAs

Uridine diphosphate ..... UDP

LIST OF FIGURES

LIST OF TABLES

ACKNOWLEDGEMENTS

I would like to first and foremost acknowledge my advisors and mentors Professor Michael Burkart, Professor Joseph Noel, and Dr. Jim La Clair for their support and mentorship. With their help and guidance, I was able to participate in a number of interesting and challenging projects that ultimately allowed me to develop as an independent scientist. I feel that I am well prepared for a career in science, and for that, I will be forever grateful.

I would also like to acknowledge my coworker, coauthor, and wife Laetitia Misson Mindrebo for her unwavering support and encouragement throughout my PhD. My successes in the lab conspicuously coincide with her arrival as a postdoctoral fellow in the Burkart lab, and indeed, the rest of my life has benefited just the same. I cannot imagine a better teammate and partner in the lab or out in the world, and I look forward to the life and family we will build together.

To all of the Burkart and Noel lab members past, present, and future thank you for all of your support and hard work. I recognize that anything I was able to accomplish during my PhD is because you either came before me or worked alongside me. A special thanks to Dr. Ashay Patel for being an amazing collaborator and endless source of informative scientific discussion. It has been an honor getting to work alongside you and becoming good friends over the years. To Dr. Woojoo Eunice Kim and Thomas Bartholow, thank you for being such great friends. Working in the Burkart Lab would not have been the same without you. Additionally, I would like to sincerely thank Dr. Gordon Louie and Professor Joseph Noel for the hands-on lessons in x-ray crystallography. Learning and applying this technique provided the necessary insights for me to learn how to develop and test hypotheses, and more

importantly, served as the motivation to continue to pursue training in structural biology as a cryo-electron microscopist.

I would also like to acknowledge all of my committee members for their time, support, and feedback. A special thank you to Professor Elizabeth Komives for always being an indispensable source of advice and encouragement.

It has been six years since entering the PhD program at UCSD, and I still remember all of the colleagues that took that journey with me in 2014. From the time that we were bright-eyed first year graduate students until now, it has been great to know that all of you have been here with me along for the ride. Additionally, thank you to all of the other friends and I've made along the way. The Burkart lab has been a second family for me, and your support, good natured humor, and constructive criticism has helped me become the person I am today.

Finally, thank you to my family Donna Mindrebo, Scott Mindrebo, and Jackie Biller who have pushed me to achieve more than I ever thought I could. I may not always have the best luck in the lab, but you are proof that I have no shortage when it comes to life.

I appreciate my collaborators allowing me to use the following publications in my dissertation:

Chapter 1, entitled Structural Basis of Acyl Carrier Protein Protein-Protein Interactions in Fatty Acid Biosynthesis, in part, is a reprint of the material as it appears in: Mindrebo JT*, Patel A*, Misson LE*, Kim E, Davis TD, Ni QZ, La Clair JJ, Burkart MD "Structural Basis of Acyl-Carrier Protein Interactions in Fatty Acid and Polyketide Biosynthesis" In Comprehensive Natural Products III. Vol. 1, 2020. The dissertation author

is the primary co-author of this manuscript along with Dr. Ashay Patel and Dr. Laetitia Misson.

Chapter 2, entitled Gating Mechanism of Elongating β-ketoacyl ACP Synthases, in full, is a reprint of the material as it appears in: Mindrebo JT*, Patel A*, Kim WE, Davis TD, Chen A, Bartholow TB, La Clair JJ, McCammon JA, Noel JP, Burkart MD. "Gating mechanism of elongating β-ketoacyl-ACP synthases", Nature Communications, vol. 11, 2020. The dissertation author is the primary co-author of this manuscript along with Dr. Ashay Patel

Chapter 3, entitled Activity Mapping the Acyl Carrier Protein – Elongating Ketosynthase Interaction in Fatty Acid Biosynthesis, in full, is a reprint of the material as it appears: Mindrebo JT*, Misson LE*, Johnson C, Noel JP, Burkart MD. "Activity Mapping the Acyl Carrier Protein - Elongating Ketosynthase Interaction in Fatty Acid Biosynthesis". Biochemistry, 2020. The dissertation author is the primary co-author of this manuscript along with Dr. Laetitia Misson.

Chapter 4, entitled Interfacial Plasticity Facilitates Catalysis in Type II FAS Malonyl-CoA ACP Transacylases, in full, , is a reprint of the material as it appears: Misson LE*, Mindrebo JT*, Davis TD*, Patel A*, McCammon JA, Noel JP, Burkart MD. "Interfacial Plasticity Facilitates High Reaction Rates of *E. coli* FAS Malonyl-CoA:ACP Transacylase, FabD" Proceedings of the National Academy of Sciences, 2020. The dissertation author is the primary author of this manuscript along with Dr. Laetitia Misson, Dr. Tony D. Davis, and Dr. Ashay Patel.

VITA

2020	Doctor of Philosophy, Chemistry, University of California San Diego
2016	Master of Science, Chemistry, University of California San Diego
2013	Bachelor of Science, Biochemistry, University of Houston

PUBLICATIONS

Mindrebo JT*, Misson LE*, Johnson C, Noel JP, Burkart MD: Activity Mapping the Acyl Carrier Protein - Elongating Ketosynthase Interaction in Fatty Acid Biosynthesis. *Biochemistry*. 2020.

Misson LE*, Mindrebo JT*, Davis TD*, Patel A*, McCammon JA, Noel JP, Burkart MD: Interfacial Plasticity Facilitates High Reaction Rates of *E. coli* FAS Malonyl-CoA:ACP Transacylase, FabD. *PNAS*. 2020.

Mindrebo JT*, Patel A*, Kim WE, Davis TD, Chen A, Bartholow TB, La Clair JJ, McCammon JA, Noel JP, Burkart MD: Gating mechanism of elongating β-ketoacyl-ACP synthases. *Nat. Commun.* Vol. 11, 2020.

Mindrebo JT*, Patel A*, Misson LE*, Kim E, Davis TD, Ni QZ, La Clair JJ, Burkart MD "Structural Basis of Acyl-Carrier Protein Interactions in Fatty Acid and Polyketide Biosynthesis" in *Comprehensive Natural Products III*. Vol. 1, 2020.

Mindrebo JT, Nartey CM, Seto Y, Burkart MD, Noel JP: Unveiling the functional diversity of the alpha/beta hydrolase superfamily in the plant kingdom. *Curr. Opin. Struct. Biol.* Vol. 41, 2016.

Craft JW, Zhang H, Charendoff MN, Mindrebo JT, Schwartz RJ, Briggs JM: Associations between the Rho kinase-1 catalytic and PH domain regulatory unit. *J. Mol. Graph. Model.* Vol. 46, 2013.

ABSTRACT OF DISSERTATION

Protein-Protein Interactions and Substrate Processing in
E. coli Type II Fatty Acid Biosynthesis

by

Jeffrey Todd Mindrebo

Doctor of Philosophy in Chemistry

University of California San Diego, 2020

Professor Michael D. Burkart, Chair

And

Professor Joseph P. Noel, Co-Chair

Fatty acid synthases (FASs) iteratively condense and reduce two carbon ketide units to produce fatty acids, which serve as precursors utilized in membrane development and homeostasis, energy storage, cofactor biosynthesis, and signaling. The core enzymatic activities of FASs are conserved, but they can exist as either large multidomain megasynthases (type I) or as diffuse monofunctional proteins (type II). Central to FAS is the small, 8kD acyl carrier protein (ACP), which carries thioester-linked pathway intermediates

to each respective enzyme active site. Each FAS enzyme, or domain, must form productive protein-protein interactions (PPIs) with ACP in addition to recognizing the ACP-tethered cargo. The robust and modular biosynthetic logic of FASs, and the evolutionarily related polyketide synthases (PKSs), make these synthases attractive metabolic engineering platforms to produce either industrially relevant feed stocks or novel bioactive compounds. Unfortunately, a fundamental lack of knowledge regarding ACP-mediated PPIs has led to limited successes in combinatorial engineering efforts.

Here we use the *Escherichia coli* type II FAS as a model system to investigate ACP-mediated PPIs and substrate processing by two important FAS enzymes, ketosynthases (KSs) and malonyl-CoA ACP transacylases (MATs). The first chapter provides an up-to-date review of ACP-mediated PPIs in *E. coli* type II FAS. In the second and third chapter we use this well-characterized system to better understand ACP-KS PPIs and KS substrate discrimination by structurally characterizing the *E. coli* elongating KSs, FabB and FabF, as substrate/intermediate complexes with ACP that approximate states formed during catalysis. In conjunction with molecular dynamics (MD) simulations and mutagenesis studies, these structures reveal conformational changes mediated by two active site loops that regulate substrate processing. Additionally, we developed three assays, one *in vitro* and two *in vivo*, to systematically evaluate and characterize the ACP-KS interface.

In the fourth chapter, we investigate PPIs between *E. coli* AcpP and its cognate MAT, FabD. We solved a high-resolution crystal structure of AcpP in complex with FabD and thoroughly interrogate this system using enzyme assays and molecular dynamics simulations. Results from these studies demonstrate that interfacial plasticity at the AcpP-FabD interface serves to facilitate rapid FabD transacylation rates.

Chapter 1. Structural Basis of Acyl-Carrier Protein Interactions in Fatty Acid Biosynthesis

Introduction

Nature has evolved a unique, iterative biosynthetic pathway in de novo fatty acid biosynthesis that polymerizes and reduces two carbon ketide units to produce fatty acids. FAS enzymes can exist as one or more polypeptide chain megasynthases possessing distinct catalytic domains (type I FAS) or as discrete catalytic enzymes (type II FAS). The core FAS enzymatic transformations include a decarboxylative thio-Claisen condensation reaction between two thioester groups to form a β-keto species, which subsequently undergoes ketoreduction, dehydration, and alkene reduction to produce saturated acyl intermediates. This process is repeated, iteratively, until a mature fatty acid is produced. Both type I and type II FAS require a small protein, the acyl carrier protein (ACP), that shuttles all building blocks and intermediates to the FAS enzymes or domains. For decades the role of the ACP was assumed to be simply a passive carrier for shuttling these intermediates. However, in recent years a growing body of evidence indicates that the ACP must form productive protein–protein interactions with each FAS enzyme in order to extend, modify, and offload mature pathway products. We have learned that type II FAS ACPs must interact with multiple enzymes or enzymatic domains outside of FAS to deliver intermediates for other metabolic pathways. For example, within *Escherichia coli* alone, ACP must interact with at least nine non-FAS enzymes, and the modes by which carrier protein engages these enzymes are distinct from those formed during FAS.

We also know that the molecular logic of FAS was evolutionarily translated to the polyketide synthase (PKS) family of enzymes. PKS pathways have evolved to repurpose the catalytic machinery of FAS for the construction of complex, bioactive molecules. Like fatty acids, polyketides (PKs) can be synthesized by both type I and II systems. In both cases, these synthases often possess domains or operate with enzymes unique to PKS that further increase the stereochemical and structural diversity of their products. PKSs also utilize ACPs to shuttle reaction intermediates between enzymatic partners or domains. Therefore, organisms have evolved sophisticated mechanisms to ensure that FAS and PKS machinery operate orthogonally with no inter-pathway crosstalk. Protein–protein interactions likely play an essential role in this regard, with differences in the sizes, shapes, and electrostatics of these proteins dictating their specificities.

The regulation of pathway specificity through protein–protein interactions, while necessary for proper cellular function, has undeniably impeded efforts in the fields of metabolic engineering and combinatorial biosynthesis. Attempts to engineer organisms with noncognate enzymes or to design novel pathways by mixing and matching enzymatic elements from different pathways/synthases have yielded only modest successes. It has become quite clear that in addition to characterizing the activities and substrate specificities of these biosynthetic enzymes, a thorough understanding of their protein–protein interactions will be required to manipulate these proteins rationally.

This chapter provides a comprehensive review of the advances made in the past decade in our understanding of the structure, function, and properties of ACPs and their interactions with associated partner proteins (PPs).

ACP Interactions in Type II FAS

Type II FAS systems are predominantly found in plant plastids and most bacteria. They are also found in mitochondria where they often play an important role in lipoic acid biosynthesis.[1,2] A significant amount of the early work characterizing FAS was performed in type II systems, specifically in plants and bacteria, due to the comparative ease of isolating and studying the individual biochemical components responsible for fatty acid (FA) production. As such, our knowledge of these systems, and the role the ACP plays in mediating biosynthesis, is more developed in type II than in type I FAS or in PKS enzymes. An overview of type II FAS in *E. coli* can be found in Figure 1.1. The following subsections will explore the current knowledge and importance of ACP-mediated protein–protein interactions in type II FAS, with special attention paid to the recent successes capturing interactions between the *E. coli* ACP (EcACP), AcpP, in complex with its different PPs.

Structure and Biophysical Properties of Type II FAS ACPs

Feodor Lynen and coworkers were the first to discover protein-bound acetoacetate intermediates in their studies with yeast fatty acid synthase, which led to the proposal that all intermediates formed during yeast FAS are protein-bound.[3] Subsequent work by Vagelos and coworkers studying *E. coli* FAS resulted in the isolation and biophysical characterization of a small, highly acidic 9 kDa protein that delivers substrates to FAS enzymes through a highly labile thioester bond provided by a phosphopantetheine (PPant) arm posttranslationally installed onto a conserved serine residue (Figure 1.2A).[4–6]-Since the first structure of EcACP was solved in 1988 using solution NMR, many structures of FAS and PKS ACPs with various

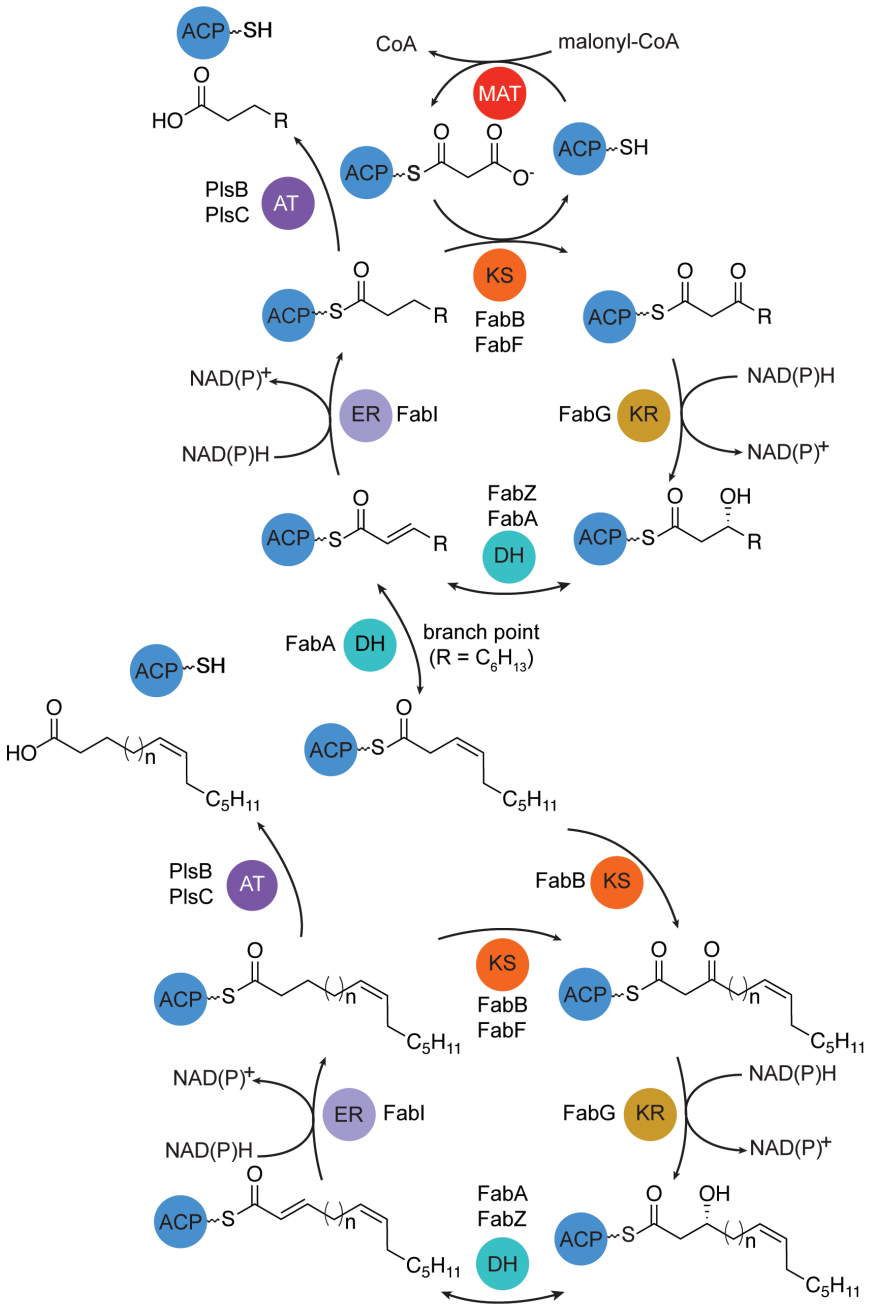

Figure 1.1: *Type II FAS in E. coli II, ACP structure, and ACP interactions*. The scheme illustrates the de novo production of both saturated and unsaturated FAs in *E. coli*. ACP (pale cyan); malonyl-CoA ACP transacylase MAT (red): malonyl-CoA AT, KS (orange): ketoacyl-ACP synthase, ketoreductase (KR) (yellow): 3-ketoacyl-ACP reductase, DH (green): 3-hydroxyacyl-ACP dehydratase, ER (purple): enoyl-ACP reductase, AT (light purple): glycerol-3-phosphate AT.

acyl-tethered moieties have been solved using both x-ray crystallography and NMR methods.[7–10] ACPs assume a canonical 4-helix bundle structure with the three long helices (helices I, II, and IV) where helix I runs antiparallel to helices II and IV and another smaller, sometimes only transiently formed, helix III that is oriented perpendicularly to the three larger helices (Figure 1.2A). Two notable flexible loop regions connect helix I to helix II (loop I) and helix II to helix III (loop II). The N-terminus of helix II harbors a highly conserved Asp-Ser-Leu, DSL, motif that serves as a recognition sequence and the site of PPant modification by *holo*-ACP synthase (AcpS), which converts *apo*-ACP into its active *holo*-ACP form.[1]-Cargo carried on the PPant arm is sequestered within the hydrophobic core of the helical bundle, which protects the growing substrate thioester bond from premature hydrolysis during FAS. The central hydrophobic pocket of EcACP can comfortably sequester substrates up to 10 carbons in length.[11] Therefore, in addition to forming protein–protein interactions, type II ACPs must "desequester" and "resequester" acyl cargo during catalytic events using a "chain flipping" mechanism.[12]

The overall structure of ACPs is thought to be flexible and dynamic, and indeed, early NMR studies of spinach ACP indicated two distinct conformations for the small protein and later studies have verified this finding in other systems as well.[13–15] Other ACPs, such as *Vibrio harveyi* ACP, are partially unstable at neutral pHs and can be stabilized by protein binding events or divalent cations, such as calcium and magnesium.[8,14] Phosphopantetheinylation of the ACP's conserved serine residue has been shown to stabilize carrier protein structure by providing contacts between the PPant arm and residues on helix II and III.[16] The acylated forms of ACPs also have slightly different electrostatic surface

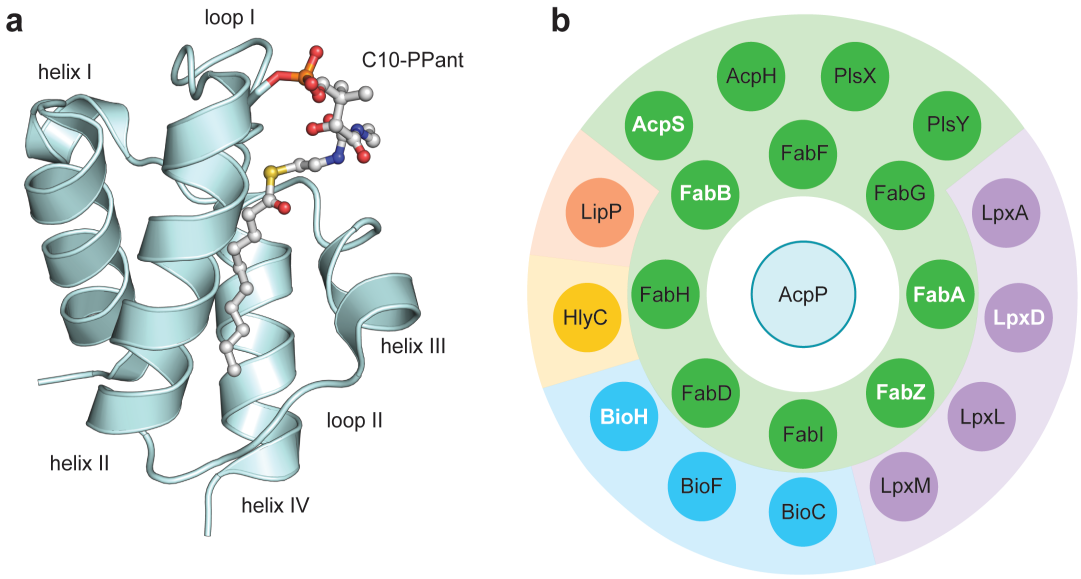

Figure 1.2: *The type II ACP structure and E. coli ACP interactome*. (a) Structure, topology, and nomenclature of ACP 4-helical bundle (PDB: 2FAE, 1.55 Å). The PPant arm along with tethered C10 cargo is shown as ball and stick sequestered inside the hydrophobic core of ACP. (b) The 21 catalytic partners from the *E. coli* "ACP interactome." Partners involved in FAS are in green, purple represents lipid A biosynthesis, blue represents biotin biosynthesis, yellow represents haemolysin biosynthesis, and red represents lipoic acid biosynthesis. Structures of crosslinked ACP=PP or noncovalent ACP–PP complexes are available for all partners labeled in bold white font.

potential and structural characteristics due to FA sequestration into their hydrophobic core.[10,11] Changes in ACP structure due to the identity of its cargo have been hypothesized to encourage interactions with the appropriate enzymatic partners in order to minimize nonproductive protein–protein interactions. An NMR study characterizing the structures of ACP intermediates during a full catalytic cycle of *S. coelicolor* FAS from hexanoyl-ACP to decanoyl-ACP indicated that sequestration and changes in cargo identity induced conformational changes in helix III, a region known to be important for ACP binding events and recognition.[7] The dynamic nature and flexibility of ACP are hypothesized to impart the small protein with its ability to interact effectively and efficiently with a multitude of PPs.

ACP–PP Interactions in Type II FASs

The *E. coli* "ACP interactome" includes 21 catalytic partners, as shown in Figure 1.2b, and the number of PPs increases when including noncatalytic partners that serve as metabolic regulatory elements. Despite the high number of PPs present in the cell, FAS is still a remarkably robust pathway capable of supporting *E. coli* doubling rates of 20 min.[17] Each PP recognition event requires energetically costly protein binding and unbinding events; therefore, these systems must employ higher order mechanisms of regulation that limit nonproductive protein–protein interactions and ensure efficient flux through the FAS pathway. Elucidating the structural basis of ACP interactions, especially by crosslinking complexes in catalytically relevant states for subsequent structural biology work, is the most direct approach to understanding the role ACPs and their cargo play in catalysis. Over the past two decades, a significant number of ACP–PP and ACP=PP (where '=' denotes crosslinked) complexes from type II FAS have been structurally characterized (Table 1).

Table 1.1: *List of all known type II FAS ACP–PP complexes.*

ACP•PP Complex	PDB ID	Method	Pathway	Organism	Year	DOI
BsACP•AcpS	1F80	X-ray	Type II FAS	*B. subtilis*	2000	https://doi.org/10.1016/S0969-2126(00)00178-7
EcACP•AcpS	2FHS	X-ray	Type II FAS	*E. coli*	2006	10.1074/jbc.M608758200
ScACP•AcpS	4DXE	X-ray	Type II FAS	*S. coelicolor*	2012	To be published
EcACP•FabA	4KEH	X-ray	Type II FAS	*E. coli*	2014	10.1038/nature12810
HpACP•FabZ	4ZJB	X-ray	Type II FAS	*H. pylori*	2016	10.1038/cr.2016.136
EcACP•FabB	5KOF	X-ray	Type II FAS	*E. coli*	2018	To be published
EcACP•FabZ	TBP	X-ray	Type II FAS	*E. coli*	2019	To be published
EcACP•BioI	3EJB	X-ray	Biotin	*B. subtilis*	2008	10.1073/pnas.0805983105
EcACP•YchM	3NY7	X-ray	Ion transport	*E. coli*	2010	10.1016/j.str.2010.08.015
SfACP•BioH	4ETW	X-ray	Biotin	*S. flexneri*	2012	10.1073/pnas.1207028109
EcACP•LpxD	4IHF	X-ray	Lipid A	*S. coelicolor*	2014	10.1038/nature12679
EcACP•LpxD	4IHG	X-ray	Lipid A	*S. coelicolor*	2014	10.1038/nature12679
EcACP•LpxD	4IHH	X-ray	Lipid A	*S. coelicolor*	2014	10.1038/nature12679

These structures have advanced our biophysical understanding of the mechanisms that govern ACP binding events.

ACP–AcpS complex

Phosphopantetheinyl transferases (PPTases) are a conserved enzyme family present in all domains of life. These enzymes use CoA as a substrate to install a prosthetic PPant arm onto a conserved serine residue of ACPs, thereby converting them from their inactive *apo*-form to active *holo*-form. In most type II FAS systems, *holo*-ACP synthase, AcpS, performs this crucial function. However, a different class of PPTases, Sfp-type PPTases, serve as the primary activators of carrier proteins in mammalian type I FAS, nonribosomal peptide synthetase (NRPS), and PKS. Phosphopantetheinylation provides carrier proteins with a 20 Å-long arm outfitted with a terminal thiol to deliver thioacyl-bound pathway intermediates to the active sites of PPs. The importance of this posttranslational modification for ACP activity makes PPTases attractive antibiotic targets.[18] Structural and biochemical data derived from these enzymes could aid in the development of future therapeutic treatments.

Nearly two decades ago, Somers and coworkers were the first to solve a crystal structure of an AcpS-type PPTase in their work studying PPTases from the gram positive bacteria *B. subtilis*.[19] Their study provided the *apo*-AcpS structure (PDB: 1F7T, 1.8 Å), AcpS in complex with CoA (PDB: 1F7L, 1.5 Å), and fortuitously, AcpS in complex with CoA and *holo*-BsACP (PDB: 1F80, 2.3 Å). The AcpS structure is trimeric and each monomer is composed of a five stranded b-sheet and three small N-terminal helices that, together, encase a larger fourth helix (Figure 1.3a).The AcpS monomers trimerize with their β sheets oriented toward the center of the complex and their helical portions facing outward (Figure 1.3).

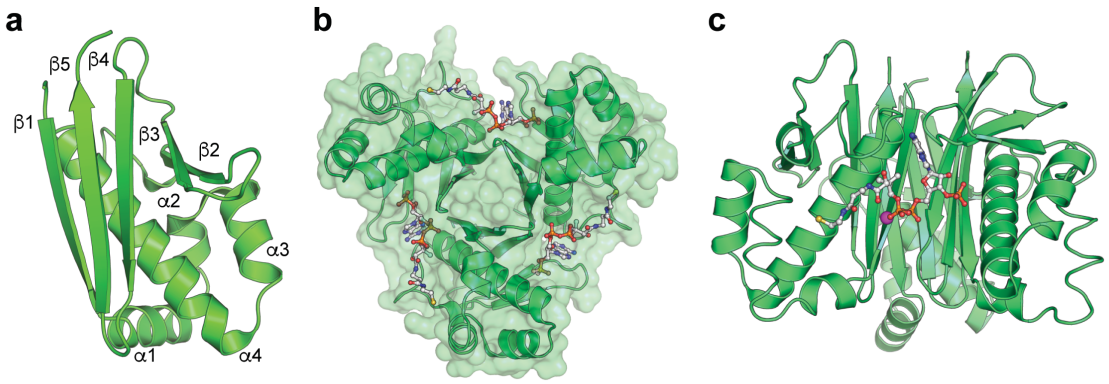

Figure 1.3: *Overview of AcpS structure, topology, and substrate binding*. (a) AcpS monomer with its secondary structure elements labeled. (b) Surface rendering of AcpS trimer with three bound CoA molecules with carbon (white), oxygen (red), nitrogen (blue), and phosphate (orange). (c) Side view of single AcpS active site with bound CoA molecule and magnesium ion (sphere, magenta) that aids in coordinating CoA and the deprotonation the Ser36 residue of ACP during catalysis.

An active site in the shape of a bowl-like depression is formed at the interface of each monomer, resulting in a total of three catalytic centers (Figure 1.3b). CoA binds at the interface of two monomers and conserved aspartate and glutamate residues coordinate a catalytically important magnesium ion (Figure 1.3c). Upon binding ACP, a magnesium-activated water molecule deprotonates the ACP Ser36 hydroxyl group facilitating the nucleophilic attack of Ser36 on the CoA β-phosphate.[19]

ACP associates almost exclusively with one monomer of AcpS trimer near the active site cleft, with the exception of a contact between Glu30 on ACP loop I and Arg45 at the bottom of the long helix on the adjacent AcpS monomer. Interactions between the two proteins, shown in Figure 1.4, are predominantly electrostatic with ACP helices II and III forming contacts with AcpS helices I and II and the α4-β4 flexible loop. The hydrophobic residues Leu37, Val40, and Met44 on ACP bind into hydrophobic pockets created by AcpS residues Met18, Arg24, Phe25, and Phe54 (Figure 1.4d).

This hydrophobic region of the interface is flanked by acidic residues at the top and bottom of helix II that form electrostatic interactions with conserved AcpS arginine residues. Arg14 of AcpS is an important and highly conserved residue that coordinates Asp35 and Asp38 at the top of ACP's helix II, thereby positioning Ser36 for attack on the β-phosphate of CoA (Figure 1.4c). Helix III of ACP forms additional electrostatic and hydrogen bonding interactions with the flexible α4-β4 loop. Interactions provided by Arg28 of AcpS pry apart helix II and helix III allowing sequestration of acylated PPant moieties inside the central cavity of ACP.

Since the landmark paper by Somers and coworkers published in 2000, both the *E. coli* EcACP–AcpS (PDB: 5VCB, 4.1 Å) and *Staphylococcus aureus* SaACP–AcpS

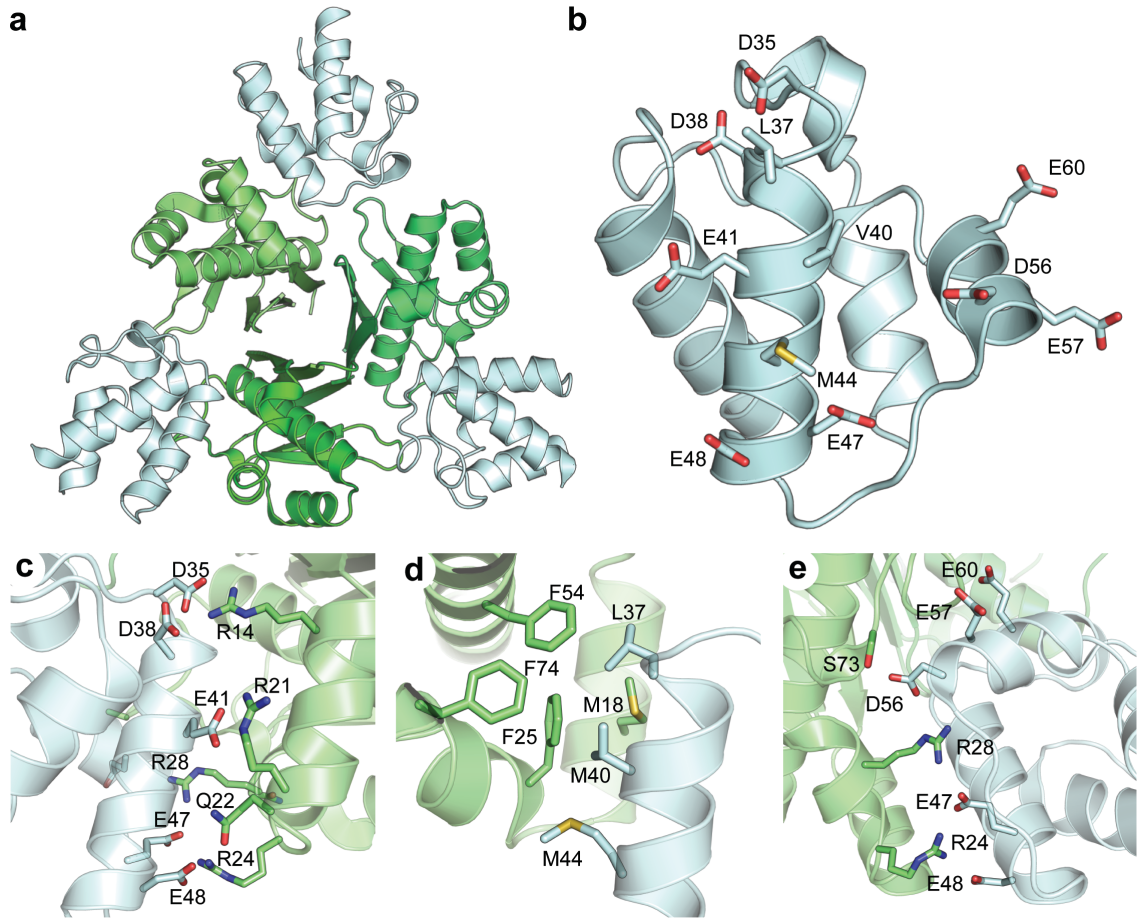

Figure 1.4: *Holo-ACP–AcpS complex and protein–protein interactions*: (PDB: 1F80, 2.3 Å). (a) Overview of the 3:3 ACP–AcpS structure. ACP is shown as pale cyan and AcpS monomers are shown in different shades of green. (b) All ACP residues within 4 Å with AcpS residues. (c) Electrostatic contacts are seen along helix II of ACP. (d) Hydrophobic interactions between ACP and AcpS at the top of ACP helix II. (e) Electrostatic interactions are along the helix II-loop II-helix III region of ACP.

(PDB: 4DXE, 2.51 Å) structures have been solved. These structures possess the same overall structural topology and ACP binding modes seen in the *B. subtilis* ACP–AcpS structure. In 2017, the EcACP–AcpS complex was resolved by Barb and coworkers, who were the first to crystallize *E. coli* AcpS as well as the EcACP–AcpS complex.[20] Their work resulted in a low-resolution x-ray model EcACP–AcpS complex (PDB: 5VCB, 4.1 Å), but subsequent NMR CSP and residual dipolar coupling (RDC) experiments served to validate their structural models. Through additional experiments verifying a 3:3 EcACP–AcpS binding stoichiometry, they determined a K_D of 2 μM for *apo*-ACP. Interestingly, *holo*-ACP was found to bind AcpS with a K_D of 62 nM and subsequent *holo*-ACP molecules bound with a K_D of 1.2 μM, thereby indicating that AcpS binds its product (*holo*-ACP) with high affinity and negative cooperativity. These findings have led to the proposal that AcpS activity is controlled by the cellular concentrations of *apo*-ACP and *holo*-ACP as well as the CoA and acetyl-CoA pool.[20]

The initial work performed by Somers and coworkers provided the first structure of an ACP–PP complex. The fundamental principles learned from the ACP–AcpS complex still drive our basic understanding of ACP-mediated protein–protein interactions today. Most ACP protein–protein recognition events are driven by electrostatic interactions (Figure 1.4c,e) between the negatively charged ACP molecule and a positive patch at the active site entrance of PPs. Helix II, loop II, and helix III are typically the most important structural motifs in all ACP–PP complexes solved to date. In fact, helix II of ACP is now often referred to as the "recognition helix" as it forms the most extensive interface contacts with respective PPs.[21] Analysis of subsequent structures in following sections will build on these basic principles.

ACP–MAT Complex

Malonyl-CoA serves as the source of extender units in FAS, but the malonate group must first be transferred from the CoA thioester to the terminal thiol of *holo*-ACP. This crucial step is performed by a malonyl-CoA-ACP transacylase (MAT), a class of transferases in the α/β hydrolase fold family that function through a conserved active site Ser-His catalytic dyad. These enzymes use a ping-pong reaction mechanism that first results in transfer the malonate group from malonyl-CoA to the active site serine residue of MAT to produce a malonyl-MAT enzyme adduct. In a second half reaction, *holo*-ACP associates with MAT and transfers the malonate moiety to its PPant thiol to produce malonyl-ACP (Figure 1.5). This reaction therefore serves to "charge" *holo*-ACP with malonate, thereby producing the pool of malonyl-ACP necessary for all subsequent condensation reactions performed by ketosynthases.

The first MAT structure, *E. coli* MAT (EcFabD), was published in 1995 (PDB: 1MLA, 1.5 Å) and since then at least 13 MAT structures from different organisms were solved and are available in the PDB.[22–25] The core MAT structure is of the α/β hydrolase fold family with residues 1–123 and 206–307 forming a 4-stranded parallel β-sheet sandwiched by 12 helices.[22,26] There is an additional small ferridoxin-like domain insertion between residues 120 and 205 that is thought to form much of the putative ACP binding interface (Figure 1.6).[27] Crystal structures of *E. coli* FabD bound to malonyl-CoA show the active site can be accessed at the groove between the core α/β hydrolase domain and the smaller ferredoxin-like domain (Figure 1.6).[25] Furthermore, transfer of malonate to the catalytic serine of EcFabD serves to organize the active site residues for malonyl transfer to *holo*-ACP.[28] There are currently no available crystal structures of a type II FAS ACP.[28]

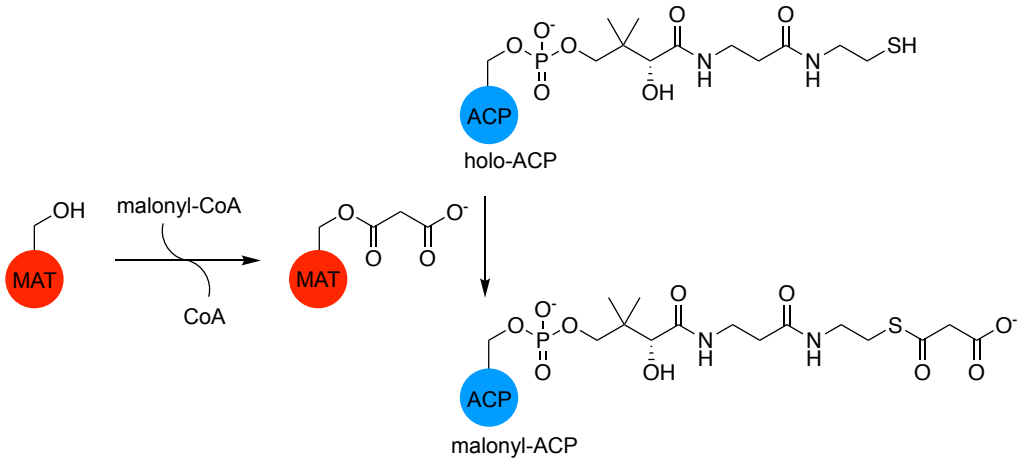

Figure 1.5: *Ping-pong mechanism of MATs*. Malonyl CoA associates with MAT and malonate is transferred onto the side chain hydroxyl of the catalytic serine residue, shown as OH, producing a malonyl-MAT intermediate. Next, holo-ACP associates with MAT and the malonyl group is transferred onto the ACP PPant arm, which is followed by dissociation of ACP with the thioester tethered substrate.

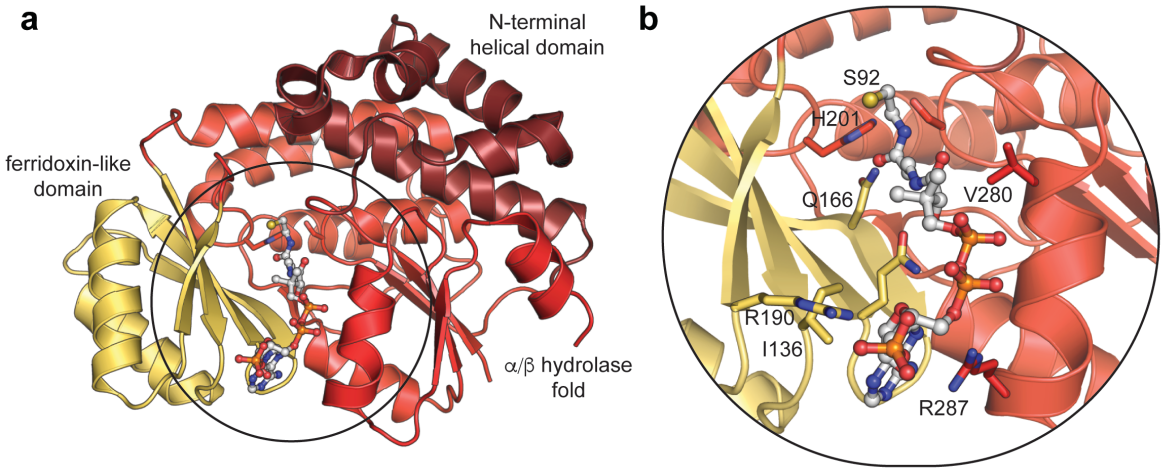

Figure 1.6: *MAT topology and substrate interactions.* (a) Overview of MAT topology (PDB: 2G2Z, 2.8 Å) with the ferridoxin-like domain colored yellow-orange, the N-terminal helical domain colored ruby red, and the core α/β hydrolase fold colored as red. Malonyl-CoA is shown bound at the active site cleft with carbon (white), oxygen (red), and nitrogen (blue), and phosphate (orange). (b) A close-up view of the interactions that coordinate malonyl-CoA in the crystal structure. The active sites Ser92 and His201 are labeled in bold.

There are currently no available crystal structures of a type II FAS ACP–MAT complex, but despite our lack of structural knowledge, the ACP–MAT interfaces of *Helicobacter pylori* and *S. coelicolor* have been characterized extensively using NMR, binding kinetics, enzyme assays, and computational docking protocols.

Interestingly, a significant number of PKS clusters in *S. coelicolor* do not contain a MAT; therefore, it was postulated that the FAS MAT of *S. coelicolor* (ScFabD) could fill in for these pathway deficiencies.[29,30] In 2003, Stroud and coworkers solved the crystal structure of ScFabD and performed macromolecular docking experiments using actinorhodin ACP (actACP) as the *S. coelicolor* FAS ACP (ScACP) structure was not available.[23] The best scored complex featured loop I, the top of helix II, helix III, and the top of helix IV forming extensive interactions with the α/β hydrolase domain of FabD (Figure 1.7a). Although this initial model placed the conserved DSL motif in a reasonable position to deliver substrate to the ScFabD active site, the binding mode of the docked ACP is not in alignment with what is currently known about FAS ACP protein–protein interactions. Although, these differences in binding mode may be attributed to the use of actACP instead of the FAS ScACP.

A more thorough follow-up study performed by Crosby and coworkers to characterize ScFabD interactions with its cognate FAS ACP, ScACP, was performed using a combination of NMR, docking simulations, binding kinetics, and enzyme assays.[27] Solution- phase NMR experiments were used to solve the structure of ScACP (PDB: 2G2Y, 2.26 Å) as well as calculate ScACP CSPs during binding events with ScFabD. ScACP's helix II, loop II, and helix III undergo the largest chemical shifts, while only modest changes are seen along loop I (Figure 1.7b). Binding kinetics and NMR CSP titration data were then used as restraints during protein-protein docking simulations to produce a more accurate

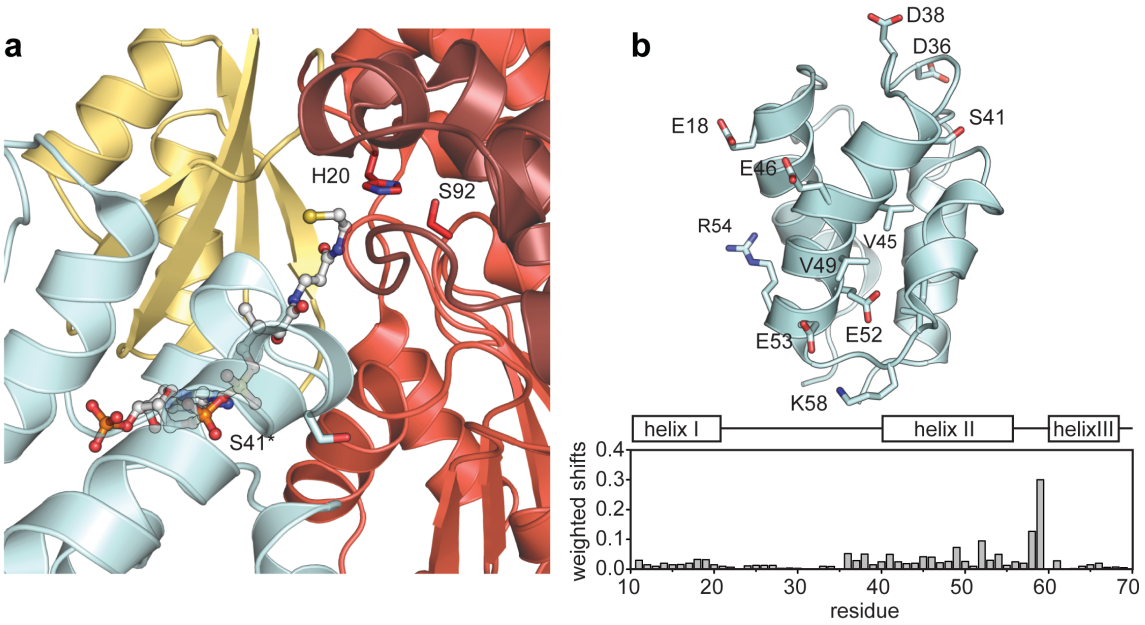

Figure 1.7: *Comparison of ACP•MAT binding studies*. (a) Docked model (PDB: 1NNZ) of actinorhodin-ACP bound to S. coelicolor MAT (ScMAT, PDB: 1NM2, 2.0 Å) from Stroud and coworkers overlaid with FabD from *E. coli* bound to malonyl-CoA (PDB: 2G2Y, 2.26 Å). The conserved Ser41 (Ser36 in *E. coli*) residue of ACP is denoted in bold and an asterisk. (b) Weighted CSPs of ScACP titrated with ScMAT. Data were interpreted from studies performed by Crosby and coworkers.[27] The 10 largest CSP shifts, excluding Ile59, are shown as stick and represented with carbon (cyan), oxygen (red), and nitrogen (blue).

ACP•FabD model. This new model identifies helix II as the main recognition motif where electrostatic interactions surround a small number of hydrophobic contacts. Interestingly, no changes in chemical shift for the amide protons of the ACP PPant arm were observed during CSP titrations. However, it is worth noting that these experiments were performed with FabD in its *apo*-form and malonylation of the active site serine residue may be necessary for ACP to "chain flip" its PPant arm into the active site. A closer analysis of the docked complex shows ACP forming more contacts with the ferridoxin-like domain than the N-terminal helical domain of FabD. Mutation of an arginine residue on the ferridoxin-like domain near the active site entrance to alanine, R189A, caused a fivefold decrease in ACP binding affinity. Additionally, the equivalent residue in EcFabD, Arg190, forms an electrostatic interaction with the 3` phosphate of the CoA ribose ring as seen in the crystal structure of *E. coli* FabD in complex with malonyl-CoA. These observations support the role of Arg189 in ACP recognition events and suggest that it is important for both CoA and ACP binding. The proposed ScACP•FabD model by Crosby and coworkers fits well with our knowledge of ACP binding modalities and currently serves as the most interrogated FAS ACP–MAT interface study to date.

Shen and coworkers solved the *H. pylori* MAT, HpMAT, structure and also subjected their model to docking protocols using the native *H. pylori* FAS, HpACP. In the docked structures, Helix II from ACP forms favorable contacts with conserved electropositive and hydrophobic residues near the HpMAT active site entrance.[24,31] Additional contacts involve residues at the top of helix I and Asp56 of ACP's helix III. This interaction is of particular interest as the crosslinked structures of the *E. coli* FAS ketosynthase (EcACP=FabB) and dehydratases (EcACP=FabA and EcACP=FabZ) also use Asp56 to coordinate with helix III

of EcACP. In addition to favorable interface contacts, the serine hydroxyl group is well oriented to deliver the PPant arm to the HpMAT active site. The results from this study are in alignment with what is currently known about ACP–PP interactions and are in agreement with the *S. coelicolor* ACP•FabD model proposed by Crosby and coworkers.[27]

MATs are essential enzymes that provide the pool of extender units for FAS as well as the specificity of the starter unit. Despite a lack of structural information, our basic understanding of ACP–MAT interactions has advanced significantly. While there have been some successes in crystallizing ACPs with trans-ATs from type I PKS pathways, new innovative approaches for trapping interactions with ATs will need to be explored.

ACP–KS Complex

KSs use a thio-Claisen condensation reaction to form carbon–carbon bonds in FAS and PKS. This reaction is irreversible and serves as the committed step in FAS, ensuring completion of the FAS catalytic cycle whereby the newly formed β-keto species is fully reduced to the saturated FA. *E. coli* possesses three KS enzymes: FabB, FabF, and FabH, which are representative of the three KS families KASI, KASII, and KASIII, respectively.[32] All three KS subfamilies are part of the larger thiolase fold family and exist as homodimers in solution. FabH serves as the initiator in FAS by condensing acetyl-CoA with malonyl-ACP to produce acetoacetyl-ACP.[33] All subsequent rounds of extension are catalyzed by the elongating KSs, FabF and FabB, using solely ACP derived starter and extender units.[34] The reaction mechanism of KSs is similar to the ping-pong mechanism used by MATs.[35,36] Acyl-ACP must first associate with the KS and transfer its acyl cargo to the active site cysteine residue, producing an acyl-enzyme intermediate. Malonyl-ACP then associates and through

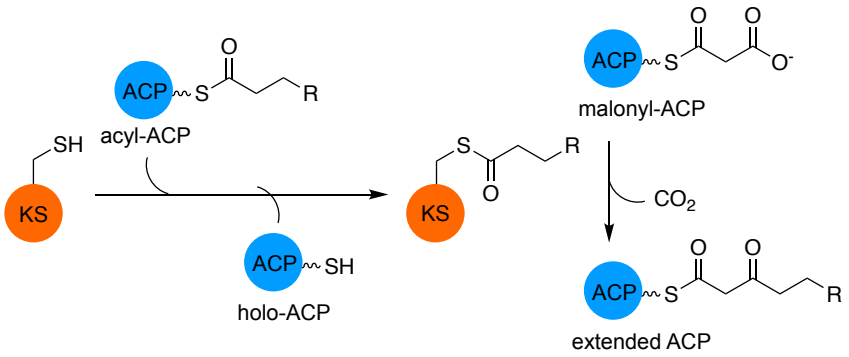

Figure 1.8: *Ping-pong mechanism of elongating KSs*. Acyl-ACP associates with the KS and the acyl group is transferred onto the catalytic cysteine residue, shown as SH, producing an acyl-KS intermediate. Next, malonyl-ACP associates with the KS and condenses with the enzyme-bound thioacyl intermediate through a decarboxylative thio-Claisen condensation reaction, to subsequently form and offload β-ketoacyl-ACP.

a decarboxylative thio-Claisen condensation forms β-ketoacyl ACP (Figure 1.8). KS enzyme mechanisms require multiple ACP association and dissociation events in a highly choreographed manner. Thus, a greater understanding of ACP•KS recognition events is essential to future work studying and engineering FAS and PKS pathways.

The elongating KSs, FabB and FabF, perform additional specific roles in *E. coli* FAS. FabB knockouts are unsaturated FA auxotrophs and are not viable without media supplementation of unsaturated FAs.[37] It has been well demonstrated *in vivo* and *in vitro* that FabB is responsible for the production of unsaturated FAs by working in concert with the dehydratase FabA (Figure 1.1).[38,39] FabA selectively isomerizes trans-2-decenoyl-ACP, the immediate product of FabA-catalyzed dehydration, to cis-3-decenoyl-ACP. This unstable intermediate is, subsequently, extended to cis-5-dodecenoyl-ACP by FabB, which immortalizes the unsaturation.[38,40,41] FabF does not perform this function *in vivo*, despite the similarity it shares with its homologue FabB. Additionally, Cronan and coworkers have shown that FabF regulates membrane fluidity in response to temperature changes by increasing the amount of cis-vaccenic acid (18:1 (11Δc)) present in membrane lipids.[42,43] This temperature sensing feature of FabF is decoupled from gene regulation and the activity of transferases at the membrane surface, and thus is governed by the structure and dynamics of FabF.[43,44] Although the underlying molecular mechanisms responsible for KS substrate discrimination at crucial branch points in *E. coli* FAS remain unknown, these early biochemical studies demonstrate the importance of KS substrate preference in *E. coli* FAS pathway flux and regulation. A better understanding of ACP–KS interactions and KS substrate preference can be achieved by crystallizing ACP=KS crosslinked complexes with substrate mimetics.

Burkart, Tsai, and coworkers recently solved a crosslinked crystal structure of EcACP=FabB at 2.4 Å (PDB: 5KOF, 2.4 Å), which is the first structure ACP–KS complex from type II FAS.[45] The EcACP–FabB complex was trapped using a mechanistic crosslinking pantetheineamide probe containing an electrophilic chloroacrylate warhead loaded onto EcACP. A covalent bond is formed between the active site cysteine residue, Cys163, and the reactive center on the PPant probe. The pantetheineamide carbonyl group forms interactions with the two catalytic histidine residues, His298 and His333, mimicking the state of malonyl-ACP during the condensation portion of the two-step reaction (Figure 1.9).

The EcACP–FabB interface consists of electrostatic interactions between the negatively charged ACP and a positive patch formed at the FabB active site entrance near the dimer interface. Most of the interactions occur along helix II of ACP, with the negatively charged residues Asp35, Asp38, Glu41, and Glu48 forming salt bridges with positively charged arginine and lysine residues along the FabB dimer interface (Figure 1.10). The majority of the FabB interactions with ACP are from the FabB monomer that is not crosslinked to the ACP, with the exceptions being residues Arg45, Val270, and Met204. Arg45 forms a salt bridge with Asp56 of ACP providing the only contact to helix III of ACP, while Val270 and Met204 are part of a hydrophobic network coordinating the EcACP–FabB interface at the active site entrance. Residues Met44, Val40, and Leu37 of ACP helix II form hydrophobic interactions along the FabB interface (Figure 1.10d). Met44 and Val40 pack into holes formed by residues 124–132 of FabB and Leu37 sits in a pocket created by FabB residues Val270, Phe67, and Tyr132. This hydrophobic region of the interface is flanked by

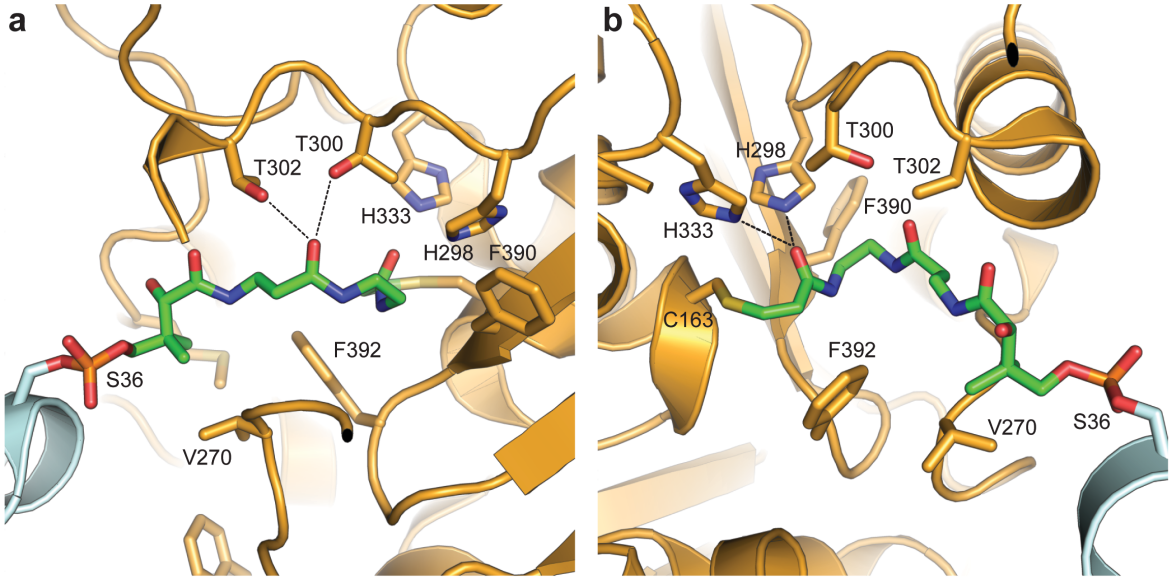

Figure 1.9: *PPant interactions in crosslinked EcACP=FabB structure (PDB: 5KOF, 2.4 Å).* (a) and (b) represent two viewing angles of all the relevant interactions between the crosslinked EcACP PPant arm and FabB active site residues. The catalytic histidines, His298 and His333, can be seen coordinating the carbonyl moiety of the PPant probe in a manner reminiscent to the expected interactions formed during association with malonyl-ACP.

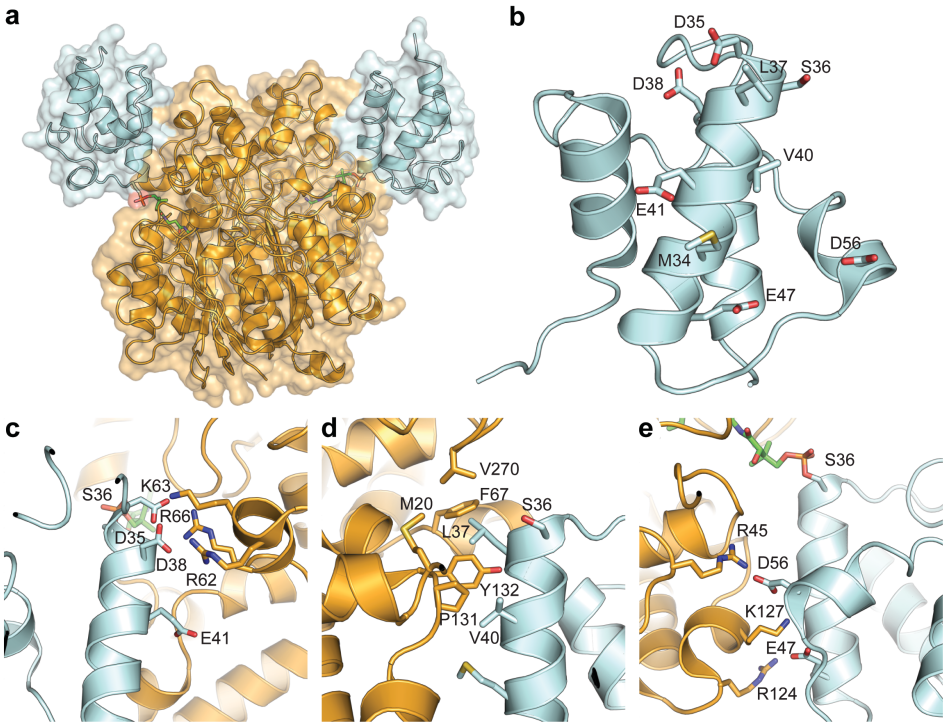

Figure 1.10: *Crosslinked EcACP=FabB complex and protein–protein interactions (PDB: 5KOF, 2.4 Å).* (a) Overview of the 2:2 EcACP=FabB crosslinked structure. The complex is shown as a transparent surface representation with ACP (pale cyan) and FabB (bright orange). The PPant probe is represented with carbon (green), oxygen (red), nitrogen (blue), and phosphate (orange). (b) All ACP residues that form contacts within 4 Å with FabB residues. (c) Electrostatic contacts as seen along helix II of ACP. (d) Hydrophobic interactions between ACP and FabB at the top of ACP helix II. The PPant probe is not shown for viewing purposes. (e) Electrostatic interactions along the helix II-loop II-helix III region of ACP.

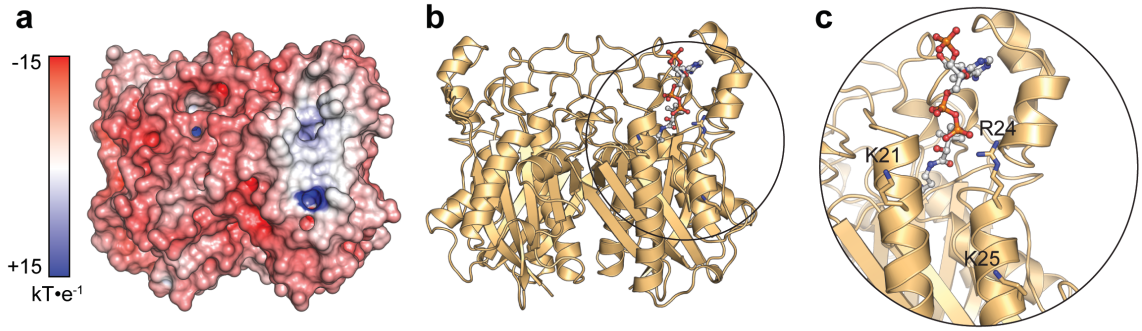

Figure 1.11: *EcACP–FabH interactions and electrostatics*. (a) Electrostatic potentials mapped onto the surface of FabH, which demonstrates a positive patch in the same region as residues assayed by Rock and coworkers. (b) Overall topology of FabH dimer shown as cartoon. CoA (ball and stick) is shown accessing the active site and residues assayed by Rock and coworkers. (c) A closer view of the FabH positive patch with assayed residues shown as ball and stick. CoA is represented with carbon (white), oxygen (red), nitrogen (blue), and phosphate (orange).

electrostatic interactions and salt bridges that serve to lock the EcACP–FabB interaction in place.

While no other structures of type II ACP–KS complexes are currently available, a biochemically validated computational model of the EcACP–FabH complex was generated using the NMR structure of EcACP (PDB: 1ACP) and the crystal structure of EcFabH (PDB: 1HNK, 1.9 Å).[46] In this model, helix II of EcACP forms extensive contacts with conserved positively charged residues near the active site entrance of FabH. Alanine scanning and charge swap mutations of residues Lys214, Arg249, and Lys256 result in a 100-fold or greater decrease in FabH activity.[47] Additionally, electrostatic potential maps of FabH demonstrate an overall negative electrostatic potential except for a positive patch near the enzyme active site that corresponds to the three mutated residues (Figure 1.11). These results have provided the best model to date of the ACP–FabH complex.

With the recent structure of ACP=FabB, our understanding of ACP–KS interactions have markedly improved. Currently, no complex of ACP=FabF or ACP=FabH has been reported, but the recent development of new probes may provide these results in the near future.[48–50] High-resolution structures of all *E. coli* KSs in complex with EcACP may provide answers to long-standing questions regarding the specific roles of FabF and FabB in *E. coli* FAS. These data would certainly aid efforts to engineer FAS and PKS pathways.

Section 1.7 ACP–KR Complex

In type I and type II FAS, KRs are responsible for the NAD(P)H-dependent reduction of β-ketoacyl-ACP to β-hydroxyacyl-ACP (Figure 1.1). KRs are in the large family of short-chain dehydrogenase/reductase enzymes that utilize a Rossmann fold to bind an NAD(P)H

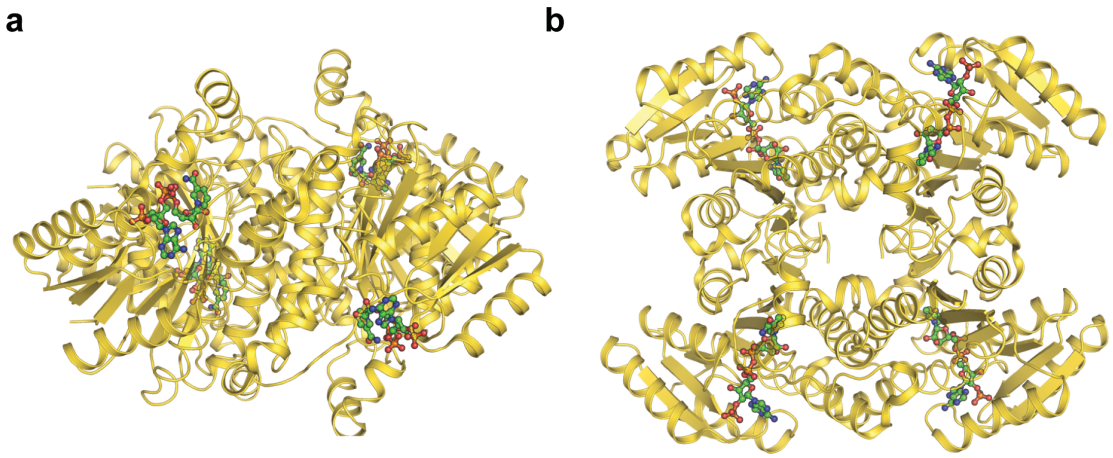

Figure 1.12: *Overall topology and structure of the E. coli KR (FabG) with NADP⁺ bound.* (a) Side view of the FabG tetramer (yellow). (b) Top view of the FabG tetramer. NADPH is represented with carbon (green), oxygen (red), nitrogen (blue), and phosphate (orange).

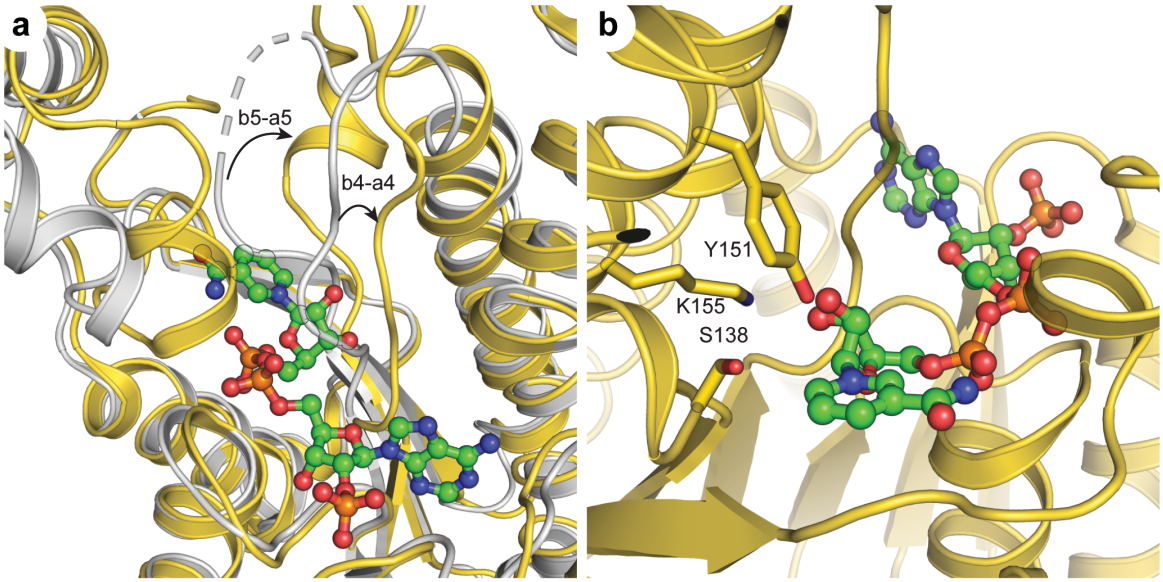

Figure 1.13: *Substrate-induced rearrangements of FabG.* (a) Overlay of EcFabG in its apo- (light-gray) and NADP⁺-bound (yellow) forms (apo-EcFabG PDB: 1I01, 2.6 Å; NADP⁺-bound EcFabG PDB: 1Q7B, 2.05 Å). Movements in the β4-α4 and β5-α5 loops are indicated in the figure. Regions with no defined density in the β5-α5 loops from apo-EcFabG are shown connected as dashed lines. Upon binding of the NADP⁺ cofactor, these loops move substantially, and the β5-α5 loop changes from an unstructured region with poor density into a well-defined helical segment in the NADP⁺-bound structure. (b) A closer view of the NADP⁺-bound cofactor along with the putative catalytic residues Tyr151, Lys155, and Ser138. In both panels NADP⁺ is represented with carbon (green), oxygen (red), nitrogen (blue), and phosphate (orange).

cofactor. A conserved Ser-Lys-Tyr triad is used to protonate the alkoxide formed by NADPH-dependent hydride reduction of the b-keto species.[51] KRs exist as tetramers and share the same fold and family as the ERs (Figure 1.12).

In *E. coli* and other bacteria, KRs are essential enzymes for cell viability.[32,52] Despite the importance of KRs and their potential as a target for antibiotic discovery, these enzymes are not well characterized in comparison with other FAS catalytic enzymes, specifically their ER cousins which are established drug targets.[53–55] Structural interest in these enzymes has increased as of late[52,56–58], but there are still no structures of an ACP–FabG complex or any relevant crosslinking probes to aid in these efforts.

Work in the early 2000s provided the KR structure from *Brassica napus* in complex with the $NADP^+$ cofactor (PDB: 1EDO, 2.3 Å) as well as the *E. coli* KR (FabG) in its *apo*-form (PDB: 1I01, 2.6 Å) and $NADP^+$ bound form (PDB: 1Q7C, 2.5 Å).[51,59,60] Comparison of the *apo*- and $NADP^+$-bound structures reveal significant structural rearrangements in the β4-α4 and β5-α5 loops that occur upon binding the $NADP^+$ cofactor (Figure 1.13). These structural changes serve to organize the KR active site and prepare the enzyme for association with ACP. Binding studies demonstrate that NADPH binds with slight negative cooperativity, which is markedly enhanced in the presence of ACP.[59,60] It was found that in the presence of NADPH, ACP binds tighter and in a 1:4 EcACP:FabG ratio, indicating that the active site rearrange- ments that occur upon cofactor binding organize a higher affinity binding site for ACP. Extensive interactions between the subunits of the tetrameric KR allow the transmission of conformational changes from one monomer to another, which provides a mechanism for controlling the binding and release of NADPH/$NADP^+$ and ACP.[59,60]

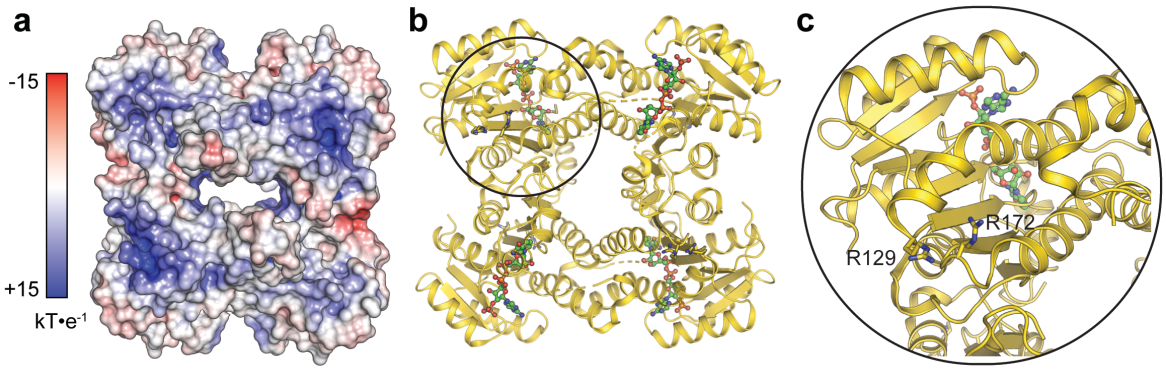

Figure 1.14: *EcACP–FabG interactions and electrostatics.* (a) Electrostatic potentials mapped onto the surface of FabG, which demonstrates a positive patch in the same region as the residues assayed by Rock and coworkers. (b) Overall topology of FabG tetramer with four bound $NADP^+$ molecules. Positive patch residues, Arg129 and Arg172, are also shown as balls and sticks. (c) A closer view of the FabG positive patch residues. $NADP^+$ is represented with carbon (green), oxygen (red), nitrogen (blue), and phosphate (orange). Potentials determined using the Adaptive Poisson-Boltzmann Solver126–129 and measured in atomic units (kT•e–1).

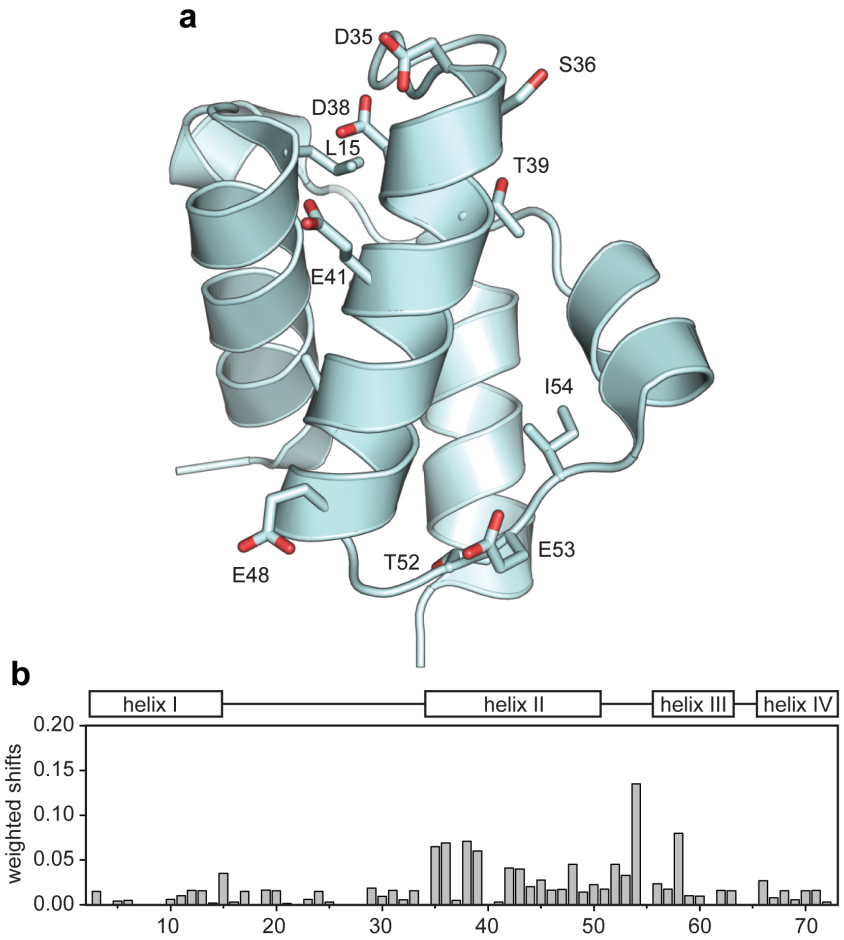

Figure 1.15: *EcACP–FabG NMR titration studies.* (a) The 10 largest CSP shifts shown on ACP from NMR titration experiments between EcACP and EcFabG. Residues are shown as sticks and colored by atom with carbon (pale cyan), oxygen (red), and nitrogen (blue). (b) Weighted CSPs of EcACP titrated with FabG. Residues possessing the 10 largest CSPs are shown are sticks. Data were interpreted from studies performed by Rock and coworkers.[47]

Electrostatic potential mapping of FabG identified a hydrophobic patch surrounded by a series of lysine and arginine residues on the enzyme surface adjacent to the entrance of the active site (Figure 1.14).[54] Mutating two of the conserved arginine residues, Arg129 and Arg172, in this region to either alanine or glutamate resulted in a nearly 10-fold loss in KR activity with ACP substrates, which was further confirmed by a marked loss in binding using a fluorescence resonance energy transfer (FRET)-based assay.[47] NMR titration experiments also identified helix II as the primary interaction motif for the EcACP–FabG complex along with additional residues on loop II (Figure 1.15). These results fit well with our current knowledge of ACP–PP interfaces, but little work has been done in the past decade to further elucidate the effects of ACP substrate recognition by FabG or the NADPH-mediated allosteric events that occur upon binding and catalysis.

ACP–DH Complex

During the course of FAS, DHs catalyze the dehydration of β-hydroxyacyl-ACP produced by KR-catalyzed reduction, producing enoyl-ACPs. *E. coli* and many other α and γ-protobacteria possess two dehydratases, FabA and FabZ. FabA and FabZ are complementary enzymes with distinct substrate chain length preferences and activities.[38] *E. coli* FabA, in addition to catalyzing the dehydration of β-ketoacyl-ACPs, possesses a unique isomerization activity that is responsible for the introduction of *cis*-unsaturation into FAs (Figure 1.1). It is important to note that FabA and FabZ-catalyzed dehydration is reversible and under equilibrium conditions the β-hydroxyacyl precursor is favored; therefore, downstream transformations are responsible for driving forward FAS.[61–63] Thus, the relative rates of association and dissociation, and consequently the protein–protein interactions

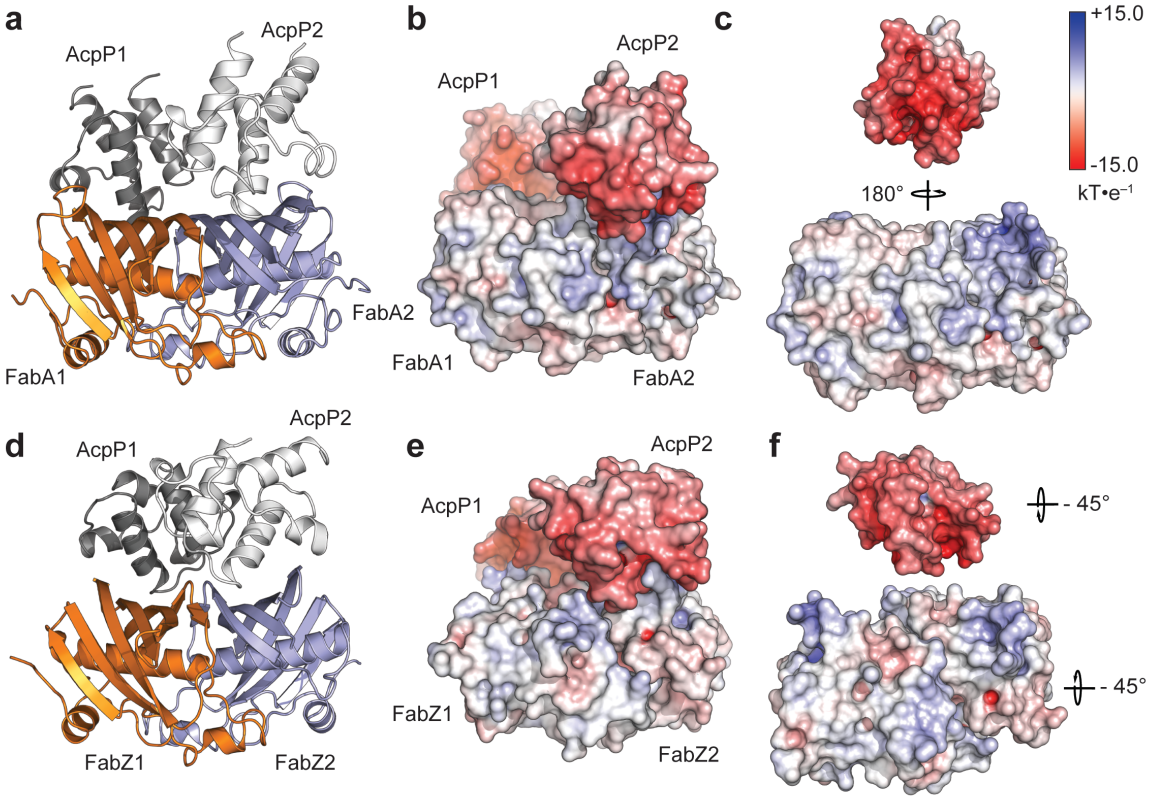

Figure 1.16: *Comparison of the topologies and electrostatic potentials of $EcACP_2$=$FabA_2$ (a–c) and $EcACP_2$-$FabZ_2$ (d–f) dimer subunit*. Note that the so-called positive patch in the $EcACP_2$=$FabA_2$ is formed exclusively by a single FabA monomer, whereas the corresponding "positive patch" in the $EcACP_2$–$FabZ_2$ involves residues from both FabZ monomers. Potentials determined using the Adaptive Poisson-Boltzmann Solver[64–67] and measured in atomic units (kT•e–1).

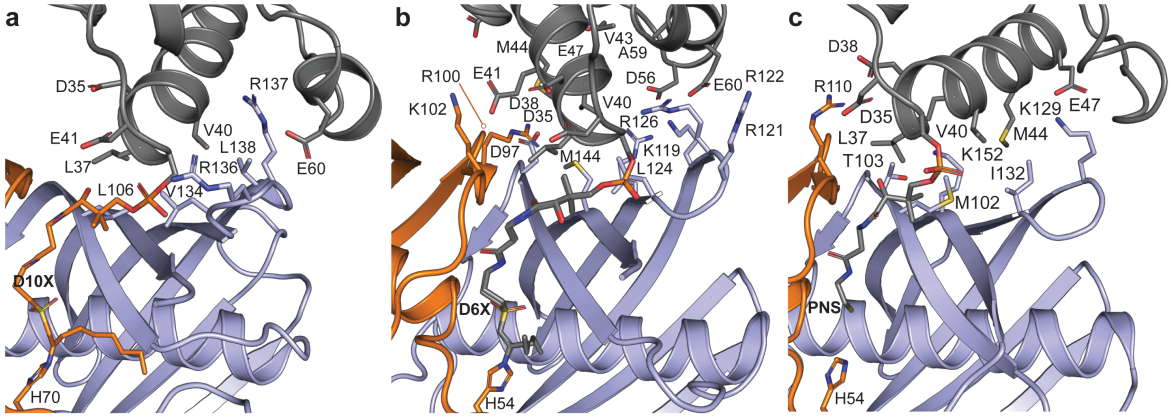

Figure 1.17: *Interfaces between the dehydratases FabA and FabZ with EcACP*. EcACP is shown in grey and the subunits of the FabA and FabZ dimer are shown in orange and light blue. (a) Interface between EcACP and EcFabA from the crosslinked EcACP2=FabA2 (PDB: 4KEH, 1.9 Å). (b) Interface between EcACP and EcFabZ from the crosslinked EcACP6=FabZ6 (unpublished results). (c) Interface between HpACP and HpFabZ from HpACP1–HpFabZ2 structures (PDB: 4ZJB, 2.55 Å). Residues that form the interface between the carrier protein and the DHs are labeled and colored according to the monomer components to which they belong. D10X: a sulfonyl-3-alkyne-based crosslinker (5, Fig. 3) that mimics FabA's preferred decanoyl substrate; D6X: a sulfonyl-3-alkyne-based crosslinker that mimics FabZ's preferred hexanoyl substrate; PNS: phosphopantetheine cofactor.

between the various FA synthases and EcACP play a central role in determining the FA profile of *E. coli*.

In 2014, Tsai, Burkart and coworkers reported the 1.9 Å crosslinked structure of EcACP=FabA (Figure 1.16a).[68] Crosslinking was carried out using a chemoenzymatically modified EcACP (crypto-EcACP), bearing a mechanistic crosslinking probe that would react between the various FA synthases and EcACP play a central role in determining the FA profile of *E. coli*. In 2014, Tsai, Burkart and coworkers reported the 1.9 Å crosslinked structure of EcACP=FabA (Figure 1.16a).[68] Crosslinking was carried out using a chemoenzymatically modified EcACP (crypto-EcACP), bearing a mechanistic crosslinking probe that would react with the nucleophilic active site residue, His70. This approach has proven successful not only in trapping the transient complex EcACP–FabA complex but also, by virtue of the probe's selectivity for FabA's active site His70, ensures that crosslinking preserves the complex in a functionally relevant state.

The crosslinked EcACP=FabA complex was crystallized as a 2:2 structure in agreement with experimental sizing data. The interaction between the carrier protein and the dehydratase is primarily electrostatic in nature with EcACP providing negatively charged residues that interact, via salt bridge interactions, with the "positive patch" of Arg and Lys residues found on the surface of FabA (Figure 1.16). In particular, Glu41, Glu47, Glu53, Asp56, and Glu60 of EcACP form salt-bridge interactions with R132, R136, and R137, and K161 residues within the "positive patch" of FabA (Figure 1.17a). The importance of the positively charged residues of FabA was evaluated by performing crosslinking experiments on various "charge-swapped" mutants of FabA, including the R132E, R136E, R137E, and K161E mutants; these mutants show reduced crosslinking activity toward crypto-EcACP

designed to target His70. Nonetheless, not all interactions at the interface are electrostatic in nature.

The salt bridges enumerated above are complemented by hydrophobic interactions involving EcACP's Leu37, Val40, and Met44 as well as FabA's Leu106, Val134, Leu138, and Met140.[68,69] Zhang and coworkers have reported a 2.55 Å noncovalent complex structure of *H. pylori* EcACP3-FabZ6.[70] The authors propose, on the basis of the 1:2 ACP to DH stoichiometry of the crystallized structure, that FabZ operates via a see-saw mechanism whereby each monomer of the dimeric FabZ subunit alternates in binding and reacting with the EcACP. Closer inspection of the electron density suggests that the 1:2 ACP to DH stoichiometry may be the consequence of crystal packing effects as an ACP from the nearest neighboring asymmetric unit actually engages the "open" FabZ binding site "observed" in the asymmetric unit (Figure 1.18). As is observed in the EcACP=FabA structure, the protein-protein interface between the carrier protein and FabZ subunit is dominated by electrostatic interactions. Zhang and coworkers have identified the following interactions: EcACP's Asp35 and Asp38 forms salt bridge interactions with Arg110 of FabZ; Glu41 and Glu47 form salt bridges with Lys152 and Lys129, respectively. In addition to these polar interactions, EcACP's Leu37, Val40, and Met44 interact with a hydrophobic patch on FabZ formed by Met102, Thr103, and Ile132.

More recently, Burkart, Smith, and coworkers have reported the structure of a 2.6 Å crosslinked EcACP=FabZ6 structure.[71] This structure differs from the structure reported by Zhang and coworkers in that it features 1:1 ACP to DH binding stoichiometry, suggesting that the active sites of all FabZ monomers can be engaged simultaneously. In order to solubilize FabZ for chemical crosslinking, a protein, Morc, was fused to the N-terminus of

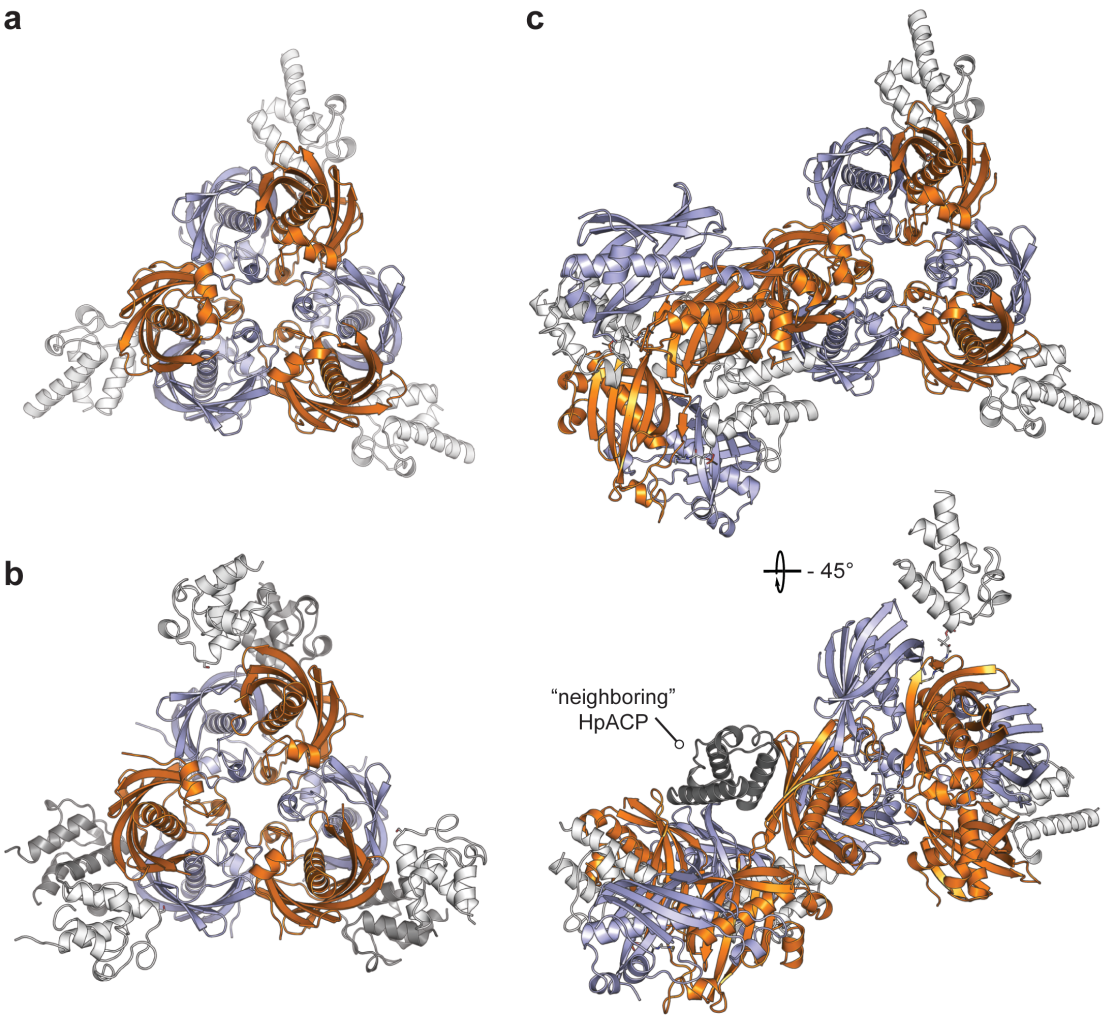

Figure 1.18: *Comparison of Zhang and coworkers' holo-HpACP•FabZ and Burkart and coworkers' EcACP=FabZ structures.* (a) Functional hexameric *holo*-hpACP–hpFabZ complex. (b) Hexameric EcACP=EcFabZ (asymmetric unit, EcACP6=EcFabZ6) reported by Burkart, Smith and coworkers. (c) Structure of the holo- HpACP–HpFabZ hexamer and components of its nearest neighbor, illustrating the packing of an ACP from this neighbor onto the open ACP-binding site.

the dehydratase. The resulting FabZ-Morc fusion protein was subjected to crosslinking using a 3-alkynyl-sulfone-pantetheinamide mimetic of hexanoyl-EcACP. Interestingly, crosslinking performed using a mimic of β-hydroxydecanoyl-EcACP yielded only 10% crosslinked product; however, a mimic of FabZ's preferred substrate, β-hydroxyhexanoyl-EcACP crosslinked much more efficiently. After crosslinking, the fusion protein was site-specifically cleaved from the crosslinked construct using TEV protease. Like FabA, FabZ reacted with the probe molecules through its active site histidine, His54. In contrast to FabA, both monomers of the dimeric FabZ subunit form contacts with EcACP. In fact, most of the protein–protein interactions formed between the carrier protein and FabZ involve the FabZ monomer not crosslinked to the carrier protein. Likely owing to this "multi-monomer" interface, the FabZ dimer buries a surface area of 745 $Å^2$ at the interface, a much larger area of EcACP than does FabA (~530 $Å^2$) in the EcACP=FabA structure.[68] The protein-protein interface between the FabZ and EcACP features a number of ionic interactions. Asp35, Asp38, and Glu41 form salt bridge interactions with Arg100 and Lys102 of the crosslinked FabZ monomer, and Lys119, Arg121, Arg122, and Arg126 of the noncrosslinked FabZ monomer interact with Glu41, Glu47, Glu48, and Asp56 (Figure 1.17). Hydrophobic interactions at the interface involve EcACP and the noncrosslinked monomer with Leu124 and Met144 of FabZ forming van der Waals contacts with Leu37, Val40, Val43, Met44, and Ala59.

Section 1.9 ACP–ER Complex

The ER, like the KR, is an NAD(P)H-dependent reductase that catalyzes the reduction of enoyl-ACP to acyl-ACP. Most ERs are also found in the short-chain

dehydrogenase/reductase enzyme family and share the same tetrameric fold as their KR cousins.[51,72,73] There are some exceptions to this rule. For instance, Streptococcus pneumoniae uses FabK, a flavin-dependent reductase, to reduce enoyl-ACPs.[72] Little is known about ACP interactions with the FabK class of ERs. Interestingly, the FabK class of ERs is similar to the ER domains of yeast type I FAS.[73] The ER plays an important role in regulating FAS and has long been considered to be the rate- limiting step in the cycle.[74] Early studies show that palmitoyl-ACP inhibits EcER, FabI, indicating that the ER also serves as a site for feedback inhibition in FAS.[75] Bacteria typically encode a single ER, and given their importance in controlling flux in FAS, they serve as a promising target for the development of antibiotics.[74] The ERs, FabI from *E. coli* and InhA from *Mycobacterium tuberculosis*, are confirmed targets of triclosan and isoniazid, respectively.[53–55,76,77] As such, most of the ER structural work has been focused on the development of inhibitors instead of the evaluation ACP–ER protein–protein interactions.

The *apo*- and NAD^+-bound structures of FabI (PDB ID: 5CF2, 1DFI), as in KRs, also show structural rearrangements near the active site upon cofactor binding.[78] These rearrangements may also organize the ER for ACP binding events. A structure of *E. coli* FabI in complex with EcACP has been solved (PDB: 2FHS, 2.7 Å), but the ACP is poorly resolved (Figure 1.19).[79] Helix II appears to serve as the recognition motif, as it packs closely with FabI's α8 helix, but the residues at the EcACP–FabI interface are unresolved. Short MD simulations performed on the EcACP–FabI complex indicate that the PPant tethered substrate can enter through a smaller active site tunnel (minor portal) adjacent to EcACP Ser36 (Figure 1.20). These results conflict with a structure of InhA in complex with a trans-

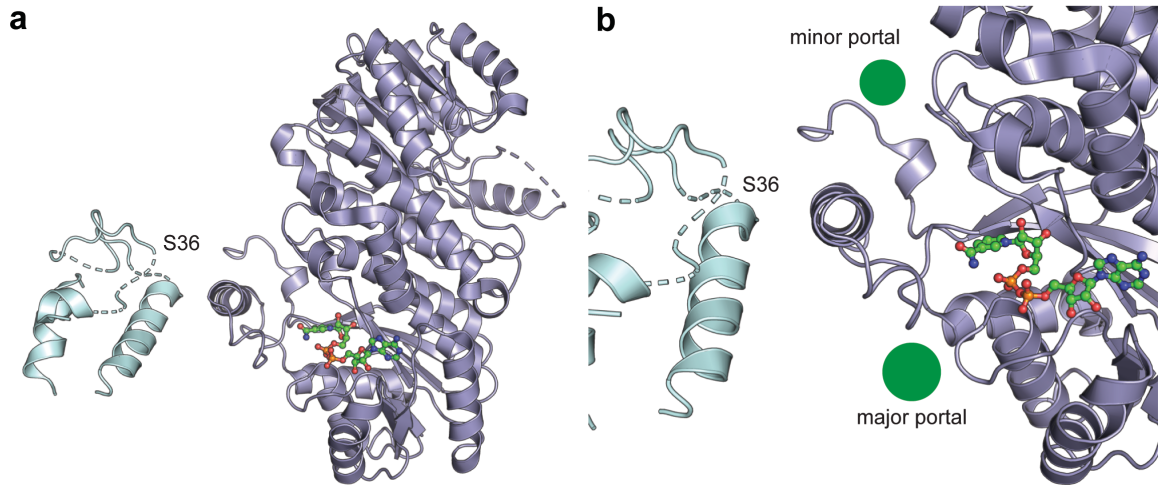

Figure 1.19: *Overview of EcACP–EcFabI structure (PDB: 2FHS, 2.7 Å).* (a) Top view of EcACP bound to a dimer of two ER (purple) monomers at a 1:2 ratio. (b) A closer view of the interface of ACP and FabI with the minor and major portal entrances to the FabI active site indicated in the panel. ACP is colored as pale cyan and the unresolved portions of the structure are shown as dotted lines. The bound $NADP^+$ cofactor is represented with carbon (green), oxygen (red), nitrogen (blue), and phosphate (orange).

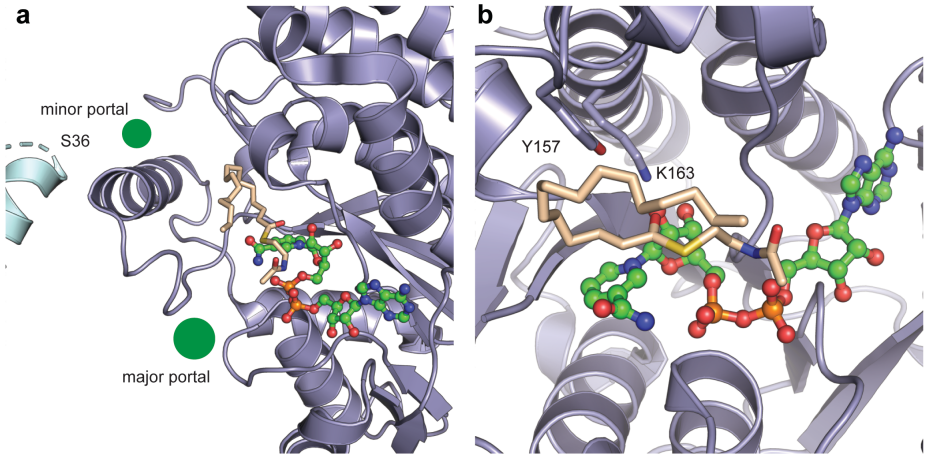

Figure 1.20: *Comparison of the EcACP–EcFabI structure (PDB: 2FHS, 2.7 Å) to SNAC-palmitate-bound M. tuberculosis FabI (PDB: 1BVR, 2.8 Å).* (a) ACP is shown oriented toward the minor portal, which is the purported substrate entrance by Rafi and coworkers.[79] The bound SNAC-palmitate molecule, wheat colored, from 1BVR (InhA) is overlaid with the EcACP•FabI structure for comparison. The orientation of SNAC-palmitate indicates that the substrate entrance may be through the major portal. (b) A closer view of the active site-bound SNAC-palmitate molecule (InhA, PDB: 1BVR, 2.8 Å). Active site residues (Tyr157 and Lys163) and the $NADP^+$-bound cofactor demonstrates that the 3-position of the SNAC-palmitate group is well positioned for hydride reduction.

2-hexadecenoyl-(N-acetylcysteamine)-thioester substrate analog (PDB: 1BVR, 2.8 Å), which suggest a different results conflict with a structure of InhA in complex with a trans-2-hexadecenoyl-(N-acetylcysteamine)-thioester substrate analog (PDB: 1BVR, 2.8 Å), which suggest a different entrance to the ER active site, the major portal (Figure 1.20).[80] Without more concrete structural evidence on the ACP–ER interface, no definitive conclusions can be drawn. Recent efforts have been made to develop noncovalent crosslinking probes to enhance the affinity between the ACP and the ER, but new structural and/or biochemical information has not yet been reported.[81]

ACP–PP Interactions Outside of FAS

The "EcACP interactome" includes 21 catalytic partners that are involved in FAS, haemolysin, lipid A, lipoic acid, and biotin pathways (Figure 1.2b). Furthermore, it expands to even greater numbers when including ACP–PP interactions with metabolic regulatory elements.[41,82–85] These other distinct pathways often "intercept" intermediates produced during FAS. For example, LipB encodes an octanoyl-ACP-protein transferase that specifically recognizes octanoyl-ACP and transfers the octanoyl group from ACP to lipoyl-accepting domains for further modification to lipoic acid, an essential metabolic cofactor.[86,87] A similar process occurs in the lipid A pathway, the Raetz Pathway[88], where LpxA, LpxD, LpxL, and LpxM are transferases that specifically utilize ACP-derived FAS intermediates as substrates. LpxA and LpxD both show strong preference for b-hydroxymyristoyl-ACP, while LpxL and LpxM show a higher preference for lauroyl-ACP and myristoyl-ACP, respectively.[89–93] Production of the active exotoxin haemolysin HylA, a class of pore forming toxins secreted by Gram-negative bacteria, also requires an ACP-dependent AT, HylC, which

activates the HylA protein by attaching a FA to proHylA, HylA zymogenic precursor.[94–96] The general biotin pathway, as shown in Figure 1.21, provides an even more unique use of ACP by first using the methyltransferase BioC to methylate malonyl-CoA to produce a malonyl-ACP methyl ester.[97] Formation of the methyl ester allows entrance into the FAS pathway for two rounds of elongation and reduction to deliver pimeloyl-ACP methyl ester. An esterase, BioH, then hydrolyzes the methyl ester to produce pimeloyl-ACP, which then associates with BioF, generating 7-keto-8-aminopelargonic acid by condensing alanine and pimeloyl-ACP.[97,98]

All known ACP-dependent pathways on the periphery of FAS are either directly linked to cell viability or play a role in virulence. Therefore, it is important to understand how these secondary metabolic enzymes can recognize and intercept specific ACP-tethered FAS pathway intermediates. Several structures of ACP in complex with enzymes outside of FAS have been reported, but they will not all be discussed here[99,100]; we will instead focus on two recently characterized complexes available from the list of ACP PPs, namely EcACP•BioH from the biotin pathway and EcACP•LpxD from the lipid A pathway.[90,98]

ACP–BioH

Biotin is a required cofactor for acetyl-CoA carboxylase, which converts acetyl-CoA to malonyl-CoA. Therefore, biotin participates in the production of malonyl-CoA, and subsequently malonyl-ACP, which is used for every condensation reaction during FAS.[101] The order of catalysis in the biotin pathway remained cryptic until 2012.[102] In the pathway shown in Figure 1.21, the malonyl-ACP methyl ester undergoes two rounds of elongation to form pimeloyl-ACP methyl ester. In order to prevent further chain extension, the ester group

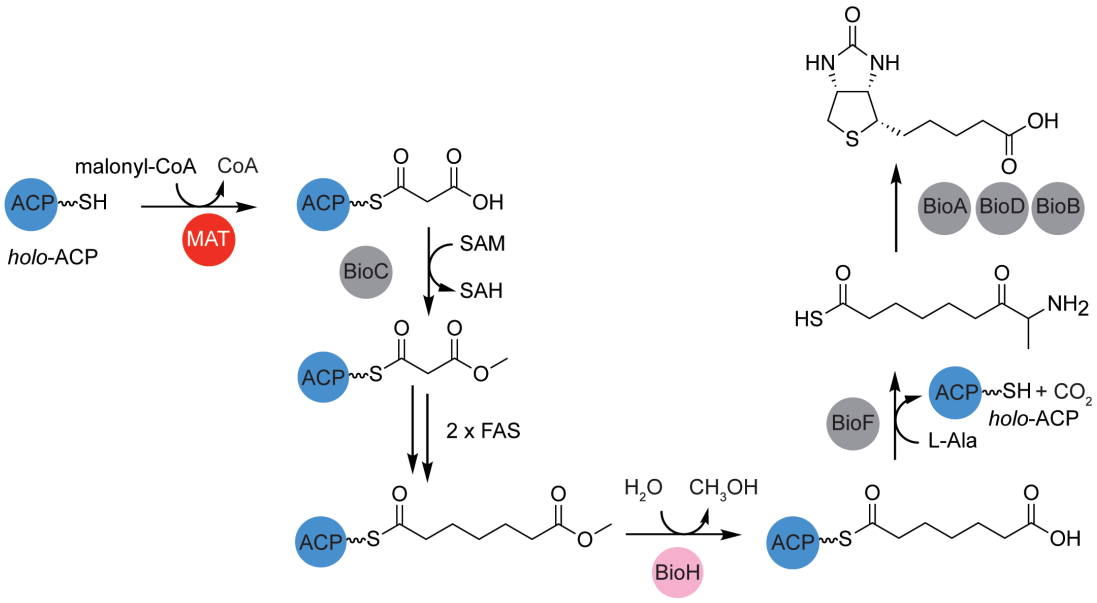

Figure 1.21: *Biotin biosynthetic pathway*. The pathway begins with the loading of malonyl-CoA onto holo-ACP and ending with the production of biotin. The catalytic step performed by BioH (bottom center) converts pimeloyl-ACP methyl ester to pimeloyl-ACP through hydrolysis of the methyl ester to the carboxylic acid.

must be removed by a gatekeeper enzyme. The gatekeeper was thought to be BioH, but the esterase is promiscuous and has been shown *in vitro* to act on a variety of short-chain p-nitrophenol esters.[103]

Additionally, the subsequent enzyme in the pathway, BioF, can also perform the gatekeeper function, as it consumes the thioester group and later enzymatic steps could hydrolyze the remaining ester.[102] Ambiguity in the pathway was resolved upon the elucidation of a 2.05 Å structure of pimeloyl-ACP methyl ester in complex with an S82A mutant of BioH (PDB: 4ETW, 2.05 Å).[98] The structure shows that pimeloyl-ACP methyl ester binds to the N-terminal 4-helical lid domain of BioH and the ester moiety is positioned at the active site for hydrolysis (Figures 1.22 and 1.23).

The ACP•BioH interface is comprised of electrostatic interactions formed between ACP's helix II and a positive patch near the BioH active site entrance. Arg155 and Arg159 of BioH coordinate between ACP helices II and III, thereby facilitating chain flipping of the ACP cargo into the BioH active site (Figure 1.22). The PPant arm, along with its pimeloyl tethered substrate, forms hydrophobic interactions along the PPant binding tunnel and substrate-binding pocket (Figure 1.23). In the BioH active site, the carbonyl methyl ester rests 3.1 Å away from Ala82 (S82A), in a catalytically competent conformation. These results taken together demonstrate that pimeloyl-ACP methyl ester is the native substrate of BioH, thereby confirming BioH as the pathway gatekeeper.

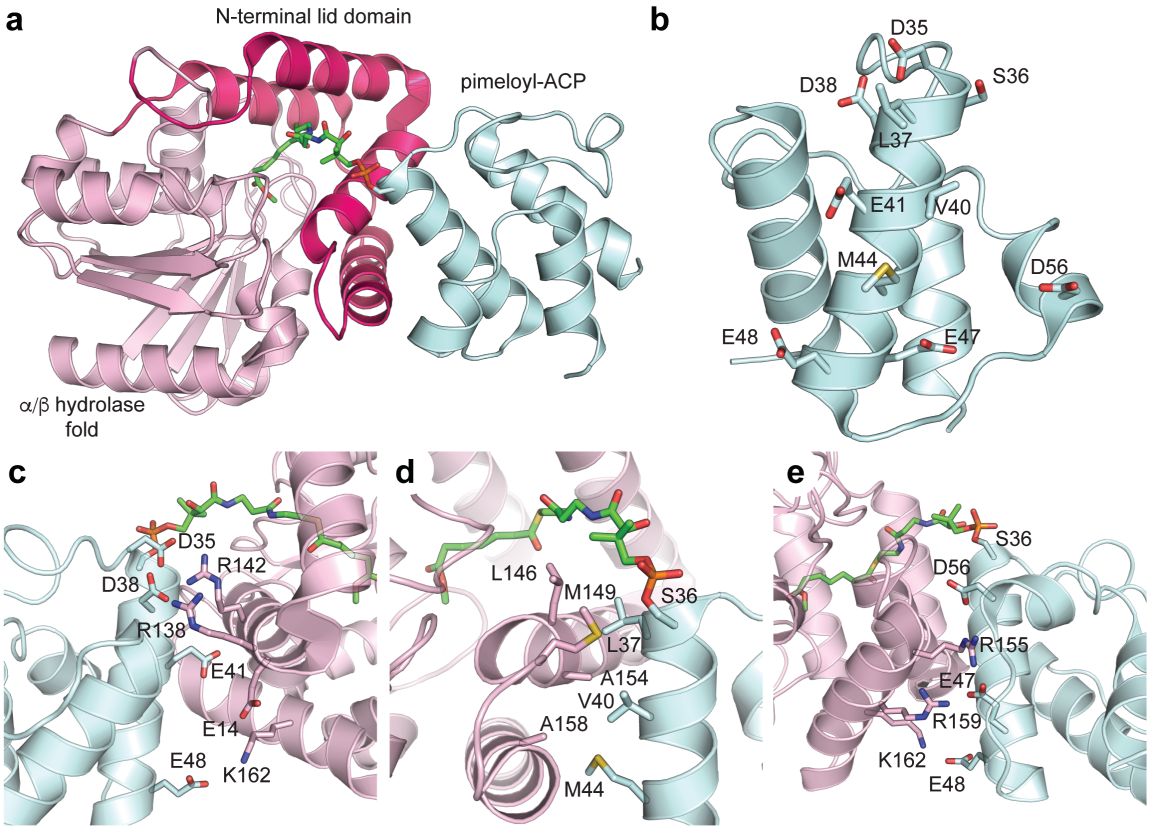

Figure 1.22: *EcACP–BioH complex and protein–protein interactions.* (a) Overview of the 1:1 pimeloyl-EcACP–BioH structure (PDB: 4ETW, 2.05 Å). The N-terminal lid domain and the a/b hydrolase core fold are colored as light pink and hot pink, respectively. The ACP is colored pale cyan. The PPant probe is represented with carbon (green), oxygen (red), nitrogen (blue), and phosphate (orange). (b)ACP residues that form contacts within 4 Å of BioH. (c) Electrostatic contacts as seen along helix II of ACP. (d) Hydrophobic interactions between ACP and BioH at the top of ACP helix II (PPant probe not shown for viewing purposes). (e) Electrostatic interactions along the helix II-loop II-helix III region of ACP.

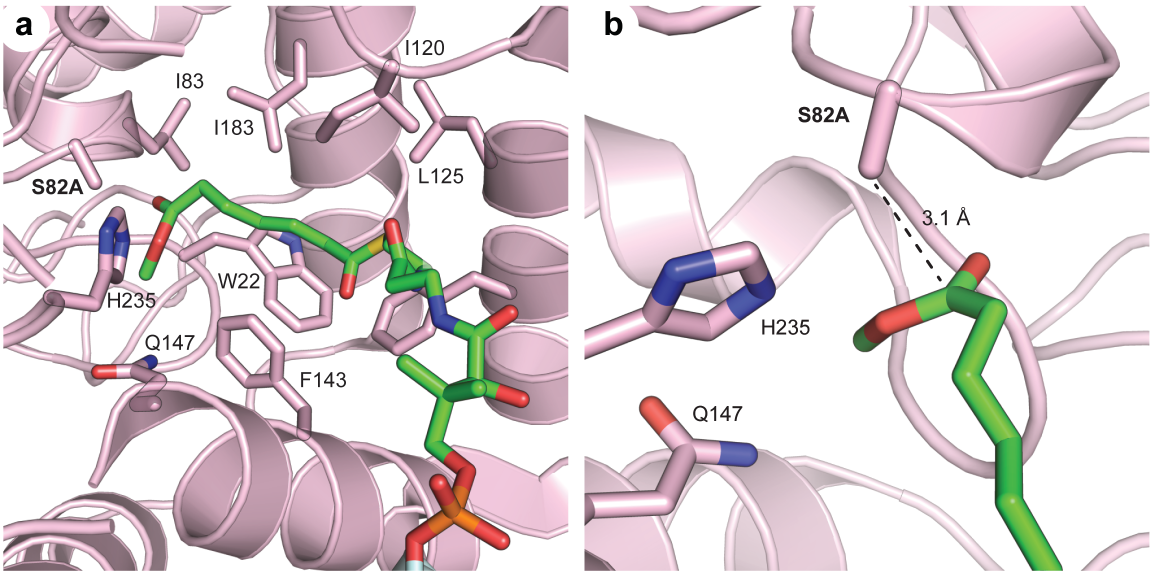

Figure 1.23: *Pimeloyl ACP methyl ester active-site interactions.* (a) Hydrophobic residues coordinate the PPant arm and tethered pimeloyl methyl ester group. The catalytic serine residue is replaced by alanine in the structure and is labeled in bold (b) BioH active-site Ser/His/Gln catalytic triad is well positioned to catalyze hydrolysis of pimeloyl methyl ester. (PDB: 4ETW, 2.05 Å). BioH is colored light pink and residues are represented as sticks with atoms colored carbon (light pink), oxygen (red), and nitrogen (blue). The PPant probe is represented with carbon (green), oxygen (red), nitrogen (blue), and phosphate (orange).

ACP–LpxD

Lipid A is a component of the lipopolysaccharides, also known as endotoxins, found on the outer membrane of Gram-negative bacteria. The lipid A portion is a disaccharide comprised of two glucose units connected through β(1-6) linkages and six esterified FA-derived acyl groups (Figure 1.24).[93] All of the esterified FAs are supplied by ATs that specifically require acyl-ACP as a substrate. Solved structures of EcACP in complex with LpxD, the uridine diphosphate (UDP)-3-*O*-acyl-glucosamine *N*-AT that catalyzes the fourth step of the lipid A pathway (Figure 1.24), provide a unique insight into the catalytic role of ACP–PP and substrate–PP interactions.[90,104]

LpxD is a trimeric enzyme with a globular N-terminal uridine binding domain, a core lipid binding domain comprised of a 10-coil left-handed β-helix, and a C-terminal helical extension comprised of two helices. An overview of the general structure and topology of LpxD is provided in Figure 1.25. Raetz, Pemble, and coworkers solved the ACP–LpxD complex in three distinct catalytic states. The first is with the bound β-hydroxy-myristoyl-ACP substrate (PDB: 4IHF, 2.1 Å), the second is a "hydrolyzed-intermediate" with *holo*-ACP bound alongside β-hydroxy-myristic acid (PDB: 4IHG, 2.89 Å), and the third is in complex with the enzyme product, *holo*-ACP (PDB: 4IHH, 2.13 Å).[90] Additionally, there are two molecules of β-hydroxymyristate present in the "hydrolyzed- intermediate" structure (second state). One is derived from the hydrolysis of β-hydroxy-myristoyl-ACP, whereas the other is bound to a hydrophobic region that coordinates the *O*-acyl group of the acyl acceptor, UDP-3-*O*-acyl-glucosamine. In this complex, the amine of UDP-3-*O*-acyl-glucosamine would be well positioned to attack the β-hydroxy-myristoyl-ACP thioester, thereby facilitating the transfer of the acyl unit. These structures together represent three distinct

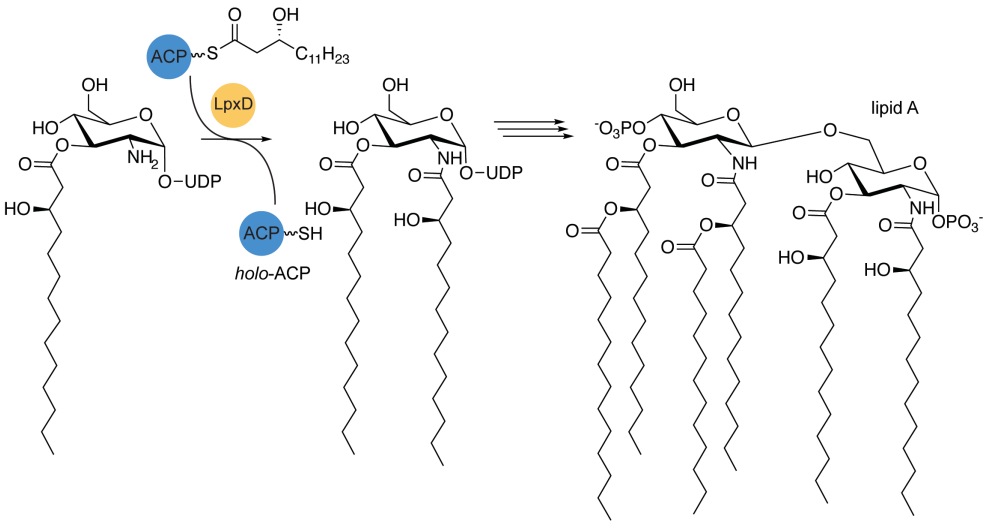

Figure 1.24: *Overview of the LpxD catalyzed reaction in lipid A biosynthesis*. LpxD catalyzes the fourth step in the Lipid A pathway by converting UDP-3-*O*-acyl-glucosamine to UDP-2-*N*-3-*O*-bisacyl-glucosamine. The final product of the 10-step pathway, Lipid A, is shown and the acyl groups transferred by LpxD from ACP are shown in light orange.

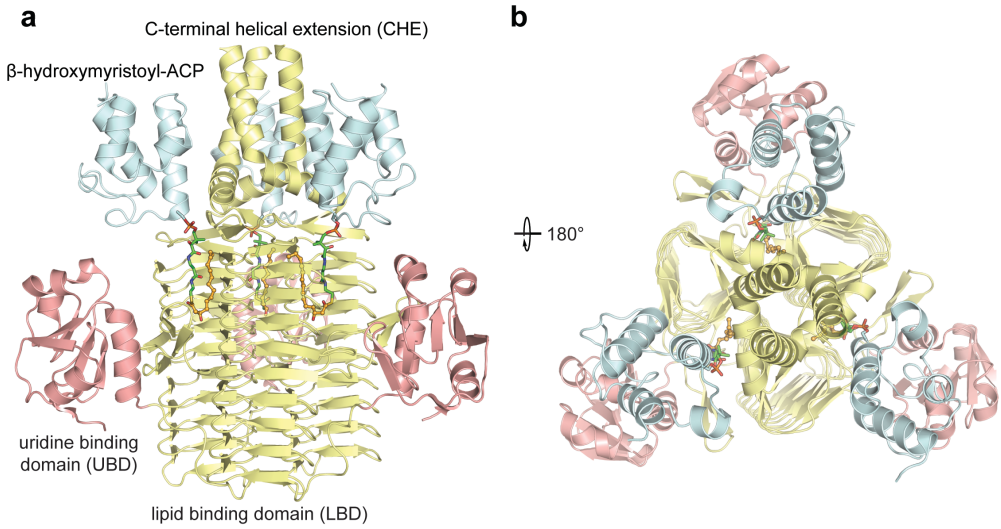

Figure 1.25: *Overview of the EcACP–LpxD complex (PDB: 4IHF, 2.1 Å).* (a) The overall topology of the β-hydroxymyristoyl-ACP-bound structure with ACP colored pale cyan, the uridine binding domain (UBD) colored light pink and the core lipid binding domain and C-terminal helical extension colored pale yellow. (b) The same complex but viewed from the top. The PPant probe is represented with carbon (green), oxygen (red), nitrogen (blue), and phosphate (orange).

states that occur along the catalytic trajectory of lipid transfer from β-hydroxymyristoyl-ACP to the amino group of UDP-3-*O*-acyl-glucosamine.

In the ACP–LpxD structures, three ACPs bind at the C-terminal region of the LpxD trimer. Each ACP forms extensive contacts with the C-terminal helical extension (CHE) and lipid-binding domain (LBD) domains and buries a surface area of 530 $Å^2$. The protein–protein interactions are primarily electrostatic in nature and are provided by helix II, loop II, and helix III. Interestingly, the ACP–LpxD interface contacts are notably different, specifically along the loop II–helix III region, for each catalytically trapped state (Figure 1.26). In the substrate-bound complex β-hydroxymyristoyl-ACP–LpxD, the PPant arm, and tethered β-hydroxymyristate are found in a horseshoe-like conformation. The acyl moiety forms extensive hydrophobic contacts with LpxD that are further stabilized by the PPant arm (Figure 1.26). Despite the extensive contacts between the PPant and acyl chain of β-hydroxy-myristoyl-ACP with LpxD, there are only a few interactions between the ACP loop II helix III region and the LpxD CHE. In comparison, ACP interactions in the "hydrolyzed intermediate" and *holo*-ACP–LpxD structures have markedly different PPant conformations. These changes are accompanied by alternate binding modes between ACP and LpxD, and more specifically, between the ACP loop II–helix III region and the CHE domain of LpxD (Figure 1.26). These structures indicate a distinct role for the PPant arm during catalysis, whereby conformational changes after the acyl transfer reaction encourage dissociation of the diacylated GlcN product.[90] These correlated changes in PPant and ACP binding modes suggest that both ACP-mediated protein–protein interactions and substrate–PP interactions are important for LpxD catalysis.

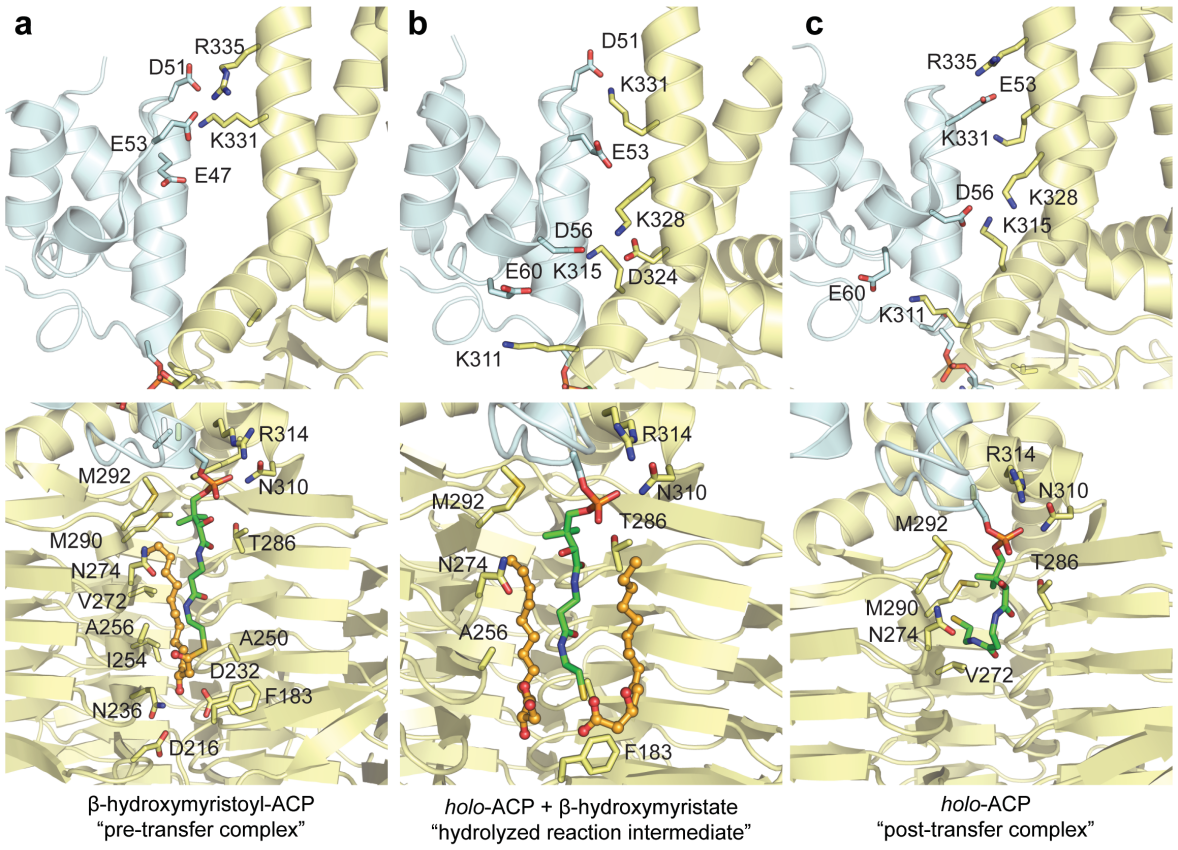

Figure 1.26: *Overview of the PPant and ACP interactions with LpxD throughout a catalytic cycle of acyl transfer from ACP to UDP-GlcNac*. In each step of the catalytic cycle, both the substrate and ACP interactions with LpxD change, indicating ACP plays an important role in catalysis. In all panels, only ACP–LpxD interactions along the helix II-loop II-helix III region of ACP are shown as the most significant changes in interactions occur here. All residues shown in the lower panels are within 4 Å of PPant. (a) β-hydroxymyristoyl-ACP-bound structure with top showing the protein–protein interactions between ACP and LpxD and the bottom showing substrate interactions between cargo-tethered PPant and LpxD. (b) Hydrolyzed ACP with two bound β-hydroxymyristate molecules representing the donor acyl group and the receiver binding site. The top panel shows the protein–protein interactions between ACP and LpxD and the bottom shows substrate interactions between cargo- tethered PPant and LpxD. All LpxD residues shown in the bottom panel are within 4 Å of PPant. (c) Holo-ACP-bound structure with top showing the protein–protein interactions between ACP and LpxD and the bottom showing substrate interactions between cargo-tethered PPant and LpxD. All LpxD residues shown in the bottom panel are within 4 Å of PPant.

Summary

Our understanding of ACP-mediated protein–protein interactions in type II FAS has expanded over the past decade. The field now has a broad picture of the elements necessary for productive interactions between an ACP and its PPs. Electrostatic interactions play a significant role in complex formation. Helix II serves as a universal binding domain, or recognition helix, while helix III serves to coordinate chain flipping of substrate from the ACP hydrophobic cleft into the active sites of PPs.

Despite the seemingly consistent nature of ACP recognition events, differences are present between complexes. NMR and crystallography data indicate that different residues are responsible for coordinating protein–protein interactions in the *E. coli* EcACP=FabB (ACP=KS) and EcACP=FabA (ACP=DH) structures. Specifically, EcACP's Asp38 has been identified as an important residue for complex formation with FabB. Interestingly, analysis of the EcACP=FabA structure indicates Asp38 makes no discernable contacts with FabA. Additionally, electrostatic surface potentials differ significantly between ACP PPs and stand as an elegant way to drive ACP interactions and decrease the amount of sampling necessary to allow complex formation. This distinction is also well demonstrated by EcACP=FabB and EcACP=FabA structures (Figure 1.27). FabB has a higher overall negative potential than FabA. This difference serves to drive ACP to the positive patch of FabB more efficiently, thereby increasing the efficacy of ACP binding events during the more complex ping-pong reaction mechanism of KSs.

Structural elucidation of ACP–PP and ACP=PP complexes has been invaluable, but x-ray models only provide a static picture and usually one that represents the lowest energy conformation. Therefore, these models cannot fully capture the dynamic nature of ACP-PP

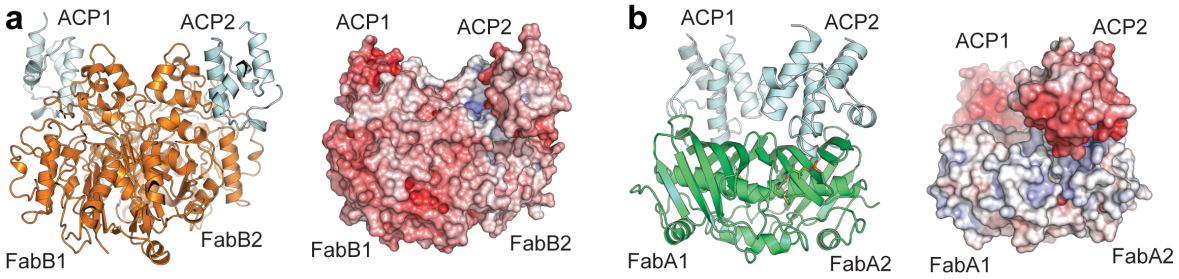

Figure 1.27: *A comparison of the electrostatic potentials of EcACP=FabB and EcACP=FabA*. Different ACP PPs have different electrostatic potentials. This point is well demonstrated by the crosslinked structures of the *E. coli* ketosynthase FabB and dehydratase FabA. Both FabA and FabB have a positive patch to bind ACP, but FabB has a much larger overall negative surface potential that serves to channel ACP to the KS active site. (A) Overall topology of EcACP=FabB and electrostatic surface potentials mapped onto structure and rendered as surface. (B) Overall topology of EcACP=FabA and electrostatic surface potentials mapped onto structure and rendered as surface.

binding events. There may be distinct intermediate states formed along a catalytic trajectory that include an “encounter complex” and/or a “dissociation complex”, as seen in the discussion regarding EcACP–LpxD. Furthermore, the role that the ACP PPant arm and its tethered substrates play in catalysis, also seen in EcACP–LpxD, has only just begun to be explored. There are clearly additional mechanisms controlling processivity in type II FAS that include ACP–substrate, ACP–PP, and substrate–PP interactions or any combination of these components accessed during binding events. The structural elucidation of ACP–PP complexes that approximate intermediate catalytic states along with thorough computational interrogation of these systems will be needed in order to develop a more in depth understanding of the complex chemical transformations mediated by type II FAS.

References

(1) Beld, J., Lee, D. J., and Burkart, M. D. (2015) Fatty acid biosynthesis revisited: structure elucidation and metabolic engineering. *Mol. Biosyst. 11*, 38–59.

(2) Hiltunen, J. K., Schonauer, M. S., Autio, K. J., Mittelmeier, T. M., Kastaniotis, A. J., and Dieckmann, C. L. (2009) Mitochondrial fatty acid synthesis type II: more than just fatty acids. *J. Biol. Chem. 284*, 9011–9015.

(3) Lynen, F. (1961) Biosynthesis of saturated fatty acids. *Fed. Proc. 20*, 941–951.

(4) Majerus, P. W., Alberts, A. W., and Vagelos, P. R. (1964) The Acyl Carrier Protein of Fatty Acid Synthesis: Purification, Physical Properties, and Substrate Binding Site. *Proc. Natl. Acad. Sci. U. S. A. 51*, 1231–1238.

(5) Majerus, P. W., Alberts, A. W., and Vagelos, P. R. (1965) Acyl Carrier Protein. IV. The dentification Of 4'-Phosphopantetheine as The Prosthetic Group of The Acyl Carrier Protein. *Proc. Natl. Acad. Sci. U. S. A. 53*, 410–417.

(6) Larrabee, A. R., McDaniel, E. G., Bakerman, H. A., and Vagelos, P. R. (1965) Acyl carrier protein. V. Identification of 4'-phosphopantetheine bound to a mammalian fatty acid synthetase preparation. *Proc. Natl. Acad. Sci. U. S. A. 54*, 267–273.

(7) Płoskoń, E., Arthur, C. J., Kanari, A. L. P., Wattana-amorn, P., Williams, C., Crosby, J., Simpson, T. J., Willis, C. L., and Crump, M. P. (2010) Recognition of intermediate functionality by acyl carrier protein over a complete cycle of fatty acid biosynthesis. *Chem. Biol. 17*, 776–785.

(8) Zornetzer, G. A., Fox, B. G., and Markley, J. L. (2006) Solution structures of spinach acyl carrier protein with decanoate and stearate. *Biochemistry 45*, 5217–5227.

(9) Holak, T. A., Kearsley, S. K., Kim, Y., and Prestegard, J. H. (1988) Three-dimensional structure of acyl carrier protein determined by NMR pseudoenergy and distance geometry calculations. *Biochemistry 27*, 6135–6142.

(10) Roujeinikova, A., Baldock, C., Simon, W. J., Gilroy, J., Baker, P. J., Stuitje, A. R., Rice, D. W., Slabas, A. R., and Rafferty, J. B. (2002) X-Ray Crystallographic Studies on Butyryl-ACP Reveal Flexibility of the Structure around a Putative Acyl Chain Binding Site. *Structure 10*, 825–835.

(11) Roujeinikova, A., Simon, W. J., Gilroy, J., Rice, D. W., Rafferty, J. B., and Slabas, A. R. (2007) Structural Studies of Fatty Acyl-(Acyl Carrier Protein) Thioesters Reveal a Hydrophobic Binding Cavity that Can Expand to Fit Longer Substrates. *J. Mol. Biol. 365*, 135–145.

(12) Cronan, J. E. (2014) The chain-flipping mechanism of ACP (acyl carrier protein)-

dependent enzymes appears universal. *Biochem. J. 460*, 157 LP – 163.

(13) Kim, Y., and Prestegard, J. H. (1989) A dynamic model for the structure of acyl carrier protein in solution. *Biochemistry 28*, 8792–8797.

(14) Crosby, J., and Crump, M. P. (2012) The structural role of the carrier protein – active controller or passive carrier. *Nat. Prod. Rep. 29*, 1111–1137.

(15) Li, Q., Khosla, C., Puglisi, J. D., and Liu, C. W. (2003) Solution structure and backbone dynamics of the holo form of the frenolicin acyl carrier protein. *Biochemistry 42*, 4648–4657.

(16) Sharma, A. K., Sharma, S. K., Surolia, A., Surolia, N., and Sarma, S. P. (2006) Solution Structures of Conformationally Equilibrium Forms of Holo-Acyl Carrier Protein (PfACP) from Plasmodium falciparum Provides Insight into the Mechanism of Activation of ACPs,. *Biochemistry 45*, 6904–6916.

(17) Sezonov, G., Joseleau-Petit, D., and Ari, R. (2007) *Escherichia coli* Physiology in Luria-Bertani Broth. *J. Bacteriol. 189*, 8746 LP – 8749.

(18) Leblanc, C., Prudhomme, T., Tabouret, G., Ray, A., Burbaud, S., Cabantous, S., Mourey, L., Guilhot, C., and Chalut, C. (2012) 4′-Phosphopantetheinyl Transferase PptT, a New Drug Target Required for *Mycobacterium tuberculosis* Growth and Persistence *In vivo*. *PLOS Pathog. 8*, e1003097.

(19) Parris, K. D., Lin, L., Tam, A., Mathew, R., Hixon, J., Stahl, M., Fritz, C. C., Seehra, J., and Somers, W. S. (2000) Crystal structures of substrate binding to *Bacillus subtilis* holo-(acyl carrier protein) synthase reveal a novel trimeric arrangement of molecules resulting in three active sites. *Structure 8*, 883–895.

(20) Marcella, A. M., Culbertson, S. J., Shogren-Knaak, M. A., and Barb, A. W. (2017) Structure, High Affinity, and Negative Cooperativity of the *Escherichia coli* Holo-(Acyl Carrier Protein):Holo-(Acyl Carrier Protein) Synthase Complex. *J. Mol. Biol. 429*, 3763–3775.

(21) Zhang, Y. M., Marrakchi, H., White, S. W., and Rock, C. O. (2003) The application of computational methods to explore the diversity and structure of bacterial fatty acid synthase. *J. Lipid Res. 44*, 1–10.

(22) Serre, L., Verbree, E. C., Dauter, Z., Stuitje, A. R., and Derewenda, Z. S. (1995) The *Escherichia coli* Malonyl-CoA:Acyl Carrier Protein Transacylase at 1.5-Å Resolution.: Crystal Structure of A Fatty Acid Synthase Component . *J. Biol. Chem. 270*, 12961–12964.

(23) Keatinge-Clay, A. T., Shelat, A. A., Savage, D. F., Tsai, S.-C., Miercke, L. J. W., O'Connell, J. D., Khosla, C., and Stroud, R. M. (2003) Catalysis, Specificity, and ACP Docking Site of Streptomyces coelicolor Malonyl-CoA:ACP Transacylase. *Structure 11*, 147–154.

(24) Zhang, L., Liu, W., Xiao, J., Hu, T., Chen, J., Chen, K., Jiang, H., and Shen, X. (2007) Malonyl-CoA: acyl carrier protein transacylase from Helicobacter pylori: Crystal structure and its interaction with acyl carrier protein. *Protein Sci. 16*, 1184–1192.

(25) Oefner, C., Schulz, H., D'Arcy, A., and Dale, G. E. (2006) Mapping the active site of *Escherichia coli* malonyl-CoA acyl carrier protein transacylase (FabD) by protein crystallography. *Acta Crystallogr. Sect. D 62*, 613–618.

(26) Mindrebo, J. T., Nartey, C. M., Seto, Y., Burkart, M. D., and Noel, J. P. (2016) Unveiling the functional diversity of the alpha/beta hydrolase superfamily in the plant kingdom. *Curr. Opin. Struct. Biol. 41*.

(27) Arthur, C. J., Williams, C., Pottage, K., Płoskoń, E., Findlow, S. C., Burston, S. G., Simpson, T. J., Crump, M. P., and Crosby, J. (2009) Structure and Malonyl CoA-ACP Transacylase Binding of Streptomyces coelicolor Fatty Acid Synthase Acyl Carrier Protein. *ACS Chem. Biol. 4*, 625–636.

(28) Marcella, A. M., and Barb, A. W. (2018) Acyl-coenzyme A:(holo-acyl carrier protein) transacylase enzymes as templates for engineering. *Appl. Microbiol. Biotechnol. 102*, 6333–6341.

(29) Szafranska, A. E., Hitchman, T. S., Cox, R. J., Crosby, J., and Simpson, T. J. (2002) Kinetic and Mechanistic Analysis of the Malonyl CoA:ACP Transacylase from Streptomyces coelicolor Indicates a Single Catalytically Competent Serine Nucleophile at the Active Site. *Biochemistry 41*, 1421–1427.

(30) Dreier, J., Shah, A. N., and Khosla, C. (1999) Kinetic Analysis of the Actinorhodin Aromatic Polyketide Synthase. *J. Biol. Chem. 274*, 25108–25112.

(31) Liu, W., Du, L., Zhang, L., Chen, J., Shen, X., and Jiang, H. (2007) Helicobacter pylori acyl carrier protein: Expression, purification, and its interaction with β-hydroxyacyl-ACP dehydratase. *Protein Expr. Purif. 52*, 74–81.

(32) White, S. W., Zheng, J., Zhang, Y.-M., and Rock, C. O. (2005) The Structural Biology of Type II Fatty Acid Biosynthesis. *Annu. Rev. Biochem. 74*, 791–831.

(33) Lai, C.-Y., and Cronan, J. E. (2003) β-Ketoacyl-Acyl Carrier Protein Synthase III (FabH) Is Essential for Bacterial Fatty Acid Synthesis. *J. Biol. Chem. 278*, 51494–51503.

(34) Parsons, J. B., and Rock, C. O. (2013) Bacterial lipids: Metabolism and membrane homeostasis. *Prog. Lipid Res. 52*, 249–276.

(35) Zhang, Y. M., Hurlbert, J., White, S. W., and Rock, C. O. (2006) Roles of the Active Site Water, Histidine 303, and Phenylalanine 396 in the Catalytic Mechanism of the Elongation Condensing Enzyme of Streptococcus pneumoniae. *J. Biol. Chem. 281*, 17390–17399.

(36) McGuire, K. A., Siggaard-Andersen, M., Bangera, M. G., Olsen, J. G., and von Wettstein-Knowles, P. (2001) β-Ketoacyl-[Acyl Carrier Protein] Synthase I of *Escherichia coli*: Aspects of the Condensation Mechanism Revealed by Analyses of Mutations in the Active Site Pocket. *Biochemistry 40*, 9836–9845.

(37) D'Agnolo, G., Rosenfeld, I. S., and Vagelos, P. R. (1975) Multiple forms of beta-ketoacyl-acyl carrier protein synthetase in *Escherichia coli*. *J. Biol. Chem. 250*, 5289–5294.

(38) Heath, R. J., and Rock, C. O. (1996) Roles of the FabA and FabZ β-Hydroxyacyl-Acyl Carrier Protein Dehydratases in *Escherichia coli* Fatty Acid Biosynthesis. *J. Biol. Chem. 271*, 27795–27801.

(39) Yu, X., Liu, T., Zhu, F., and Khosla, C. (2011) *In vitro* reconstitution and steady-state analysis of the fatty acid synthase from *Escherichia coli*; *Proc. Natl. Acad. Sci. 108*, 18643 LP – 18648.

(40) Kass, L. R., and Bloch, K. (1967) On the enzymatic synthesis of unsaturated fatty acids in *Escherichia coli*. *Proc. Natl. Acad. Sci. U. S. A. 58*, 1168–1173.

(41) Feng, Y., and Cronan, J. E. (2011) Complex Binding of the FabR Repressor of Bacterial Unsaturated Fatty Acid Biosynthesis to its Cognate Promoters. *Mol. Microbiol. 80*, 195–218.

(42) Garwin, J. L., Klages, A. L., and Cronan, J. E. (1980) Structural, enzymatic, and genetic studies of beta-ketoacyl-acyl carrier protein synthases I and II of *Escherichia coli*. *J. Biol. Chem. 255*, 11949–11956.

(43) de Mendoza, D., and Cronan, J. E. (1983) Thermal regulation of membrane lipid fluidity in bacteria. *Trends Biochem. Sci. 8*, 49–52.

(44) Garwin, J. L., and Cronan, J. E. (1980) Thermal modulation of fatty acid synthesis in *Escherichia coli* does not involve de novo enzyme synthesis. *J. Bacteriol. 141*, 1457–1459.

(45) Milligan, J. C., Lee, D. J., Jackson, D. R., Schaub, A. J., Beld, J., Barajas, J. F., Hale, J. J., Luo, R., Burkart, M. D., and Tsai, S.-C. (2019) Molecular basis for interactions between an acyl carrier protein and a ketosynthase. *Nat. Chem. Biol. 15*, 669–671.

(46) Davies, C., Heath, R. J., White, S. W., and Rock, C. O. (2000) The 1.8 Å crystal structure and active-site architecture of β-ketoacyl-acyl carrier protein synthase III (FabH) from *Escherichia coli*. *Structure 8*, 185–195.

(47) Zhang, Y.-M., Wu, B., Zheng, J., and Rock, C. O. (2003) Key Residues Responsible for Acyl Carrier Protein and β-Ketoacyl-Acyl Carrier Protein Reductase (FabG) Interaction. *J. Biol. Chem. 278*, 52935–52943.

(48) Ye, Z., and Williams, G. J. (2014) Mapping a Ketosynthase:Acyl Carrier Protein Binding Interface via Unnatural Amino Acid-Mediated Photo-Cross-Linking. *Biochemistry*

53, 7494–7502.

(49) Thiele, G. A. R., Friedman, C. P., Tsai, K. J. S., Beld, J., Londergan, C. H., and Charkoudian, L. K. (2017) Acyl Carrier Protein Cyanylation Delivers a Ketoacyl Synthase–Carrier Protein Cross-Link. *Biochemistry 56*, 2533–2536.

(50) Finzel, K., Beld, J., Burkart, M. D., and Charkoudian, L. K. (2017) Utilizing Mechanistic Cross-Linking Technology To Study Protein–Protein Interactions: An Experiment Designed for an Undergraduate Biochemistry Lab. *J. Chem. Educ. 94*, 375–379.

(51) Fisher, M., Kroon, J. T., Martindale, W., Stuitje, A. R., Slabas, A. R., and Rafferty, J. B. (2000) The X-ray structure of Brassica napus beta-keto acyl carrier protein reductase and its implications for substrate binding and catalysis. *Structure 8*, 339–347.

(52) Cukier, C. D., Hope, A. G., Elamin, A. A., Moynie, L., Schnell, R., Schach, S., Kneuper, H., Singh, M., Naismith, J. H., Lindqvist, Y., Gray, D. W., and Schneider, G. (2013) Discovery of an Allosteric Inhibitor Binding Site in 3-Oxo-acyl-ACP Reductase from Pseudomonas aeruginosa. *ACS Chem. Biol. 8*, 2518–2527.

(53) Yao, J., and Rock, C. O. (2017) Bacterial fatty acid metabolism in modern antibiotic discovery. *Biochim. Biophys. Acta - Mol. Cell Biol. Lipids 1862*, 1300–1309.

(54) Wright, H. T., and Reynolds, K. A. (2007) Antibacterial targets in fatty acid biosynthesis. *Curr. Opin. Microbiol. 10*, 447–453.

(55) Zhang, Y.-M., White, S. W., and Rock, C. O. (2006) Inhibiting Bacterial Fatty Acid Synthesis. *J. Biol. Chem. 281*, 17541–17544.

(56) Küssau, T., Flipo, M., Van Wyk, N., Viljoen, A., Olieric, V., Kremer, L., and Blaise, M. (2018) Structural rearrangements occurring upon cofactor binding in the Mycobacterium smegmatis β-ketoacyl-acyl carrier protein reductase MabA. *Acta Crystallogr. Sect. D, Struct. Biol. 74*, 383–393.

(57) Nanson, J. D., and Forwood, J. K. (2015) Structural Characterisation of FabG from Yersinia pestis, a Key Component of Bacterial Fatty Acid Synthesis. *PLoS One 10*, e0141543.

(58) Hou, J., Zheng, H., Chruszcz, M., Zimmerman, M. D., Shumilin, I. A., Osinski, T., Demas, M., Grimshaw, S., and Minor, W. (2016) Dissecting the Structural Elements for the Activation of β-Ketoacyl-(Acyl Carrier Protein) Reductase from Vibrio cholerae. *J. Bacteriol. 198*, 463–476.

(59) Price, A. C., Zhang, Y.-M., Rock, C. O., and White, S. W. (2001) Structure of β-Ketoacyl-[acyl carrier protein] Reductase from *Escherichia coli*: Negative Cooperativity and Its Structural Basis,. *Biochemistry 40*, 12772–12781.

(60) Price, A. C., Zhang, Y.-M., Rock, C. O., and White, S. W. (2004) Cofactor-Induced Conformational Rearrangements Establish a Catalytically Competent Active Site and a Proton Relay Conduit in FabG. *Structure 12*, 417–428.

(61) Helmkamp, G. M. J., and Bloch, K. (1969) Beta-hydroxydecanoyl thioester dehydrase. Studies on molecular structure and active site. *J. Biol. Chem. 244*, 6014–6022.

(62) Schwab, J. M., Klassen, J. B., and Lin, D. C. (1985) beta-Hydroxydecanoylthioester dehydrase: a rapid, convenient, and accurate product distribution assay. *Anal. Biochem. 150*, 121–124.

(63) Schwab, J. M., Klassen, J. B., and Habib, A. (1986) Stereochemical course of the hydration reaction catalysed by β-hydroxydecanoylthioester dehydrase. *J. Chem. Soc. Chem. Commun.* 357–358.

(64) Jurrus, E., Engel, D., Star, K., Monson, K., Brandi, J., Felberg, L. E., Brookes, D. H., Wilson, L., Chen, J., Liles, K., Chun, M., Li, P., Gohara, D. W., Dolinsky, T., Konecny, R., Koes, D. R., Nielsen, J. E., Head-Gordon, T., Geng, W., Krasny, R., Wei, G.-W., Holst, M. J., McCammon, J. A., and Baker, N. A. (2018) Improvements to the APBS biomolecular solvation software suite. *Protein Sci. 27*, 112–128.

(65) Dolinsky, T. J., Nielsen, J. E., McCammon, J. A., and Baker, N. A. (2004) PDB2PQR: an automated pipeline for the setup of Poisson-Boltzmann electrostatics calculations. *Nucleic Acids Res. 32*, W665-7.

(66) Dolinsky, T. J., Czodrowski, P., Li, H., Nielsen, J. E., Jensen, J. H., Klebe, G., and Baker, N. A. (2007) PDB2PQR: expanding and upgrading automated preparation of biomolecular structures for molecular simulations. *Nucleic Acids Res. 35*, W522-5.

(67) Baker, N. A., Sept, D., Joseph, S., Holst, M. J., and McCammon, J. A. (2001) Electrostatics of nanosystems: application to microtubules and the ribosome. *Proc. Natl. Acad. Sci. U. S. A. 98*, 10037–10041.

(68) Nguyen, C., Haushalter, R. W., Lee, D. J., Markwick, P. R. L., Bruegger, J., Caldara-Festin, G., Finzel, K., Jackson, D. R., Ishikawa, F., O'Dowd, B., McCammon, J. A., Opella, S. J., Tsai, S.-C., and Burkart, M. D. (2014) Trapping the dynamic acyl carrier protein in fatty acid biosynthesis. *Nature 505*, 427–431.

(69) Finzel, K., Nguyen, C., Jackson, D. R., Gupta, A., Tsai, S.-C., and Burkart, M. D. (2015) Probing the Substrate Specificity and Protein-Protein Interactions of the *E. coli* Fatty Acid Dehydratase, FabA. *Chem. Biol. 22*, 1453–1460.

(70) Zhang, L., Xiao, J., Xu, J., Fu, T., Cao, Z., Zhu, L., Chen, H.-Z., Shen, X., Jiang, H., and Zhang, L. (2016) Crystal structure of FabZ-ACP complex reveals a dynamic seesaw-like catalytic mechanism of dehydratase in fatty acid biosynthesis. *Cell Res. 26*, 1330–1344.

(71) Dodge, G. J., Patel, A., Jaremko, K. L., McCammon, J. A., Smith, J. L., and Burkart, M. D. (2019) Structural and dynamical rationale for fatty acid unsaturation in; *Escherichia coli*; *Proc. Natl. Acad. Sci. 116*, 6775 LP – 6783.

(72) Marrakchi, H., Dewolf Jr, W. E., Quinn, C., West, J., Polizzi, B. J., So, C. Y., Holmes, D. J., Reed, S. L., Heath, R. J., Payne, D. J., Rock, C. O., and Wallis, N. G. (2003) Characterization of Streptococcus pneumoniae enoyl-(acyl-carrier protein) reductase (FabK). *Biochem. J. 370*, 1055–1062.

(73) Maier, T., Leibundgut, M., Boehringer, D., and Ban, N. (2010) Structure and function of eukaryotic fatty acid synthases. *Q. Rev. Biophys. 43*, 373–422.

(74) Heath, R. J., and Rock, C. O. (1995) Enoyl-Acyl Carrier Protein Reductase (fabI) Plays a Determinant Role in Completing Cycles of Fatty Acid Elongation in *Escherichia coli*. *J. Biol. Chem. 270*, 26538–26542.

(75) Bergler, H., Fuchsbichler, S., Högenauer, G., and Turnowsky, F. (2018) The Enoyl-[Acyl-Carrier-Protein] Reductase (FabI) of *Escherichia coli*, which Catalyzes a Key Regulatory Step in Fatty Acid Biosynthesis, Accepts NADH and NADPH as Cofactors and is Inhibited by Palmitoyl-CoA. *Eur. J. Biochem. 242*, 689–694.

(76) Rawat, R., Whitty, A., and Tonge, P. J. (2003) The isoniazid-NAD adduct is a slow, tight-binding inhibitor of InhA, the *Mycobacterium tuberculosis* enoyl reductase: adduct affinity and drug resistance. *Proc. Natl. Acad. Sci. U. S. A. 100*, 13881–13886.

(77) Heath, R. J., Rubin, J. R., Holland, D. R., Zhang, E., Snow, M. E., and Rock, C. O. (1999) Mechanism of Triclosan Inhibition of Bacterial Fatty Acid Synthesis. *J. Biol. Chem. 274*, 11110–11114.

(78) Jordan, C. A., Sandoval, B. A., Serobyan, M. V, Gilling, D. H., Groziak, M. P., Xu, H. H., and Vey, J. L. (2015) Crystallographic insights into the structure-activity relationships of diazaborine enoyl-ACP reductase inhibitors. *Acta Crystallogr. Sect. F, Struct. Biol. Commun. 71*, 1521–1530.

(79) Rafi, S., Novichenok, P., Kolappan, S., Zhang, X., Stratton, C. F., Rawat, R., Kisker, C., Simmerling, C., and Tonge, P. J. (2006) Structure of Acyl Carrier Protein Bound to FabI, the FASII Enoyl Reductase from *Escherichia coli*. *J. Biol. Chem. 281*, 39285–39293.

(80) Rozwarski, D. A., Vilchèze, C., Sugantino, M., Bittman, R., and Sacchettini, J. C. (1999) Crystal structure of the *Mycobacterium tuberculosis* enoyl-ACP reductase, InhA, in complex with NAD+ and a C16 fatty acyl substrate. *J. Biol. Chem. 274*, 15582–15589.

(81) Tallorin, L., Finzel, K., Nguyen, Q. G., Beld, J., La Clair, J. J., and Burkart, M. D. (2016) Trapping of the enoyl-acyl carrier protein reductase-acyl carrier protein interaction. *J. Am. Chem. Soc. 138*.

(82) Battesti, A., and Bouveret, E. (2006) Acyl carrier protein/SpoT interaction, the switch linking SpoT-dependent stress response to fatty acid metabolism. *Mol. Microbiol. 62*, 1048–1063.

(83) Keating, D. H., Carey, M. R., and Cronan, J. E. (1995) The Unmodified (Apo) Form of *Escherichia coli* Acyl Carrier Protein Is a Potent Inhibitor of Cell Growth . *J. Biol. Chem. 270*, 22229–22235.

(84) Davis, M. S., and Cronan, J. E. (2001) Inhibition of; *Escherichia coli*; Acetyl Coenzyme A Carboxylase by Acyl-Acyl Carrier Protein. *J. Bacteriol. 183*, 1499 LP – 1503.

(85) Gully, D., Moinier, D., Loiseau, L., and Bouveret, E. (2003) New partners of acyl carrier protein detected in *Escherichia coli* by tandem affinity purification. *FEBS Lett. 548*, 90–96.

(86) Jordan, S. W., and Cronan Jr, J. E. (2003) The *Escherichia coli* lipB gene encodes lipoyl (octanoyl)-acyl carrier protein:protein transferase. *J. Bacteriol. 185*, 1582–1589.

(87) Booker, S. J. (2004) Unraveling the Pathway of Lipoic Acid Biosynthesis. *Chem. Biol. 11*, 10–12.

(88) Dowhan, W. (2011) The Raetz pathway for lipid A biosynthesis: Christian Rudolf Hubert Raetz, MD PhD, 1946–2011. *J. Lipid Res. 52*, 1857–1860.

(89) Williams, A. H., and Raetz, C. R. H. (2007) Structural basis for the acyl chain selectivity and mechanism of UDP-acetylglucosamine acyltransferase. *Proc. Natl. Acad. Sci. 104*, 13543 LP – 13550.

(90) Masoudi, A., Raetz, C. R. H., Zhou, P., and Pemble, C. W. (2014) Chasing Acyl-Carrier-Protein Through a Catalytic Cycle of Lipid A Production. *Nature 505*, 422–426.

(91) Xu, H., Ling, J., Gao, Q., He, H., Mu, X., Yan, Z., Gao, S., and Liu, X. (2013) Role of the lpxM lipid A biosynthesis pathway gene in pathogenicity of avian pathogenic *Escherichia coli* strain E058 in a chicken infection model. *Vet. Microbiol. 166*, 516–526.

(92) Six, D. A., Carty, S. M., Guan, Z., and Raetz, C. R. H. (2008) Purification and Mutagenesis of LpxL, the Lauroyltransferase of *Escherichia coli* Lipid A Biosynthesis. *Biochemistry 47*, 8623–8637.

(93) Whitfield, C., and Trent, M. S. (2014) Biosynthesis and Export of Bacterial Lipopolysaccharides. *Annu. Rev. Biochem. 83*, 99–128.

(94) Issartel, J.-P., Koronakis, V., and Hughes, C. (1991) Activation of *Escherichia coli* prohaemolysin to the mature toxin by acyl carrier protein-dependent fatty acylation. *Nature 351*, 759.

(95) Hughes, C., Issartel, J.-P., Hardie, K., Stanley, P., Koronakis, E., and Koronakis, V.

(1992) Activation of *Escherichia coli* prohemolysin to the membrane-targetted toxin by HlyC-directed ACP-dependent fatty acylation. *FEMS Microbiol. Immunol. 5*, 37–43.

(96) Trent, M. S., Worsham, L. M. S., and Ernst-Fonberg, M. Lou. (1999) HlyC, the Internal Protein Acyltransferase That Activates Hemolysin Toxin: Role of Conserved Histidine, Serine, and Cysteine Residues in Enzymatic Activity As Probed by Chemical Modification and Site-Directed Mutagenesis. *Biochemistry 38*, 3433–3439.

(97) Lin, S., Hanson, R. E., and Cronan, J. E. (2010) Biotin synthesis begins by hijacking the fatty acid synthetic pathway. *Nat. Chem. Biol. 6*, 682.

(98) Agarwal, V., Lin, S., Lukk, T., Nair, S. K., and Cronan, J. E. (2012) Structure of the enzyme-acyl carrier protein (ACP) substrate gatekeeper complex required for biotin synthesis. *Proc. Natl. Acad. Sci. 109*, 17406 LP – 17411.

(99) Babu, M., Greenblatt, J. F., Emili, A., Strynadka, N. C. J., Reithmeier, R. A. F., and Moraes, T. F. (2010) Structure of a SLC26 Anion Transporter STAS Domain in Complex with Acyl Carrier Protein: Implications for *E. coli* YchM in Fatty Acid Metabolism. *Structure 18*, 1450–1462.

(100) Cryle, M. J., and Schlichting, I. (2008) Structural insights from a P450 Carrier Protein complex reveal how specificity is achieved in the P450 ACP complex. *Proc. Natl. Acad. Sci. 105*, 15696 LP – 15701.

(101) Polyak, S. W., Abell, A. D., Wilce, M. C. J., Zhang, L., and Booker, G. W. (2012) Structure, function and selective inhibition of bacterial acetyl-coa carboxylase. *Appl. Microbiol. Biotechnol. 93*, 983–992.

(102) Lin, S., and Cronan, J. E. (2011) Closing in on complete pathways of biotin biosynthesis. *Mol. Biosyst. 7*, 1811–1821.

(103) Akatsuka, H., Kawai, E., Sakurai, N., and Omori, K. (2003) The Serratia marcescens bioH gene encodes an esterase. *Gene 302*, 185—192.

(104) Buetow, L., Smith, T. K., Dawson, A., Fyffe, S., and Hunter, W. N. (2007) Structure and reactivity of LpxD, the N-acyltransferase of lipid A biosynthesis. *Proc. Natl. Acad. Sci. 104*, 4321 LP – 4326.

Chapter 1, entitled Structural Basis of Acyl Carrier Protein Protein-Protein Interactions in Fatty Acid Biosynthesis, in part, is a reprint of the material as it appears in: Mindrebo JT*, Patel A*, Misson LE*, Kim E, Davis TD, Ni QZ, La Clair JJ, Burkart MD "Structural Basis of Acyl-Carrier Protein Interactions in Fatty Acid and Polyketide Biosynthesis" In Comprehensive Natural Products III. Vol. 1, 2020. The dissertation author is the primary co-author of this manuscript along with Dr. Ashay Patel and Dr. Laetitia Misson.

Chapter 2: The Gating Mechanism of Elongating β-ketoacyl ACP Synthases

Abstract

Carbon-carbon bond forming reactions are essential transformations in natural product biosynthesis. During de novo fatty acid and polyketide biosynthesis, β-ketoacyl-acyl carrier protein (ACP) synthases (KS), catalyze this process via a decarboxylative Claisen-like condensation reaction. KSs must recognize multiple chemically distinct ACPs and choreograph a ping-pong mechanism, often in an iterative fashion. Here we report x-ray crystal structures of substrate mimetic bearing ACPs in complex with the elongating KSs from *Escherichia coli*, FabF and FabB, in order to better understand the stereochemical features governing substrate discrimination by KSs. Complemented by molecular dynamics (MD) simulations and mutagenesis studies, these structures reveal conformational states accessed during KS catalysis. These data taken together support a gating mechanism that regulates acyl-ACP binding and substrate delivery to the KS active site. Two active site loops undergo large conformational excursions during this dynamic gating mechanism and are likely evolutionarily conserved features in elongating KSs.

Introduction

Fatty acid synthases (FASs) and polyketide synthases (PKSs) iteratively condense and modify ketide units to produce a variety of natural compounds, ranging from fatty acids to complex bioactive molecules.[1,2] FASs and PKSs can exist as one or more polypeptide "mega-synthases" that contain distinct catalytic domains (type I) or as discrete enzymes, each possessing specific activities (type II).[3–8] In these pathways, β-ketoacyl ACP synthases, alternatively ketosynthases (KSs), catalyze car`bon-carbon formation via a precisely

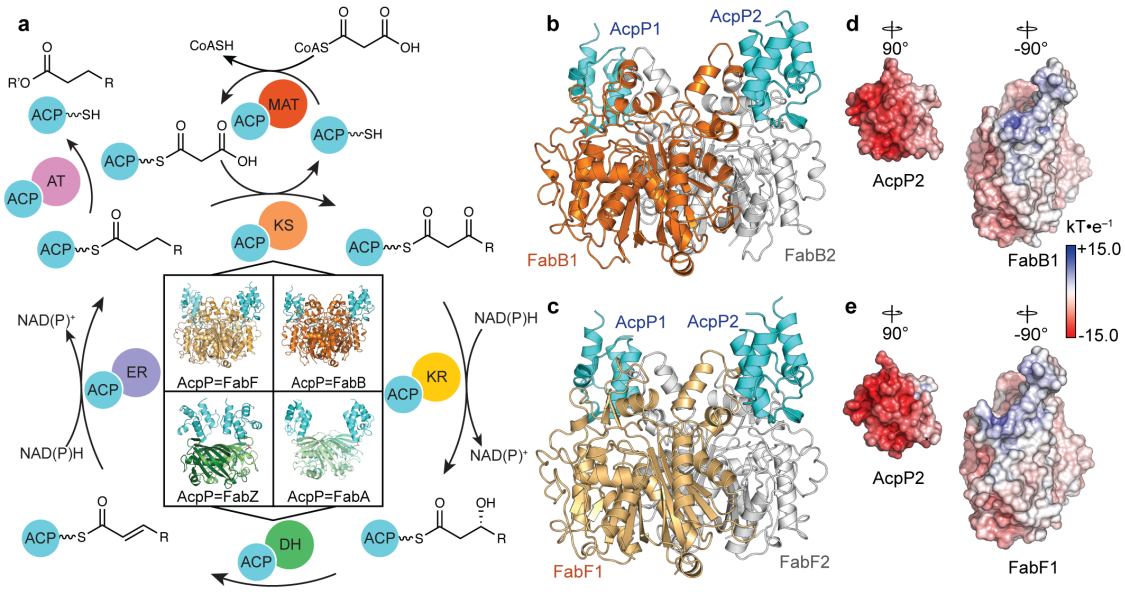

Figure 2.1: *FAB cycle and known AcpP-PP complexes*. **a**) A schematic representation of the chemical transformations that occur during fatty acid biosynthesis, highlighting the importance of protein-protein interactions required at each step for substrate processing. The four quadrants at the center of the scheme show the structures of all FAS AcpP crosslinked complexes solved thus far. The top two structures are the crosslinked AcpP-KSs (AcpP-FabF and AcpP-FabB) reported herein, while depicted below are the crosslinked AcpP-DHs (AcpP-FabZ and AcpP-FabA) solved in previous publications.[9,10] Abbreviations for each domain as acyl carrier protein (ACP), malonyl-ACP transacylase (MAT), ketosynthase (KS), ketoreductase (KR), dehydratase (DH), enoylreductase (ER), and acyl transferase (AT). Structures depict AcpP-FabZ (PDB: 6N3P), AcpP-FabA (PDB: 4KEH). **b,c**) Cartoon representations of the crosslinked AcpP-FabB and AcpP-FabF dimers. AcpP is colored cyan; the first KS monomer of AcpP-FabB and AcpPFabF is colored orange or light orange, respectively, while the second is colored white in both structures. **d)** Electrostatic potentials (ESP) maps of the FabB and AcpP monomers. **e**, ESP map of the FabF and AcpP monomers. In all cases, the ESP is mapped onto the Connelly surfaces of the FabF and AcpP monomers using a blue to white to red color range, spanning from +15.0 kT•e^{-1} to –15.0 kT•e^{-1}.

choreographed decarboxylative Claisen-like condensation to produce a β-ketoacyl species. In fatty acid biosynthesis (FAB, Figure 2.1a), complete reduction at the β-position occurs before further chain extension, while in polyketide biosynthesis (PKB), the β-positions of pathway intermediates can be completely, partially, or not reduced to produce structurally and functionally complex natural products.[1,11] The small, 4-helical acyl carrier protein (ACP) is used to shuttle substrates and intermediates to each catalytic domain or discrete enzyme in these pathways.[12,13] ACPs are initially translated to an inactive apo form and are subsequently post-translationally modified to an active *holo* form via attachment of a 4'-phosphopantetheine (PPant) arm at a conserved serine residue, providing a thiol moiety that ligates substrates and pathway intermediates to the ACP.[12] Protein-protein interactions (PPIs) between ACPs and their enzymatic partners (or domains) regulate the catalytic activities of FASs and PKSs and additionally provide a mechanism to ensure pathway orthogonality between primary (i.e. FAB) and secondary metabolism (i.e. PKB).[3,5,7,9,14–18]

KS-catalyzed carbon-carbon bond formation is an essential reaction common to both FAB and PKB. The decarboxylative condensation reaction provides a thermodynamic driving force for the formation of complex natural products.[19,20] Additionally, KS domains play an important role in chain length determination, ensuring product fidelity and controlling pathway flux.[16,21,22] Therefore, efforts to engineer FASs and PKSs will depend on our ability to manipulate the specificities and activities of these domains/enzymes, as evidenced by the recent successes engineering the yeast FAS.[22–27]

KSs can be classified as elongating or initiating based on their role within a given pathway. Initiating KSs serve to catalyze the first condensation reaction of FAB or PKB pathways, converting holo-ACP to acyl-ACP, while all subsequent condensation reactions

are catalyzed by elongating KSs.[3,4] Despite their distinct biosynthetic roles, both types of KS operate via a common ping-pong reaction mechanism, which can be disaggregated into two discrete steps.[22,28,29] In the first step, an acyl-ACP associates with a KS, and its acyl cargo is transferred from the PPant arm to a conserved, active site cysteine, producing a covalent acyl-KS adduct and holo-ACP. In the second step, malonyl-ACP replaces holo-ACP as the KS's binding partner, subsequently undergoing a decarboxylative Claisen-like condensation with the acyl-KS adduct that produces β-ketoacyl-ACP (Figure S2.1). During the course of this ping-pong process, two distinct ACPs must sequentially interact with the KS, and thus must enforce exquisite temporal and spatial discrimination among the subtly different chemical states of these acyl-ACPs. The mechanisms used by KSs to coordinate these two half-reactions and how this coordination determines substrate specificity remains cryptic despite extensive biochemical and structural characterization.

The *E. coli* type II FAS has served as a model system for understanding ACP-mediated PPIs and FAB.[10,20,30–36] We used this well-characterized system to better understand ACP•KS PPIs and KS substrate discrimination by structurally characterizing *E. coli* elongating KSs, FabB (KASI family KS) and FabF (KASII family KS), as substrate/intermediate complexes with ACP that approximate states formed during catalysis. In conjunction with molecular dynamics (MD) simulations and mutagenesis studies, these structures provide the first dynamical descriptions of an ACP•KS complex, revealing conformational changes that regulate substrate processing. Specifically, we propose that the KS employs two conserved active site loops that open and close through a double drawbridge-like gating mechanism in order to regulate substrate processing.[37] When open, the drawbridge expands the KS active site in order to accommodate PPant-tethered acyl-

AcpP substrates. The structural features underlying this gating machinery are conserved in related enzymes and similar conformational transitions will likely determine substrate selectivity and processing in other FAB and PKB pathways.

Results

Crosslinking and crystallization of AcpP-KS Complexes. We synthesized C12-α-bromo- (1a) and C16-α-bromopantetheineamide (1b) and loaded them onto the *E. coli* ACP (AcpP) using a one-pot chemoenzymatic method[38] to produce *crypto*-1a-AcpP (C12AcpP) and *crypto*-1b-AcpP (C16AcpP) that bear a reactive warhead on their PPant arm[38–40] (Figure 2.2). These *crypto*-AcpPs were then reacted with FabF and FabB to produce uniformly crosslinked complexes, referred to herein as AcpP-KS, where the "-" denotes a crosslinked complex (Figures S2.1, S2.22). Using this method, we grew crystals of C12AcpP-FabF and C16AcpP-FabF and obtained x-ray crystallographic data sets with 2.35 Å and 2.30 Å resolution, respectively. The crystallographic asymmetric unit (ASU) of these complexes were identical and contained one monomer of FabF crosslinked to a single AcpP. Additionally, C12AcpP-FabB crystals diffracted to 1.55 Å and C16AcpP-FabB diffracted to 2.50 Å. The C12AcpP-FabB and C16AcpP-FabB ASUs both contain the functional FabB dimer crosslinked to two AcpP molecules.

The AcpP-KS interface. The AcpP-KS interacting surfaces are electrostatic (Figure 2.1b-e) and composed largely of flanking charged and polar groups surrounding a central hydrophobic patch (Figure 2.3). The AcpP and KS monomers provide negatively and positively charged residues, respectively, to the interface. Figure 2.3 provides a comparison of the AcpP-FabF and AcpP-FabB interfaces from this work. A thorough analysis of the

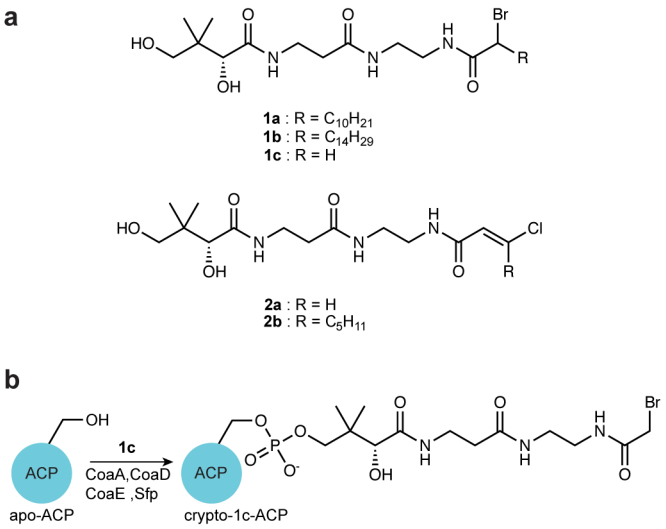

Figure 2.2: *KS pantetheineamide crosslinking probes and ACP one-pot method*. **a)** Pantetheineamide-derived α-bromo and chlorovinyl crosslinking probes used in this study. **b)** An illustration of the one-pot chemoenzymatic loading of apo-ACP with panetheinamide probe 1c to produce crypto-1c-ACP using the coenzyme A biosynthetic enzymes CoaA, CoaD, and CoaE and a promiscuous phosphopantetheinyl transferase (PPTase) Sfp.

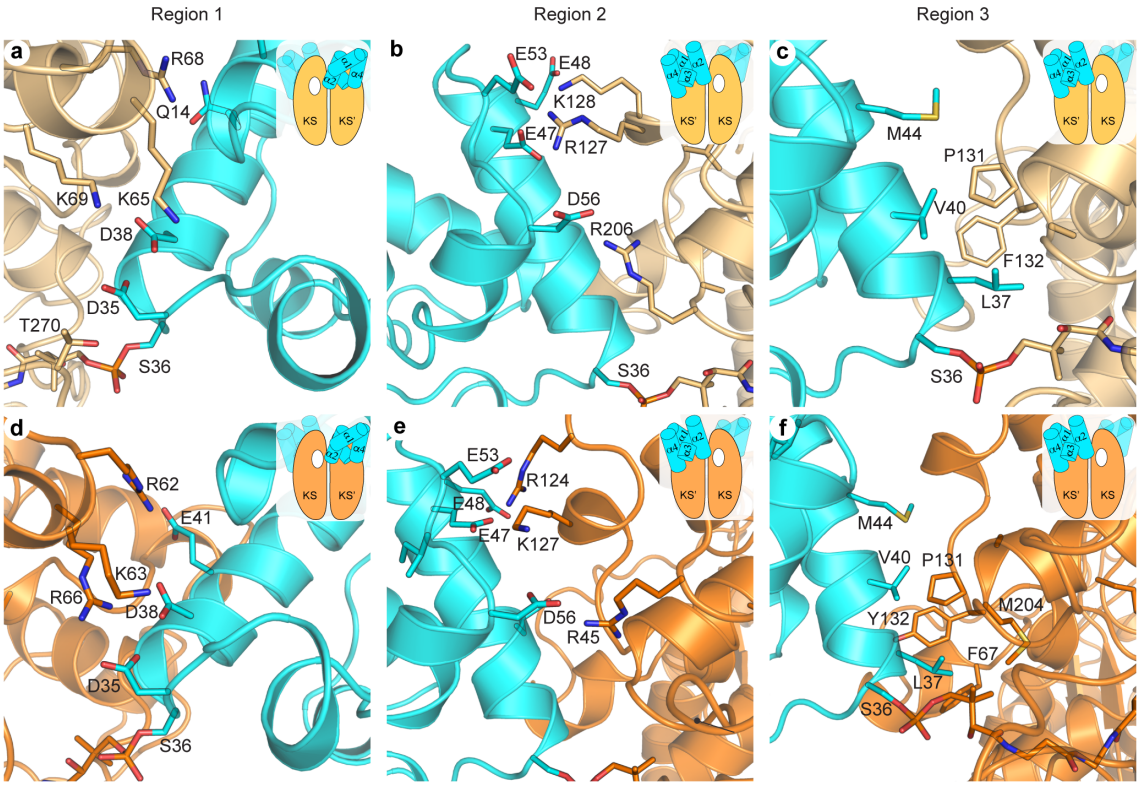

Figure 2.3: *AcpP-FabF and AcpP-FabB interface interactions*. The FabF (light orange) and FabB (bright orange) interfaces can be broken up into three regions, the first two are comprised of electrostatic interactions and the third is a hydrophobic patch. The above panels provide close-up views of these three regions and the cartoon inset provides context to the viewing angle and the positional relationship of AcpP (cyan) to the overall AcpP-KS complex. Additionally, the white hole represents the active site to which the viewed AcpP is crosslinked as the majority of contacts are provided by the KS monomer not covalently crosslinked to AcpP. **a)** A close-up view of the AcpP-FabF region 1 electrostatic interactions. **b)** A close-up view of the AcpP-FabF region 2 electrostatic interactions. **c)** A close-up view of the AcpP-FabF region 3 hydrophobic interactions. *d*, A close-up view of the AcpP-FabB region 1 electrostatic interactions. **e)** A close-up view of the AcpP-FabB region 2 electrostatic interactions. *f*, A close-up view of the AcpP-FabB region 3 hydrophobic interactions.

AcpP-FabB interface was recently reported by Milligan et al.[34] Herein, we report the first example of a KASII-type KS in complex with an ACP, AcpP-FabF. The AcpP-FabF and AcpP-FabB complexes can be broken into three regions. Region 1 electrostatic interactions include Lys65, Arg68, and Lys69 of FabF interacting with Glu13, Gln14, Asp35, and Asp38 of AcpP (Figure 2.3a). Additionally, Thr270 of FabF, which sits on a flexible loop that undergoes conformational rearrangements upon acyl-AcpP binding, interacts with Asp35 of AcpP. Region 2 interactions are formed between Arg127, Lys128, and Arg206 of FabF and Glu47, Glu48, Glu53, and Asp56 of AcpP (Figure 2.3b). The central hydrophobic patch is comprised of interactions between Met44, Val40, and Leu37 of AcpP and Ile129, Ser130, Pro131, Phe132, Ala205, and Arg206 of FabF (Figure 2.3c).

Comparisons of the AcpP-FabF and AcpP-FabB interfaces reveal that they share similar chemical features, but structural alignments of the KS subunits show that the orientations of AcpPs in the AcpP-KS complexes are distinct (Figures S2.3a,b). In FabF, individual ACP monomers, AcpP1 and AcpP2, bury surface areas of 671.2 $Å^2$ and 675.4 $Å^2$, respectively, while in FabB, AcpP1 and AcpP2 bury surface areas of 597.5 $Å^2$ and 607.4 $Å^2$, respectively. These small contact areas are consistent with the transient nature of molecular recognition between ACP and its binding partners.[9,10] In addition, the differences in contact areas of AcpP-FabF and AcpP-FabB interfaces are consistent with the differing orientations that the AcpPs adopt relative to their KS partners. It is also worth noting that when comparing the interfaces of these AcpP-KS complexes, AcpP's helix I forms more extensive contacts with FabF than FabB, while FabB forms more hydrophobic interactions at region 3 (Figure 2.3). While the differences at these interfaces are subtle, the manner in which AcpP engages with each of its cognate KSs may modulate the activities of FabF and FabB.[41,42]

Changes in the FabF active site accompany substrate binding. Electron density maps calculated using the 2.30 Å C16AcpP-FabF data set demonstrate adequate density for ACP's Ser36, the PPant moiety, and acyl cargo. The FabF active site cysteine residue (Cys163) forms a covalent bond with the α-carbon of the fatty acid substrate mimetic (1b), and the resulting stereocenter is found in the *S* configuration (Figure 2.4a). The carbonyl group of the substrate coordinates to the FabF active site histidine residues, His303 and His340, in a manner similar to the published structure of AcpP-FabB[34] (PDB: 5KOF) (Figure 2.4b). Modeling and refinement of the crosslinker's acyl chain required the remodeling of two active site loops. The first of which is the conserved GFGG loop (loop 1, residues 399-402) adjacent to the active site that contains the putative Phe400 gating residue[28], and a second less conserved loop (loop 2, residues 265-275) that caps loop 1 (Figure 2.5a). These loops undergo significant conformational changes, revealing a hydrophobic pocket that accommodates the acyl chain (Figures S2.4a-c). This pocket is distinct from the substrate binding site identified in the crystallized acyl-KS intermediate structures 2GFY[43] and 1EK4[44] (Figure 2.4c). Close analysis of the C16AcpP-FabF structure indicates that crystal contacts do not play a role in the conformational changes seen in these loops.

C16AcpP-FabF adopts an open conformation. A comparison of the apo-FabF (PDB: 2GFW[43]), acyl-FabF (PDB: 2GFY[43]), and C16AcpP-FabF structures shows that Phe400 of loop 1 moves ~7 Å, as measured by changes in the Phe400 Cα position, into a pocket revealed by a conformational rearrangement of loop 2 (Figure 2.5a). Gly399 and Gly402 of loop 1 act as pivot points as the loop transitions from a closed conformation to an

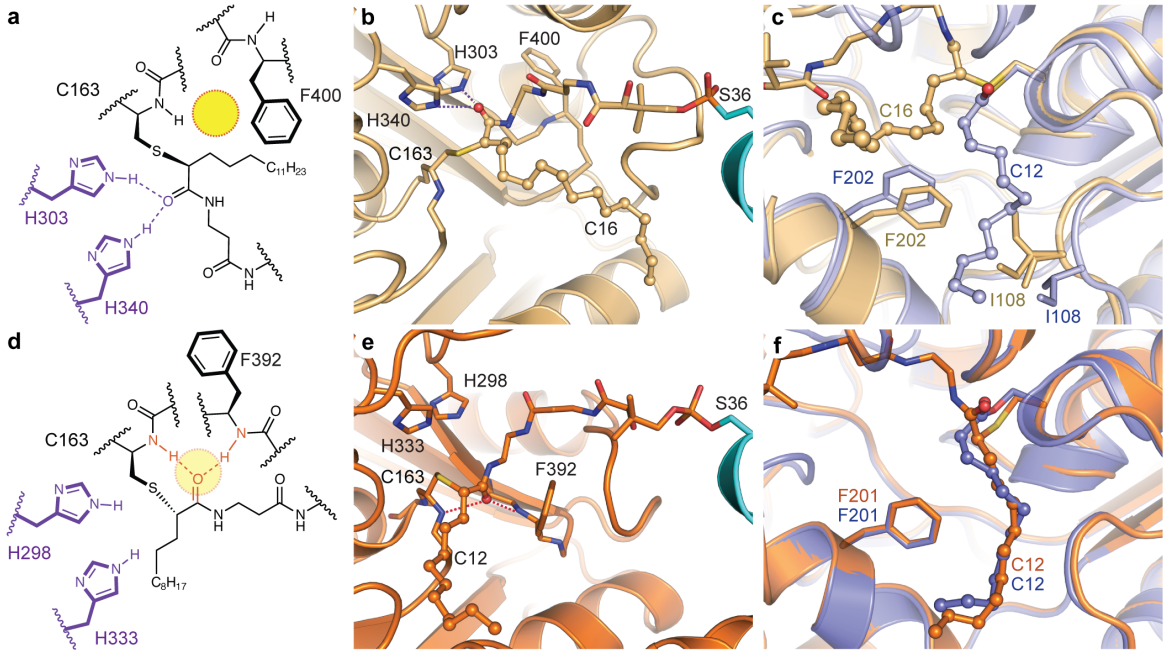

Figure 2.4: *FabF active site interactions with C16 substrate analog*. **a)** Schematic representation of the 4'-phosphopantetheineamide crosslinker within the FabF active site. The disorganized oxyanion hole is shown as a yellow circle. **b)** Active site interactions depicting the PPant crosslinker and C16 acyl chain from the crystal structure of C16AcpP-FabF. H340 and H303 coordinate the carbonyl of the acyl mimetic (blue dotted lines) and the active site oxyanion hole is disorganized. AcpP and FabF are colored cyan and light orange, respectively. **c)** Comparison of acyl binding pocket and associated gating residues, F202 and I108, in dodecanoyl-FabF (12:0-FabF) (2GFY[43], light purple), and C16AcpP-FabF (6OKG, light orange). **d)** Representation of the 4'-phosphopantetheine crosslinker within the FabB active site. The organized oxyanion hole is shown as a transparent yellow circle with associated backbone amides and coordinated PPant carbonyl shown in red. **e**) The carbonyl of the acyl mimetic in the crystal structure of C12AcpP-FabB is coordinated in the active site oxyanion hole formed by backbone amides of Cys163 and Phe392 (Phe400 in FabF). **f)** Comparison of acyl binding pocket in dodecanoyl-FabB (12:0-FabB) (PDB ID: 1EK4[45], bright purple), and C12AcpP-FabB (PDB ID: 6OKC, bright orange). Residues in panels are numbered according to their respective protein, FabF is numbered in FabF residue numbering and FabB is numbered in FabB residue numbering. Hydrogen-bonding interactions are represented as dotted lines, all side chain residues are represented as sticks, and the 4'-phosphopantetheinyl arm is represented as sticks while the acyl chains are represented as ball and stick.

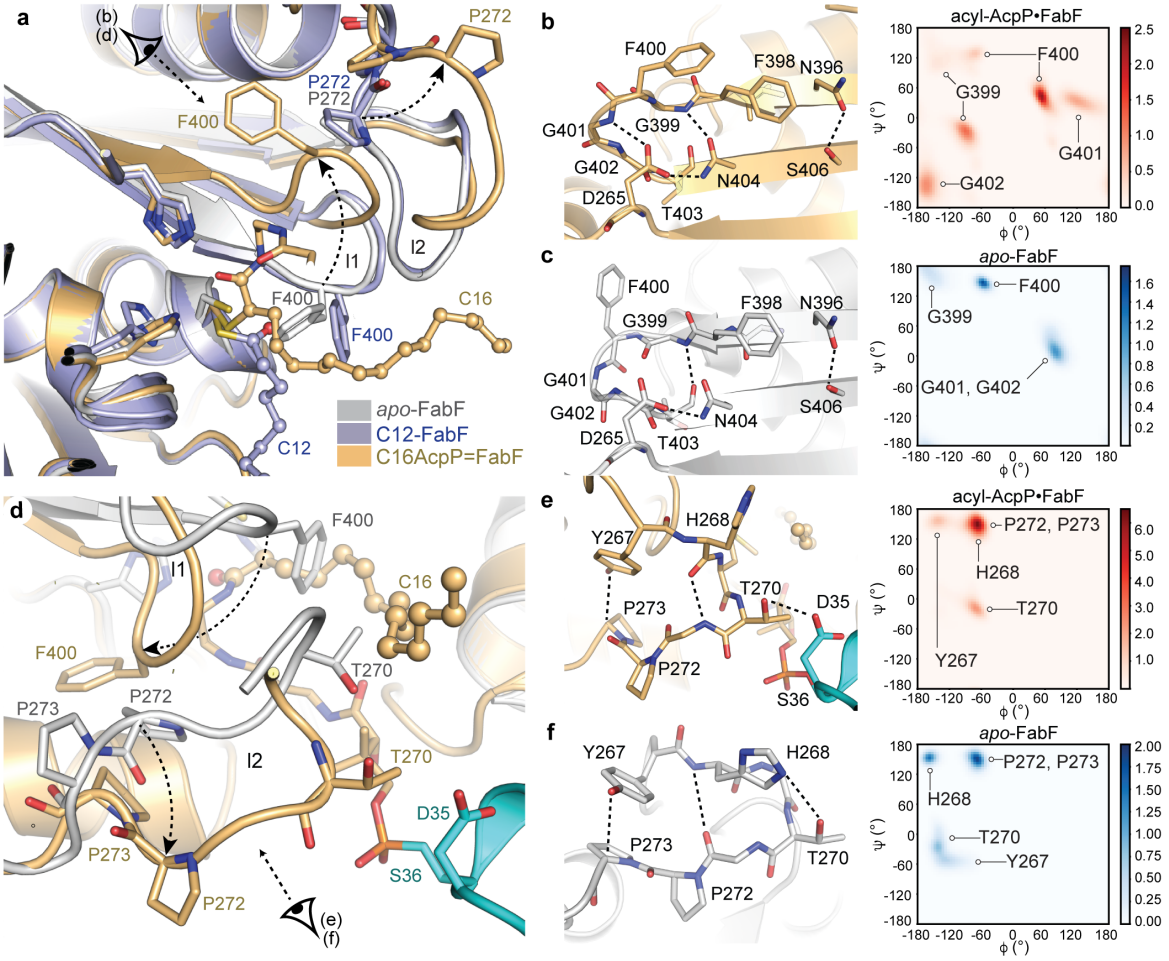

Figure 2.5: *Conformational changes in FabF active site loops.* **a)** Comparison of F400, loop 1, and loop 2 conformations of apo-FabF (light grey, PDB: 2GFW[43]), dodecanoyl-FabF (light purple, PDB: 2GFY[43]), and C16AcpP-FabF (light orange, PDB: 6OKG). **b)** Interactions that stabilize the open-conformation of the β-turn motif of loop 1 in C16AcpP-FabF and associated Ramachandran analysis of the conserved GFGG sequence within loop 1 from 1.5 μs of 10:0-AcpP•FabF, 12:0-AcpP•FabF, 16:0-AcpP•FabF (total of 4.5 μs) of molecular dynamics (MD) simulation data. **c)** Interactions that stabilize the closed-conformation of the β-turn motif of loop 1 in apo-FabF (light grey) and associated Ramachandran analysis of the conserved GFGG sequence within loop 1 from 1.5 μs of MD simulation data of apo-FabF. **d)** Loop 2 overlay of apo-FabF (light grey, PDB: 2GFW) and C16AcpP-FabF (light orange) with the crosslinked AcpP colored cyan. **e)** Interactions that stabilize the β-turn "open conformation" of loop 2 in C16AcpP-FabF (light orange) and Ramachandran analysis of key loop 2 residues of FabF monomers of acyl-AcpP•FabF complexes ("gate-open" conformation) from 1.5 μs of 10:0-AcpP•FabF, 12:0-AcpP•FabF, 16:0-AcpP•FabF (total of 4.5 μs) of MD simulation data. **f)** Interactions that stabilize the loop 2 "closed conformation" in apo-FabF (white) and Ramachandran analysis of key loop 2 residues of FabF of apo-FabF ("gate-closed" conformation) from 1.5 μs of MD simulation data of apo-FabF. In **a**, **b, c, d, e, and f** residues are shown as sticks and colored according to element. Hydrogen-bond interactions are highlighted using dotted lines. In **b**, **c, e,** and **f** simulated backbone φ and ψ dihedrals were binned using widths of 5°. Color bars indicates density of data points within each 2D bin.

open conformation (Figure 2.5b,c). The open conformation is stabilized by a network of hydrogen-bonding interactions between the backbone amides of Gly399, Phe400, Gly401, and Gly402 and the side chains of Asn404 and Asp265 from loop 2 (Figure 2.5b,c). Overlays of the apo-FabF and C16AcpP-FabF structures indicate that the C16-acyl chain of 1b would clash with Phe400 in the closed conformation of loop 1 (Figure 2.5a). These results indicate that these loop rearrangements may act as a gate to provide access to the active site for acyl-ACP substrates. Interestingly, the backbone amide of Phe400 provides one of the two hydrogen bonds that form the FabF oxyanion hole when loop 1 assumes the closed conformation; therefore, the open conformation is likely catalytically inactive.

In apo-FabF, loop 2 rests on top of loop 1 and must undergo a rearrangement to allow loop 1 to assume the open conformation. A comparison of apo-FabF to our C16AcpP-FabF structure demonstrates that loop 2 pivots about a Pro-Pro motif, whereby Pro273 undergoes a 165° change in its ψ angle, causing the loop to swing outward by 5 Å towards the bound AcpP (Figure 2.5d). Analysis of the loop 2 backbone dihedral angles suggests that the loop transitions from a type VIII β-turn in the closed conformation to a type I β-turn in the open conformation. In the closed conformation, loop 2 is stabilized by a Ser271(O)C-His268(H)N main-chain hydrogen bond, a Thr270-His268 side-chain hydrogen bond, and a Pro273-Tyr267 C-H π interaction[46] (Figure 2.5e,f). Transition to the open conformation causes the β-turn backbone hydrogen-bonding pattern to flip from Ser271(O)C-His268(H)N to Ser271(N)H-His268(O)C and Thr270 breaks its hydrogen bond with His268 to interact with Asp35 of AcpP.

C12AcpP-FabB trapped in closed acyl transfer conformation. Analysis of the 1.55 Å C12AcpP-FabB data (Figure S2.4d) demonstrates well-resolved electron density for

the 4'-phosphopantetheineamide arm and the C12-acyl chain. In this structure, loops 1 and 2 are found in a catalytically competent closed conformation (Figure 2.4d-f). Like the catalytic cysteine of FabF, Cys163 of FabB, reacts stereoselectively with the α carbon of 1a to produce the *S* stereoisomer (Figure 2.4d). The carbonyl group of the substrate is coordinated to the oxyanion hole formed by the backbone amides of Cys163 and Phe400, and the probe's acyl chain is positioned inside FabB's fatty acid binding pocket (Figure S2.4d,e). Interestingly, the recently deposited AcpP-FabB structure (PDB: 5KOF)[34] does not feature these interactions, and instead the carbonyl group forms hydrogen bonds with His298 and His333.

Comparison of C12AcpP-FabB and dodecanoyl-FabB (C12-FabB, PDB: 1EK4[44])demonstrates that the active site and acyl chain geometries are nearly identical in the two structures (Figure 2.4f). The similarity between the C12-FabB and C12AcpP-FabB indicates that the latter approximates a catalytically relevant state for the transfer of substrate from acyl-AcpP to FabB's active site cysteine. Both steps of the KS reaction form a tetrahedral intermediate that is stabilized by the oxyanion hole, which is only organized when loop 1 and the associated Phe392 residue (Phe400 in FabF), is in the gate-closed conformation.

MSA analysis suggests conservation of loops 1 and 2. Multiple sequence alignments (MSA) of type II FAS elongating KSs indicate that residues of loop 1 are highly conserved across the KASI (FabB) and KASII (FabF) families of KSs, while loop 2 is only conserved within, but not between, the two families (Figure S2.5). The consensus sequence for loop 1 is comprised of the conserved GFGG β-turn motif flanked by two conserved asparagine residues, Asn396 and Asn404 (FabF numbering). Interestingly, Asn404 interacts with a highly conserved Asp265 found at the start of loop 2 in both the open and closed states,

providing a physical basis for the (proposed) coordinated movement of loops 1 and 2 (Figure 2.5b,c). The conserved nature of loop 1 and Asp265 suggests that their proposed gating function is a general feature of type II FAS elongating KSs.

To determine if these proposed gating elements are conserved in condensing enzymes outside of type II FAS, we aligned *E. coli* FabF with representative KSs from type II PKS, type I FAS, and type I PKS (Figure 2.6a). Loop 1 of FAS and PKS KSs is generally conserved, although there is modest sequence variation. Notably, the Phe400 FabF gating residue is conserved in type I FAS and type II PKS but is replaced by valine or isoleucine in the KS domains of the type I PKS deoxyerythronolide B synthase (DEBS). Modification of the gating residue may modulate substrate specificity, as the KS domains from DEBS accept and extend substrates with β-substituents and utilize bulkier α-branched extender units, namely methylmalonyl-CoA.[47]

Loop 2 of these KSs is significantly less conserved than loop 1. Only Asp265 can be considered highly conserved, as it is present in all KSs except the KS monomer (actKS) of the heterodimeric type II PKS KS/chain length factor (CLF) complex from actinorhodin biosynthesis.[48,49] In contrast to FAS KSs, these enzymes iteratively extend a growing polyketide within the KS binding pocket only unbinding the polyketide once multiple extensions using malonyl-ACP have been catalyzed to produce the fully extended poly-β-keto-ACP. The size of the polyketide produced by actKS is determined by CLF, which accommodates the growing polyketide chain, mediating substrate dissociation when the polyketide intermediate can no longer be accommodated within its binding pocket.[50] Therefore, given that iterative type II KSs do not accept acyl-ACPs and instead only process

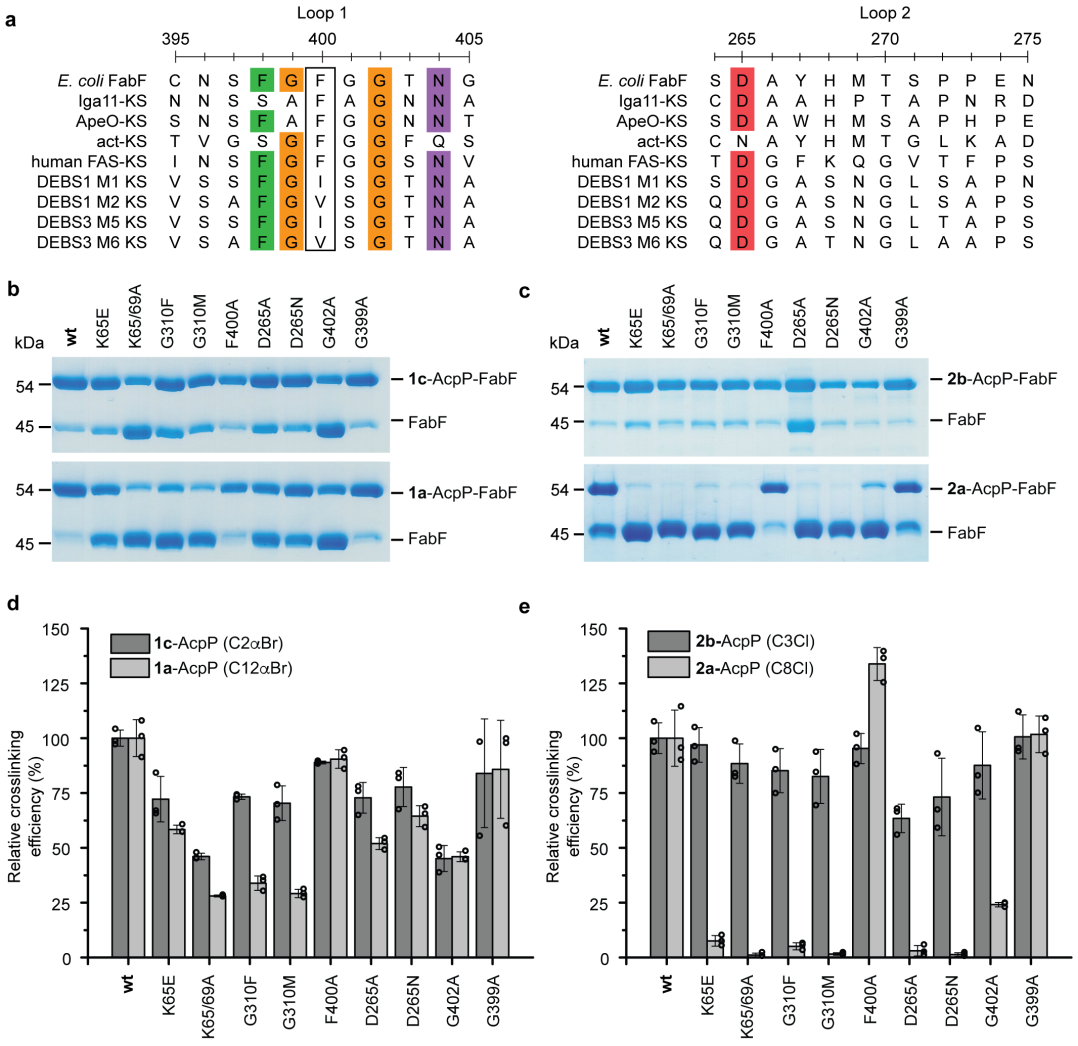

Figure 2.6: *Loop 1 and 2 Sequence conservation and mutagenesis*. **a)** Sequence alignment of loops 1 and 2 of FabF with representative KS sequences from non-iterative type II PKS (Iga11, ApeO), iterative type II PKS (act-KS), type I FAS (Human-FAS-KS), and type I PKS (DEBS KSs). The putative gating residue (Phe400 in FabF) for each synthase is outlined in a black box. **b)** Single time point crosslinking gels of **1c**-AcpP (C2αBr-AcpP) and **1a**-AcpP (C12αBr-AcpP) with FabF gating mutants. **c)** Single time point crosslinking gels of **2b**-AcpP (C3Cl-AcpP) and **2a**-AcpP (C8Cl-AcpP) with FabF gating mutants. **d)** Densitometric analysis of single time-point crosslinking efficiency of **1c**-AcpP (C2αBr-AcpP) and **1a**-AcpP (C12αBr-AcpP) with FabF mutants. **e)** Densitometric analysis of single time-point crosslinking efficiency of **2b**-AcpP (C3Cl-AcpP) and **2a**-AcpP (C8Cl-AcpP) with FabF mutants. All crosslinking experiments from **b** and **c** were performed as biologically independent experiments (n = 3) and all data represented in **d** and **e** are the average crosslinking efficiency of each mutant normalized to the average of wt FabF crosslinking efficiency. The error bars in **d** and **e** are represented as standard deviation (± SD) and the individual normalized measurements from each independent experiment are overlaid on top of the associated bar plot as open circles. Source data for all experiments are provided as a Source Data file.

malonyl-ACPs, these iterative type II KSs may need to disfavor gating events to prevent premature product off-loading and ensure the growing polyketide is transferred back to the KS cysteine after condensation with malonyl-ACP. In actKS, this is may be realized by disfavoring the open conformation of loops 1 and 2 , relative to type II FAS KSs, through the substitution of the negatively charged Asp265 residue of loop 2 with an Asn residue (Figure 2.6a), as the ion•dipole interactions involving Asp265 found in FabB or FabF are substituted with weaker dipole•dipole interactions in actKS. Interestingly, in KSs from non-iterative type II polyene PKSs, such as Iga11[51,52] and ApeO[53], that require substrate offloading in-between condensation steps, the same substitution is not observed, instead these enzymes possess the conserved Asp265 found in type II FAS KSs.

Mutagenesis studies of FabF gating mutants. To determine if the proposed gating function of loops 1 and 2 have any effect on KS activity, we identified a panel of FabF mutations that we hypothesized would attenuate FabF's ability to accept and/or process acyl-AcpP substrates. These mutations were designed to alter the FabF's proposed gate function by modulating loop 1's flexibility (flex modulation), destabilizing (disfavoring) the gate-open conformation (destabilization), or occluding the pocket occupied by Phe400 in the gate-open conformation (pocket blockage). To test this hypothesis, we adapted a crosslinking assay that utilizes α-bromo and chloroacrylate mechanistic crosslinkers with different fatty acid chain lengths as substrate mimetics[39] (Figure 2.2a). We hypothesized that our panel of FabF gating mutants would generally retain wildtype (wt) activity towards smaller C2 and C3 chain length crosslinkers, 1c and 2a, but would crosslink less efficiently with longer C8 and C12 chain length crosslinkers, 2b and 1a, which would require transitions between gate conformations to access the KS active site.

Before assaying these gating mutants, we first evaluated the crosslinking activity of a gate removal mutant, F400A. The results show that both F400A and wt FabF crosslink with generally equal efficiency with short- and long-chain acyl-AcpP substrates (Figure 2.6). Interestingly, the F400A mutant underwent crosslinking with the C8Cl (2b) with higher relative efficiency to wt (133%) both in our single time point assay and at a faster rate in our time-course crosslinking studies (Figures S2.6-S2.11). These results suggest that mutating Phe400, a key gating residue[28], to alanine enhances the accessibility of probe to the KS active site cysteine.[28] Additionally, we prepared two FabF interface mutants, K65E and K65A/K69A, to demonstrate that crosslinking can also report on PPIs. Both of these mutants showed reduced crosslinking towards all probes, but crosslinking efficiency was most significantly reduced with long-chain crosslinkers (Figure 2.6). These results suggest that well-coordinated PPIs are important for chain-flipping[54] substrates into the KS active site.

To prevent loop 1 transitions from the closed to open conformation, we mutated FabF's Gly310 to a phenylalanine or methionine residue to introduce a bulky amino acid at a position that would occlude the pocket occupied by Phe400 in the open conformation (pocket-blockage, Figure S2.12). Interestingly, G310F and G310M crosslink with 73% and 70% efficiency with C2αBr (1c) but only 33% and 30% efficiency with C12αBr (1a), respectively. Differential crosslinking activity between short and long substrates was more pronounced for the chloroacrylate crosslinkers as G310F and G310M crosslinked with 85% and 82% efficiency with C3Cl (2a) but only 5% and 1% efficiency with C8Cl (2b), respectively (Figure 2.6). These results indicate that blocking the open conformation reduces FabF's ability to accept longer acyl-ACP substrates but not that of smaller substrates that more closely resemble malonyl-AcpP.

Similar patterns emerge when examining the crosslinking efficiencies of our D265A and D265N mutants of loop 2. These mutants are hypothesized to disfavor the open conformation by replacing the ion•dipole interactions involving the conserved Asp265 from loop 2 with weaker interactions. These mutations should therefore disrupt the conserved D265 coordinated hydrogen-bonding network between loops 1 and 2 that stabilizes the open conformation. D265A and D265N mutants crosslinked with 72% and 77% efficiency with C2αBr (1c) and 51% and 64% efficiency with C12αBr (1a), respectively. Furthermore, D265A and D265N crosslinked with 63% and 73% efficiency with C3Cl (2a) but only 2% and 1% efficiency with C8Cl (2b), respectively.

In contrast, loop flexibility-modulated mutants, G399A and G402A, did not demonstrate pronounced differences in crosslinking relative to wt FabF in our assay. The G399A mutant reacted with all crosslinkers with similar efficiency as wt FabF, while crosslinking efficiencies of the G402A mutant only showed differential crosslinking activity when comparing C3Cl (2a) (87%) and C8Cl (2b) (24%) (Figure 2.6). G399A also crosslinked similarly to wt FabF in our time-course crosslinking assay (Figure S2.6). While it was expected that the G399A mutant would show a difference in crosslinking efficiency, it is important to note that such a substitution is observed in nature, as the KSs from type II polyene synthases, Iga11[51,52] and ApeO[53], both have alanine at this position (Figure 2.6a). Additionally, the dihedral angles of G399A in both the closed and open conformation are not in the Ramachandran forbidden zone (Figure 2.5b,c) and can therefore be reasonably accessed by the G399A mutant.

MD simulations support a KS gating mechanism. Using these AcpP-KS crystal structures as initial coordinates, we performed MD simulations of C10, C12, and C16-

AcpP•KS complexes, where "•" denotes a noncovalent complex (Figures S2.1, S2.13), to probe the dynamic properties of the gating processes in acyl-AcpP•KS complexes. Models of the ACP-bound acyl-AcpP•KSs were constructed by manually replacing the crosslinkers present in the crystal structures with natural saturated substrates encountered by the KSs (Online Methods). In addition, simulations of apo-FabB and apo-FabF were performed using previously reported crystal structures (PDB: 2VB9[55] and 2GFW[43], respectively) as initial coordinates. Lastly, in an attempt to computationally visualize the transition between the open and closed conformations of loops 1 and 2, we performed additional MD simulations of apo-FabF and apo-FabB using KS structures prepared by removing the AcpP monomers from the AcpP-KS complexes reported herein. We distinguish these structures from the crystallographic apo-FabB and apo-FabF structures by referring to them as apo-FabB* and apo-FabF*. Because these apo-structures feature their loops in conformations that may not be stable in the absence of an associated acyl-ACP, we hypothesized that they may more readily undergo conformational transitions. Each of the ten systems described above was subjected to three independent 500 ns MD simulations. Replicates were initiated using different velocities and a total of 15 μs of MD data were collected. General analysis for all simulated systems is provided in Figures S2.14-S2.27.

From this data, no transition between the closed and open loop conformations was sampled during the course of any simulation, suggesting that the coordinated movement of loops 1 and 2 between their open and closed states is a relatively slow process, likely

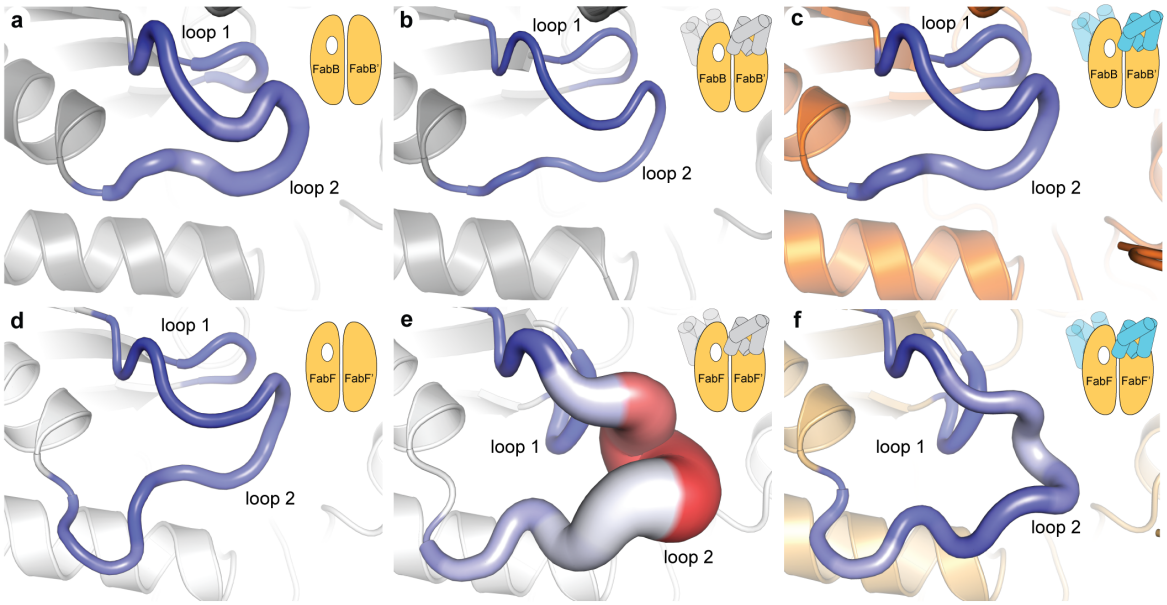

Figure 2.7: *Loop dynamism sampled via computer simulations.* Root mean square fluctuations (RMSFs) of **a)** *apo*-FabB$_2$; **b)** *apo*-FabB$_2$* (*apo* structure derived from AcpP$_2$-FabB$_2$ structure); **c**) AcpP$_2$•FabB$_2$; **d**) *apo*-FabF$_2$; **e)** *apo*-FabF$_2$* (*apo* structure derived from AcpP$_2$-FabF$_2$ structure); **f**) AcpP$_2$•FabF $_2$. Larger (per residue) backbone RMSF values correspond to a thicker "sausage"; color range (blue to white to red) illustrates (per residue) side chain RMSFs with the blue-to-red color range indicating small-to-large RMSF values.

occurring on timescales of 10s or 100s of μs.[56] Nonetheless, analysis of the per residue backbone and side chain root mean square fluctuations (RMSFs) of the loop residues, shown in Figure S2.7d-i and Figures S2.28-S2.30, suggests the following: Firstly, while the loops of apo-FabB and apo-FabF have similar RMSFs, the loops of apo-FabF* and the acyl-AcpP•FabF complexes show greater fluctuations than do those of apo-FabB* and the acyl-AcpP•FabB complexes, respectively. Of the structures shown in Figure S2.7d-i, apo-FabF* is the most significant. RMSF analysis shows that loop 2 of apo-FabF* fluctuates more in this structure than any other simulated structures. Despite this dynamism, apo-FabF*'s loop 1 remains fairly rigid. It is possible that the transition of loop 2 from its open to closed conformation first requires the motion of loop 1 toward the active site. In fact, this movement of loop 1 would restore the oxyanion hole absent in the C16AcpP-FabF structure (Figure 2.3). Therefore, the large RMSFs observed for apo-FabF*s loop 2 reveal a so-called frustrated loop unable to assume its preferred open conformation in the absence of acyl-AcpP (Figure 2.7). These findings, along with published studies of PKS ACPs[17], suggest that ACPs may not only be responsible for substrate delivery but also may induce loop motions that promote catalysis through allostery.

Identification of this frustrated loop suggests that the motions of loops 1 and 2 are associated. To evaluate this hypothesis, we determined the average correlations of the motions of residues of loops 1 and 2 sampled during the course of the MD simulations of apo-KS, apo-KS*, and acyl-AcpP•KS structures. Both FabB and FabF appear to form the same general network of interloop interactions to choreograph loop motion (Figure 2.8). Nonetheless, the "co-relatedness" of the loops are distinct in the open (Figure 2.8c,e) and closed (Figure 2.8a-d) states, with a greater correlation found in the closed conformation.

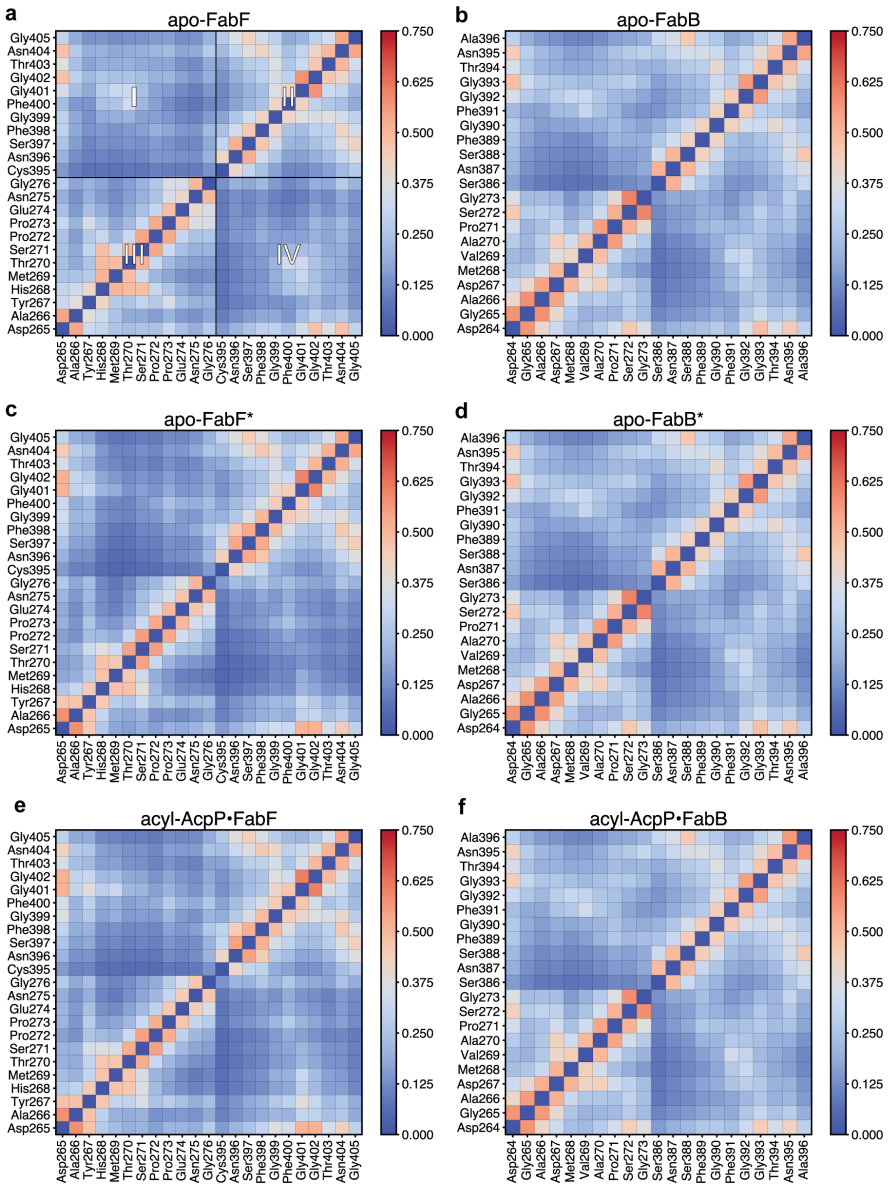

Figure 2.8: *Average cross correlations of the motions of key loop 1 and 2 residues sampled computationally.* Cross correlations were determined by computing a motion vector for each residue of loop 1 and loop 2 from its prior position to its current over the course of each simulation. In this manner, motion vectors for each pair of residues of loop 1 and 2 are calculated for each frame of simulation data. Heat maps generated from the cross-correlation analysis of the motions of loop 1 and 2 residues of **a**) *apo*-FabF, **b)** *apo*-FabB, **c)** *apo*-FabF*, **d)** *apo*-FabB*, **e)** acyl-AcpP•FabF, and **f)** acyl-AcpP•FabB, respectively, sampled using molecular dynamics (MD) simulations. In **a**, the heat map has been divided into four quadrants; quadrants II and III illustrates cross correlations of the motions of residues within loops 1 and 2, respectively. Inter-loop cross correlations are shown in quadrants I and IV. Note that each heatmap is symmetric about the diagonal that bisects quadrants II and III.

Furthermore, the average correlation of loop 1 and 2 residues is slightly greater in simulations of acyl-AcpP•FabF complexes than simulations of either apo-FabF or apo-FabF*. On the basis of this analysis, it is evident that loops 1 and 2 move in concert with one another and that the GFGG "hinge" motif is found to be most correlated to the highly conversed Asp265 residue of loop 2. Interestingly, these motifs are more highly correlated in FabF than in FabB, although higher positive average correlations between Asp265 and intra-loop 2 residues Pro271, Ser272, and Gly273 are observed in simulations of apo-FabB and its acyl-AcpP complexes.

The residues of loop 1 and 2 of FabB and FabF, regardless of enzyme state, that are most strongly correlated are residues of the GFGG motif of loop 1 and Asp265 of loop 2. In fact, the closed and open conformations of these loops can be clearly distinguished by differences in these intra- and interloop interactions. That we do not observe changes in these networks of interactions within any KS simulation indicates the stability of the open and closed states. According to simulation data, the open conformation (apo-FabF* and acyl-AcpP•FabF) is characterized by hydrogen-bonding interactions involving the GFGG motif and Asp265 and Asn404. Namely, Gly399 forms a hydrogen bond with Asn404 while the negatively charged Asp265 residue simultaneously coordinates Asn404 and the backbone amides of all residues of the GFGG motif. In the open conformation of FabF, average distances of 5.09 Å, 3.91 Å, 3.66 Å, and 4.12 Å, respectively, are computationally observed between the center of mass of the carboxylate moiety of Asp265 and the backbone amide nitrogens of Gly399, Phe400, Gly401, and Gly402 (Figure 2.9). Given the highly conserved nature of Asp265 and its substitution with a less potent hydrogen-bond acceptor (e.g., Asn265

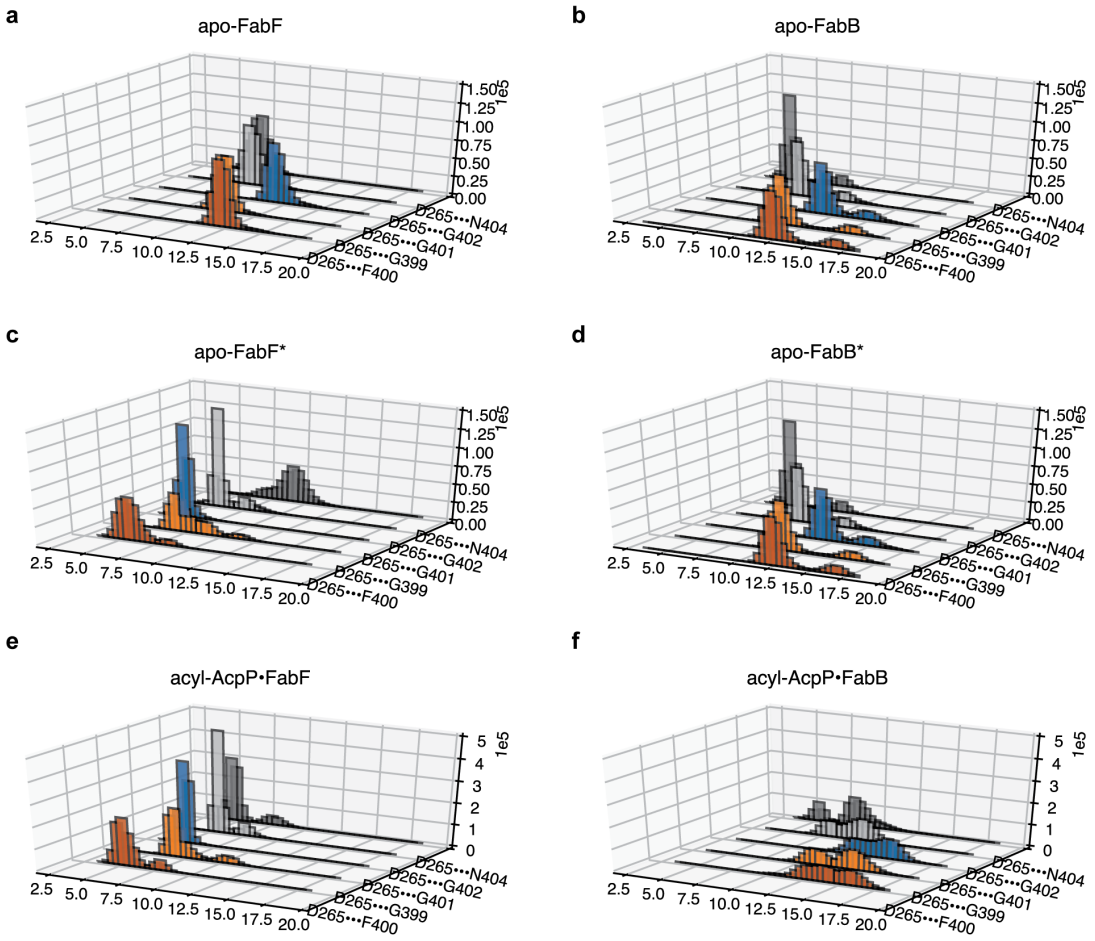

Figure 2.9: *Analysis of the fluctuations of inter-loop hydrogen bonding networks.* Histograms showing the distances between the hydrogen-bond donating Asp265 and highly conversed (hydrogen-bonding accepting) resudes, Gly399, Phe400, Gly401, Gly402, and Asn404 sampled computationally. Histograms of these distances sampled in molecular dynamics (MD) simulations of **a)** *apo*-FabF, **b)** *apo*-FabB, **c)** *apo*-FabF*, **d)** *apo*-FabB*, **e)** acyl-AcpP•FabF, and **f)** acyl-AcpP•FabB, respectively.

in actKS) in iterative type II KSs, it is reasonable to postulate that the coordination of the motion of loop 1 and loop 2 is mediated by Asp265.

Discussion. KSs catalyze multi-step reactions that require the association and dissociation of two distinct acyl-AcpPs and involve the intermediacy of an acyl-enzyme adduct. Enzymes that catalyze such complex chemical transformations often implement gating mechanisms to control solvent access, exert mechanistic selectivity, and/or control reaction order.[37] Zhang and colleagues previously showed that Phe400 of Streptococcus pneumoniae FabF (SpFabF) acts as a KS gating residue.[28] The F400A mutant of SpFabF has reduced catalytic activity relative to wt for its native reaction, but efficiently produces triacetic acid lactone (TAL), a common shunt product of condensing enzymes that results from the mispriming and extension of malonyl-ACP. These results suggest a compromised gating system that no longer controls reaction order. The proposed gating role of Phe400 is also supported with previously published structural data.[28,43,57] In structures of apo-FabB and apo-FabF, Phe400 initially blocks access to the active site cysteine but after transacylation rotates away to form the malonyl-ACP binding site for the pong half-reaction.[28,43,57]

Results reported herein not only confirm and build upon the role of Phe400 as a KS gating residue but also provide additional context for its mechanism and regulation. With this new information, we propose that elongating KSs use a double drawbridge-like gating mechanism[37] to direct substrate binding and control the timing and sequence of the transacylation and condensation half-reactions. From this study we propose the model shown in Figure 2.10. Here, ACP binds to apo-KS, upon which ACP chain-flips[54] its cargo into the KS active site as KS loops 1 and 2 move in a coordinated manner to assume an open conformation, forming a transient, hydrophobic delivery/extraction pocket that temporarily

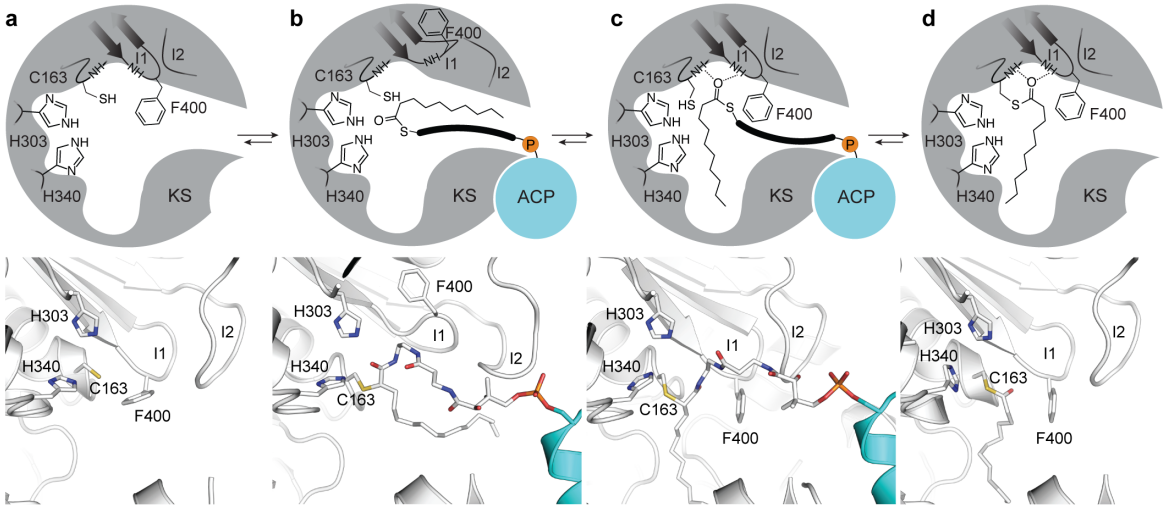

Figure 2.10: *Proposed gating mechanism of elongating ketosynthases*. Figure demonstrates the active site conformational changes that facilitate acyl-chain transfer in elongating KSs as demonstrated by trapped crystallographic states from this work and previous studies. **a),** The *apo*-form of the KS active site illustrated by a 2D schematic of the active site architecture (top) and the crystal structure of apo-FabF (PDB: 2GFW) (bottom). **b)** Active site reorganization to the "gate-open" conformation upon association of acyl-AcpP with KSs as seen in the C16AcpP-FabF structure reported herein with a 2D schematic of the active site (top) and pymol rendering of the active site (bottom). **c)** Active site of C12AcpP-FabB, illustrating the "gate-closed" transacylation competent form of the active sites of elongating KSs shown as 2D schematic (top) and pymol rendering (bottom). Residues are represented in FabF numbering. **d)** the acyl-enzyme adduct form of FabF (PDB: 2GFY) shown as a schematic (top) and rendering (bottom). Active site catalytic residues Cys163, His303, His340, and Phe400 are provided in FabF residue numbering, represented as sticks, and colored according to element (C-white, O-red, N-blue, S-yellow). Hydrogen-bonding interactions are represented as dotted lines.

accommodates the substrate (Figure 2.10b). Loops 1 and 2 then return to their closed conformations, directing the substrate's acyl chain into the acyl binding pocket while simultaneously restoring the oxyanion hole that facilitates transacylation (Figure 2.10c). Upon transacylation, holo-ACP dissociates and Phe400 rotates to form the malonyl-ACP binding pocket (Figure 2.10d).

The proposed gating mechanism coordinated by loops 1 and 2 is in agreement with our mutagenesis studies, MD simulations, and MSA analysis. FabF pocket-blockage mutants, G310M and G310F, and loop 2 destabilization mutants, D265A and D265N, show reduced crosslinking with long-chain acyl-AcpP substrates as compared to short-chain substrates. These results, taken together, indicate that blocking transitions to the gate-open conformation or disfavoring the gate-open conformation by disruption of the Asp265 coordinated interaction network impairs KS activity with acyl-AcpPs. Interrogation of these trapped catalytic states using long time-scale MD simulations demonstrates that the open and closed conformations of FabF are stable and coordinated by a conserved network of hydrogen bonding interactions. Furthermore, this network of interactions serves to correlate the motions of loops 1 and 2 and is generally conserved in elongating KSs in type I PKS, type I FAS, and type II PKS.

Given our gating model (Figure 2.10), we now propose a general mechanism used by these synthases to regulate substrate processing and catalysis. Transition to the open-conformation disrupts the oxyanion hole, which suggests that (trans)acylation of the active site cysteine occurs after the gate adopts the closed conformation. Consequently, the gate could act as a sensor that only reorganizes the oxyanion hole when the correct substrate is

bound. Therefore, the gate and F400 may prohibit FAS KSs from reacting with fatty acyl intermediates that are not appropriate condensation substrates (i.e. β-hydroxy-acyl-ACPs).

A careful consideration of loops 1 and 2 and their potential specific functions reveals some interesting insights as well. Ramachandran analyses of the GFGG motif's fluctuations during MD simulations illustrate the rigidity of loop 1 in both the closed and open conformations. The φ and ψ angles of the GFGG residues sampled computationally are narrowly distributed with hinge residues, Gly399 and Gly402, possessing distinct backbone dihedral angles in the open and closed conformations (Figure 2.5b,c). This is in contrast to Ramachandran analysis of the hinge residues in loop 2, which shows that although the φ and ψ angles of Pro272 and Pro273 are distinct in the open and closed states in our crosslinked structures, they sample similar φ, ψ angle distributions during simulations (Figure 2.5e,f and S2.31,S2.32). These results, along with the increased sequence variation in different condensing enzyme families, suggests loop 2 may modulate loop 1 gating events, potentially conferring different activities or substrate specificities to distinct KSs. This is an appealing hypothesis, as loop 2 sits on top of loop 1, effectively capping it in when in the closed conformation. Furthermore, the dynamism of loop 2 in our apo-FabF* simulations indicates that acyl-AcpP substrates stabilize the gate-open conformation. In fact, AcpP binding or the chain flipping of acyl cargo into the KS active site may serve to trigger gating events by stabilizing loop 2's open position. Movement of loop 2 would thereby allow loop 1 to assume the gate-open conformation, raising the drawbridge and allowing substrate access to the active site. While more work is needed to test this hypothesis, a recent study by Robbins et al. demonstrated that mutation of S315A from loop 2 of DEBS KS1 increased the formation of propionate, which results from the decarboxylation of the methylmalonyl-ACP substrate.[58] These findings suggest an

important role for loop 2 residues in DEBS and that the altered S315A mutant activity may be indicative of an impaired gating system.

The importance of KS-catalyzed carbon-carbon bond formation in biosynthetic pathways cannot be overstated. These enzymes perform complex reactions and employ poorly understood biochemical regulatory mechanisms to ensure substrate specificity and product fidelity. Here, the combination of chemical, structural, and computational biology together support a gating mechanism used by elongating KSs to recognize and process acyl-ACP substrates. These results provide broadly applicable insights into KS activity, function, and substrate selectivity as well as further our understanding of the *E. coli* AcpP interactome.

Methods

Ketosynthase protein production, purification, and tag cleavage: The N-terminal His8-tag FabF and FabB recombinant proteins were expressed in *E. coli* BL21 and cultured in Terrific Broth (MilliporeSigma). Cells were grown in the presence of 50 $mg{\bullet}L^{-1}$ kanamycin, induced with 0.5 mM Isopropyl β-d-1-thiogalactopyranoside (IPTG) at OD600 = 0.8, and incubated at 37 °C for 4 h. The cells were spun down by centrifugation at 500 xg for 30 min and the collected pellets were resuspended in lysis buffer (50 mM Tris, 150 mM NaCl, 10% glycerol, pH 8.0) along with 0.5 $mg{\bullet}mL^{-1}$ lysozyme (Worthington Biochemical Corp). The pelleted cells were lysed by sonication (4 s pulses for 5 min), followed by another centrifugation at 17,400 xg for 30 min to clear the lysate. The proteins were purified using Ni-NTA resin (Thermo) in the column and were washed sequentially with wash buffer (50 mM Tris, 150 mM NaCl, 10% glycerol, pH 8.0) followed by elution with 250 mM buffered imidazole. The His8-tags of purified proteins were cleaved with bovine thrombin (2 U per 1 mg protein) for 16 h at 6 °C while dialyzing against the dialysis buffer (50 mM Tris pH 8.0,

150 mM NaCl, 10% glycerol, .5mM TCEP). Resulting solutions were re-purified using Ni-NTA resin (Thermo Fisher Scientific) to trap the un-cleaved proteins. The FabF and FabB were further purified by FPLC using the HiLoad Superdex 200 (GE Biosciences) size exclusion column. The eluted proteins were collected and concentrated to 2-4 mg•mL^{-1} using Amicon Ultra Centrifuge Filters (MilliporeSigma) with 10 kDa molecular weight cut off.

Native AcpP recombinant protein purification: Native AcpP recombinant protein was expressed in *E. coli* BL21 (DE3) and grown in Terrific Broth (Source). Cells were grown at 37 °C in the presence of 100 mg•L^{-1} ampicillin, induced with 0.5 mM IPTG at OD600 = 0.8, and incubated at 18 °C for 16 h. The cells were spun down by centrifugation at 500 xg for 30 min, and the collected pellets were resuspended in lysis buffer (50 mM Tris, 5% glycerol, pH 7.4) along with 0.1 mg•mL^{-1} lysozyme (Worthington Biochemical Corp). The pelleted cells were lysed by sonication (4 s pulses for 5 min). Due to the high stability of AcpP, irrelevant proteins were precipitated by dripping in same volume of isopropanol into the lysate at the speed of 0.1 mL•s^{-1}. The resulting mixture was spun down by centrifugation at 11,200 xg for 1 h and the supernatant was injected directly into FPLC. AcpP was purified by HiTrap Q HP anion exchange chromatography column in 50 mM Tris buffer with a gradient of NaCl from 0 M to 1 M and the native AcpP eluted around 0.3 M NaCl. The eluted protein was collected and concentrated using Amicon Ultra Centrifuge Filters (Millipore) with 3 kDa molecular weight cut off.

Holo-AcpP apofication and apo-AcpP purification: The purified protein was resulted in a mixture of holo-AcpP and apo-AcpP. The phosphopantetheine moiety on holo-AcpP was removed by acyl carrier protein hydrolase (AcpH) in lysis buffer for 16 h.[59] Final reaction concentrations: 5 mg•mL–1 AcpP mixture, 0.01 mg•mL–1 AcpH, 50 mM Tris (pH 7.4), 10%

glycerol, 10 mM MgCl2, 5 mM MnCl2, 0.25 % DTT. The resulting pure apo-AcpP, was analyzed by conformationally sensitive urea PAGE (2.5 M urea), and further purified by FPLC using HiLoad 16/600 Superdex 75 PG (GE Biosciences) size exclusion column to remove AcpH. The eluted protein was collected and concentrated using Amicon Ultra Centrifuge Filters (Millipore Sigma) with 3 kDa molecular weight cut off.

Apo-AcpP loading and crypto-AcpP purification: All crosslinkers were loaded onto apo-AcpP using a one-pot chemoenzymatic method.[38] This method utilizes three CoA biosynthetic enzymes (CoaA, CoaD, CoaE) to form CoA analogues and a phosphopantetheinyl transferase (PPTase, Sfp) to load them onto apo-AcpP, resulting in crypto-AcpP. Final reaction concentrations: 1 mg•mL^{-1} apo-AcpP, 0.04 mg•mL^{-1} Sfp, 0.01 mg•mL^{-1} CoaA, 0.01 mg•mL^{-1} CoaD, 0.01 mg•mL^{-1} CoaE, 50 mM potassium phosphate pH 7.2, 12.5 mM MgCl2, 1 mM DTT, 0.2 mM pantetheineamide probe (1a,1c or 2a,2b) (Figure 2.2), and 8 mM ATP. The stock solutions of crosslinkers 1a-1c, 2a, and 2c were prepared by dissolving them in DMSO to a final concentration of 50 mM. Reactions were incubated at 37 °C for 16 h and then purified by HiLoad Superdex 75 (GE Biosciences) size exclusion column. The eluted protein was collected and concentrated using Amicon Ultra Centrifuge Filters (Millipore Sigma) with 3 kDa molecular weight cut off up to a concentration at 1-3 mg•mL^{-1}.

Crosslinking reaction and crosslinked complex purification: The crosslinking reactions were carried out by mixing crypto-AcpP with its partner protein (FabF or FabB) in 5:1 ratio at 37 °C for 16 h. Reactions were examined by 12 % SDS PAGE and purified by HiLoad 16/600 Superdex 200 PG (GE Biosciences) size exclusion column using minimal buffer (20 mM Tris, 50 mM NaCl, pH 7.4). The resulting protein complex was greater than

95 % in purity, determined by SDS PAGE, and was concentrated to 8-10 mg•mL^{-1} using Amicon Ultra Centrifuge Filters (MilliporeSigma) with 30 kDa molecular weight cut off. The concentrated crosslinked complex was immediately used for protein crystallization or flash-frozen and stored in –80 °C freezer for later use.

Construction of ketosynthase mutants: Ketosynthase mutants were generated using the site directed mutagenesis method developed by Liu and Naismith.[60] All constructs were verified via sanger sequencing (Eton Bioscience Inc.). Primers used for mutagenesis can be found in Figure S2.33.

Crosslinking assay: Each reaction was set up to contain 40 μM of crypto-AcpP, 20 μM of FabF, and buffer (25 mM Tris, 150 mM NaCl, 10% glycerol, 0.5 mM TCEP, pH 7.4). To stop the reaction at the designated time point, 2.5 μL of the reaction solution was mixed with 10 μL of 3X SDS dye. Samples were analyzed by 12% SDS-PAGE and the intensity of protein bands was measured by ImageJ.[61] The crosslinking efficiency was calculated by [(Icrosslink)/(Icrosslink+IFabF)] × 100% where "I" stands for band intensity. All reactions were performed in biological triplicate and the crosslinking efficiency of mutants was normalized to the average wild type crosslinking efficiency to obtain a normalized relative crosslinking efficiency. The plotted data represents the average normalized crosslinking efficiency of each mutant and the error bars are represented as standard deviation (±SD).

General synthetic methods: General synthetic methods are provided as a supplementary note (Supplementary Note 8) and NMR characterization of compounds and intermediates is provided in Supplementary Note S2.8.

Crystallization, structure determination and refinement: The crystals of the crosslinked complexes were grown by vapor diffusion at 6 °C. In detail, 1 μL of crosslinked

complex (8-10 mg•mL^{-1}) was mixed with 1 μL of corresponding crystallographic condition and the mixture was placed inverted over 500 μL of the well solution (hanging-drop method). The AcpP-FabF complexes crystallized in 26-30 % PEG 8K, 0.1 M sodium cacodylate pH 6.5, and 0.3 M NaOAc, yielding numerous orange rods amongst a heavy precipitate. Seeding trials were performed to increase size and quality of the samples. The C12AcpP-FabB complexes produced crystals in two conditions: 20% PEG 8K, 0.2 M $Mg(OAc)_2$, 0.1 M sodium cacodylate pH 6.5 as well as 30% PEG 8K, 0.2 M $(NH_4)_2SO4$, 0.1 M sodium cacodylate, pH 6.5. Both conditions yielded square plates and required one to two weeks for complete growth of crystals. The C16AcpP-FabB complexes produced crystals in 18-24 % PEG 8K, 0.1 M sodium cacodylate, and 0.3 M NaOAc, pH 6.5.

All data were collected at the Advanced Light Source (ALS) synchrotron at Berkeley. Data were indexed using iMosflm[62] then processed and scaled using aimless from the CCP4 software suite62,63.[63,64] Scaled reflection output data was used for molecular replacement and model building in PHENIX[65]. For AcpP-FabF complexes, phases were solved using molecular replacement by first locating the larger FabF (PDB: 2GFW[43]) monomer followed by a second search function to place the smaller AcpP (PDB: 2FAC[66]) molecule in the residual density. For C12AcpP-FabB and C16AcpP-FabB complexes, initial phases were solved using molecular replacement by first performing a search function using the FabB monomer (PDB: 1G5X30) and then manually placing the AcpP molecules in the residual electron density. The parameter file for the covalently bonded 4'-phosphopantetheine was generated using Jligand (CCP4)[64]. Manually programmed parameter restraints were used to create the associated covalent bonds between 4'-phosphopantetheine to Ser36 and Cys163

during refinement. These parameters are provided in the parm-file folder located in the online Source Data file.

Preparation of apo-KS structures for MD simulations: Simulations of apo-FabB and apo-FabF were performed using two sets of initial coordinates: one derived from previously reported 1.55 Å apo-FabB (PDB: 2VB9[55]) and 2.40 Å apo-FabF (PDB: 2GFW[43]) and a second set generated by modifying the crosslinked structures of *E. coli* AcpP-FabB and AcpP-FabF reported herein by deleting coordinates corresponding to atoms from AcpP.

Preparation of acyl-AcpP•KS structures for MD simulations: The crosslinked structures of *E. coli* AcpP-FabB and AcpP-FabF reported herein were used to prepare the initial coordinates used to perform molecular dynamics. The asymmetric unit of the AcpP-FabF structure is –unlike that of crosslinked AcpP-FabB– the 1:1 AcpP•FabF complex. In order to prepare coordinates for the (functional) biological unit, AcpP2•FabF2, the asymmetric unit of the AcpP1-FabF1 structure was rotated about the twofold symmetry axis of the AcpP-FabF biological unit. The 2:2 complexes of acyl-AcpPs shown in Scheme S1 and either FabB or FabF were constructed by manually modifying the chemical crosslinker present the experimental structures. Modifications of this moiety were performed using Avogadro 1.1.1[67], Gaussview 5.0.9, and Pymol v.1.8.6, and Pymol v.2.2.3. Schrodinger was used to add poorly resolved C- and N-terminal residues omitted in the dimeric AcpP•FabB and AcpP•FabF complexes. The protonation state of titratable residues in the apo-KSs and acyl-AcpP•KS didomains were assigned using the H^{++} webserver, with the exception of the active site Cys163 of FabB and FabF; this residue was simulated in as a thiolate.[68–70] Histidine protonation states were inspected manually.

Parameter generation for acyl-AcpP: For each simulated AcpP•KS complex, the acyl substrate, phosphopantetheine cofactor, and the conserved serine residue of AcpP to which the cofactor is affixed were treated as a single nonstandard residue. AMBER (ff14SB[71]) and GAFF[72] type force field parameters were assigned to the atoms of these nonstandard residues using ANTECHAMBER[73]. Partial charges for all atoms in all nonstandard residues were determined using the RESP methodology[74]. All quantum calculations were performed using Gaussian 09.

Preparation of simulation cells: Proteins were solvated in a water box with TIP3P[75] water molecules. Using TLEAP, the simulation cell was constructed such that its edges were placed 10 Å away from the closest proteinogenic atom. TLEAP was used to neutralize and salt the water box to mimic physiological conditions (0.15 M). Counterions (Na^+ and Cl^-) were also added to the simulation cell randomly.

Simulation details: Amber16 and Amber18 were used to perform all molecular dynamics (MD) simulations. All simulations were performed using the ff14SB[71] and GAFF[72] force fields. A 2 fs time-step was utilized via the SHAKE algorithm, which constrains all nonpolar bonds involving hydrogen atoms[76]. Long-range electrostatic interactions were treated using the Particle Mesh Ewald (PME) method with a 10 Å cutoff for all non-bonded interactions[77]. Both solvated protein complexes were energy minimized in a two-step fashion. In a first step, solvent molecules and counterions were allowed to relax, while all protein atoms were restrained using a harmonic potential ($k = 500$ kcal mol^{-1} $Å^{-2}$). This geometry optimization was followed by an unrestrained energy minimization of the entire system. The thermal energy available at a physiological temperature of 310 K was slowly added to each system over the course of a 3.5 ns NVT ensemble simulation. The solvated complexes were

then subjected to unbiased isobaric-isothermal (NPT) simulations for 25 ns in order to equilibrate the heated structures. Three independent 500 ns production MD (NPT ensemble) of each system were performed with different initial velocities. For both NVT and NPT simulations, the Langevin thermostat (λ = 5.0 ps^{-1}) was used to maintain temperature control84. Pressure regulation in NPT simulations (target pressure of 1 atm) was achieved by isotropic position scaling of the simulation cell volume using a Berendsen barostat.

Analysis and visualization of simulation data: Analysis was performed using CPPTRAJ Version V4.14.0 (AmberTools V19.00), PYTRAJ v2.02.dev0, a Python front-end for the CPPTRAJ analysis code, and MDTRAJ v1.9.385. Trajectories were visualized using VMD 1.9.4 and Pymol v1.8.6 and Pymol v2.2.3. Coordinate data was written to disk every 10 ps.

Supplementary Information

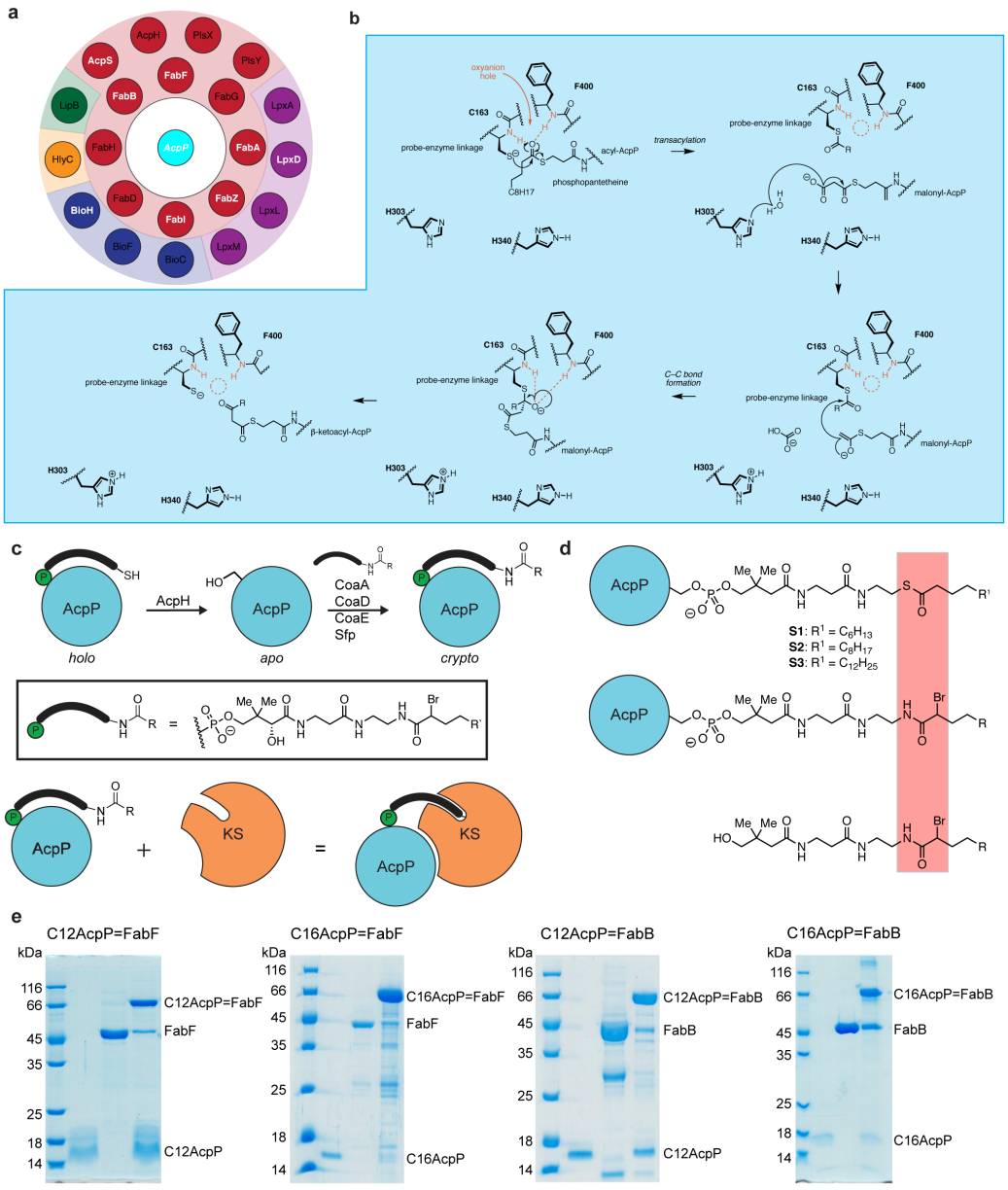

Figure S2.1: *Chemistry and biology of ketosynthases*. **a**. ACP "Interactome" in *E. coli*. Proteins are colored by biosynthetic pathway (red: fatty acid biosynthesis, purple: lipid A biosynthesis, Blue: biotin biosynthesis, yellow: hemolysin activation, green: lipoyl activation of lipoate-dependent enzymes. **b.** Proposed reaction mechanism of elongating β-ketoacyl-AcpP-synthase FabB (KASI) and FabF (KASII). Top row of mechanism shows the transacylation half-reaction, while the bottom portion illustrates the condensation half-reaction. **c.** Crosslinking workflow scheme demonstrating apofication and loading of ACP with crosslinking probes to produce *crypto*-ACP, which is then mixed with partner protein to produce a crosslinked complex. **d.** Comparison of acyl-AcpP to crypto-AcpP loaded with substrate or crosslinking substrate mimetic, respectively. **S1**, **S2**, and **S3** indicate the acyl-AcpPs subjected to simulations as constituents of acyl-AcpP•KS complexes reported herein **e.** Crosslinking gels of C12AcpP-FabF, C16AcpP-FabF, C12AcpP-FabB, and C16AcpP-FabB that were used to verify the formation of crosslinked complex before purification and crystallization.

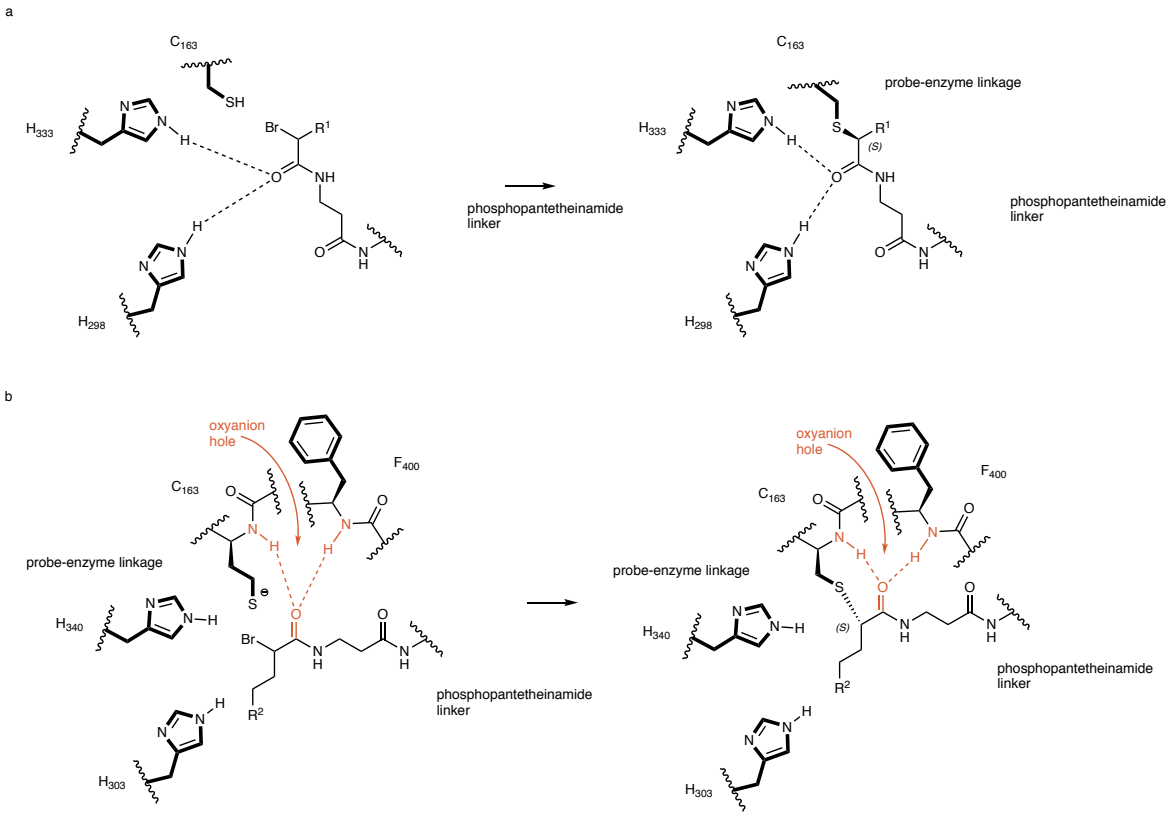

Figure S2.2: *Illustration of crosslinking reactions between the α-bromo pantetheineamide probe and KS active site cysteine residues.* Hypothetical crosslinking reactions of C16αBr-crypto-AcpP and C12αBr-crypto-AcpP with FabF and FabB. C16AcpP-FabF (**a**) and C12AcpP-FabB (**b**). $R^1 = C_{12}H_{25}$ and $R^2 = C_8H_{17}$

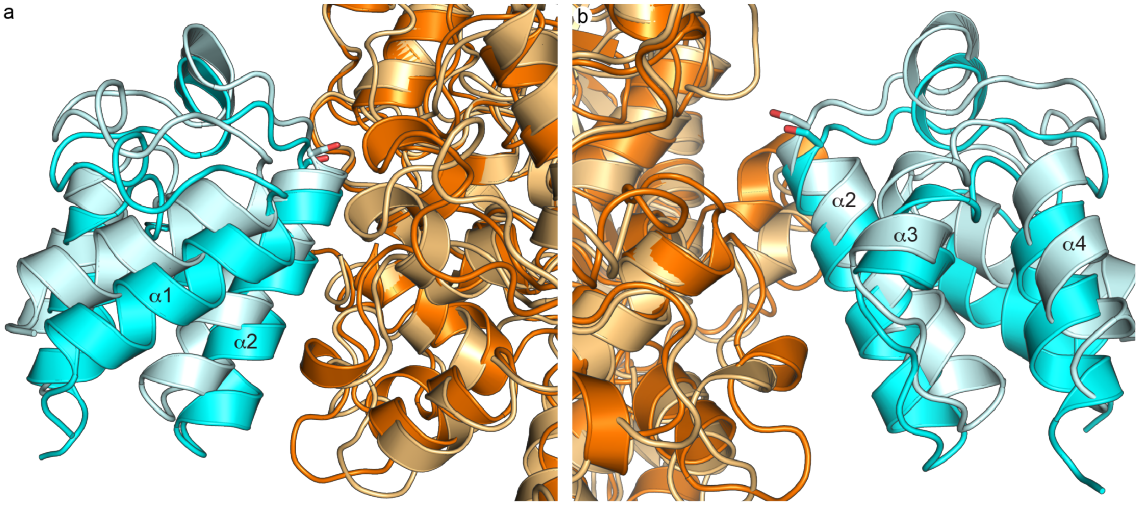

Figure S2.3: *Comparison of C16AcpP-FabF and C12AcpP-FabB binding modes.* **a. b.** Superposition of C12AcpP=FabB (AcpP shown as light cyan) with C16AcpP=FabB (AcpP shown as cyan) shown from two 180° related views demonstrating differences in the angle and conformation of AcpP engagement with each KS interface.

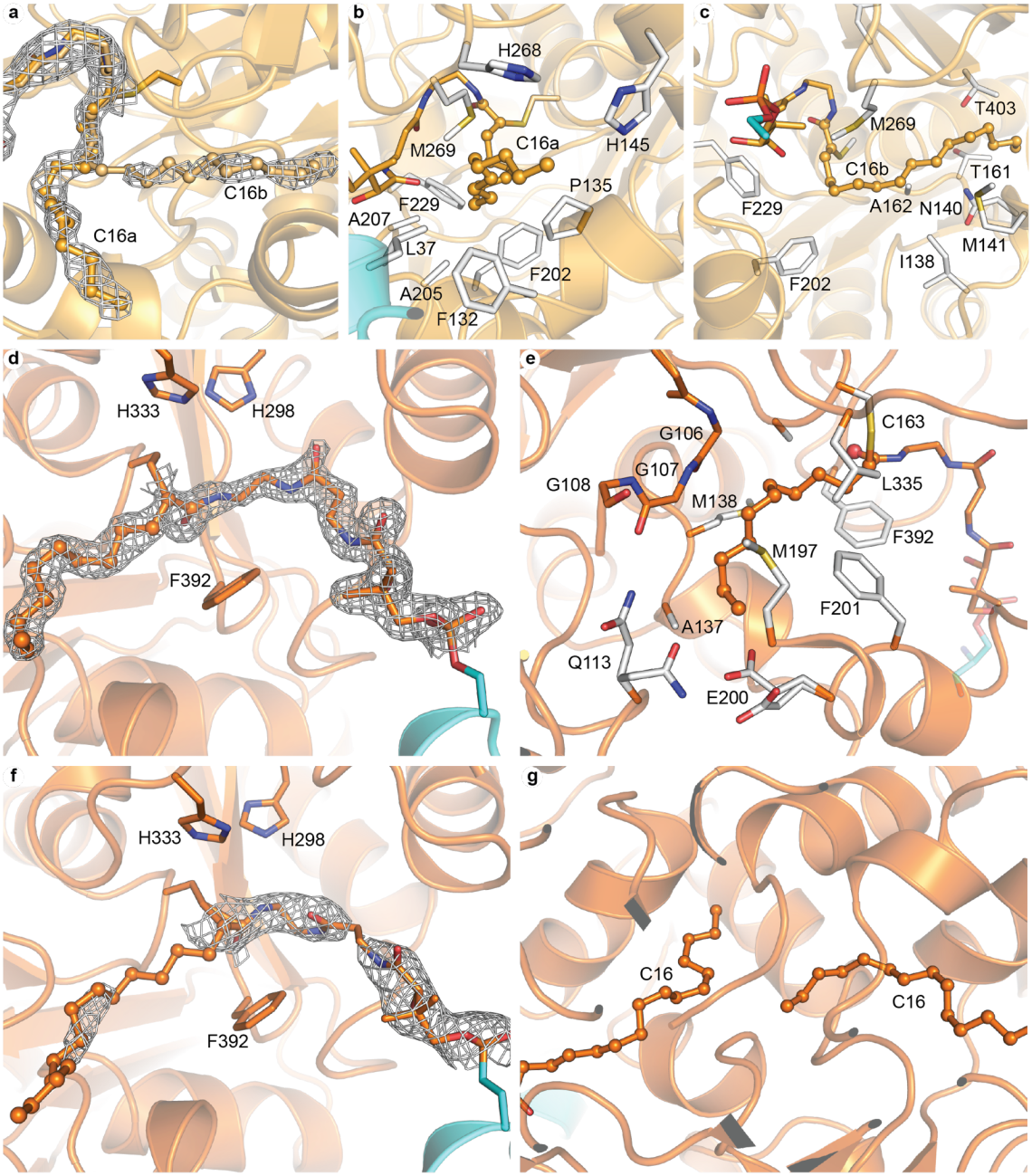

Figure S2.4: *Comparison of alkyl chain electron density and substrate•KS interactions in C16AcpP-FabF, C12AcpP-FabB, and C16AcpP-FabB crystal structures.* AcpP is shown as cyan in all panels. FabF is shown in light orange and FabB is shown in bright orange. **a.** Electron density of C16 alkyl chain in conformations a (C16a) and b (C16b) from the C16AcpP-FabF structure contoured with 2Fo-Fc maps at 1.0 σ **b.** All FabF residues within 4 Å of alkyl chain conformation a (C16a). **c.** All residues within 4 Å of alkyl chain conformation b (C16b). **d.** Electron density of C12 alkyl chain from C12AcpP-FabB structure contoured at 1.0 σ. **e.** All FabB residues within 4 Å of the C12 alkyl chain substrate analog. **f.** Electron density of C16PPant probe from the C16AcpP-FabB structure contoured at 1.0 σ. **g.** Attempts to model a C16 probe reveal a constricted active site that places alkyl chains bound within the active site of both KS monomers in close proximity to one another and in unfavorable conformations

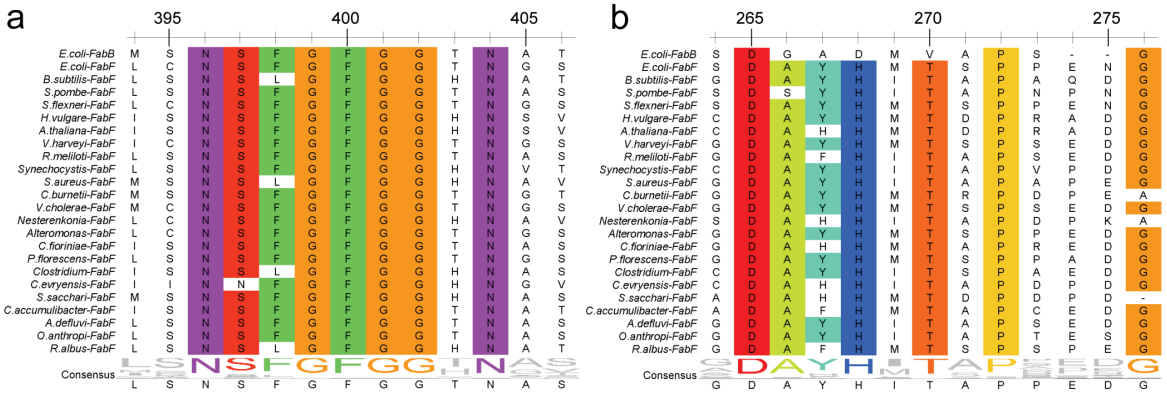

Figure S2.5: *Analysis of loop 1 and 2 conservation by multi-sequence alignment (MSA).* **a.** MSA alignment of FabB and 100 FabF orthologues comparing the Loop 1 GFGG β-turn region and surrounding conserved residues (FabF numbering). **b**. MSA Alignment of FabB and 100 FabF orthologues comparing the loop 2 sequence and surrounding conserved residues (FabF numbering).

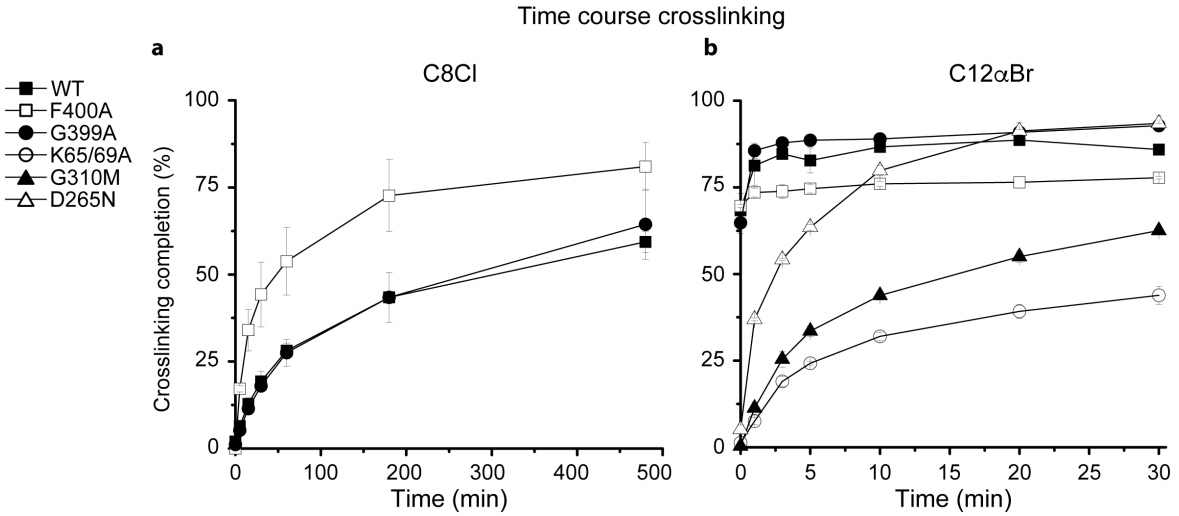

Figure S2.6: *Time-course crosslinking results of of wt FabF and select gating mutants*. C8-chloroacrylate-AcpP (**a**) and C12-α-Bromo-AcpP (**b**). Results in panel **a** indicate that the F400A gate removal mutant crosslinks faster than the wt enzyme using C8Cl probes and G399 crosslinks similarly to wt FabF. Results using the C12αBr probes in panel **b** show that the gating mutant K65A/K69A, pocket-block mutant G310M, and destabilization mutant D265N all crosslinked at slower rates as compared to wt FabF, G399A, and F400A. G310M and K65A/K69A show the most pronounced reduction in crosslinking rate. All gel-based time-course crosslinking assays were run as biologically independent experiments (n = 3) and analyzed by densitometry using ImageJ. The data are plotted as the average crosslinking efficiency at each respective time point and error bars are represented as standard deviation (± SD). The scanned images of associated gels can be found in Supplementary Figs. 10 and 11. wt FabF (black square), F400A (white square), G399A (black circle), K65A/K69A (white circle), G310M (black triangle), D265N (white triangle). Source data for all experiments are provided as a Source Data file.

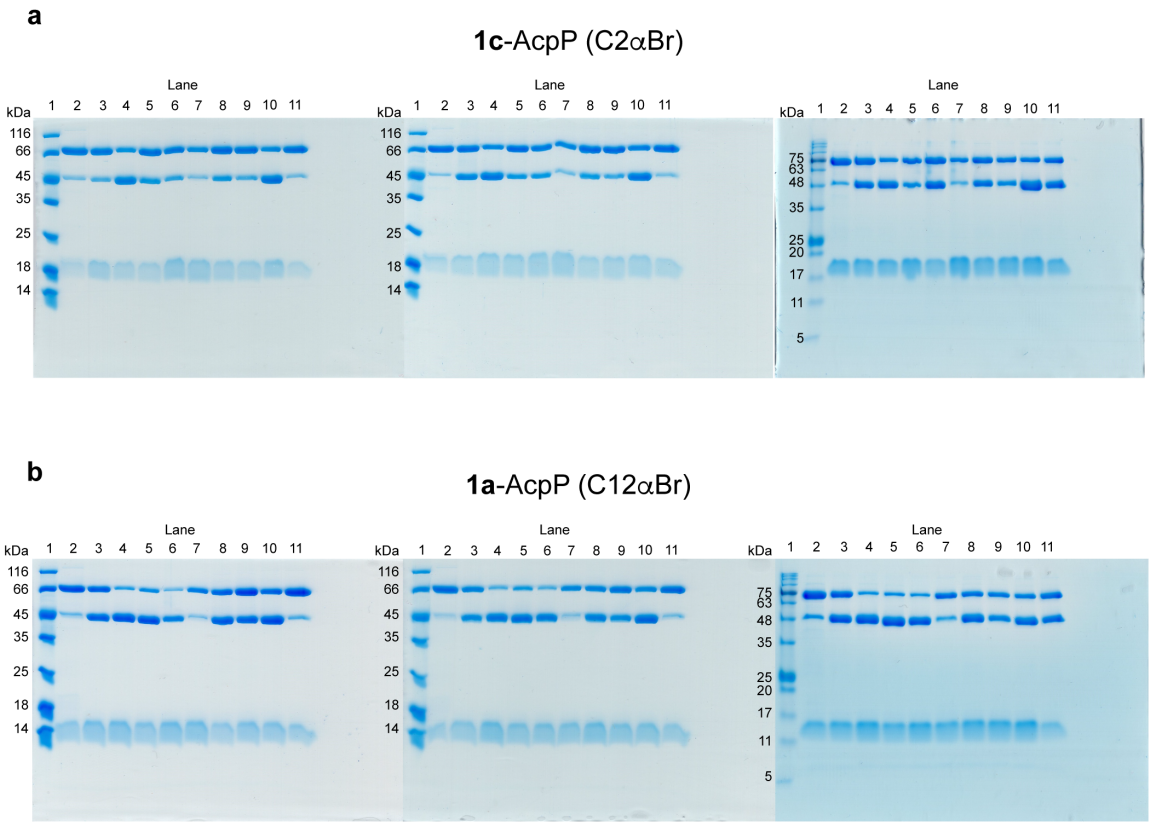

Figure S2.7: *Single time point crosslinking gels of 1a-AcpP (C12αBr) and 1c-AcpP (C2αBr).* The gels shown above are the full scans of the single time point crosslinking gels of **1c**-AcpP (C2αBr) and **1a**-AcpP (C12αBr) with FabF gating mutants from three independent biological experiments (n = 3). More specifically, these gels represent the raw crosslinking gel data used for the data reported in panels **d** and **e** of Figure 2.6 in the main text. **a.** Biological independent experiments (n = 3) of **1c**-AcpP (C2αBr) crosslinking experiments with FabF mutant. Lane 1 - ladder, lane 2 – wt FabF, lane 3 – K65E, lane 4 – K65A/K65E, lane 5 – G310F, lane 6 – G310M, lane 7 – F400A, lane 8 – D265A, lane 9 – D265N, lane 10 – G402A, lane 11 -G399A. **b.** Biological independent experiments (n = 3) of **1a**-AcpP (C12αBr) crosslinking with FabF mutant panel. Lane 1 - ladder, lane2 – wt FabF, lane 3 – K65E, lane 4 – K65A/K65E, lane 5 – G310F, lane 6 – G310M, lane 7 – F400A, lane 8 – D265A, lane 9 – D265N, lane 10 – G402A, lane 11 -G399A.

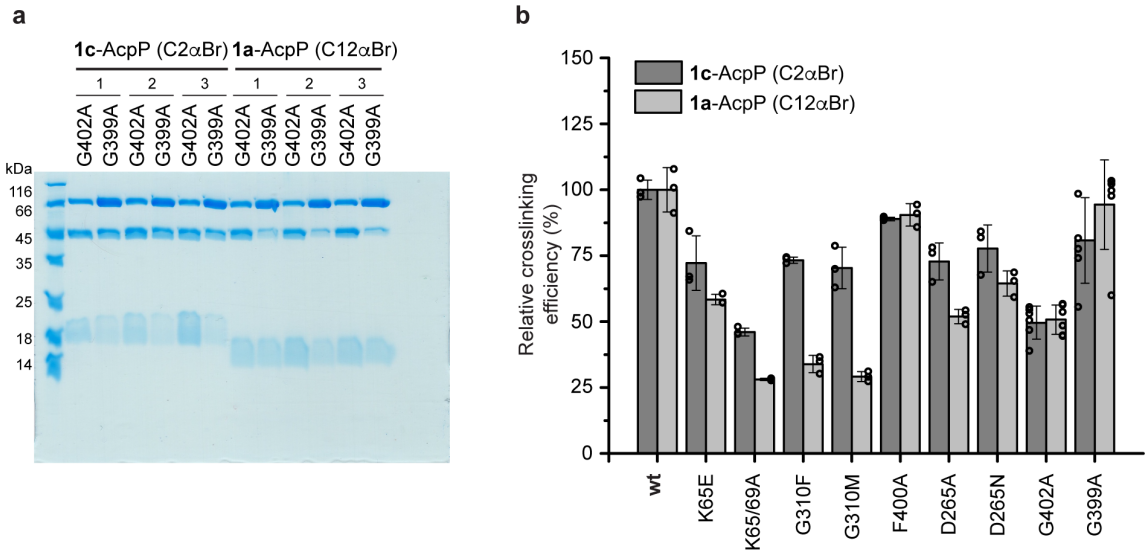

Figure S2.8: *Additional G399A and G402A single time point crosslinking gels of 1a-AcpP (C12αBr) and 1c-AcpP (C2αBr).* **a.** The gel shown above is the full scan of single time point crosslinking analysis of **1c**-AcpP (C2αBr) and **1a**-AcpP (C12αBr) with FabF gating mutants G399A and G402A performed separately from the original experiments due to an outlier measurement in G399A (see lowest open circle in G399A in graph found in panel **b**). These data represent three additional independent biological experiments (n = 3) for G399A and G402A with **1c**-AcpP (C2αBr) and **1a**-AcpP (C12αBr). **b.** Densitometric analysis of single time-point crosslinking efficiency of **1c**-AcpP (C2αBr-AcpP) and **1a**-AcpP (C12αBr-AcpP) with FabF mutants including the three additional biologically independent data points derived from the G399A and G402A crosslinking assay shown in panel **a**. All crosslinking experiments from were performed as biologically independent experiments (n = 3), except for G399A and G402A which were done in sextuplicate (n = 6). All data represented in **b** are the average crosslinking efficiency of each mutant normalized to the average of wt FabF crosslinking efficiency. The error bars in d and e are represented as standard deviation (± SD) and the individual normalized measurements from each independent experiment are overlaid on top of the associated bar plot as open circles. Source data for all experiments are provided as a Source Data file.

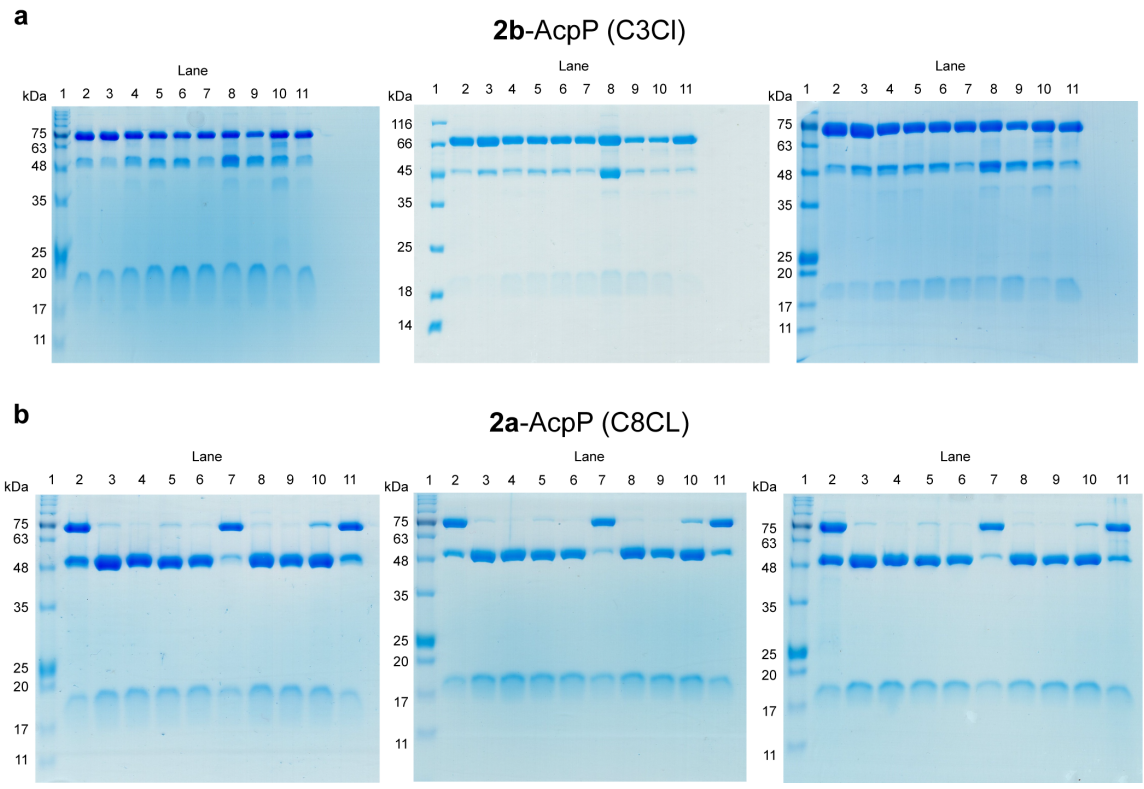

Figure S2.9: ***2a****-AcpP (C8Cl) and* ***2b****-AcpP (C3Cl) crosslinking gels.* The gels shown above are the full scans of the single time point crosslinking gels of **2b**-AcpP (C3Cl) and **2a**-AcpP (C8Cl) with FabF gating mutants from three independent biological experiments (n = 3). More specifically, these gels represent the raw crosslinking gel data used for the data reported in panels **c** and **f** of Figure 2.6 in the main text. **a.** Biological independent experiments (n = 3) of **2b**-AcpP (C3Cl) crosslinking experiments with FabF mutant panel. Lane 1 - ladder, lane2 – wt FabF, lane 3 – K65E, lane 4 – K65A/K65E, lane 5 – G310F, lane 6 – G310M, lane 7 – F400A, lane 8 – D265A, lane 9 – D265N, lane 10 – G402A, lane 11 -G399A. **b.** Biological independent experiments (n = 3) of **2a**-AcpP (C8Cl) crosslinking experiments with FabF mutant panel. Lane 1 - ladder, lane2 – wt FabF, lane 3 – K65E, lane 4 – K65A/K65E, lane 5 – G310F, lane 6 – G310M, lane 7 – F400A, lane 8 – D265A, lane 9 – D265N, lane 10 – G402A, lane 11 -G399A. All reactions were run in parallel for 8 hours then quenched with SDS loading buffer and boiled.

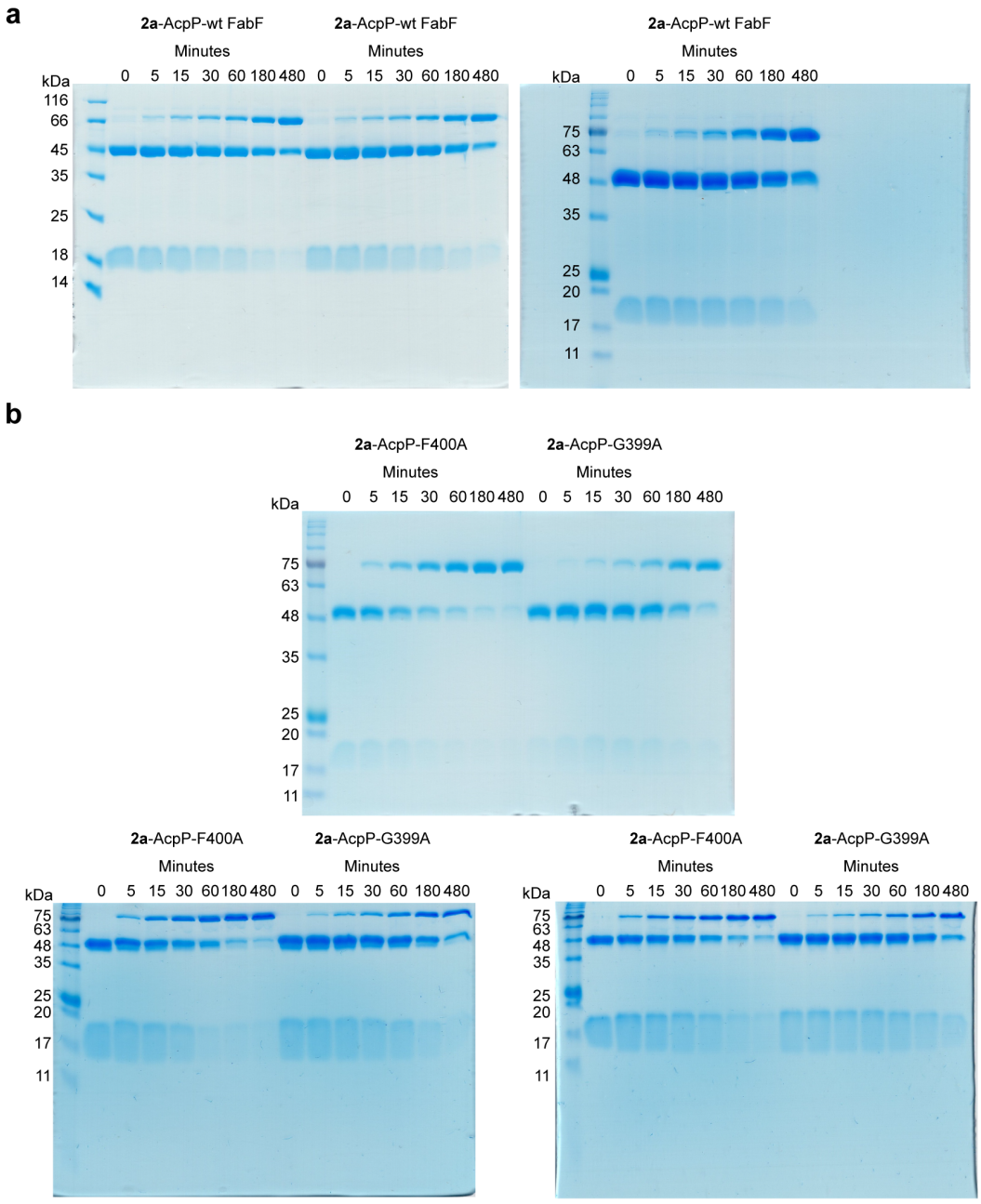

Figure S2.10: *2a-AcpP (C8Cl) time course crosslinking gels.* The gels shown above are the full scans of the time course crosslinking gels of **2a**-AcpP (C8Cl) with FabF gating mutants run as three independent biological experiments (n = 3). More specifically, these gels represent the raw crosslinking gel data used for the data reported in Figure S2.6a. **a.** Biological independent experiments (n = 3) of **2a**-AcpP crosslinking with wt FabF. **b.** Biological independent experiments (n = 3) of **2a**-AcpP crosslinking with FabF mutants F400A and G399A. All reactions were run in parallel and quenched at their respective timepoints by boiling after treatment with SDS loading buffer.

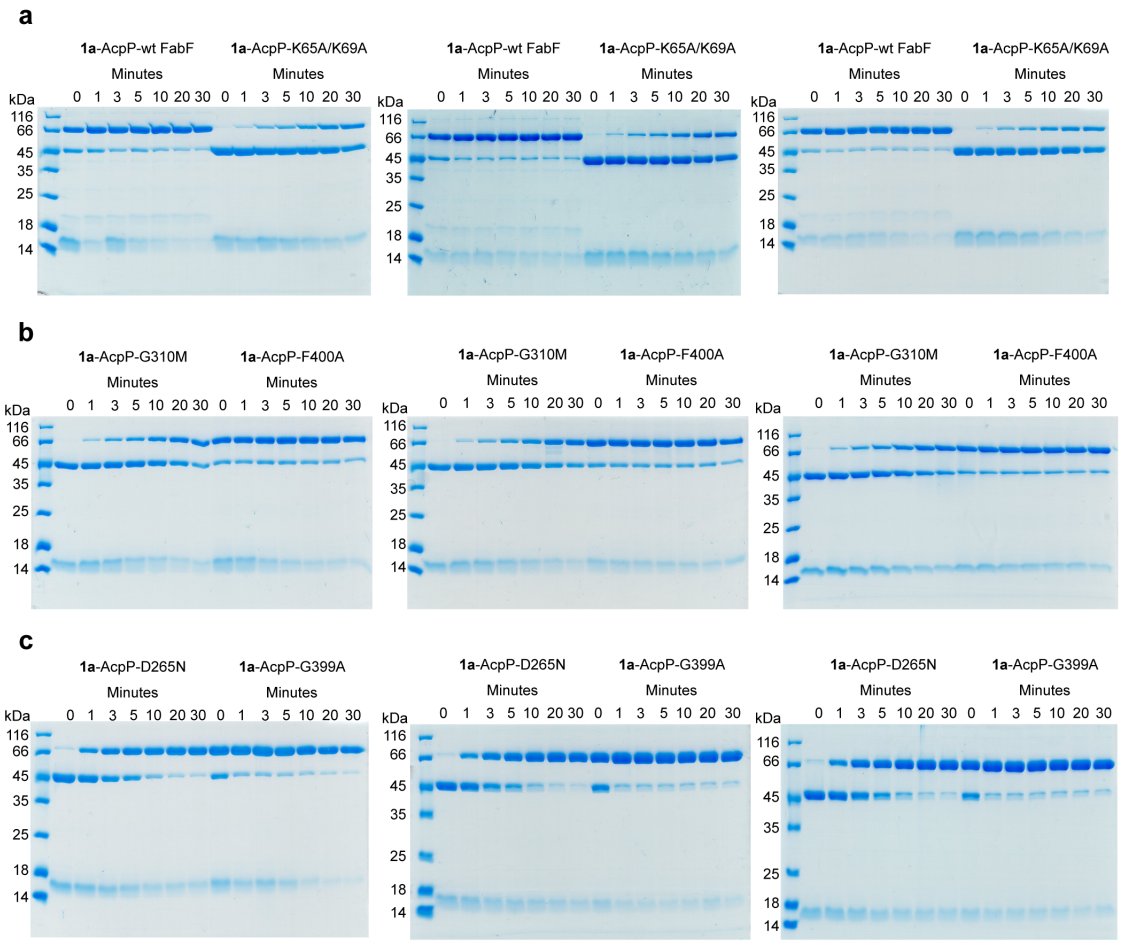

Figure S2.11: *1a-AcpP (C12αBr) time course crosslinking gels.* The gels shown above are the full scans of the time course crosslinking experiment gels of **1a**-AcpP (C12αBr) with FabF gating mutants run as three independent biological experiments (n = 3). More specifically, these gels represent the raw crosslinking gel data used for the data reported in Figure S2.6b. **a.** Biological independent experiments (n = 3) of **1a**-AcpP crosslinking with FabF wt and K65A/K69A FabF interface mutant. **b.** Biological independent experiments (n = 3) of **1a**-AcpP crosslinking with FabF mutants G310M and F400A. **c.** Biological independent experiments (n = 3) of **1a**-AcpP crosslinking with FabF mutants D265N and G399A. All reactions were run in parallel and quenched at their respective timepoints by boiling after treatment with SDS loading buffer.

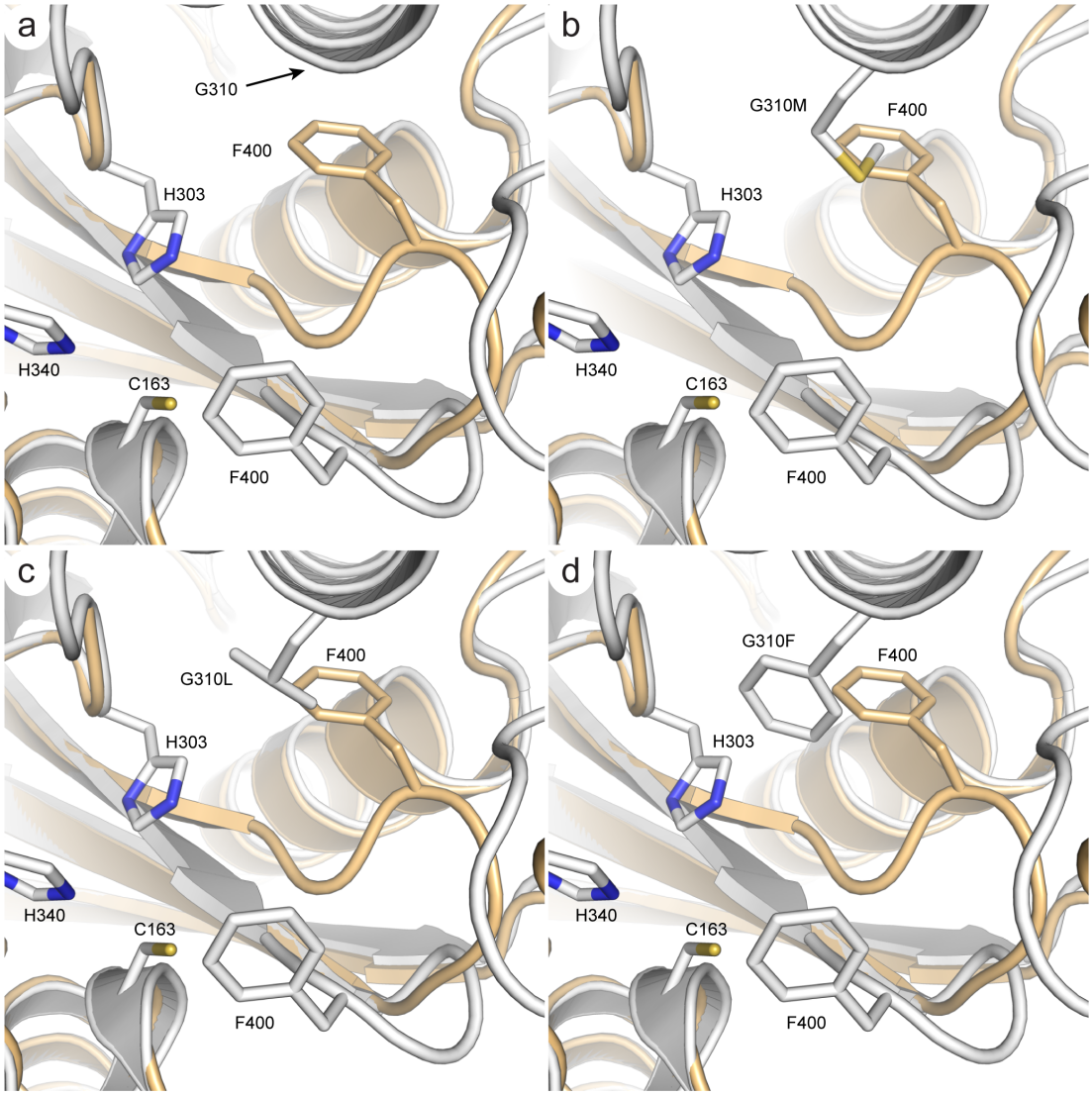

Figure S2.12: *Pocket block mutations.* Figures were generated by mutating Gly310 into bulky hydrophobic residues in PyMOL. G310, when replaced by larger amino acids, occupies the same pocket as Phe400 in the open conformation (light orange) and would likely inhibit transitions of loop 1 from the closed conformation (light-grey) (PDB: 2GFW) to the open conformation (light orange) (C16AcpP-FabF, PDB: 6OKG). **a.** wt G310 FabF. **b.** G310M. **c.** G310F. **d.** G310L.

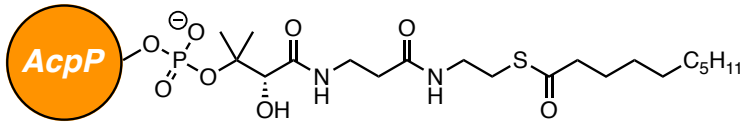

decanoyl-AcpP

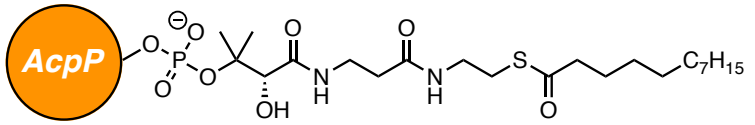

dodecanoyl-AcpP

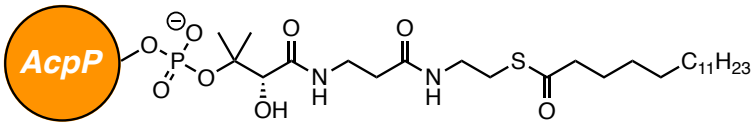

hexadecanoyl-AcpP

Figure S2.13: *Acyl-AcpP substrates used in simulations of the acyl-AcpP2•FabB2 and acyl-AcpP2•FabF2 complexes.*

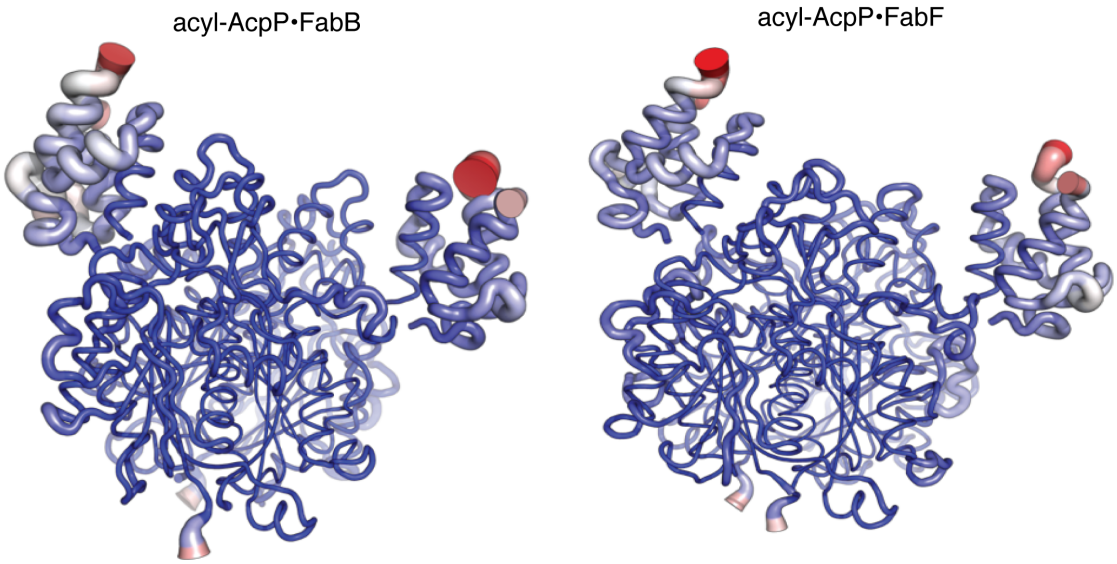

Figure S2.14: *Root mean square fluctuations (RMSFs) of acyl-AcpP2•FabB2 and acyl-AcpP2•FabF2* (determined from simulations) "mapped" onto the x-ray crystal structure of the crosslinked acyl-AcpP-FabB and acyl-AcpP-FabF complexes. Larger (per residue) backbone RMSF values correspond to a thicker "sausage"; color range (blue to white to red) illustrates (per residue) side chain RMSFs with the blue-to-red color range indicating small-to-large RMSF values.

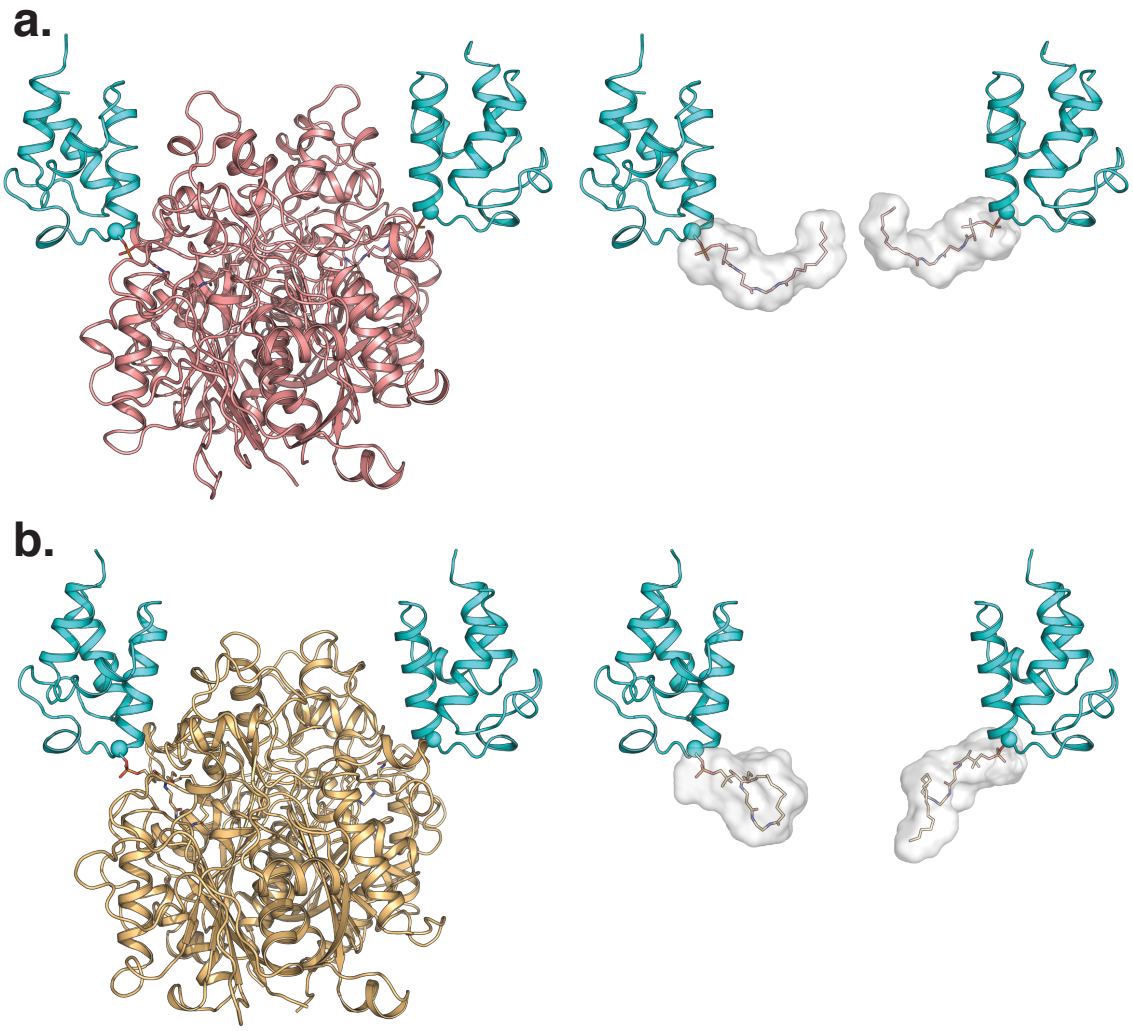

Figure S2.15: *Analysis of the substrate binding pocket determined using POVME (POcket Volume Measurer).* a, acyl-AcpP•FabB. b,acyl-AcpP-FabF.

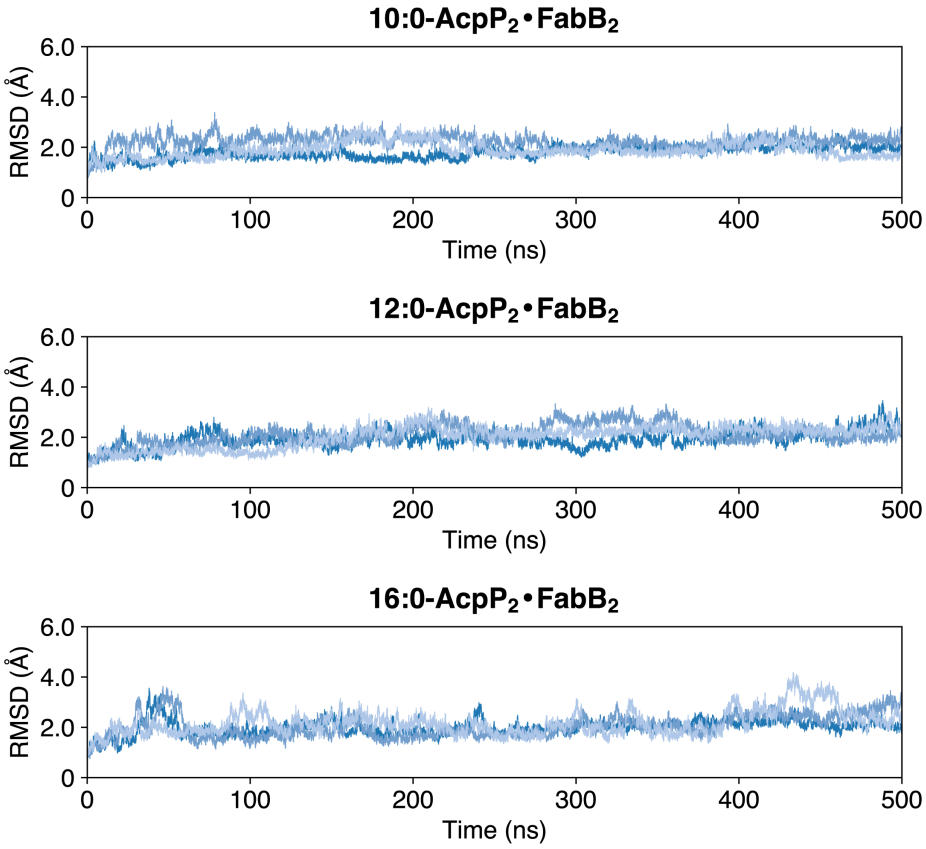

Figure S2.16: *RMSDs of acyl-AcpP2•FabB2 complexes sampled during cMD simulations.* Each blue curve represents an independent 500 ns simulation. Plots were generated by taking every 10th snapshot of the simulation data.

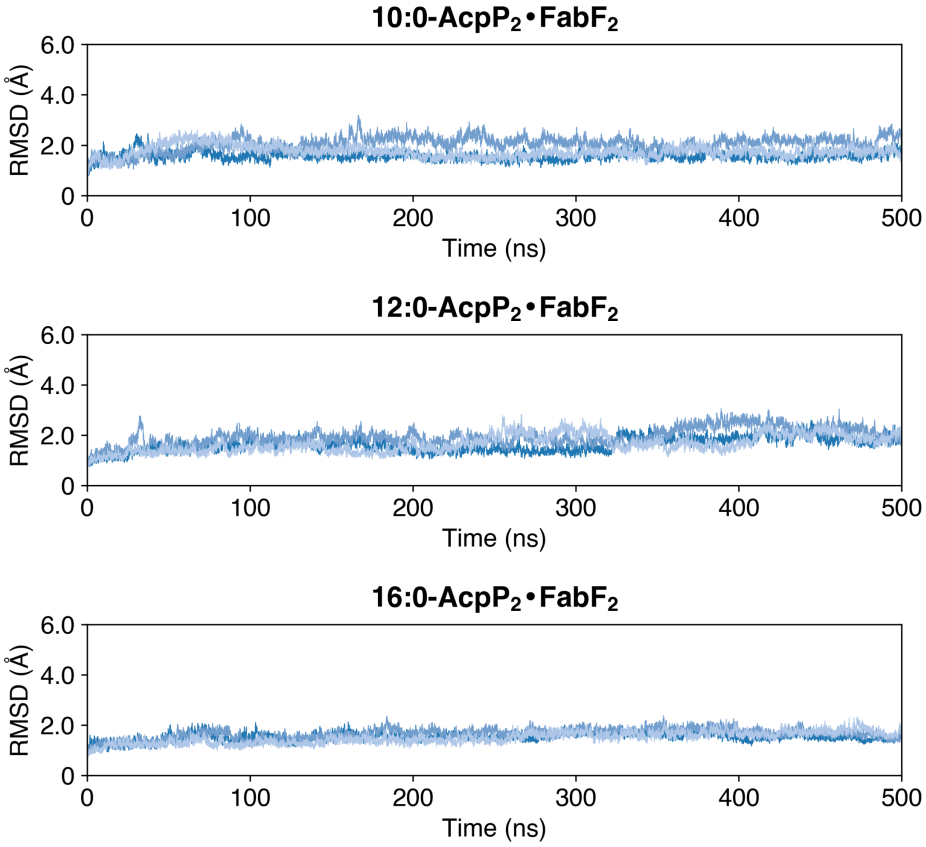

Figure S2.17: *RMSDs of acyl-AcpP2•FabF2 complexes sampled during cMD simulations.* Each blue curve represents an independent 500 ns simulation. Plots were generated by taking every 10th snapshot of the simulation data.

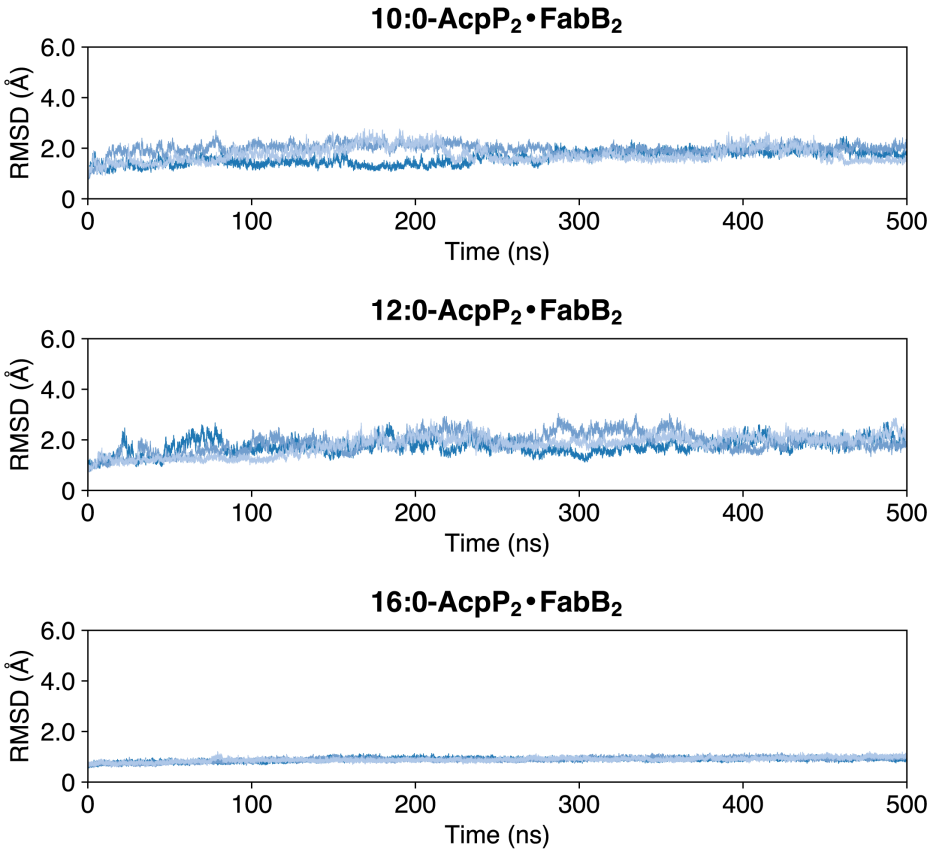

Figure S2.18: *RMSDs of ketosynthase domains of acyl-AcpP2•FabB2 complexes sampled during cMD simulations.* Each red curve represents an independent 500 ns simulation. Plots were generated by taking every 10th snapshot of the simulation data.

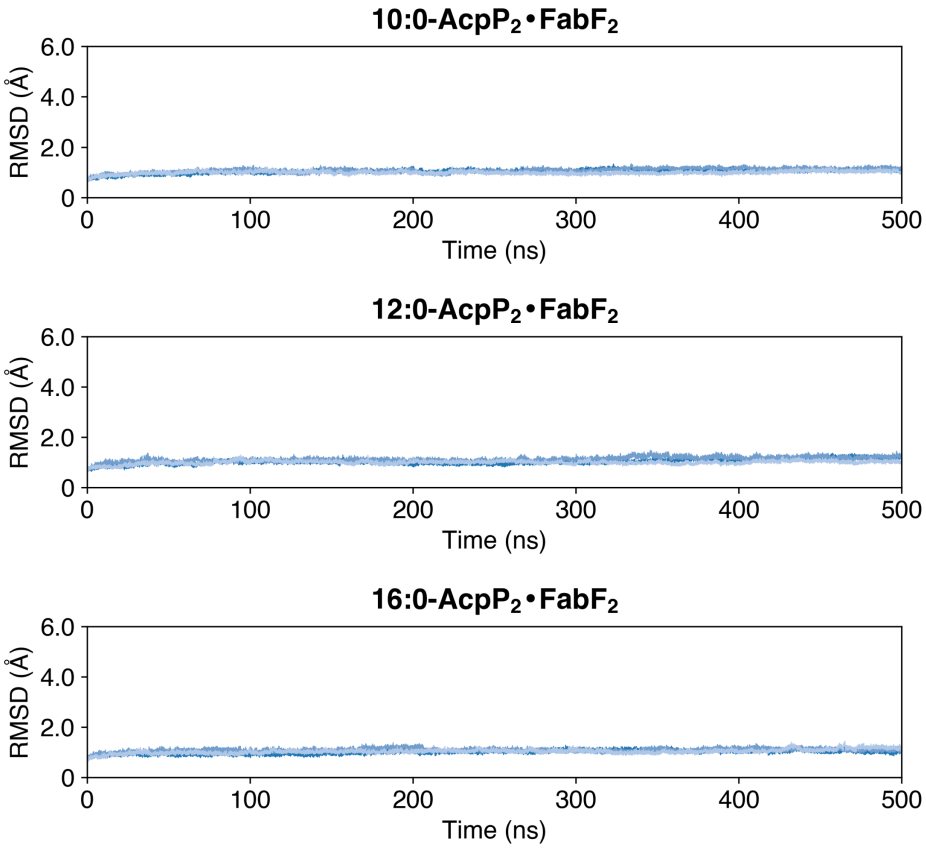

Figure S2.19: *RMSDs of ketosynthase domains of acyl-AcpP2•FabF2 complexes sampled during cMD simulations.* Each red curve represents an independent 500 ns simulation. Plots were generated by taking every 10^{th} snapshot of the simulation data.

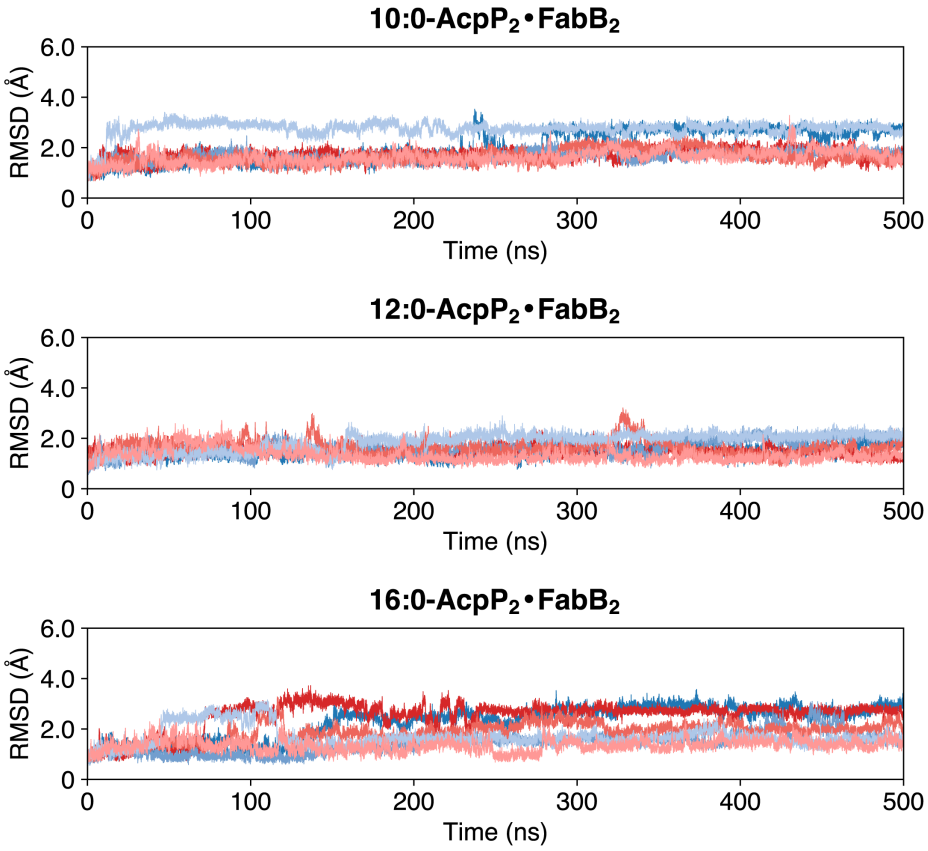

Figure S2.20: *RMSDs of AcpPs of acyl-AcpP2•FabB2 complexes sampled during cMD simulations.* Each blue (AcpP1) and red (AcpP2) curve represents data from an independent 290 ns simulation. Plots were generated by taking every 10th snapshot of the simulation data.

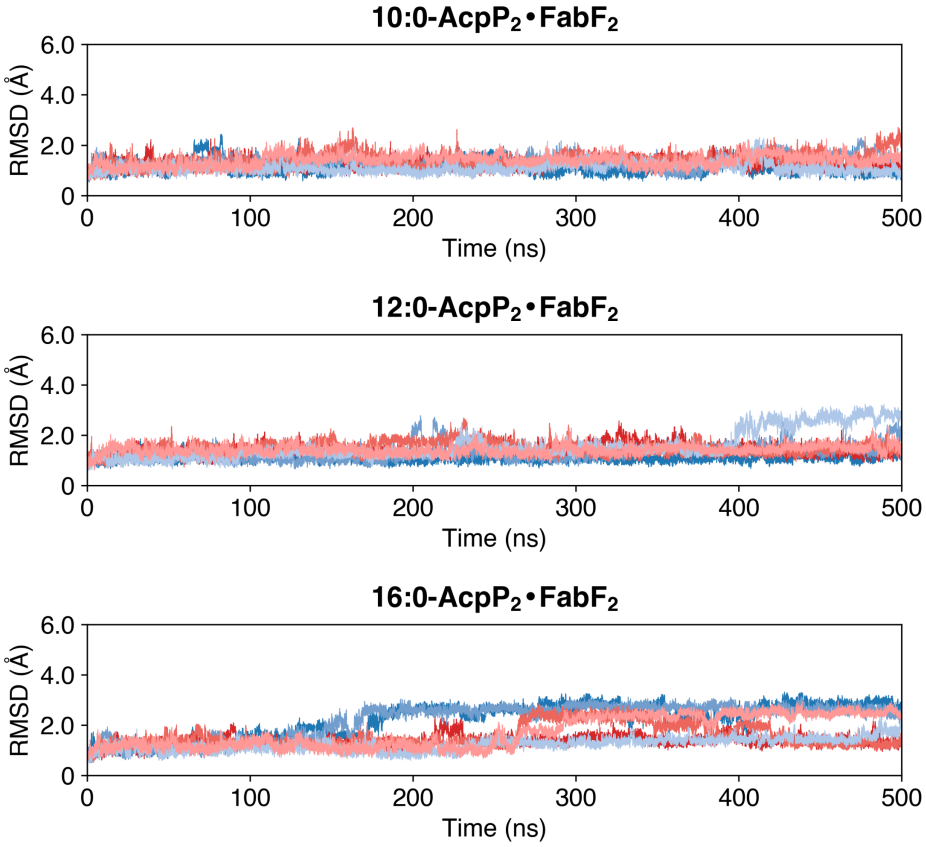

Figure S2.21: *RMSDs of AcpPs of acyl-AcpP2•FabF2 complexes sampled during cMD simulations.* Each blue (AcpP1) and red (AcpP2) curve represents data from an independent 500 ns simulation. Plots were generated by taking every 10th snapshot of the simulation data.

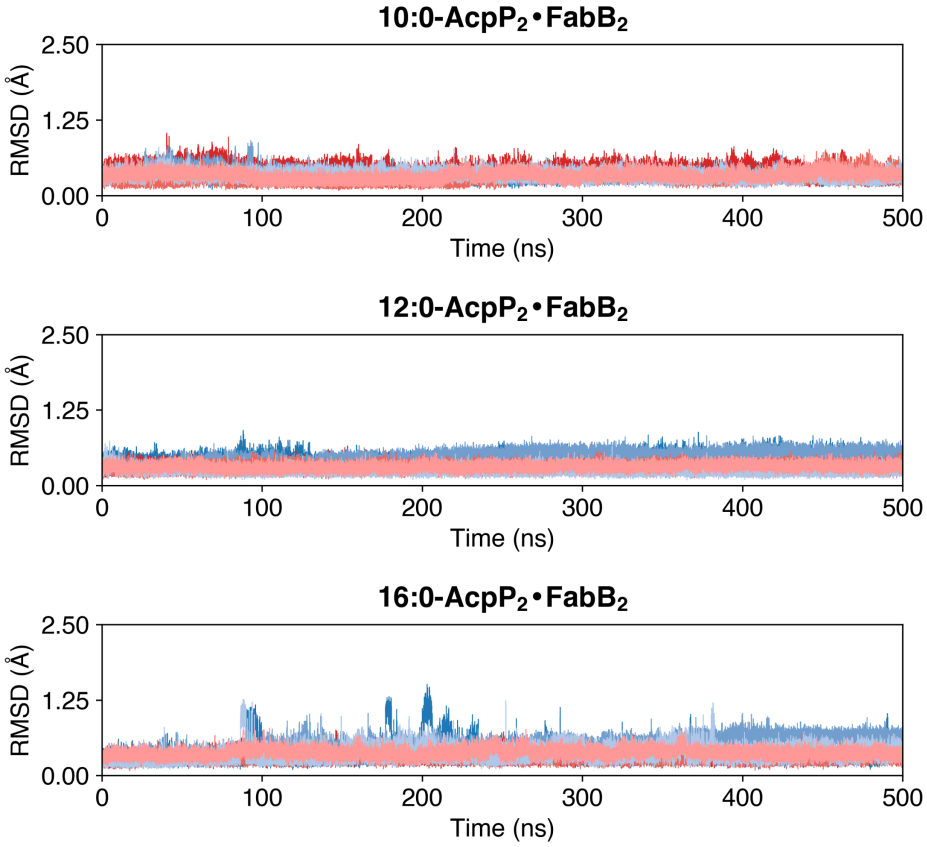

Figure S2.22: *RMSDs of loop 1 region of FabB within acyl-AcpP2•FabB2 complexes sampled during cMD simulations.* Each blue (loop 1 of FabB1) and red (loop 1 of FabB2) curve represents data from an independent 500 ns simulation.

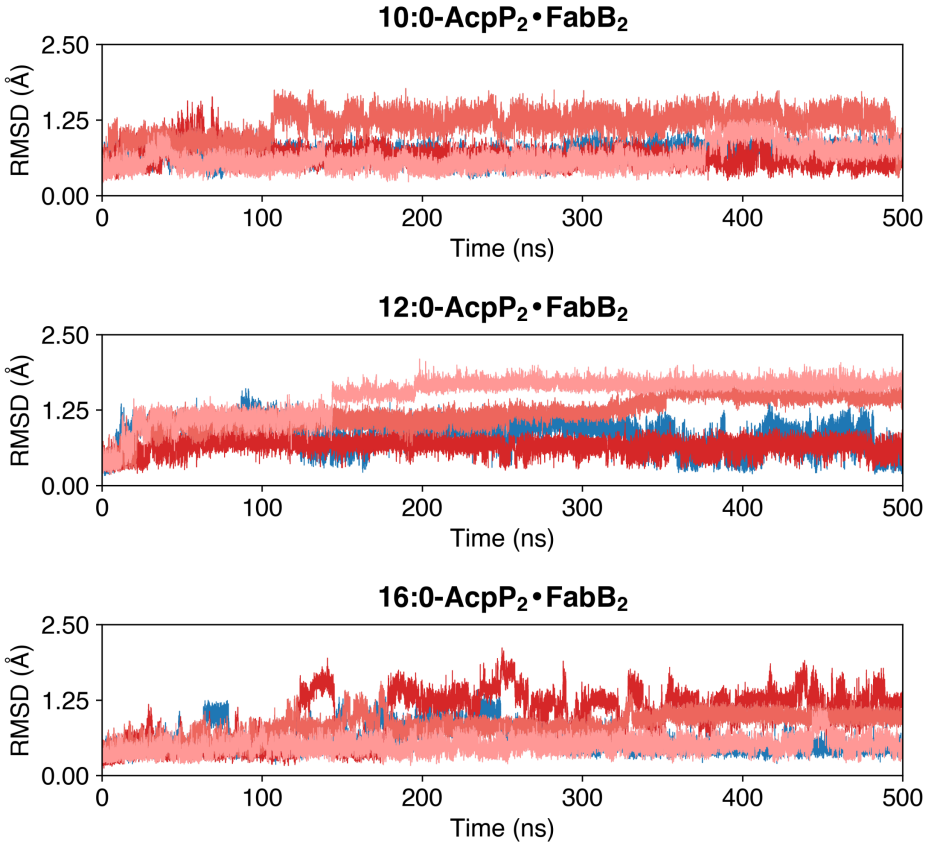

Figure S2.23: *RMSDs of loop 2 region of FabB within acyl-AcpP2•FabB2 complexes sampled during cMD simulations.* Each blue (loop 1 of FabB1) and red (loop 1 of FabB2) curve represents data from an independent 500 ns simulation.

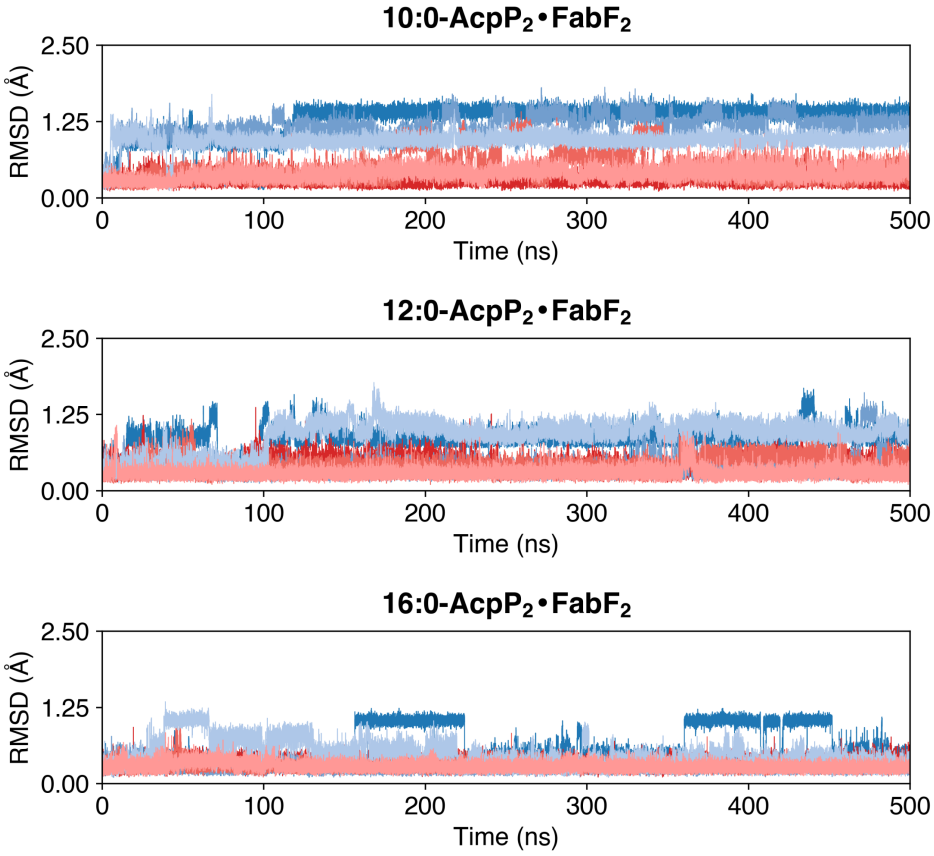

Figure S2.24: *RMSDs of loop 1 region of FabF within acyl-AcpP2•FabF2 complexes sampled during cMD simulations.* Each blue (loop 1 of FabF1) and red (loop 1 of FabF2) curve represents data from an independent 500 ns simulation.

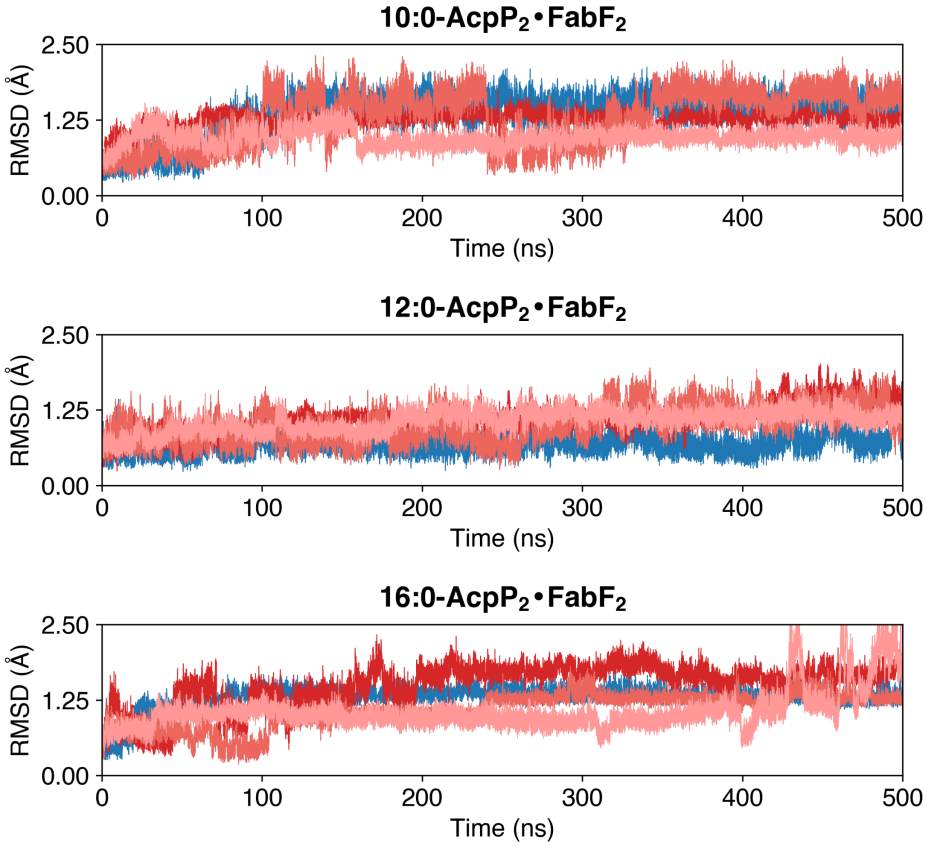

Figure S2.25: *RMSDs of loop 2 region of FabF within acyl-AcpP2•FabF2 complexes sampled during cMD simulations.* Each blue (loop 2 of FabB1) and red (loop 2 of FabB2) curve represents data from an independent 500 ns simulation.

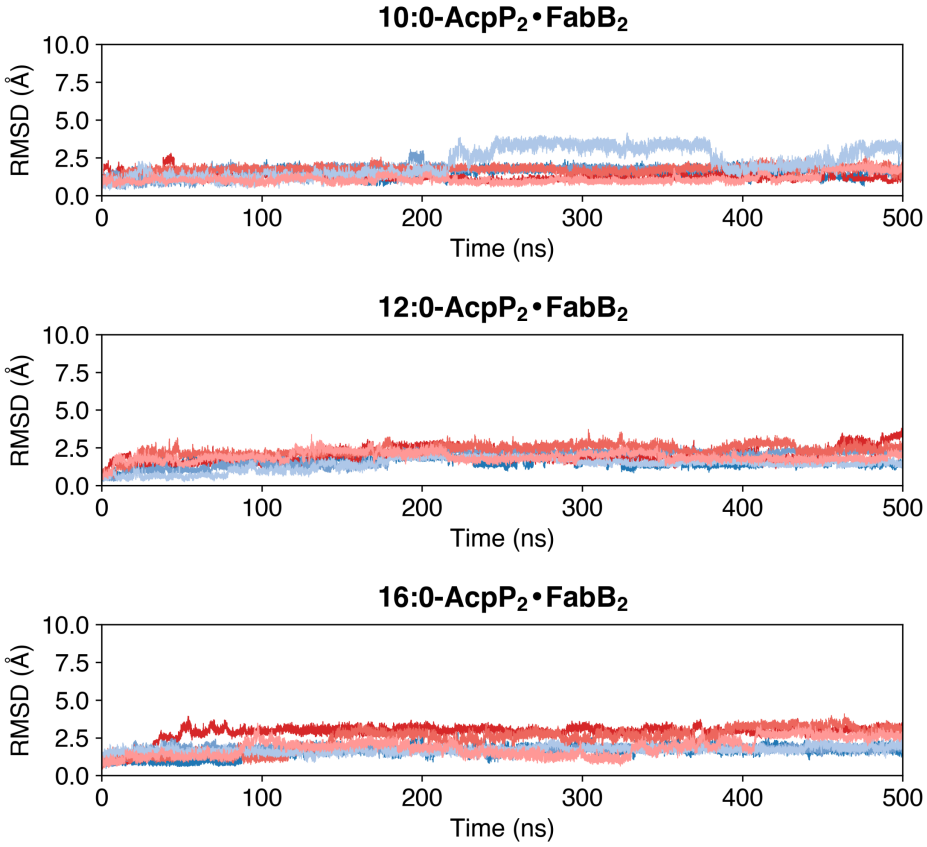

Figure S2.26: *RMSDs of the nonstandard residue of acyl-AcpP2•FabB2 complexes sampled during cMD simulations.* Each blue (FabB1) and red (FabB2) curve represents data from an independent 500 ns simulation.

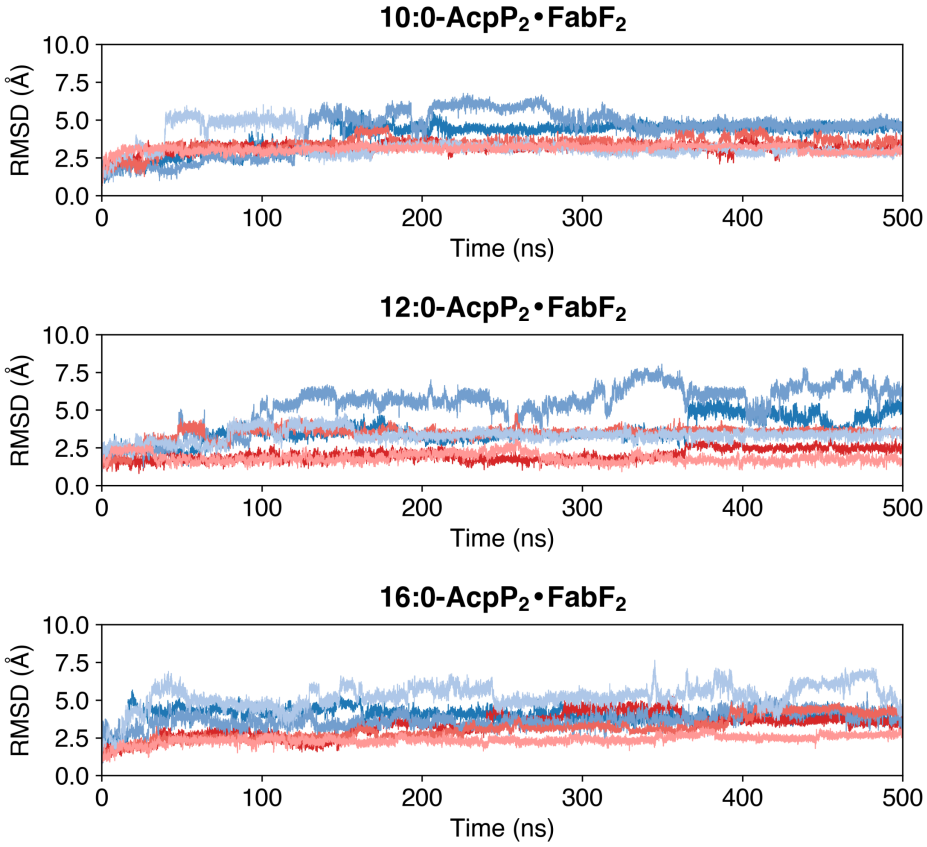

Figure S2.27: *RMSDs of the nonstandard residue of acyl-AcpP2•FabF2 complexes sampled during cMD simulations.* Each blue (FabF1) and red (FabF2) curve represents data from an independent 500 ns simulation.

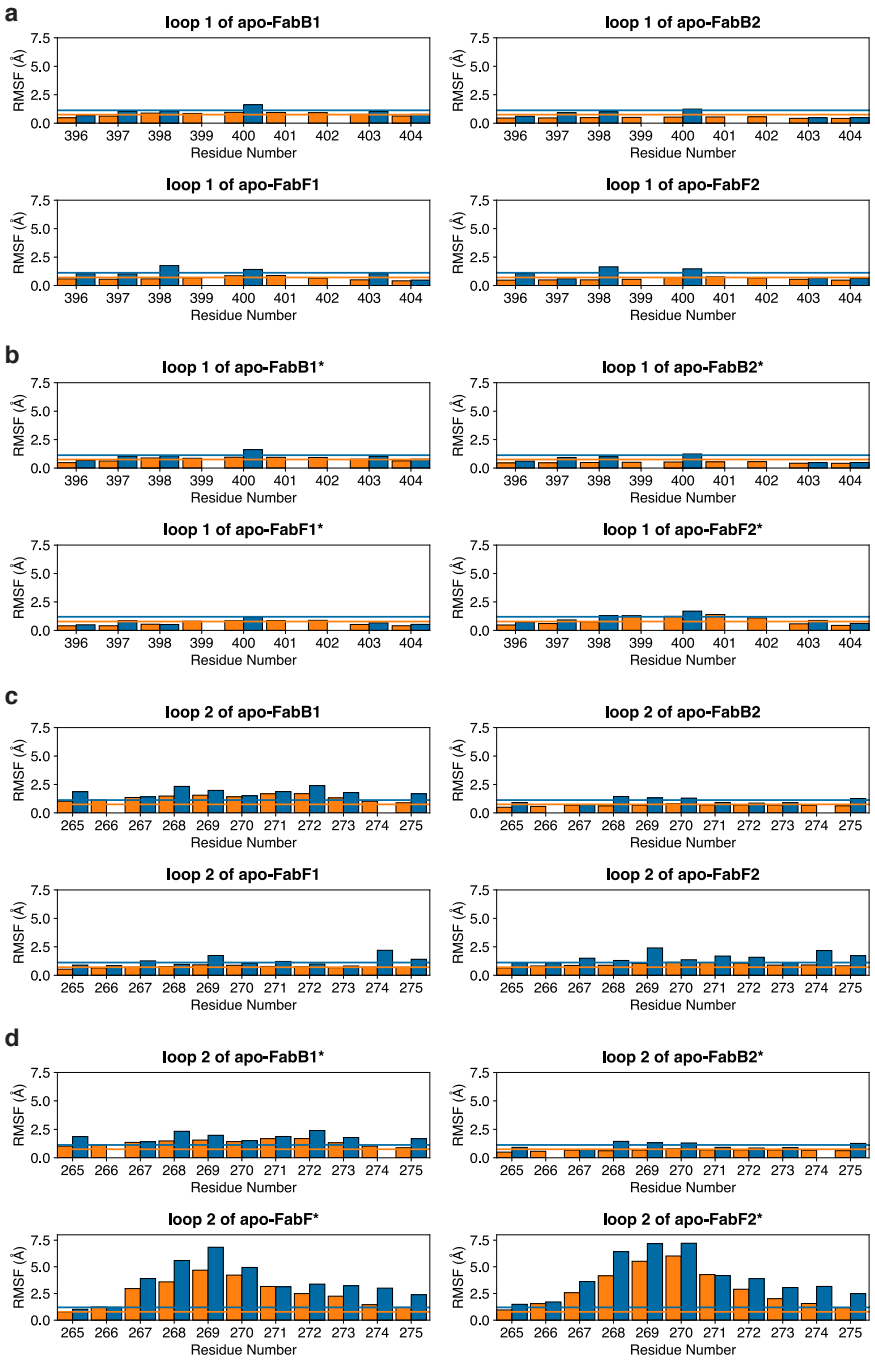

Figure S2.28: *Root mean square (RMS) fluctuations each residue of loops 1 and 2 of FabB and FabF monomers of the apo-AcpP•KS sampled during MD simulations.* **a.** Per residue RMSF of loop 1 of either monomer of *apo*-KS dimer. **b.** Per residue RMSF of loop 1 of either monomer of *apo*-KS dimer derived from the crosslinked AcpP=KS (*apo*-KS*) structure. **c.** Per residue RMSF of loop 2 of either monomer of *apo*-KS dimer. **d.** Per residue RMSF of loop 2 of either monomer of apo-*KS* dimer derived from the crosslinked AcpP=KS (*apo*-KS*) structure. The bar graphs show the per residue backbone RMS fluctuations (blue, measured using backbone heavy atoms) and the side chain RMS fluctuation of sidechains (orange, measured using each residue's sidechain heavy atoms). Residues 396-404 and residues 265-275 (FabF residue numbering) define loops 1 and 2, respectively.

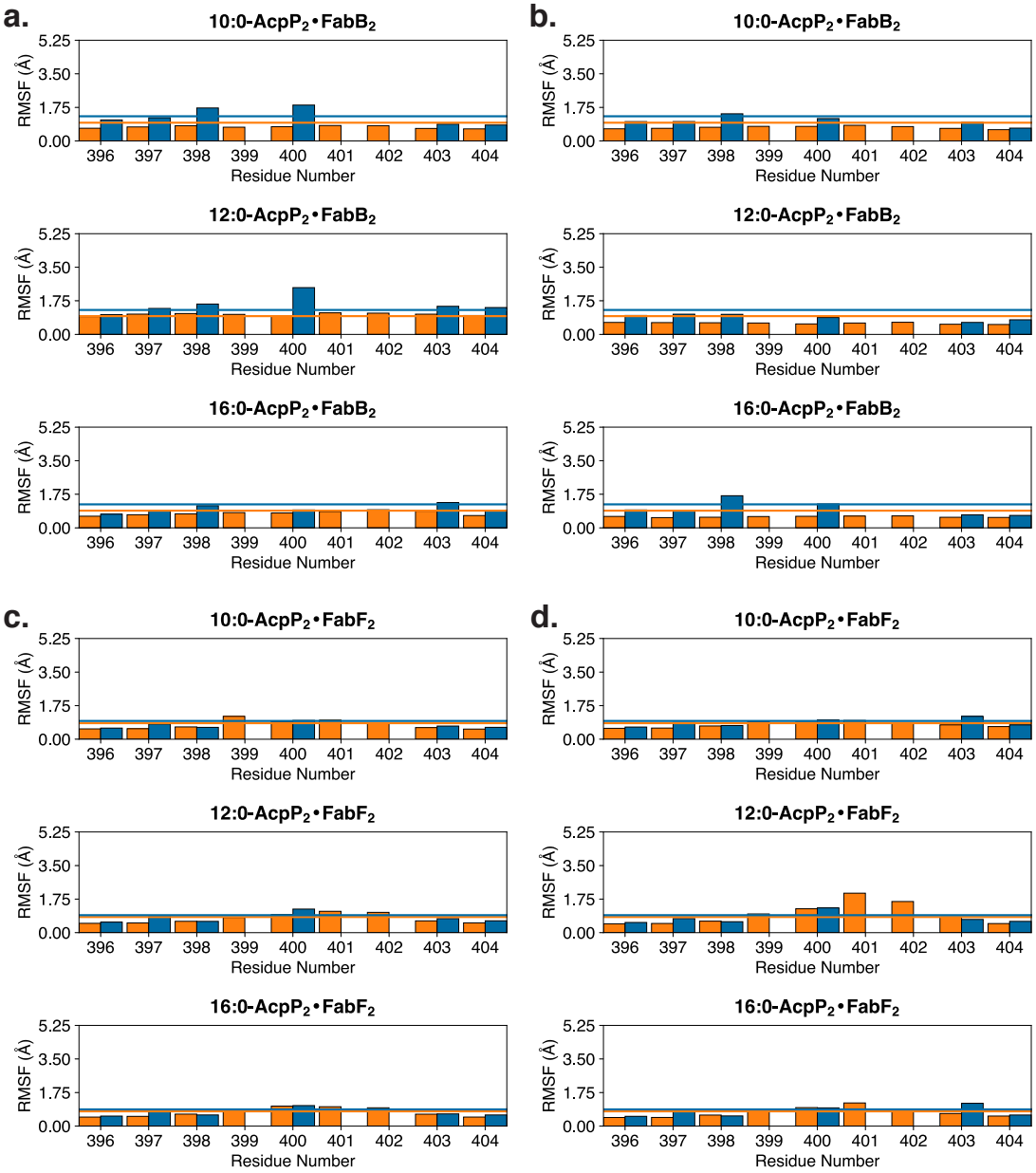

Figure S2.29: *Root mean square (RMS) fluctuations each residue of loop 1 of FabB and FabF monomers of the acyl-AcpP•KS sampled during MD simulations.* **a.** Per residue RMSF of loop 1 of the FabB1 monomer of acyl-AcpP•FabB. **b.** Per residue RMSF of loop 1 of the FabB2 monomer of acyl-AcpP•FabB. **c.** Per residue RMSF of loop 1 of the FabF1 monomer of acyl-AcpP•FabF. **d.** Per residue RMSF of loop 1 of the FabF2 monomer of acyl-AcpP•FabF. The bar graphs show the per residue backbone RMS fluctuations (blue, measured using backbone heavy atoms) and the side chain RMS fluctuation of sidechains (orange, measured using each residue's sidechain heavy atoms). Residues 396-404 (FabF residue numbering) define loop 1.

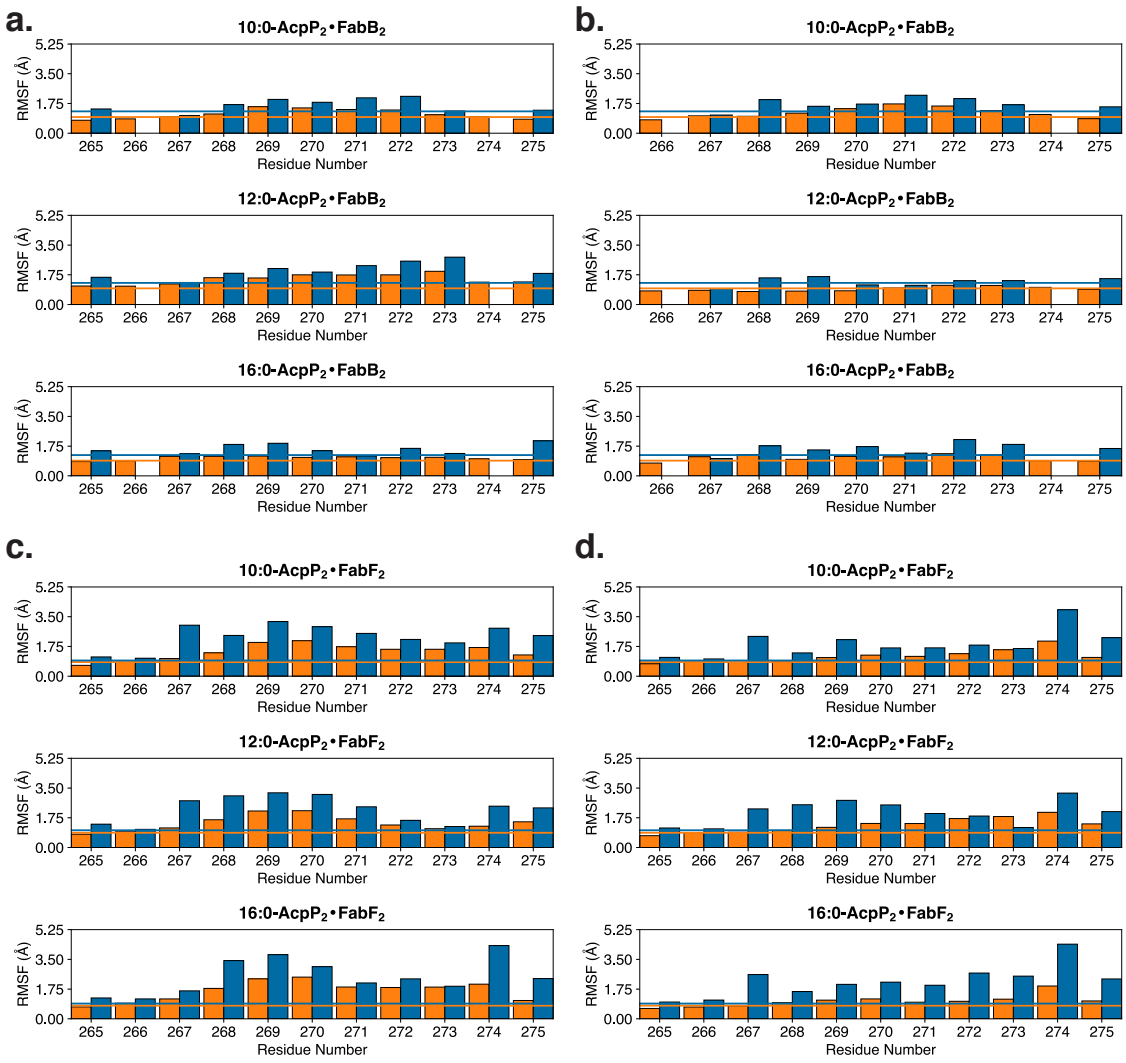

Figure S2.30: *Root mean square (RMS) fluctuations each residue of loop 2 of FabB and FabF monomers of the acyl-AcpP2•KS2 sampled during MD simulations.* **a.** Per residue RMSF of loop 2 of the FabB1 monomer of acyl-AcpP•FabB. **b.** Per residue RMSF of loop 2 of the FabB2 monomer of acyl-AcpP•FabB. **c.** Per residue RMSF of loop 2 of the FabF1 monomer of acyl-AcpP•FabF. **d.** Per residue RMSF of loop 2 of the FabF2 monomer of acyl-AcpP•FabF. The bar graphs show the per residue backbone RMS fluctuations (blue, measured using backbone heavy atoms) and the side chain RMS fluctuation of sidechains (orange, measured using each residue's sidechain heavy atoms). Residues 265-275 (FabF residue numbering) define loop 2.

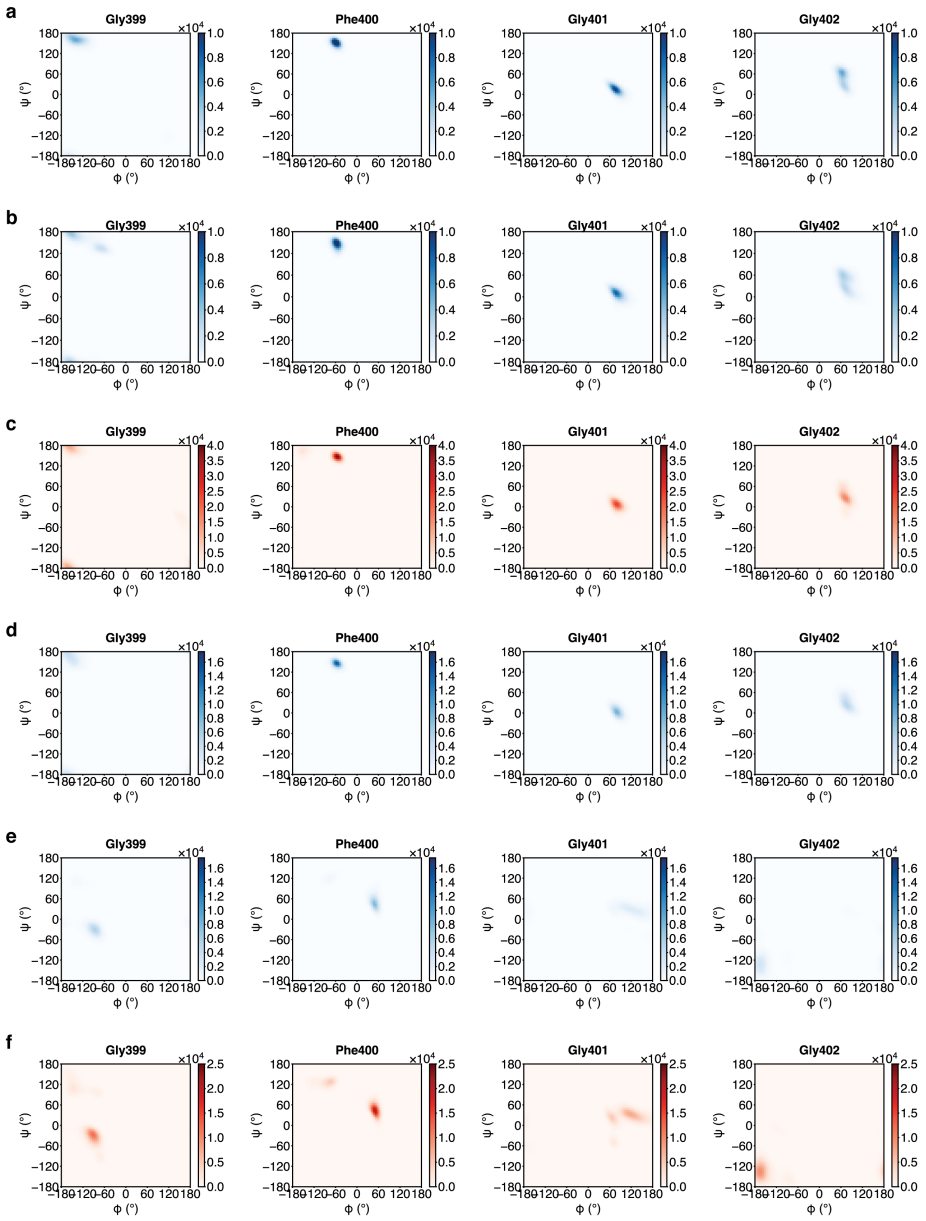

Figure S2.31: *Ramachandran plots of the GFGG motifs of FabB or FabF simulated in various states.* **a.** Analysis of the GFGG backbone dihedrals of *apo*-FabB performed using 1.5 μs of molecular dynamics (MD) simulation data of *apo*-FabB. **b.** Analysis of GFGG backbone dihedrals on apo-FabB* (apo-FabB constructed using the coordinates from the crosslinked AcpP=FabB structure reported herein) using 1.5 μs of molecular dynamics (MD) simulation data of *apo*-FabB*. **c.** Analysis of the GFGG backbone dihedral of acyl-AcpP•FabB using 4.5 μs of molecular dynamics (MD) simulation data of acyl-AcpP•FabB. **d.** Analysis of the GFGG backbone dihedrals of *apo*-FabF performed using 1.5 μs of molecular dynamics (MD) simulation data of *apo*-FabF. **e.** Analysis of GFGG backbone dihedrals on apo-FabF* (apo-FabF constructed using the coordinates from the crosslinked AcpP=FabF structure reported herein) using 1.5 μs of molecular dynamics (MD) simulation data of *apo*-FabF*. **f.** Analysis of the GFGG backbone dihedral of acyl-AcpP•FabF using 4.5 μs of molecular dynamics (MD) simulation data of acyl-AcpP•FabF. Data is binned based backbone ψ and φ dihedral angles residues assume during MD simulations using bin widths of 5°

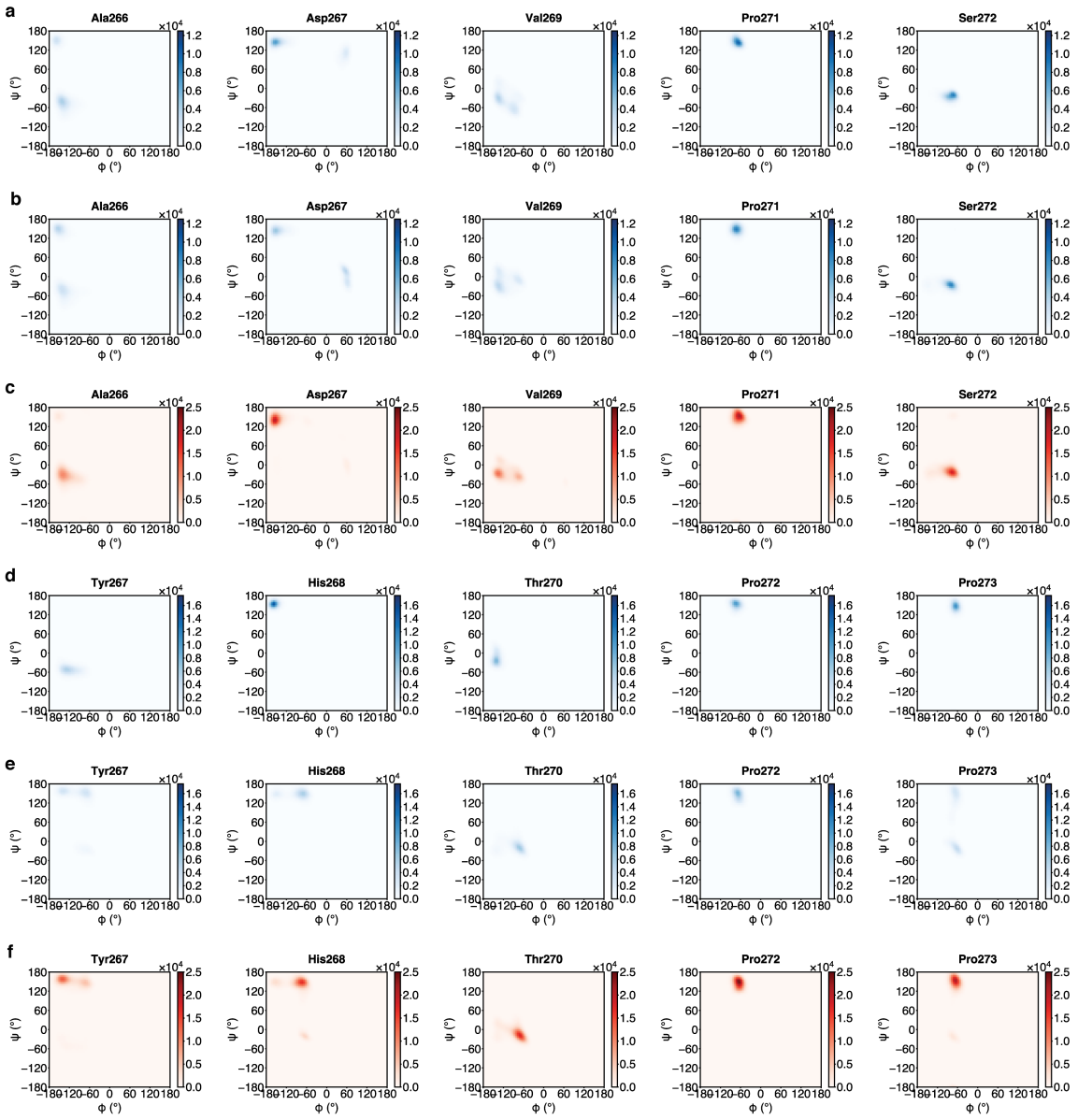

Figure S2.32: *Ramachandran plots of the key residues of loop 2 of FabB or FabF simulated in various states.* **a.** Analysis of the loop 2 backbone dihedrals of *apo*-FabB performed using 1.5 μs of molecular dynamics (MD) simulation data of *apo*-FabB. **b.** Analysis of loop 2 backbone dihedrals on apo-FabB* (apo-FabB constructed using the coordinates from the crosslinked AcpP=FabB structure reported herein) using 1.5 μs of molecular dynamics (MD) simulation data of *apo*-FabB*. **c.** Analysis of the loop 2 backbone dihedrals of acyl-AcpP•FabB using 4.5 μs of molecular dynamics (MD) simulation data of acyl-AcpP•FabB. **d.** Analysis of the loop 2 backbone dihedrals of *apo*-FabF performed using 1.5 μs of molecular dynamics (MD) simulation data of *apo*-FabB. **e.** Analysis of loop 2 backbone dihedrals on apo-FabF* (apo-FabF constructed using the coordinates from the crosslinked AcpP=FabF structure reported herein) using 1.5 μs of molecular dynamics (MD) simulation data of *apo*-FabB*. **f.** Analysis of the loop 2 backbone dihedral of acyl-AcpP•FabF using 4.5 μs of molecular dynamics (MD) simulation data of acyl-AcpP•FabF. Data is binned based backbone ψ and φ dihedral angles residues assume during MD simulations using bin widths of 5°.

Primer	Sequence
FabF-G399A-F	GCGTTCGGTGGCACTAATGGTTCTTTGATCTTTAAAAAGATCTAA
FabF-G399A-R	AGTGCCACCGAACGCGAAGGAGTTACACAGAGTGTATTC
FabF-F400A-F	*GGCGCAGGTGGCACTAATGGTTCTTTGATCTTTAAAAAGATCTAA*
FabF-F400A-R	AGTGCCACCTGCGCCGAAGGAGTTACACAGAGTGTATTC
FabF-G401A-F	*GGCTTCGCGGGCACTAATGGTTCTTTGATCTTTAAAAAGATCTAA*
FabF-G401A-R	AGTGCCCGCGAAGCCGAAGGAGTTACACAGAGTGTATTC
FabF-G402A-F	*GGCTTCGGTGCGACTAATGGTTCTTTGATCTTTAAAAAGATCTAA*
FabF-G402A-R	AGTCGCACCGAAGCCGAAGGAGTTACACAGAGTGTATTC
FabF-D265A-F	*ATG AGC AGC GCA GCT TAT CAT ATG ACG TCA CCG CCA GAA AAT G*
FabF-D265A-R	ATA AGC TGC GCT GCT CAT ACC AAA GCC GAC GAG TTC AGC
FabF-D265N-F	*ATG AGC AGC AAC GCT TAT CAT ATG ACG TCA CCG CCA GAA AAT G*
FabF-D265N-R	ATA AGC GTT GCT GCT CAT ACC AAA GCC GAC GAG TTC AGC
FabF-G310F-F	*TCT ACG CCG GCT TTT GAT AAA GCT GAA GCG CAG GCG GTG*
FabF-G310F-R	ATC AAA AGC CGG CGT AGA AGT ACC GTG CGC GTT AAC GTA
FabF-G310M-F	*TCT ACG CCG GCT ATG GAT AAA GCT GAA GCG CAG GCG GTG*
FabF-G310M-R	ATC CAT AGC CGG CGT AGA AGT ACC GTG CGC GTT AAC GTA

Figure S2.33: *Primers for generating FabF mutants.* F and R indicate forward and reverse primers

	C16AcpP-FabB	C12AcpP-FabB	C16AcpP-FabF	C12AcpP-FabF
Data collection				
Space group	P 1 21 1	P 21 21 21	P 43 21 2	P 43 21 2
Cell dimensions				
a, *b*, *c* (Å)	58.94 100.78 79.26	59.07 112.17 140.68	86.89 86.89 113.73	86.45 86.45 115.16
α, β, γ (°)	90.00 108.64 90.00	90.0 90.0 90.0	90.0 90.0 90.0	90.0 90.0 90.0
Resolution (Å)	60.22-2.5(2.59-2.5)*	87.7-1.55(1.60-1.55)*	69.04-2.3(2.382-2.3)*	69.14-2.35(2.43-2.35)*
R_{sym} or R_{merge}	0.136 (.8075)	0.109(0.857)	0.3746 (2.379)	0.327 (3.604)
I / σI	7.59 (2.34)	14.25 (3.65)	9.28 (1.70)	9.91 (1.08)
Completeness (%)	98.74 (98.19)	99.43 (98.28)	99.80 (99.95)	99.74 (99.67)
Redundancy	6.2 (6.4)	11.8 (11.7)	19.1 (19.9)	15.4 (15.9)
Refinement				
Resolution (Å)	60.22-2.5	87.7-1.55	69.04-2.3	69.14-2.35
No. reflections	300780 (2991)	1593391 (155305)	381910 (38754)	288893 (29114)
R_{work} / R_{free}	.178/.218	.148/.163	.195/.228	.201/.239
No. atoms	7337	8287	3914	3867
Protein	7160	7343	3640	3727
Ligand/ion	70	102	77	48
Water	107	842	197	92
B-factors	65.50	22.28	31.90	59.21
Protein	66.25	20.97	31.87	59.54
Ligand/ion	61.03	28.79	33.43	58.36
Water	50.24	32.86	31.91	46.56
R.m.s. deviations				
Bond lengths (Å)	.004	.008	.004	.004
Bond angles (°)	.99	1.3	.97	.96

Figure S2.34: *Table 1 Refinement statistics from structures solved in this work.*

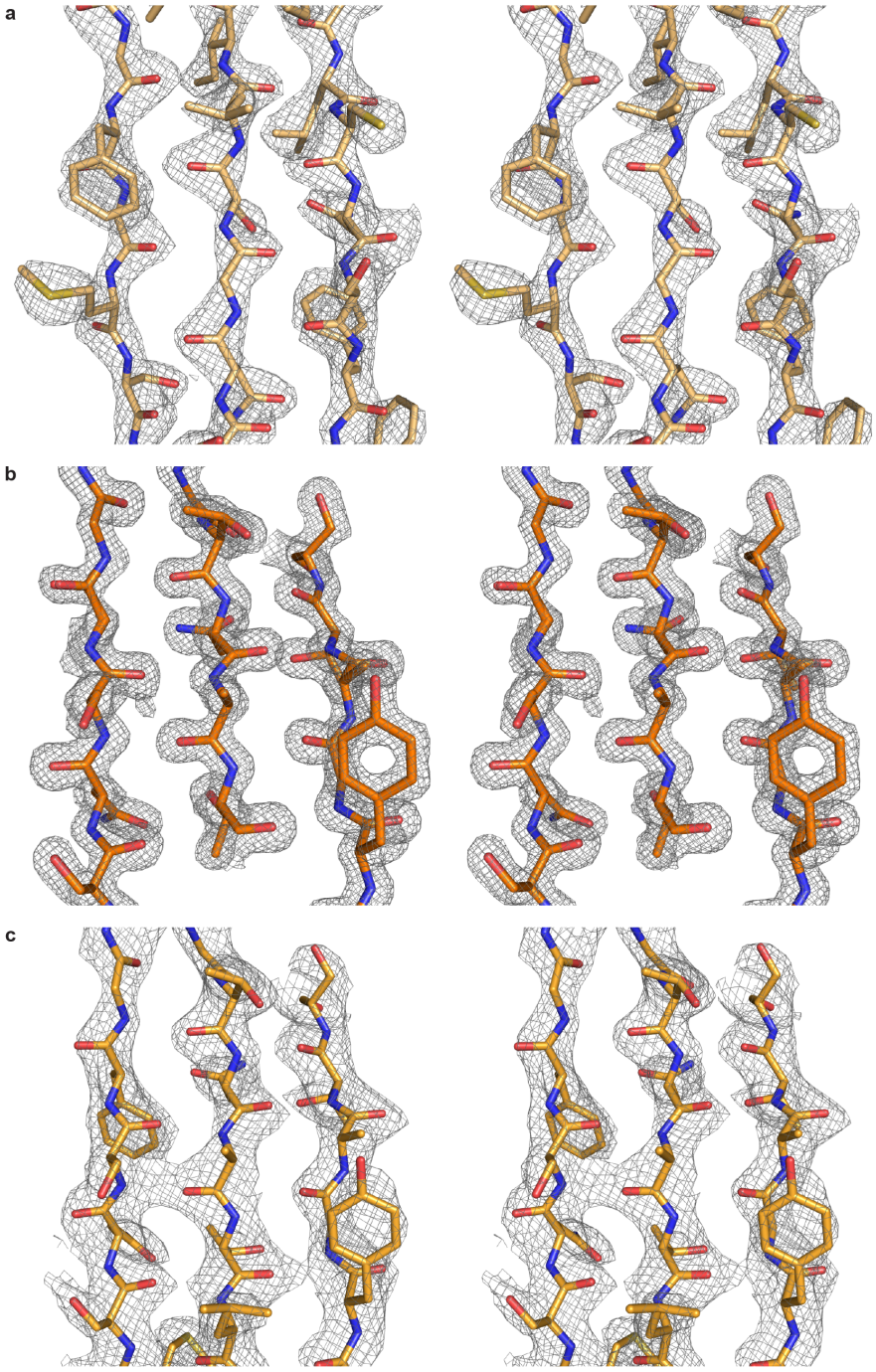

Figure S2.35: *Electron density maps of reported structures*. Stereo images of 2Fo-Fc electron density maps contoured at 1.5 σ for **a.** C16AcpP-FabF, (PDB: 6OKG, 2.4 Å), beta sheet shown consists of residues Leu257-Ser263, Thr393-G399, and Thr403-Phe409. b. C12AcpP-FabB, (PDB: 6OKC ,1.55 Å), beta sheet shown consists of residues Gly259-Ser264, Gly394-Thr398, and Ser387-F392. c. C16AcpP-FabB, beta sheet shown consists of residues Gly259-Ser264, Gly394-Thr398, and Ser387-F392 (PDB: 6OKF, 2.5 Å.)

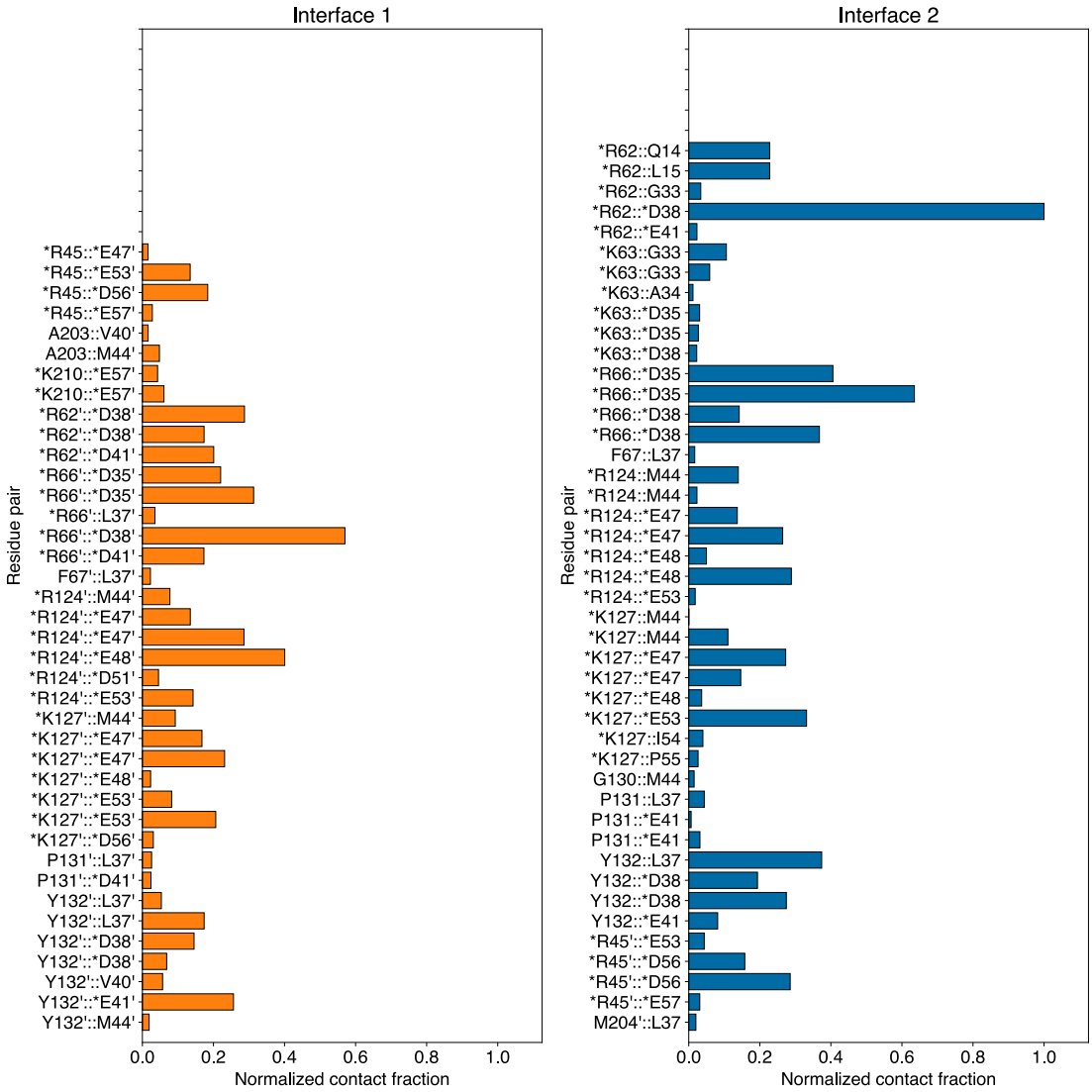

Figure S2.36: *Native contact analysis of MD simulations data of acyl-AcpP2•FabB2 (10:0-AcpP2•FabB2, 12:0-AcpP2•FabB2, 16:0-AcpP2•FabB2).* Residues on the dimeric $FabB_2$ subunit within 7.5 Å and those of either AcpP1 (Interface 1) and AcpP2 (Interface 2) within 7.5 Å dimer subunit were subjected to this analysis. The bar graphs illustrate the frequency with interfacial residues contact with one another at either interface of these acyl-$AcpP_2$•$FabB_2$. The contact fraction is defined as the total fraction of simulation data in which a residue pair is engaged in an intermolecular contact. A distance criterion of 3.5 Å or less between a pair of heavy atoms of two residue belonging two distinct protein monomers defines such a contact. This value before normalization assume values greater than 1.0, if a residue pair possesses multiple atoms that satisfy the distance criteria used to define a contact. Only pairwise contacts with contact fractions greater than or equal to 0.05 are included in the plots above. Every 10^{th} frame of simulation data starting with the first was used to perform this analysis. Note that "primed" residues (e.g., K127', D35') refer to residues belonging to FabB2 or AcpP2. Charged residues are marked by an asterisk.

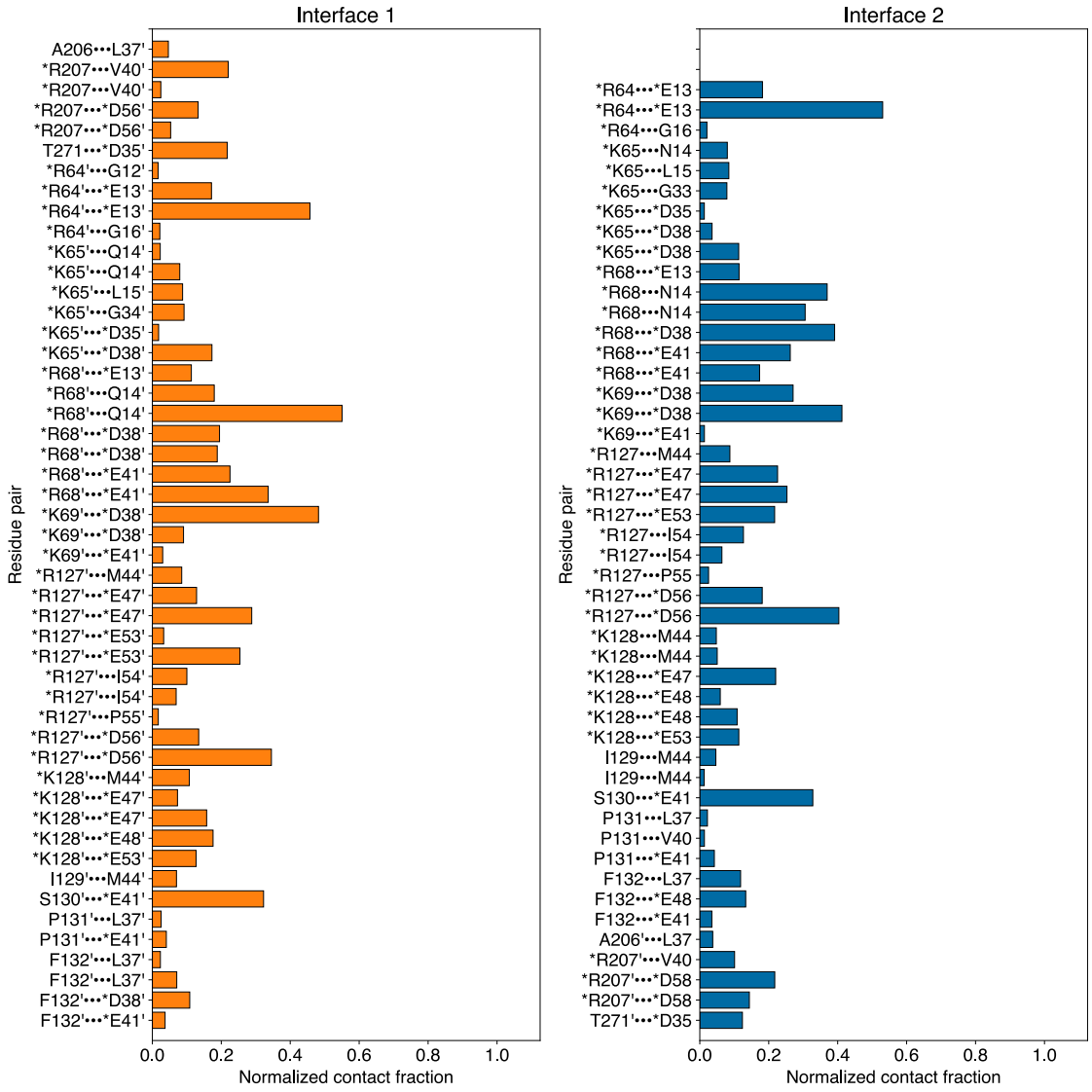

Figure S2.37: *Native contact analysis of MD simulations data of acyl-AcpP2•FabF2 (10:0-AcpP2•FabF2, 12:0-AcpP2•FabF2, 16:0-AcpP2•FabF2).* Residues on the dimeric $FabF_2$ subunit within 7.5 Å and those of either AcpP1 (Interface 1) and AcpP2 (Interface 2) within 7.5 Å dimer subunit were subjected to this analysis. The bar graphs illustrate the frequency with interfacial residues contact with one another at either interface of these acyl-$AcpP_2$•$FabF_2$. The contact fraction is defined as the total fraction of simulation data in which a residue pair is engaged in an intermolecular contact. A distance criterion of 3.5 Å or less between a pair of heavy atoms of two residue belonging two distinct protein monomers defines such a contact. This value before normalization assume values greater than 1.0, if a residue pair possesses multiple atoms that satisfy the distance criteria used to define a contact. Only pairwise contacts with contact fractions greater than or equal to 0.05 are included in the plots above. Every 10^{th} frame of simulation data starting with the first was used to perform this analysis. Note that "primed" residues (e.g., K127', D35') refer to residues belonging to FabF2 or AcpP2. . Charged residues are marked by an asterisk.

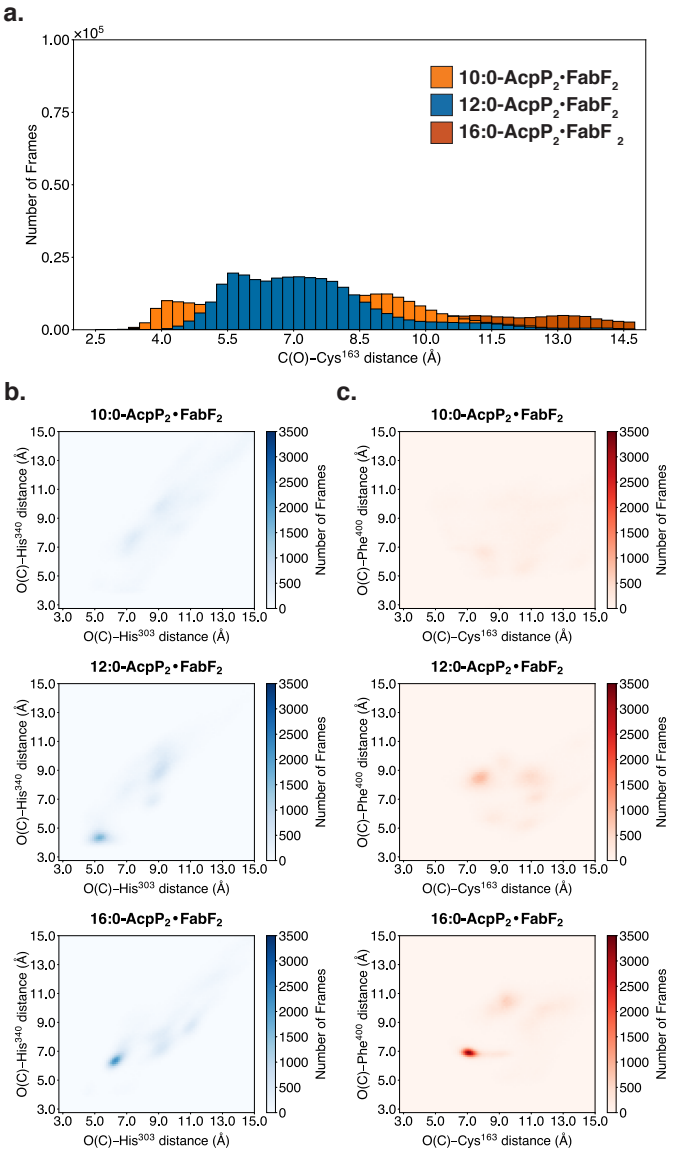

Figure S2.38: *Analysis of contacts between active site residues and substrate of acyl-AcpP•FabF complexes sampled computationally.* **a.** Distribution of distances sampled between carbonyl carbon of the acyl chain of 10:0-AcpP•FabF (orange), 12:0-AcpP-FabF (blue), or 16:0-AcpP•FabF (red) and sulfur atom of catalytic cysteine (Cys163). 1D histogram was generated using a bin width of 0.25 Å **b.** Analysis of hydrogen bonding interactions involving the substrate and His303 and His340 (2D histogram, blue). Simulation data is binned along two coordinates The first of which is the distance between the carbonyl oxygen of the substrate and the imidazole moiety of His303 (center of geometry) of FabF, while the second measures the distance between the imidazole moiety of His340 (center of geometry) and its carbonyl oxygen. **c.** Analysis of backbone (oxyanion hole) hydrogen-bonding interactions (2D histogram, red). Simulation data is binned along two coordinates. The first of which is the distance between the carbonyl oxygen of the substrate and the backbone amide nitrogen of Cys163 of FabF, while the second measures the distance between substrate's carbonyl oxygen and the backbone amide nitrogen of Phe400. Simulation data is binned along two coordinates. Data was sorted into 0.05 Å × 0.05 Å bins. Color bars indicate the absolute population of each histogram bin.

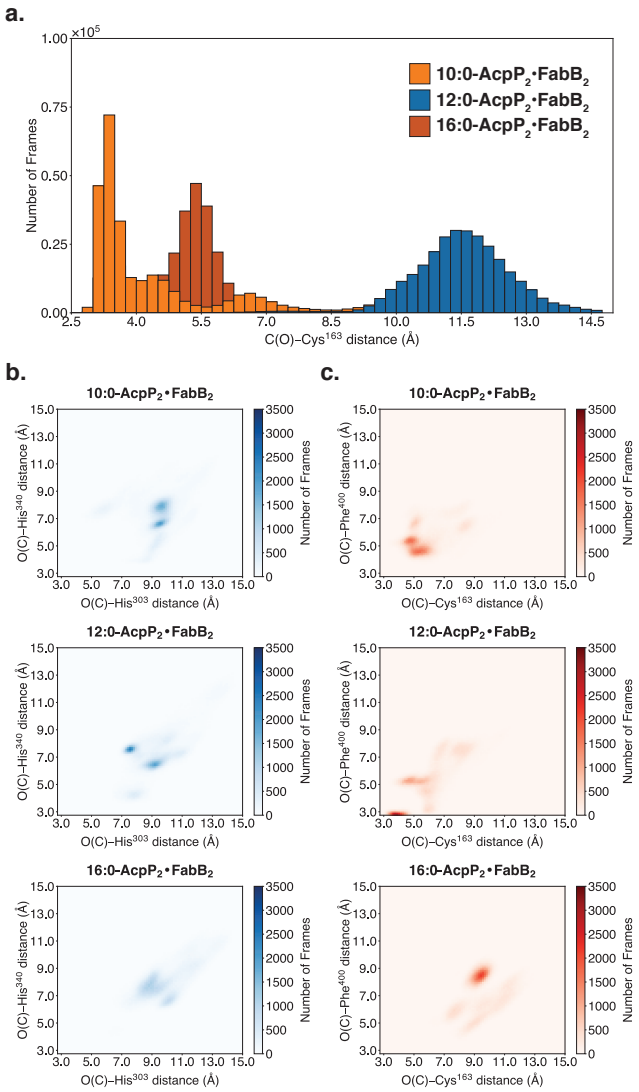

Figure S2.39: *Analysis of contacts between active site residues and substrate of acyl-AcpP•FabB complexes sampled computationally.* **a.** Distribution of distances sampled between carbonyl carbon of the acyl chain of 10:0-AcpP•FabB (orange), 12:0-AcpP-FabB (blue), or 16:0-AcpP•FabB (red) and sulfur atom of catalytic cysteine (Cys163). 1D histogram was generated using a bin width of 0.25 Å **b.** Analysis of hydrogen bonding interactions involving the substrate and His303 and His340 (2D histogram, blue). Simulation data is binned along two coordinates The first of which is the distance between the carbonyl oxygen of the substrate and the imidazole moiety of His303 (center of geometry) of FabB, while the second measures the distance between the imidazole moiety of His340 (center of geometry) and its carbonyl oxygen. **c.** Analysis of backbone (oxyanion hole) hydrogen-bonding interactions (2D histogram, red) Simulation data is binned along two coordinates. The first of which is the distance between the carbonyl oxygen of the substrate and the backbone amide nitrogen of Cys163 of FabB, while the second measures the distance between substrate's carbonyl oxygen and the backbone amide nitrogen of Phe400. Simulation data is binned along two coordinates. Data was sorted into 0.05 Å × 0.05 Å bins. Color bars indicate the absolute population of each histogram bin.

Supplementary Note S2.1: *C12AcpP-FabF complex*

The C12AcpP-FabF complex crystalized in the same conditions and space group as our C16AcpP-FabF structure and produced electron density maps of similar quality (Figure S2.34). Structural alignments of the two complexes show that C12AcpP-FabF overlays with C16AcpP-FabF with an RMSD of 0.19 Å. The electron density map is well defined for the majority of the complex except for loops 1 and 2, which appear to be dynamic in the C12AcpP-FabF structure. These loops adopt at least two conformations, which are representative of apo-FabF (closed state) and our C16 bound state (open state), making the interpretation of these regions difficult. Given the presence of electron density for both the open and closed states, both loop conformations were modelled for loops 1 and 2.

Analysis of the PPant crosslinking probe demonstrates discernable density for the PPant arm but not for the C12 alkyl chain. This is not surprising as the conformational heterogeneity in loops 1 and 2 make it difficult to accurately model this region of the complex. Therefore, the finalized structure does not include an alkyl chain, which is instead modelled as a C2 with a crosslink at the two-position (α position). The lack of density for the alkyl chain may indicate that it is dynamic and that the gate is switching between the open and closed conformation. Extension of the chain four carbons from C12 to C16, as seen in our C16AcpP-FabF structure, appears to stabilize the open over the closed conformation, which is likely due to the large size of the alkyl chain.

Supplementary Note S2.2: *C16AcpP-FabB complex*

The 2.50 Å C16AcpP-FabB x-ray refinement statistics and electron density map can be found in Figures S2.34,S2.35c. The C16AcpP-FabB structure overlays with the C12AcpP-FabB with a root-mean-square deviation (RMSD) of 0.25 Å. Despite the overall structural similarities, the C16AcpP-FabB data reveals a lack of electron density for the C16-acyl chain in the acyl-binding pocket, despite showing interpretable electron density for the 4'-phosphopantetheineamide portion of the probe (Figure S2.4f). A C12-acyl chain was modeled into the acyl-binding pocket, but low levels of electron density were only observed for the alkyl chain in 2Fo-Fc maps at or below contour levels of 1σ (Figure S2.4f). A similar result was found by Olsen et al.[45] in a study where they soaked acyl-CoAs into FabB crystals to trap the FabB acyl-enzyme adduct with different fatty acid chain lengths.[45] Their soaking experiments only showed strong density for C8, C10, and C12 chains but little to no electron density with C14 and C16. Despite the lack of alkyl chain density, we attempted to model the complete C16 alkyl chain into the FabB binding pocket, but in doing so recognized a constricted fatty acid binding pocket that places the alkyl chains of the two protomers in close proximity to one another at the dimer interface (Figure S2.4g). Furthermore, clashes between the terminal carbons of the C16-acyl chain with Glu200 and Gln113 along the back wall of the binding pocket restrict accommodation of the C16 substrate. Interestingly, in our C12AcpP-FabB datasets, the end of the C12 chain stops just short of these residues (Figure S2.4e), indicating that they may play a role in the substrate specificity of FabB.[41,42,78]

Supplementary Note S2.3: *Time resolved analysis of AcpP-KS interfaces*

MD simulations of the various acyl-AcpP-KS complexes (Figure S2.13) show the extent to which atoms interact intermolecularly at the AcpP-KS interface. FabF, unlike FabB, forms long-lived contacts with AcpP's helix I residues Glu13 and Gln14 during the course of the simulations (Figure 2.3, Figures S2.36,S2.37). FabF forms additional short-lived hydrophobic contacts with AcpP throughout the MD simulations, consistent with the larger contact area of the AcpP-FabF interface (Figures S2.36,S2.37). Simulations also reveal that the charged residues of regions 1 and 2 of the AcpP-KS interface form and break interactions with one another throughout the course of the simulation (Figures S2.36,S2.37), showcasing the dynamism of the PPIs of these complexes. Simulations show that AcpP's Asp35 and Asp38 are the residues most frequently forming interactions at the AcpP-FabB interface (Figures S2.36,S2.37).

Supplementary Note S2.4. *C16AcpP-FabF delineates a potential minor conformation for the C16 alky chain*

The refined structure of C16AcpP-FabF may delineate density for a second conformation of the alkyl chain, which we define as C16b, that passes towards the dimer interface in the opposite direction of the fatty acyl-binding pocket (Figure S2.4a-c). Movement of loop 1 to the open conformation creates a hydrophobic cavity of significant size with in the FabF active site, potentially allowing access to this minor conformation by a rotation around the C5-C6 bond of the alkyl chain. Modeling a C16 chain into this density is possible and the chain is not constricted by the size of the pocket. A comparison of the C16a and C16b conformations shows significantly higher electron density for the C16a conformation, but both conformations have been modeled into the final structure. Analysis of the substrate-protein interactions show that the C16a conformation has significantly more favorably hydrophobic contacts than that of the C16b pocket (Figure S2.4g). The composition of the pocket surrounding the alkyl chain in the C16b conformation is slightly more polar than that of the C16a conformation and is comprised of residues Ile138, Asn140, Met141, Thr161, Ala162, Met269, and Thr403 (Figure S2.4g).

Supplementary Note S2.5: *Comparison of FabF and FabB structural features*

E. coli and most other γ-proteobacteria possess three ketosynthases which are representatives of the KASI, KASII, and KASIII families of condensing enzymes. KASIII enzymes are also considered initiating KSs and serve to perform the first condensation reaction of FAS by condensing acetyl-CoA with malonyl-AcpP. All subsequent extensions are performed by the elongating KSs, KASI and KASII. FabH is the KASIII representative in *E. coli*, while FabB and FabF are the KASI and KASII representatives, respectively. Early work by Vagelos, Cronan, and Rock established differences in activity and substrate specificity for the *E. coli* elongating KSs, FabB and FabF. [41,42,78] *In vivo*, FabB, in conjunction with the dehydratase FabA, serve to create a branchpoint responsible for the production of unsaturated fatty acids from *de novo* FAB.[79,80] FabA isomerizes the *trans*-2-decenoyl-AcpP intermediate to *cis*-3-decenoyl-AcpP and FabB preferentially elongates *cis*-3-decenoyl-AcpP to *cis*-5-dodecenoyl-AcpP. The condensation reaction catalyzed by FabB at the branchpoint is essential as the FabA catalyzed isomerization is reversible. Therefore, FabB extension of *cis*-3-decenoyl-AcpP immortalizes the unsaturation, thereby producing the unsaturated fatty acids branch of the FAB pathway in *E. coli*. Additionally, Cronan and coworkers demonstrated that FabF regulates membrane fluidity in response to changes in temperature through the conversion of *cis*-palmitoleoyl-AcpP (16:1-AcpP) into *cis*-vaccenoyl-AcpP (18:1-AcpP) at lower temperatures *in vivo* and *in vitro*, thereby increasing the amount of unsaturated fatty acids present in the membrane.[78]

Given the differences in reactions catalyzed by FabB and FabF, it is reasonable to assume that there are some important structural differences in these two enzymes. Indeed, x-

ray structures of these synthases have shown that there are additional gating residues that control access to the fatty acid binding pocket. In FabF, this gate is composed of Ile108 and F202 while in FabB Ile108 is replaced by a glycine residue. Replacement of the bulky Isoleucine for a small flexible glycine likely allows more facile access to the FabB substrate binding pocket. Additional differences between these synthases can also be found in their fatty acid binding pockets. The FabF acyl-binding pocket appears more hydrophobic than that of FabB, which is somewhat truncated at its back wall by Gln113 and Glu200. These two residues come together to form a hydrogen bond that decreases the depth of this pocket (Figure S2.4e). Interestingly, there appears to be crosstalk between the two FabB protomers mediated by these two residues. Gln113 sits at the dimer interface and is present in two conformations in our C12AcpP-FabB structure, one of which shortens the binding pocket and the other where Gln113 can move away from Glu200 and provide more space for an alkyl chain. Movement of Gln113 away from Glu200 can only happen in one binding pocket at a time as the Gln113 from the neighboring protomer would occupy the same location. Effectively, a small pocket exists at the interface of the two protomers and only one Gln113 can occupy this space at a time, potentially providing a mechanism for one protomer to affect the substrates specificity of the other.

Despite these structural differences, the molecular mechanisms responsible for the distinct activities of FabF and FabB remain unknown. The proposal of a double drawbridge gating system coordinated by loops 1 and 2 may provides a new approach to answering some of these questions. Gates can be evolutionarily tuned for certain substrates or a certain activity[37], and it may be that differences in the loop 2 sequence of FabF and FabB may be a good place to start. This may still be complicated by the previously listed differences, namely

the additional gate regulating access to the acyl-binding pocket. FabB lacks the Ile108 present in FabF, and it may be that differences in both gates play a role in determining substrate specificity and may be effectively tuned to one another to favor or disfavor entry of certain substrates. Moving forward, a holistic approach looking at multiple aspects of the actives sites of FabF and FabB will likely be needed to answer some of the remaining questions for these enzymes.

Some of the differences in structure and sequence between FabF and FabB may also be responsible for stabilizing the conformations seen in our trapped AcpP-KS complexes. Both FabF structures solved in this work demonstrate a gate open conformation, although in the case of C12AcpP-FabF both the open and closed conformations appear to be present. On the other hand, both C12AcpP-FabB and C16AcpP-FabB complexes present a gate closed conformation with the alkyl chain placed into the acyl-binding pocket. The easiest explanation for such a result might be that FabB has a single gating residue (Phe201) regulating access to the acyl-binding pocket while FabF has two (Ile108 and Phe202). In FabF, Ile108 has to rotate away from Phe202 to create space for the alkyl chain in the dodecanoyl bound FabF structure, 2GFY. With the bound AcpP present, it may be that the AcpP-FabF complex favors a gate open conformation while FabB favors a gate closed conformation because it can more easily accommodate the alkyl chain in the acyl-binding pocket. Another difference in these complexes is their loop 2 sequences, which are not conserved between the KASI and KASII condensing enzyme families. The fact that Thr270 of FabF interacts with Asp35 of the bound AcpP molecule is an interesting point and it may be that the bound AcpP molecule helps stabilize the gate open conformation, as proposed in the main text. FabF's loop 2 is also stabilized by an interesting CH-π interaction found

between Pro273 and Tyr267, which is not found in FabB. Additionally, these differences, together, may also be responsible for the ability to trap these complexes in different conformations.

Supplementary Note S2.6: *Substrate interaction analysis in AcpP•FabF simulations*

Unlike C16AcpP-FabF, MD simulations suggest that the acyl chain carbonyls in 10:0-AcpP-FabF, 12:0-AcpP-FabF, 16:0-AcpP-FabF complexes do not form hydrogen bonds with either active site histidine (Figure S2.3a). Over the course of the simulation, the substrate relaxes to assume a distinct (pre-transacylation/post-condensation) disposition within the hydrophobic pocket. Furthermore, the oxyanion hole comprising Cys163 and Phe400 backbone amides was not engaged by the substrate during the course of the simulations (Figure S2.38). These findings, in addition to long distances ($d > 5.0$ Å) between the substrates and the thiolate moiety of the active site cysteine (Figure S2.38), suggest the AcpP-FabF structure features a pose wherein the crosslinker mimics a substrate conformation prior to transacylation, or a production conformation before dissociation.

Supplementary Note 7: *Substrate interaction analysis in AcpP•FabB simulations*

MD simulations of the acyl-AcpP-FabB complexes suggest that the dynamic features of these active sites are consistent with an active site preorganized for transacylation. The active site cysteine's thiolate moiety is significantly closer to the electrophilic carbon of the substrate (ca. 3.0 Å < d < 5.5 Å) than is observed in MD simulations of acyl-AcpP-FabF complexes (Figure S2.39). Backbone hydrogen-bonding interactions involving the substrate, Cys163, and Phe400 were only maintained in simulations of 12:0-AcpP-FabB (Figure S2.39). These interactions are disrupted during simulations of 16:0-AcpP-FabB, whereas in simulations of 10:0-AcpP-FabB, the substrate is ~5 Å away from either backbone hydrogen-bonding donor. Finally, no hydrogen bonds between the active site histidines (His303 and His340) and any substrate modeled are sampled during MD simulations (Figure S2.39).

Supplementary Note S2.8. General synthetic methods. Chemical reagents were purchased from Acros, Fluka, Sigma-Aldrich, or TCI. Deuterated NMR solvents were purchased from Cambridge Isotope Laboratories. All reactions were conducted with vigorously dried anhydrous solvents that were obtained by passing through a solvent column exposed of activated A2 alumina. All reactions were performed under positive pressure of argon in flame-dried glassware sealed with septa, and stirring with Teflon coated stir bars using an IKAMAG TCT-basic mechanical stirrer (IKA GmbH). Analytical Thin Layer Chromatograpy (TLC) was performed on Silica Gel 60 F254 precoated glass plates (EM Sciences). Visualization was achieved with UV light and/or appropriate stain (I_2 on SiO_2, $KMnO_4$, bromocresol green, dinitrophenylhydrazine, ninhydrin, or ceric ammonium molybdate). Flash column chromatography was carried out with Geduran Silica Gel 60 (40–63 mesh) from EM Biosciences. Yield and characterization data correspond to isolated, chromatographically, and spectroscopically homogeneous materials. ^{1}H NMR spectra were recorded on Varian Mercury 400 or Varian Mercury Plus 400 spectrometers. ^{13}C NMR spectra were recorded at 100 MHz on Varian Mercury 400 or Varian Mercury Plus 400 spectrometers. Chemical shifts for ^{1}H NMR and ^{13}C NMR analyses were referenced to the reported values of Gottlieb[81] using the signal from the residual solvent for ^{1}H spectra, or to the ^{13}C signal from the deuterated solvent. Chemical shift δ values for the ^{1}H and ^{13}C spectra are reported in parts per millions (ppm) relative to these referenced values, and multiplicities are abbreviated as s=singlet, d=doublet, t=triplet, q-quartet, m=multiplet, b=broad. All ^{13}C NMR spectra were recorded with complete proton decoupling. FID files were processed using MestreNova 10.0 (MestreLab Research). Electrospray ionization (ESI) mass

spectrometric analyses were preformed using a ThermoFinnigan LCQ Deca spectrometer. Spectral data, procedures, and copies of spectra are provided for all new compounds.

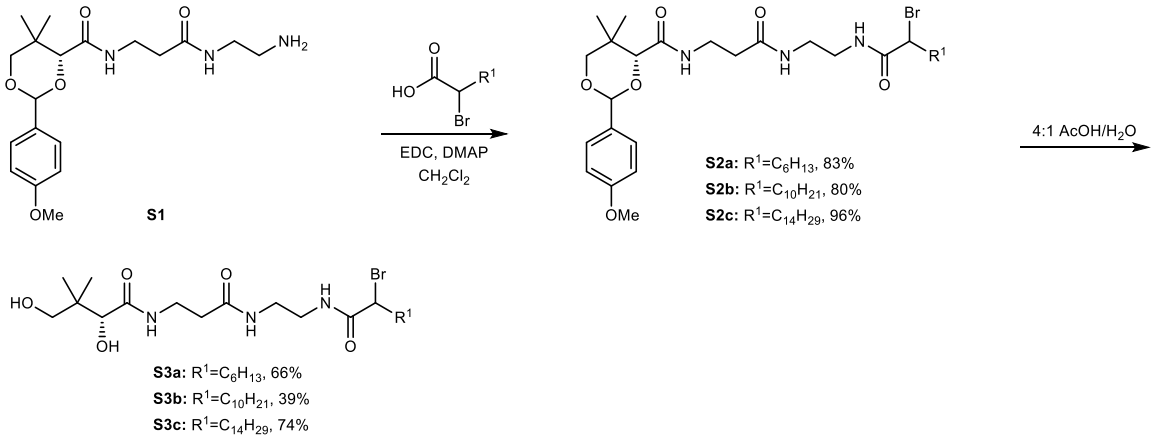

Synthesis of α-bromopantetheineamide crosslinkers. EDC=1-Ethyl-3-(3-dimethylaminopropyl)carbodiimide); DMAP=4-(dimethylamino)-pyridine; AcOH=acetic acid.

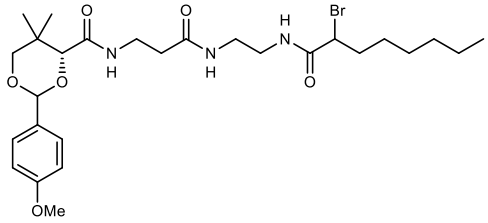

(4R)-N-(3-((2-(2-bromooctanamido)ethyl)amino)-3-oxopropyl)-2-(4-methoxy- phenyl)-5,5-dimethyl-1,3-dioxane-4-carboxamide (S2a). In a 10 mL pear-shaped flask, (4*R*)-*N*-(3-((2-aminoethyl)amino)-3-oxopropyl)-2-(4-methoxyphenyl)-5,5-dimethyl-1,3-dioxane-4-carboxamide **S1**[82] (100.8 mg, 0.2656 mmol, 1.0 equiv.), 2-bromooctanoic acid (69.6 µL, 0.3987 mmol, 1.5 equiv.), and 2.7 mL CH_2Cl_2 were added. To the solution was added EDC•HCl (85.2 mg, 0.4444 mmol, 1.7 equiv.) and DMAP (9.7 mg, 0.0794 mmol, 0.30 equiv.). After 18 h, the reaction was dissolved in 100 mL CH_2Cl_2 and washed with brine (10 mL). The organic phase was dried ($MgSO_4$), filtered, and concentrated by rotary evaporation. Purification by silica flash chromatography (39:1 → 19:1 CH_2Cl_2/MeOH) afforded **S2a** (128.7 mg, 83%) as a white solid.

TLC (CH_2Cl_2/MeOH, 19:1 v:v): R_f = 0.24; ^{1}H-NMR (400 MHz, $CDCl_3$): δ 7.50 (bs, 1H), 7.38 (d, *J* = 8.6 Hz, 2H), 7.30 (bs, 1H), 7.11 (t, *J* = 5.8 Hz, 1H), 6.90 – 6.82 (d, *J* = 8.3 Hz, 2H), 5.40 (s, 1H), 4.22–4.09 (m, 1H), 4.02 (s, 1H), 3.75 (s, 3H), 3.62 (q, *J* = 11.4 Hz, 2H), 3.51–3.40 (m, 2H), 3.36 (bs, 5H), 3.26 (bs, 3H), 3.03 (s, 3H), 2.35 (t, *J* = 6.3 Hz, 2H), 1.21 (bs, 6H), 1.04 (s, 3H), 1.01 (s, 3H), 0.81 (t, *J* = 6.5 Hz, 2H). ^{13}C-NMR (100 MHz, $CDCl_3$): δ 172.31, 170.31, 169.74, 160.15, 130.02, 127.49, 113.65, 101.26, 83.76, 78.32, 55.27, 50.25, 39.97, 38.91, 35.83, 35.79, 35.37, 35.20, 33.01, 31.48, 28.47, 27.23, 22.46, 21.76, 19.07, 13.99; (*m/z*): 606.31([M+Na]$^+$.

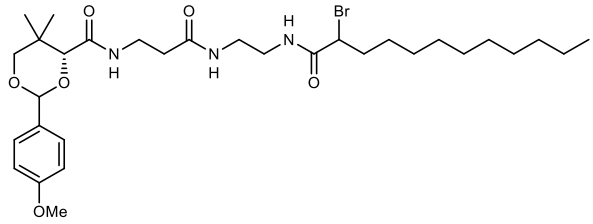

(4R)-N-(3-((2-(2-bromododecanamido)ethyl)amino)-3-oxopropyl)-2-(4-methoxy-phenyl)-5,5-dimethyl-1,3-dioxane-4-carboxamide (S2b). Prepared as described for **S2a** from **S1** and 2-bromododecanoic acid to give **S2b** (146.6 mg, 80%) as a clear oil.
TLC (CH_2Cl_2/MeOH, 19:1 v:v): R_f = 0.24; ^{1}H-NMR (400 MHz, $CDCl_3$): δ 7.43 (d, *J* = 8.1 Hz, 2H), 7.03 (s, 2H), 6.92 (d, *J* = 8.0 Hz, 2H), 6.61 (bs, 1H), 5.47 (s, 1H), 4.33–4.19 (m, 3H), 4.19–4.12 (m, 1H), 4.10 (s, 1H), 3.82 (s, 2H), 3.69 (q, *J* = 11.4 Hz, 2H), 3.59–3.51 (m, 2H), 3.37 (bs, 2H), 2.45 (t, *J* = 5.5 Hz, 2H), 1.99–1.88 (m, 2H),1.29–1.21 (m, 14H), 1.10 (d, *J* = 6.5 Hz, 6H), 0.92–0.82 (m, 5H). ^{13}C-NMR (100 MHz, $CDCl_3$): δ 172.48, 171.13, 170.61, 170.33, 160.26, 130.09, 127.59, 113.74, 101.39, 83.80, 78.42, 74.53, 69.15, 62.37, 62.02, 55.34, 50.68, 40.22, 39.20, 36.11, 35.56, 35.23, 34.97, 34.14, 33.13, 31.93, 31.77, 29.73, 29.60, 29.44, 29.36, 29.26, 29.11, 28.92, 27.38, 25.34, 24.88, 22.72, 21.87, 20.93, 20.74, 19.20, 14.17. ESI-MS (*m/z*): 663.39([M+Na]$^+$, 582.50 [M-Br+Na]$^+$.

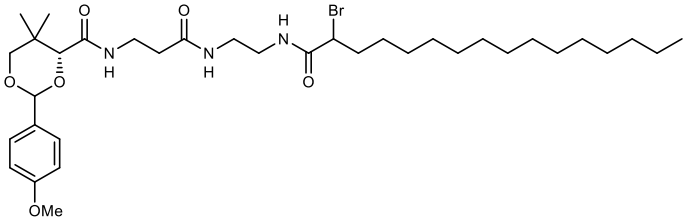

(4R)-N-(3-((2-(2-bromohexadecanamido)ethyl)amino)-3-oxopropyl)-2-(4-methoxy-phenyl)-5,5-dimethyl-1,3-dioxane-4-carboxamide (S2c). Prepared as described for **S2a** from **S1** and 2-bromohexadecanoic acid to give **S2c** (178.4 mg, 96%) as a white solid. Characterization data were consistent with those previously reported.[18]

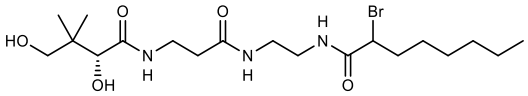

2-bromo-N-(2-(3-((R)-2,4-dihydroxy-3,3-dimethylbutanamido)propanamido)ethyl)-octanamide (S3a). In a 20 mL vial, **S2a** (128.7 mg, 0.2202 mmol, 1.0 equiv.) and 2.2 mL 4:1 AcOH/H_2O were added. After 5 h, the mixture was concentrated by rotary evaporation, and azeotroped from cyclohexane (3x10 mL) and benzene (3x10 mL). Purification by silica flash chromatography (19:1 → 4:1 CH_2Cl_2/MeOH) afforded **S3a** (65.8 mg, 66%) as a white solid.

TLC (CH_2Cl_2/MeOH, 9:1 v:v): R_f = 0.37; ^{1}H-NMR (400 MHz, $CDCl_3$): δ 7.35–7.28 (m, 1H), 7.11–7.01 (m, 1H), 6.71–6.64 (m, 1H), 6.61–6.55 (m, 1H), 4.37– 4.14 (m, 2H), 4.02 (d, *J* = 4.9 Hz, 1H), 3.78–3.58 (m, 1H), 3.57–3.52 (m, 1H), 3.48–3.23 (m, 4H), 2.45 (q, *J* = 6.9, 6.4

Hz, 2H), 2.14–1.90 (m, 2H), 1.51–1.37 (m, 2H), 1.36–1.23 (m, 6H), 1.03 (s, 3H), 0.94 (s, 3H), 0.88 (t, J = 6.6 Hz, 3H). ^{13}C-NMR (100 MHz, $CDCl_3$): δ 174.47, 172.65, 170.78, 70.62, 50.38, 39.95, 39.35, 36.07, 35.50, 31.65, 28.66, 27.43, 22.63, 21.28, 20.85, 14.17.ESI-MS (*m/z*): 488.28 ([M+Na]$^+$.

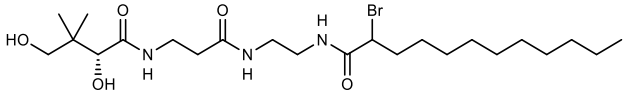

2-bromo-N-(2-(3-((R)-2,4-dihydroxy-3,3-dimethylbutanamido)propanamido)ethyl)-dodecanamide (S3b). Prepared as described for **S3a** from **S2b**, to give **S3b** (47.1 mg, 39%) as a white solid.

TLC (CH_2Cl_2/MeOH, 9:1 v:v): R_f = 0.46; ^{1}H-NMR (400 MHz, $CDCl_3$): δ 7.63–7.48 (m, 2H), 7.32 (s, 1H), 4.25 (bs, 1H), 3.99 (s, 1H), 3.65–3.53 (m, 1H), 3.52–3.38 (m, 5H), 3.37–3.25 (m, 2H), 2.44 (s, 2H), 1.98 (d, J = 31.1 Hz, 2H), 1.42 (s, 1H), 1.23 (bs, 16H), 0.96 (s, 3H), 0.91 (s, 3H), 0.88–0.82 (m, 3H); ^{13}C-NMR (100 MHz, $CDCl_3$): δ 174.41, 172.66, 170.74, 70.76, 50.56, 40.07, 39.36, 36.10, 35.54, 32.00, 29.68, 29.53, 29.43, 29.03, 27.51, 22.78, 21.38, 20.79, 14.24. ESI-MS (*m/z*): 544.31[M+Na]$^+$, 464.40 [M-Br+Na]$^+$, 520.17 [M-H]$^-$.

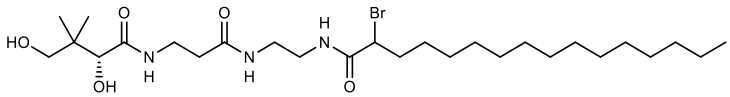

2-bromo-N-(2-(3-((R)-2,4-dihydroxy-3,3-dimethylbutanamido)propanamido)ethyl)-hexadecanamide (S3c). Prepared as described for **S3a** from **S2c**, to give **S3c** (110.4 mg, 74%) as a white solid. Characterization data were consistent with those previously reported.

NMR characterization of S2a

1H NMR (400 MHz) Spectrum of S2a

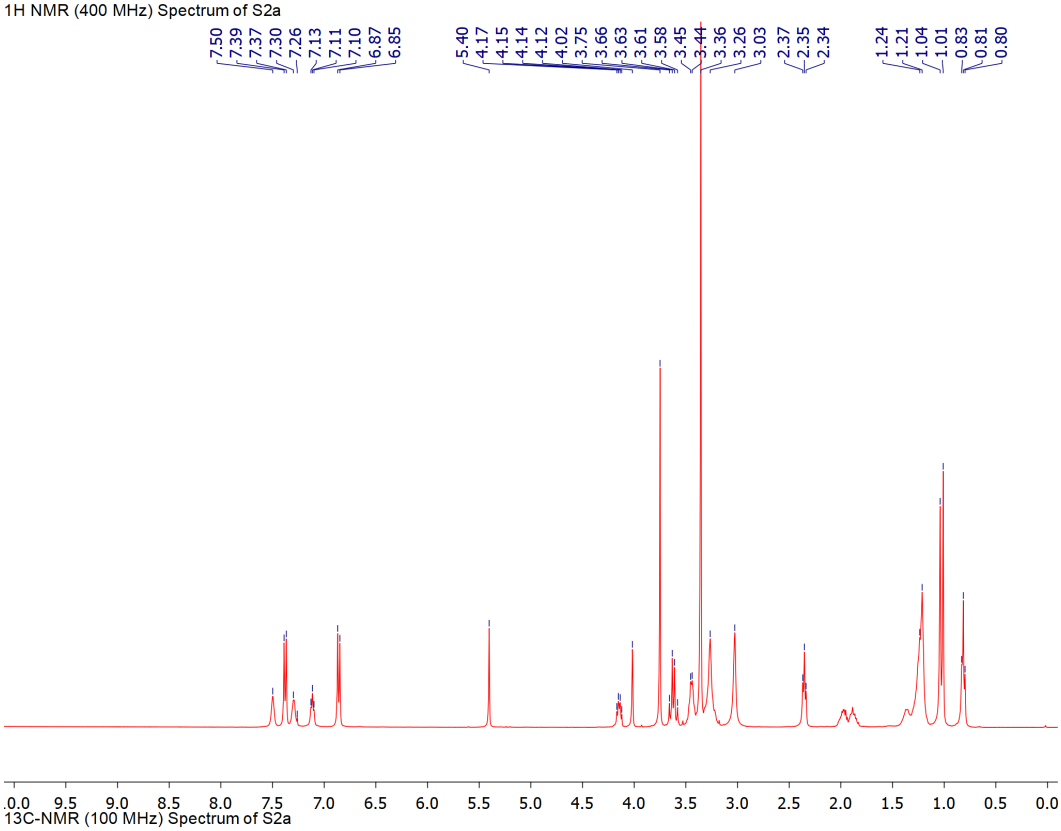

13C-NMR (100 MHz) Spectrum of S2a

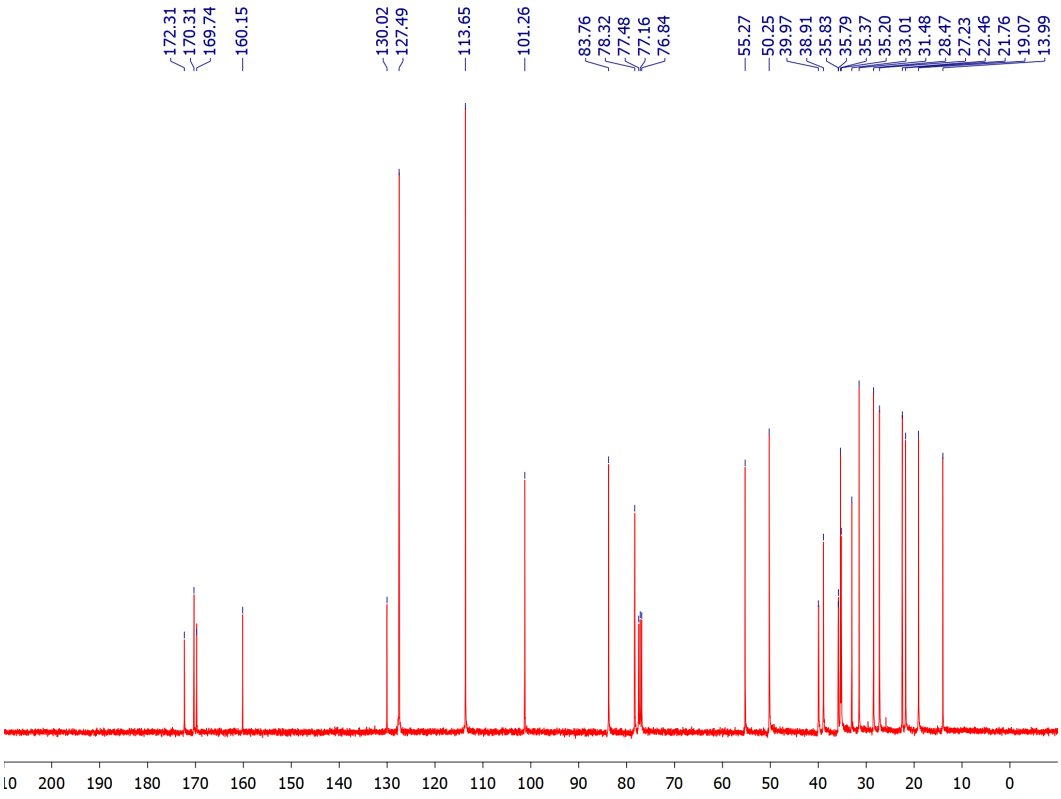

NMR characterization of S2b

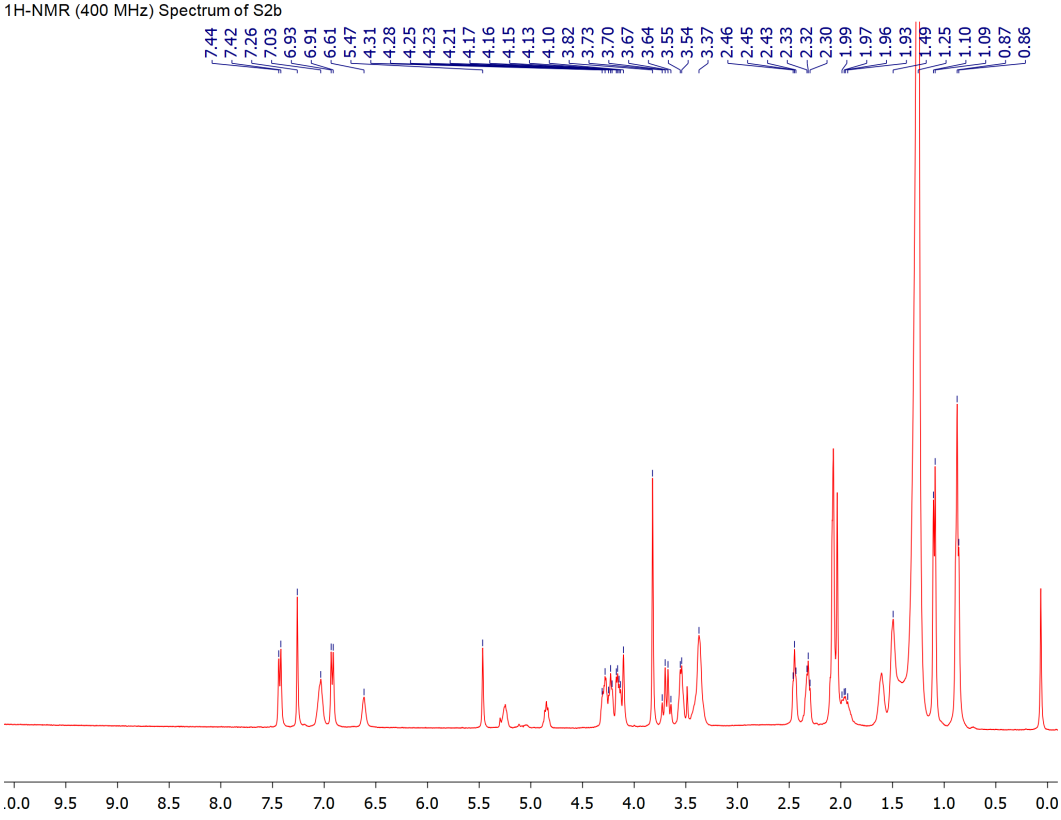

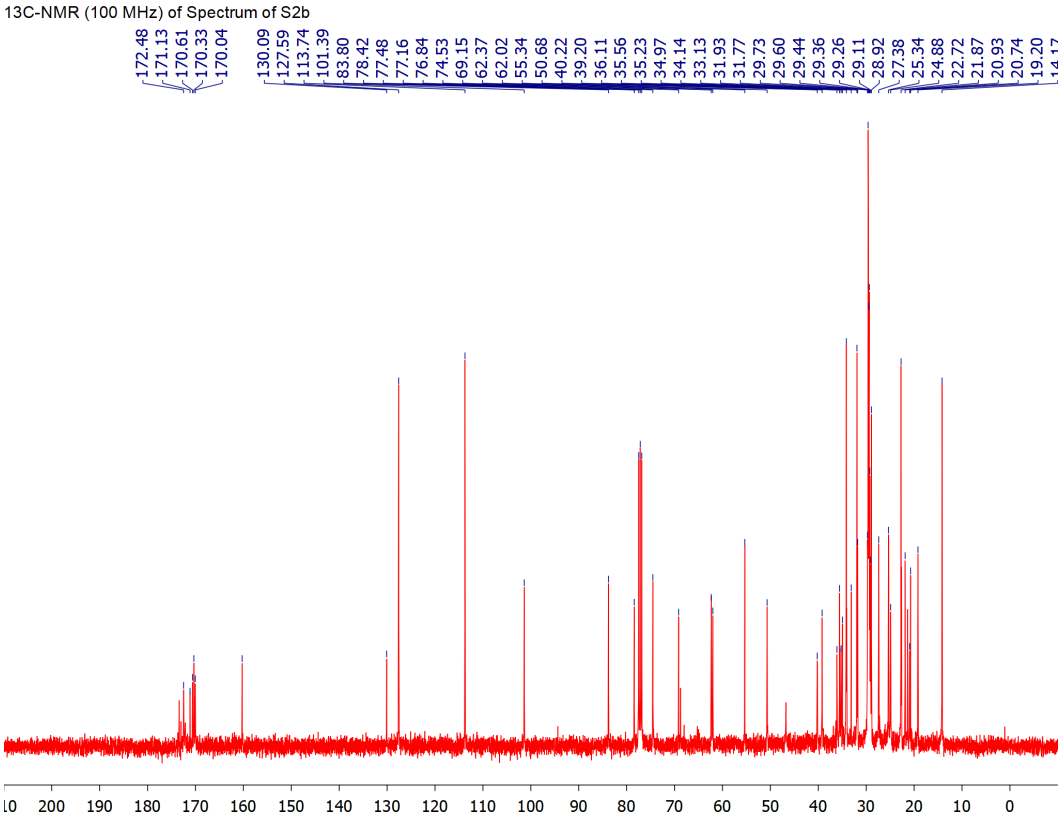
13C-NMR (100 MHz) of Spectrum of S2b
172.48
171.13
170.61
170.33
170.04
130.09
127.59
113.74
101.39
83.80
78.42
77.48
77.16
76.84
74.53
69.15
62.37
62.02
55.34
50.68
40.22
39.20
36.11
35.56
35.23
34.97
34.14
33.13
31.93
31.77
29.73
29.60
29.44
29.36
29.26
29.11
28.92
27.38
25.34
24.88
22.72
21.87
20.93
20.74
19.20
200
190
180
170
160
150
140
130
120
110
100
90
80
70
60
50
40
30
20
10
0

NMR characterization of S3a

1H-NMR (400 MHz) Spectrum of S3a

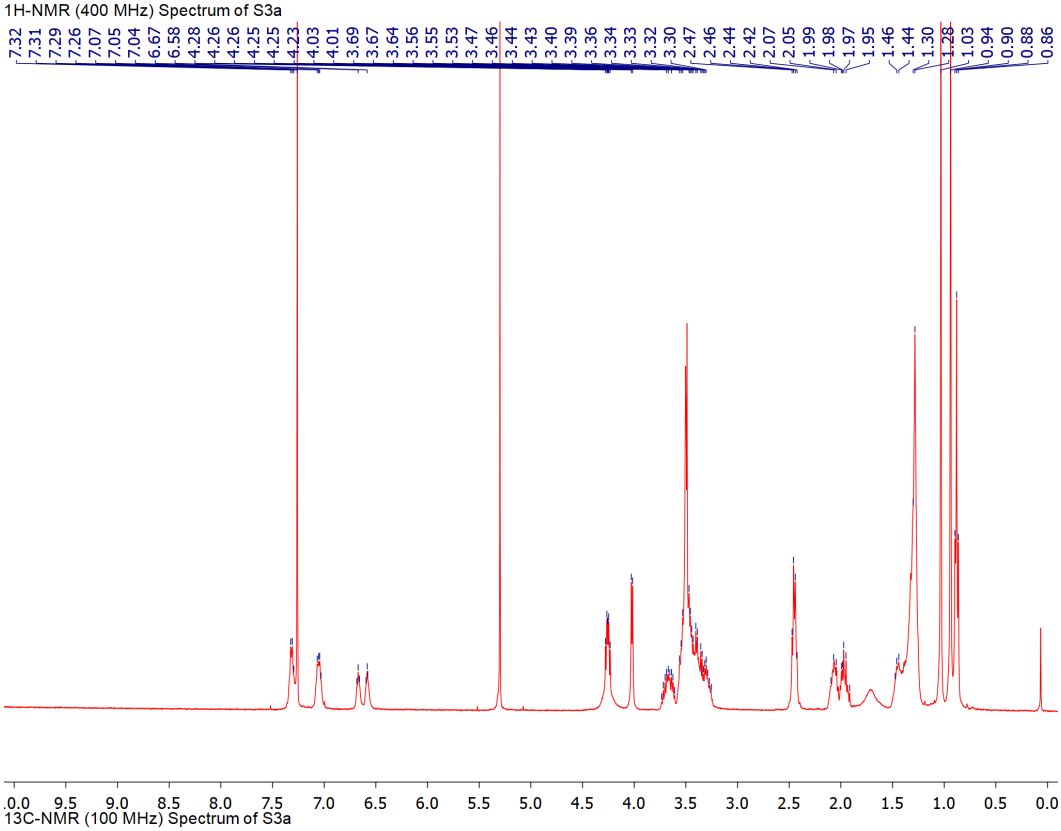

13C-NMR (100 MHz) Spectrum of S3a

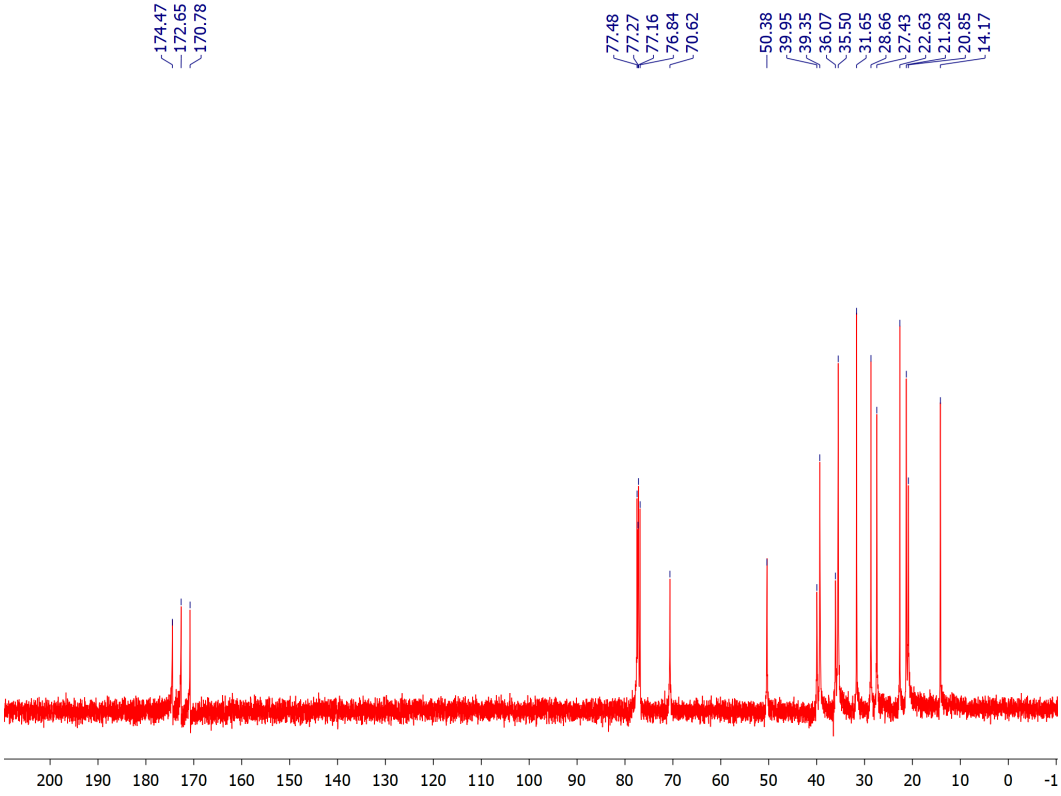

NMR characterization of S3b

1H-NMR (400 MHz) Spectrum of S3b

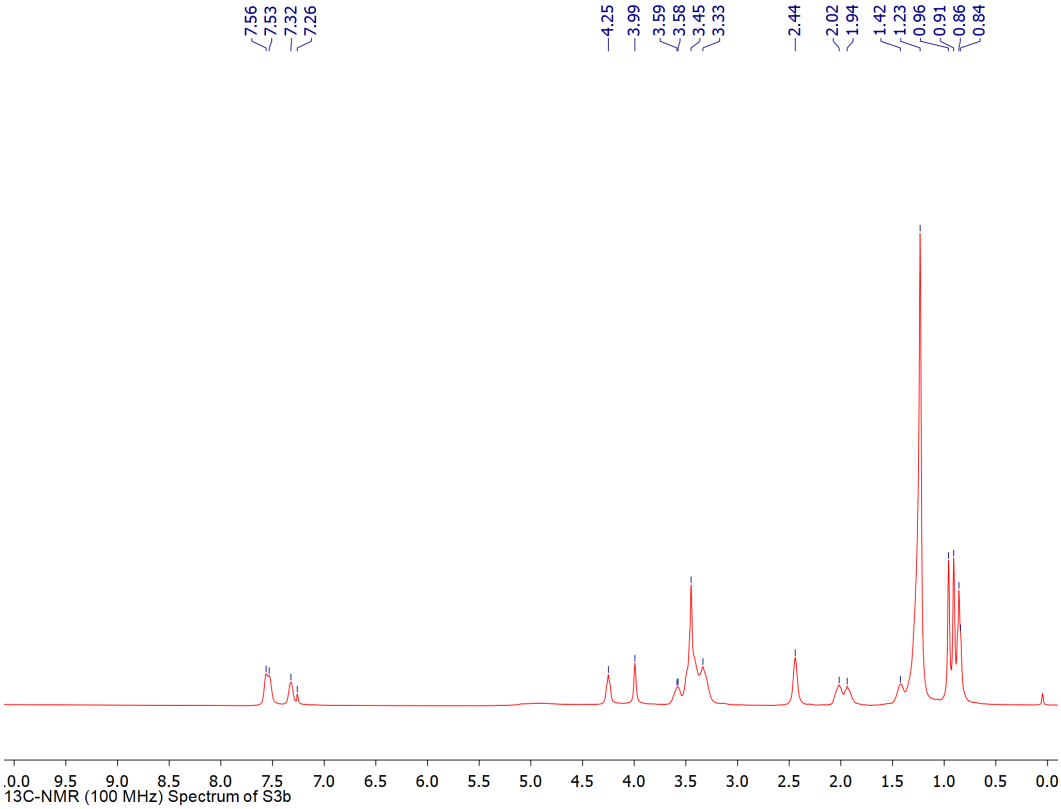

13C-NMR (100 MHz) Spectrum of S3b

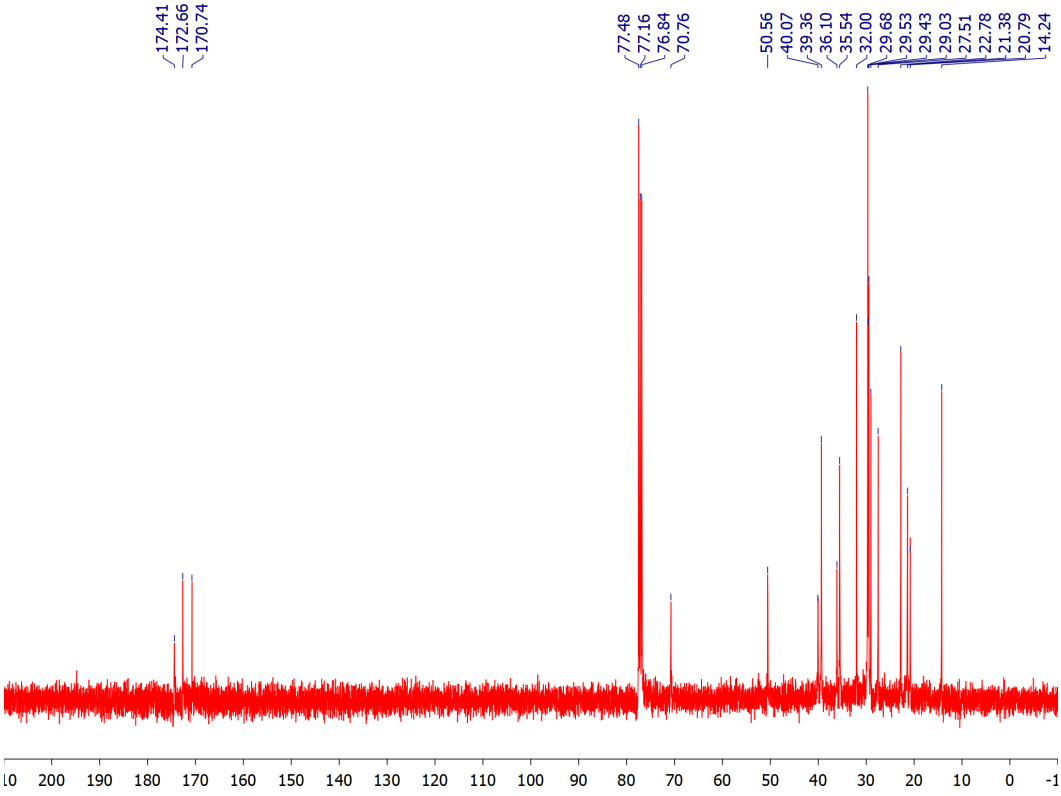

References

(1) Hertweck, C. (2009) The Biosynthetic Logic of Polyketide Diversity. *Angew. Chemie Int. Ed. 48*, 4688–4716.

(2) Staunton, J., and Weissman, K. J. (2001) Polyketide biosynthesis: a millennium review. *Nat. Prod. Rep. 18*, 380–416.

(3) Beld, J., Lee, D. J., and Burkart, M. D. (2015) Fatty acid biosynthesis revisited: structure elucidation and metabolic engineering. *Mol. Biosyst. 11*, 38–59.

(4) White, S. W., Zheng, J., Zhang, Y.-M., and Rock, C. O. (2005) The Structural Biology of Type II Fatty Acid Biosynthesis. *Annu. Rev. Biochem. 74*, 791–831.

(5) Herbst, D. A., Townsend, C. A., and Maier, T. (2018) The architectures of iterative type I PKS and FAS. *Nat. Prod. Rep.* 1046–1069.

(6) Herbst, D. A., Jakob, R. P., Zähringer, F., and Maier, T. (2016) Mycocerosic acid synthase exemplifies the architecture of reducing polyketide synthases. *Nature 531*, 533–537.

(7) Herbst, D. A., Huitt-Roehl, C. R., Jakob, R. P., Kravetz, J. M., Storm, P. A., Alley, J. R., Townsend, C. A., and Maier, T. (2018) The structural organization of substrate loading in iterative polyketide synthases. *Nat. Chem. Biol. 14*, 474–479.

(8) Maier, T., Leibundgut, M., and Ban, N. (2008) The Crystal Structure of a Mammalian Fatty Acid Synthase. *Science (80-.). 321*, 1315 LP – 1322.

(9) Nguyen, C., Haushalter, R. W., Lee, D. J., Markwick, P. R. L., Bruegger, J., Caldara-Festin, G., Finzel, K., Jackson, D. R., Ishikawa, F., O/'Dowd, B., McCammon, J. A., Opella, S. J., Tsai, S.-C., and Burkart, M. D. (2014) Trapping the dynamic acyl carrier protein in fatty acid biosynthesis. *Nature 505*, 427–431.

(10) Dodge, G. J., Patel, A., Jaremko, K. L., McCammon, J. A., Smith, J. L., and Burkart, M. D. (2019) Structural and dynamical rationale for fatty acid unsaturation in *Escherichia coli*. *Proc. Natl. Acad. Sci. 116*, 6775–6783.

(11) Maier, T., Leibundgut, M., Boehringer, D., and Ban, N. (2010) Structure and function of eukaryotic fatty acid synthases. *Q. Rev. Biophys. 43*, 373–422.

(12) Crosby, J., and Crump, M. P. (2012) The structural role of the carrier protein – active controller or passive carrier. *Nat. Prod. Rep. 29*, 1111–1137.

(13) Chen, A., Re, R. N., and Burkart, M. D. (2018) Type II fatty acid and polyketide synthases: deciphering protein–protein and protein–substrate interactions. *Nat. Prod. Rep. 35*, 1029–1045.

(14) Kapur, S., Lowry, B., Yuzawa, S., Kenthirapalan, S., Chen, A. Y., Cane, D. E., and Khosla, C. (2012) Reprogramming a module of the 6-deoxyerythronolide B synthase for iterative chain elongation. *Proc. Natl. Acad. Sci. 109*, 4110–4115.

(15) Masoudi, A., Raetz, C. R. H., Zhou, P., and Pemble, C. W. (2014) Chasing Acyl-Carrier-Protein Through a Catalytic Cycle of Lipid A Production. *Nature 505*, 422–426.

(16) Lowry, B., Li, X., Robbins, T., Cane, D. E., and Khosla, C. (2016) A Turnstile Mechanism for the Controlled Growth of Biosynthetic Intermediates on Assembly Line Polyketide Synthases. *ACS Cent. Sci. 2*, 14–20.

(17) Jiménez-Osés, G., Osuna, S., Gao, X., Sawaya, M. R., Gilson, L., Collier, S. J., Huisman, G. W., Yeates, T. O., Tang, Y., and Houk, K. N. (2014) The role of distant mutations and allosteric regulation on LovD active site dynamics. *Nat. Chem. Biol. 10*, 431.

(18) Blatti, J. L., Beld, J., Behnke, C. A., Mendez, M., Mayfield, S. P., and Burkart, M. D. (2012) Manipulating fatty acid biosynthesis in microalgae for biofuel through protein-protein interactions. *PLoS One 7*, 1–12.

(19) Ruppe, A., and Fox, J. M. (2018) Analysis of Interdependent Kinetic Controls of Fatty Acid Synthases. *ACS Catal. 8*, 11722–11734.

(20) Cronan, J. E., and Thomas, J. B. T.-M. in E. (2009) Chapter 17 Bacterial Fatty Acid Synthesis and its Relationships with Polyketide Synthetic Pathways, in *Complex Enzymes in Microbial Natural Product Biosynthesis, Part B: Polyketides, Aminocoumarins and Carbohydrates*, pp 395–433. Academic Press.

(21) Jenner, M., Afonso, J. P., Bailey, H. R., Frank, S., Kampa, A., Piel, J., and Oldham, N. J. (2015) Acyl-Chain Elongation Drives Ketosynthase Substrate Selectivity in trans-Acyltransferase Polyketide Synthases. *Angew. Chemie Int. Ed. 54*, 1817–1821.

(22) Heil, C. S., Wehrheim, S. S., Paithankar, K. S., and Grininger, M. (2019) Fatty Acid Biosynthesis: Chain-Length Regulation and Control. *ChemBioChem 0*.

(23) Klaus, M., and Grininger, M. (2018) Engineering strategies for rational polyketide synthase design. *Nat. Prod. Rep. 35*, 1070–1081.

(24) Gajewski, J., Buelens, F., Serdjukow, S., Janßen, M., Cortina, N., Grubmüller, H., and Grininger, M. (2017) Engineering fatty acid synthases for directed polyketide production. *Nat. Chem. Biol. 13*, 363.

(25) Zhu, Z., Zhou, Y. J., Krivoruchko, A., Grininger, M., Zhao, Z. K., and Nielsen, J. (2017) Expanding the product portfolio of fungal type I fatty acid synthases. *Nat. Chem. Biol. 13*, 360.

(26) Fischer, M., and Grininger, M. (2017) Strategies in megasynthase engineering - fatty

acid synthases (FAS) as model proteins. *Beilstein J. Org. Chem. 13*, 1204–1211.

(27) Gajewski, J., Pavlovic, R., Fischer, M., Boles, E., and Grininger, M. (2017) Engineering fungal de novo fatty acid synthesis for short chain fatty acid production. *Nat. Commun. 8*, 14650.

(28) Zhang, Y. M., Hurlbert, J., White, S. W., and Rock, C. O. (2006) Roles of the Active Site Water, Histidine 303, and Phenylalanine 396 in the Catalytic Mechanism of the Elongation Condensing Enzyme of Streptococcus pneumoniae. *J. Biol. Chem. 281*, 17390–17399.

(29) von Wettstein-Knowles, P., Olsen, J. G., McGuire, K. A., and Henriksen, A. (2006) Fatty acid synthesis. *FEBS J. 273*, 695–710.

(30) Zhang, Y.-M., Wu, B., Zheng, J., and Rock, C. O. (2003) Key Residues Responsible for Acyl Carrier Protein and β-Ketoacyl-Acyl Carrier Protein Reductase (FabG) Interaction. *J. Biol. Chem. 278*, 52935–52943.

(31) Zhang, Y.-M., Rao, M. S., Heath, R. J., Price, A. C., Olson, A. J., Rock, C. O., and White, S. W. (2001) Identification and Analysis of the Acyl Carrier Protein (ACP) Docking Site on β-Ketoacyl-ACP Synthase III. *J. Biol. Chem. 276*, 8231–8238.

(32) Tallorin, L., Finzel, K., Nguyen, Q. G., Beld, J., La Clair, J. J., and Burkart, M. D. (2016) Trapping of the enoyl-acyl carrier protein reductase-acyl carrier protein interaction. *J. Am. Chem. Soc. 138*.

(33) Yu, X., Liu, T., Zhu, F., and Khosla, C. (2011) In vitro reconstitution and steady-state analysis of the fatty acid synthase from *Escherichia coli*. *Proc. Natl. Acad. Sci. 108*, 18643–18648.

(34) Milligan, J. C., Lee, D. J., Jackson, D. R., Schaub, A. J., Beld, J., Barajas, J. F., Hale, J. J., Luo, R., Burkart, M. D., and Tsai, S.-C. (2019) Molecular basis for interactions between an acyl carrier protein and a ketosynthase. *Nat. Chem. Biol. 15*, 669–671.

(35) Marcella, A. M., Culbertson, S. J., Shogren-Knaak, M. A., and Barb, A. W. (2017) Structure, High Affinity, and Negative Cooperativity of the *Escherichia coli* Holo-(Acyl Carrier Protein):Holo-(Acyl Carrier Protein) Synthase Complex. *J. Mol. Biol. 429*, 3763–3775.

(36) Rafi, S., Novichenok, P., Kolappan, S., Zhang, X., Stratton, C. F., Rawat, R., Kisker, C., Simmerling, C., and Tonge, P. J. (2006) Structure of Acyl Carrier Protein Bound to FabI, the FASII Enoyl Reductase from *Escherichia coli*. *J. Biol. Chem. 281*, 39285–39293.

(37) Gora, A., Brezovsky, J., and Damborsky, J. (2013) Gates of enzymes. *Chem. Rev. 113*, 5871–5923.

(38) Worthington, A. S., and Burkart, M. D. (2006) One-pot chemo-enzymatic synthesis of reporter-modified proteins. *Org. Biomol. Chem. 4*, 44–46.

(39) Worthington, A. S., Porter, D. F., and Burkart, M. D. (2010) Mechanism-based crosslinking as a gauge for functional interaction of modular synthases. *Org. Biomol. Chem. 8*, 1769–1772.

(40) Finzel, K., Lee, D. J., and Burkart, M. D. (2015) Using Modern Tools To Probe the Structure–Function Relationship of Fatty Acid Synthases. *ChemBioChem 16*, 528–547.

(41) D'Agnolo, G., Rosenfeld, I. S., and Vagelos, P. R. (1975) Multiple forms of beta-ketoacyl-acyl carrier protein synthetase in *Escherichia coli*. *J. Biol. Chem. 250*, 5289–5294.

(42) Garwin, J., Klages, A., and Cronan, J. (1980) Structural, enzymatic, and genetic studies of beta-ketoacyl-acyl carrier protein synthases I and II of *Escherichia coli*. *J. Biol. Chem. 255*, 11949–11956.

(43) Wang, J., Soisson, S. M., Young, K., Shoop, W., Kodali, S., Galgoci, A., Painter, R., Parthasarathy, G., Tang, Y. S., Cummings, R., Ha, S., Dorso, K., Motyl, M., Jayasuriya, H., Ondeyka, J., Herath, K., Zhang, C., Hernandez, L., Allocco, J., Basilio, Á., Tormo, J. R., Genilloud, O., Vicente, F., Pelaez, F., Colwell, L., Lee, S. H., Michael, B., Felcetto, T., Gill, C., Silver, L. L., Hermes, J. D., Bartizal, K., Barrett, J., Schmatz, D., Becker, J. W., Cully, D., and Singh, S. B. (2006) Platensimycin is a selective FabF inhibitor with potent antibiotic properties. *Nature 441*, 358.

(44) Olsen, J. G., Kadziola, A., von Wettstein-Knowles, P., Siggaard-Andersen, M., and Larsen, S. (2001) Structures of beta-Ketoacyl-Acyl Carrier Protein Synthase I Complexed with Fatty Acids Elucidate its Catalytic Machinery. *Structure 9*, 233–243.

(45) Olsen, J. G., Kadziola, A., von Wettstein-Knowles, P., Siggaard-Andersen, M., and Larsen, S. (2001) Structures of β-Ketoacyl-Acyl Carrier Protein Synthase I Complexed with Fatty Acids Elucidate its Catalytic Machinery. *Structure 9*, 233–243.

(46) Zondlo, N. J. (2013) Aromatic–Proline Interactions: Electronically Tunable CH/π Interactions. *Acc. Chem. Res. 46*, 1039–1049.

(47) Robbins, T., Liu, Y.-C., Cane, D. E., and Khosla, C. (2016) Structure and mechanism of assembly line polyketide synthases. *Curr. Opin. Struct. Biol. 41*, 10–18.

(48) Dreier, J., Shah, A. N., and Khosla, C. (1999) Kinetic Analysis of the Actinorhodin Aromatic Polyketide Synthase. *J. Biol. Chem. 274*, 25108–25112.

(49) Keatinge-Clay, A. T., Maltby, D. A., Medzihradszky, K. F., Khosla, C., and Stroud, R. M. (2004) An antibiotic factory caught in action. *Nat. Struct. &Amp; Mol. Biol. 11*, 888.

(50) Hertweck, C., Luzhetskyy, A., Rebets, Y., and Bechthold, A. (2007) Type II polyketide

synthases: gaining a deeper insight into enzymatic teamwork. *Nat. Prod. Rep. 24*, 162–190.

(51) Du, D., Katsuyama, Y., Shin-ya, K., and Ohnishi, Y. (2018) Reconstitution of a Type II Polyketide Synthase that Catalyzes Polyene Formation. *Angew. Chemie Int. Ed. 57*, 1954–1957.

(52) Du, D., Katsuyama, Y., Onaka, H., Fujie, M., Satoh, N., Shin-ya, K., and Ohnishi, Y. (2016) Production of a Novel Amide-Containing Polyene by Activating a Cryptic Biosynthetic Gene Cluster in Streptomyces sp. MSC090213JE08. *ChemBioChem 17*, 1464–1471.

(53) Grammbitter, G. L. C., Schmalhofer, M., Karimi, K., Shi, Y.-M., Schöner, T. A., Tobias, N. J., Morgner, N., Groll, M., and Bode, H. B. (2019) An Uncommon Type II PKS Catalyzes Biosynthesis of Aryl Polyene Pigments. *J. Am. Chem. Soc.*

(54) Cronan, J. E. (2014) The chain-flipping mechanism of ACP (acyl carrier protein)-dependent enzymes appears universal. *Biochem. J. 460*, 157–163.

(55) Pappenberger, G., Schulz-Gasch, T., Kusznir, E., Müller, F., and Hennig, M. (2007) Structure-assisted discovery of an aminothiazole derivative as a lead molecule for inhibition of bacterial fatty-acid synthesis. *Acta Crystallogr. Sect. D 63*, 1208–1216.

(56) Henzler-Wildman, K., and Kern, D. (2007) Dynamic personalities of proteins. *Nature 450*, 964.

(57) Trajtenberg, F., Altabe, S., Larrieux, N., Ficarra, F., de Mendoza, D., Buschiazzo, A., and Schujman, G. E. (2014) Structural insights into bacterial resistance to cerulenin. *Febs J. 281*, 2324–2338.

(58) Robbins, T., Kapilivsky, J., Cane, D. E., and Khosla, C. (2016) Roles of Conserved Active Site Residues in the Ketosynthase Domain of an Assembly Line Polyketide Synthase. *Biochemistry 55*, 4476–4484.

(59) Kosa, N. M., Haushalter, R. W., Smith, A. R., and Burkart, M. D. (2012) Reversible labeling of native and fusion-protein motifs. *Nat. Methods 9*, 981.

(60) Liu, H., and Naismith, J. H. (2008) An efficient one-step site-directed deletion, insertion, single and multiple-site plasmid mutagenesis protocol. *BMC Biotechnol. 8*, 91.

(61) Schneider, C. A., Rasband, W. S., and Eliceiri, K. W. (2012) NIH Image to ImageJ: 25 years of image analysis. *Nat. Methods 9*, 671–675.

(62) Battye, T. G. G., Kontogiannis, L., Johnson, O., Powell, H. R., and Leslie, A. G. W. (2011) iMOSFLM: a new graphical interface for diffraction-image processing with MOSFLM. *Acta Crystallogr. D. Biol. Crystallogr. 67*, 271–281.

(63) Winn, M. D., Ballard, C. C., Cowtan, K. D., Dodson, E. J., Emsley, P., Evans, P. R., Keegan, R. M., Krissinel, E. B., Leslie, A. G. W., McCoy, A., McNicholas, S. J., Murshudov, G. N., Pannu, N. S., Potterton, E. A., Powell, H. R., Read, R. J., Vagin, A., and Wilson, K. S. (2011) Overview of the CCP4 suite and current developments. *Acta Crystallogr. D. Biol. Crystallogr. 67*, 235–242.

(64) Lebedev, A. A., Young, P., Isupov, M. N., Moroz, O. V, Vagin, A. A., and Murshudov, G. N. (2012) JLigand: a graphical tool for the CCP4 template-restraint library. *Acta Crystallogr. D. Biol. Crystallogr. 68*, 431–440.

(65) Adams, P. D., Afonine, P. V, Bunkóczi, G., Chen, V. B., Davis, I. W., Echols, N., Headd, J. J., Hung, L.-W., Kapral, G. J., Grosse-Kunstleve, R. W., McCoy, A. J., Moriarty, N. W., Oeffner, R., Read, R. J., Richardson, D. C., Richardson, J. S., Terwilliger, T. C., and Zwart, P. H. (2010) PHENIX: a comprehensive Python-based system for macromolecular structure solution. *Acta Crystallogr. D. Biol. Crystallogr. 66*, 213–221.

(66) Roujeinikova, A., Simon, W. J., Gilroy, J., Rice, D. W., Rafferty, J. B., and Slabas, A. R. (2007) Structural Studies of Fatty Acyl-(Acyl Carrier Protein) Thioesters Reveal a Hydrophobic Binding Cavity that Can Expand to Fit Longer Substrates. *J. Mol. Biol. 365*, 135–145.

(67) Hanwell, M. D., Curtis, D. E., Lonie, D. C., Vandermeersch, T., Zurek, E., and Hutchison, G. R. (2012) Avogadro: an advanced semantic chemical editor, visualization, and analysis platform. *J. Cheminform. 4*, 17.

(68) Jurrus, E., Engel, D., Star, K., Monson, K., Brandi, J., Felberg, L. E., Brookes, D. H., Wilson, L., Chen, J., Liles, K., Chun, M., Li, P., Gohara, D. W., Dolinsky, T., Konecny, R., Koes, D. R., Nielsen, J. E., Head-Gordon, T., Geng, W., Krasny, R., Wei, G.-W., Holst, M. J., McCammon, J. A., and Baker, N. A. (2018) Improvements to the APBS biomolecular solvation software suite. *Protein Sci. 27*, 112–128.

(69) Myers, J., Grothaus, G., Narayanan, S., and Onufriev, A. (2006) A simple clustering algorithm can be accurate enough for use in calculations of pKs in macromolecules. *Proteins 63*, 928–938.

(70) Anandakrishnan, R., Aguilar, B., and Onufriev, A. V. (2012) H++ 3.0: automating pK prediction and the preparation of biomolecular structures for atomistic molecular modeling and simulations. *Nucleic Acids Res. 40*, 537–541.

(71) Maier, J. A., Martinez, C., Kasavajhala, K., Wickstrom, L., Hauser, K. E., and Simmerling, C. (2015) ff14SB: Improving the Accuracy of Protein Side Chain and Backbone Parameters from ff99SB. *J. Chem. Theory Comput. 11*, 3696–3713.

(72) Wang, J., Wolf, R. M., Caldwell, J. W., Kollman, P. A., and Case, D. A. (2004) Development and testing of a general amber force field. *J. Comput. Chem. 25*, 1157–1174.

(73) Wang, J., Wang, W., Kollman, P. A., and Case, D. A. (2006) Automatic atom type and bond type perception in molecular mechanical calculations. *J. Mol. Graph. Model. 25*, 247–260.

(74) Bayly, C. I., Cieplak, P., Cornell, W., and Kollman, P. A. (1993) A well-behaved electrostatic potential based method using charge restraints for deriving atomic charges: the RESP model. *J. Phys. Chem. 97*, 10269–10280.

(75) Jorgensen, W. L., Chandrasekhar, J., Madura, J. D., Impey, R. W., and Klein, M. L. (1983) Comparison of simple potential functions for simulating liquid water. *J. Chem. Phys. 79*, 926–935.

(76) Jatana, N., Jangid, S., Khare, G., Tyagi, A. K., and Latha, N. (2011) Molecular modeling studies of Fatty acyl-CoA synthetase (FadD13) from Mycobacterium tuberculosis--a potential target for the development of antitubercular drugs. *J. Mol. Model. 17*, 301–313.

(77) Darden, T., York, D., and Pedersen, L. (1993) Particle mesh Ewald: An N·log(N) method for Ewald sums in large systems. *J. Chem. Phys. 98*, 10089–10092.

(78) de Mendoza, D., and Cronan, J. E. (1983) Thermal regulation of membrane lipid fluidity in bacteria. *Trends Biochem. Sci. 8*, 49–52.

(79) Heath, R. J., and Rock, C. O. (1996) Roles of the FabA and FabZ β-Hydroxyacyl-Acyl Carrier Protein Dehydratases in *Escherichia coli* Fatty Acid Biosynthesis. *J. Biol. Chem. 271*, 27795–27801.

(80) Feng, Y., and Cronan, J. E. (2009) *Escherichia coli* Unsaturated Fatty Acid Synthesis: Complex Transcription of The fabA Gene and In Vivo Identification of The Eessential Reaction Catalyzed By FabB. *J. Biol. Chem. 284*, 29526–29535.

(81) Gottlieb, H. E., Kotlyar, V., and Nudelman, A. (1997) NMR Chemical Shifts of Common Laboratory Solvents as Trace Impurities. *J. Org. Chem. 62*, 7512–7515.

(82) Meier, J. L., and Burkart, M. D. (2009) Chapter 9. Synthetic probes for polyketide and nonribosomal peptide biosynthetic enzymes. *Methods Enzymol. 458*, 219–254.

Chapter 2, entitled Gating Mechanism of Elongating β-ketoacyl ACP Synthases, in full, is a reprint of the material as it appears in: Mindrebo JT*, Patel A*, Kim WE, Davis TD, Chen A, Bartholow TB, La Clair JJ, McCammon JA, Noel JP, Burkart MD. "Gating mechanism of elongating β-ketoacyl-ACP synthases", Nature Communications, vol. 11, 2020. The dissertation author is the primary co-author of this manuscript along with Dr. Ashay Patel.

Chapter 3: Activity Mapping the Acyl Carrier Protein - Elongating Ketosynthase Interaction in Fatty Acid Biosynthesis

Abstract

Elongating ketosynthases (KSs) catalyze carbon-carbon bond forming reactions during the committed step for each round of chain extension in both fatty acid synthases (FASs) and polyketide synthases (PKSs). A small α-helical acyl carrier protein (ACP) shuttles fatty acyl intermediates between enzyme active sites. To accomplish this task, ACP relies on a series of dynamic interactions with multiple partner enzymes of FAS and associated FAS-dependent pathways. Recent structures of the *Escherichia coli* FAS ACP, AcpP, in covalent complexes with its two cognate elongating KSs, FabF and FabB, provide high-resolution detail of these interfaces, but a systematic analysis of specific interfacial interactions responsible for stabilizing these complexes has not yet been undertaken. Here, we use site-directed mutagenesis with both *in vitro* and *in vivo* activity analyses to quantitatively evaluate these contacting surfaces between AcpP and FabF. We delineate the FabF interface into three interacting regions and demonstrate the effects of point mutants, double mutants, and region delete variants. Results from these analyses reveal a robust and modular FabF interface capable of tolerating seemingly critical interface mutations with only the deletion of entire regions significantly compromising activity. Structure and sequence analysis of FabF orthologs from related type II FAS pathways indicate significant conservation of type II FAS KS interface residues and, overall, support its delineation into interaction regions. These findings strengthen our mechanistic understanding of molecular recognition events between ACPs and FAS enzymes and provide a blueprint for engineering ACP-dependent biosynthetic pathways.

Introduction

Fatty acid biosynthesis (FAB) is a primary metabolic pathway in prokaryotes and eukaryotes, serving as a central biosynthetic hub for precursors utilized in membrane development and homeostasis, energy storage, cofactor biosynthesis, and signaling.[1–8] FAB involves the iterative condensation and reduction of two carbon acetyl-CoA derived units, with each round of chain elongation requiring four separate chemical reactions. (Figure 3.1a).[1,3] The first step of each cycle is carbon-carbon bond formation *via* a ketosynthase (KS) mediated Claisen-like condensation reaction between two ketide units to produce a β-keto intermediate. Subsequent reactions by the ketoreductase (KR), dehydratase (DH), and enoylreductase (ER) catalyze overall reduction of the β-position before another round of chain extension occurs. The central player in this process is the acyl carrier protein (ACP) that shuttles thioester-linked pathway intermediates to each respective enzyme active site.[9,10] The ACP is posttranslationally modified with a prosthetic 4'-phosphopantetheine arm (PPant) at a conserved serine residue that provides the free thiol moiety to ligate pathway intermediates via a thioester bond.[11] During ACP-mediated substrate delivery, productive protein-protein interactions (PPIs) between the ACP and partner enzymes are required.[10,12,13] The enzymatic activities and chemical transformations in fatty acid synthases (FAS) are generally conserved, but their structural organization can be separated into two classes. Metazoans and fungi possess large megasynthases with individual domains having distinct catalytic functions (type I FAS),[14–18] whereas bacterial and plant plastid FASs are expressed as discrete enzymes corresponding to specific genes (type II FAS).

The most studied of the type II FAS systems is the *Escherichia coli* FAS, which has provided much of our understanding of the mechanisms and structures of FAS.[2] In *E. coli*,

biosynthesis of a single fatty acid (FA) requires that the ACP, AcpP, interacts with five protein partners during each round of chain extension. Commonly, seven rounds of chain extension occur before the acyl chain is offloaded by an acyltransferase (Figure 3.1a). Therefore, PPIs in type II systems between the ACP and its partner enzymes (PEs) must be fast and dynamic to ensure efficient iteration of the biosynthetic cycle.[10] Over the past decade, a number of crystal structures of AcpP in complex with several PEs have been reported,[19–22] and in some cases facilitated by employing phosphopantetheinamide analogs designed to ensure mechanistically-compatible crosslinking [23–27] to covalently trap ACP-PE complexes.[28–32]

KSs catalyze the carbon-carbon bond forming reactions that commit substrates/intermediates for each round of chain extension during FAB. Furthermore, KS substrate specificity plays a central role in the FA profile of each organism.[33] The essential role of KSs in FAB also makes them attractive targets for the development of antimicrobials, such as platensimycin, a promising broad-spectrum antibiotic.[34–38] *E. coli* FAS utilizes three KSs, FabB, FabF, and FabH, two elongating KSs and an initiating KS, respectively.[1,39–41] FabH initiates *E. coli* FAB by condensing acetyl-CoA with malonyl-AcpP, while all subsequent rounds of carbon-carbon bond formation are catalyzed by the elongating KSs, FabF and FabB, using only AcpP-tethered substrates (Figure 3.1).[1,10] FabF and FabB have similar substrate preferences[39,42], but early work by Vagelos, Cronan, and Rock demonstrated that FabB is required for the *de novo* production of essential unsaturated fatty acids (UFAs).[43,44] FabF plays an important role in homeoviscous adaptation by increasing levels of *cis*-vaccenate-containing lipids in the *E. coli* plasma membrane in response to reductions

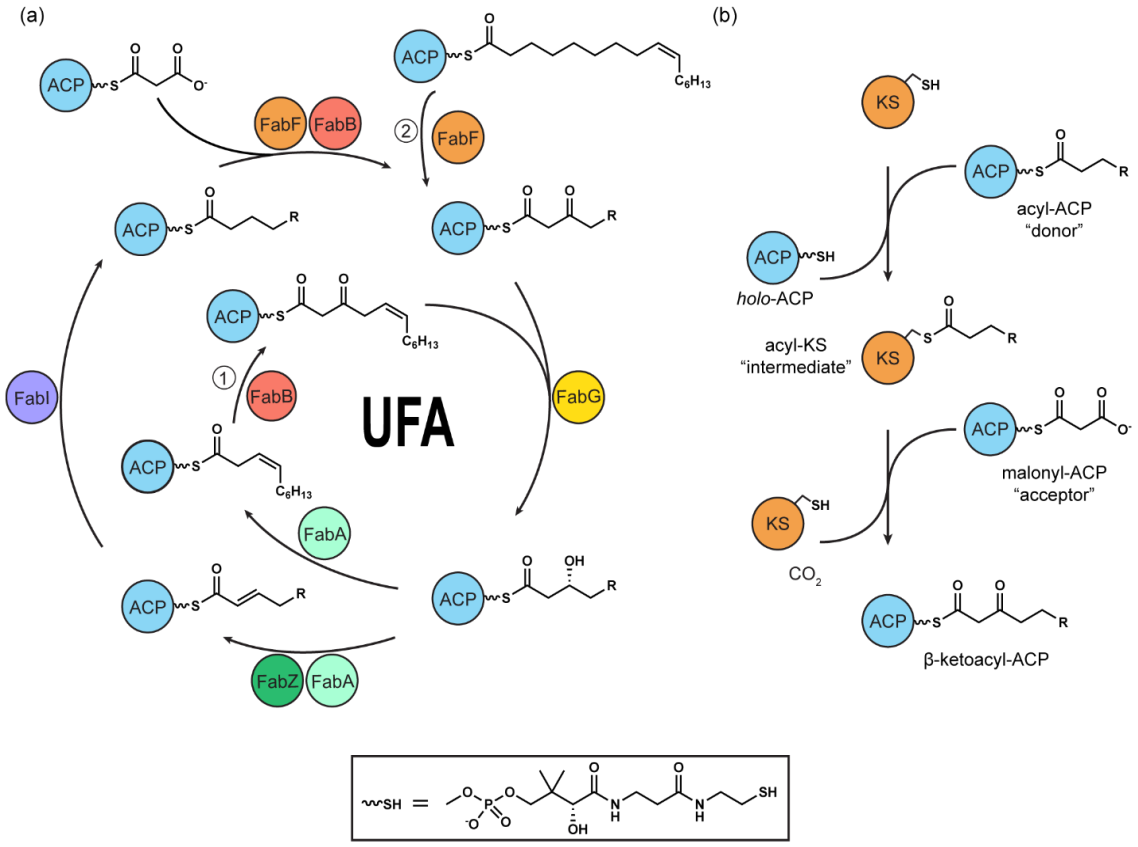

Figure 3.1: (a) *1coli* focusing on the elongating KSs, FabF and FabB, and their roles in specific FAS branchpoints. For clarity, FabD-dependent production of malonyl-AcpP, cycle initiation by FabH, and PlsB/PlsC mediated chain offloading are not shown. FabA/FabB dependent branchpoint ① is responsible for the *de novo* production of unsaturated fatty acids (UFAs). Branchpoint ② is mediated by FabF and is responsible for homeoviscous adaption due to changes in temperature via the extension of *cis*-palmitoleoyl-AcpP (C16:1) to produce *cis*-vaccenic acid (C18:1). Other enzymes from FAS are: FabG, the ketoreductase (KR), FabA and FabZ the dehydratases (DH), and FabI the enoyl-reductase (ER). **(b)** Ketosynthase ping-pong reaction overview.

in temperature (Figure 3.1a).[45–47] Despite these specialized roles in some cases, KSs share a two-step, ping-pong kinetic mechanism to condense malonyl-AcpP with acyl-AcpP (Figure 3.1b). In the first half-reaction, acyl-AcpP binds to the KS and delivers its thioester-bound cargo to the KS active site cysteine, producing an acyl-KS intermediate. In the second half-reaction, malonyl-AcpP binds to the KS and undergoes a decarboxylative Claisen-like condensation reaction with the acyl-KS intermediate, to produce a β-ketoacyl-AcpP (Figure 3.1b). During this process, the KS must undergo two separate ACP binding events and distinguish between similar, yet chemically distinct, AcpPs.

Recently, we crystallized FabF and FabB as covalent complexes with AcpPs bearing reactive fatty acyl mimetics. These structures have provided significant insight into KS-substrate recognition and AcpP-KS interactions.[29,31] The AcpP-KS interface can be delineated into three specific interacting regions, with two flanking regions comprised predominantly of electrostatic interactions and one central hydrophobic patch.[31] Here, we present thorough residue-by-residue and region-by-region analyses to quantify the formation of productive AcpP-KS interactions. We employed site-directed mutagenesis of the FabF interfacial residues and measured the *in vitro* and *in vivo* activities of these variants using three assays, two biochemical and one microbiological. Our results generally confirm the delineation of the AcpP-FabF interface into regions and reveal a robust interface tolerant of mutations. Additionally, we identify a catalytically important interface residue, Arg206 of FabF, that likely stabilizes the AcpP-FabF complex during chain flipping[48,49] of acyl chain cargo from the AcpP hydrophobic core into the FabF active site. These findings further advance our quantitative understanding of the role of PPIs during bacterial FAB that may guide future metabolic engineering efforts and antibiotic development.

- MATERIAL AND METHODS-

Protein expression and purification. All recombinant proteins tested *in vitro* were expressed and purified as previously described (Figure S3.1a).[31] Modifications on AcpP (holofication and acylation) were performed as previously described (Figure S3.1b).[50–53] Additional details are given in the associated Supplementary Information (SI).

Site directed mutagenesis. All FabF mutants were generated using the site-directed mutagenesis method developed by Liu and Naismith.[54] All constructs were verified via Sanger sequencing (Genewiz). Primers used for mutagenesis in this study can be found in Table S3.1.

FabF activity assay. The FabF assay mixture contained 50 mM sodium phosphate, pH 6.8, 50 mM NaCl, 0.5 mM TCEP, 250 μM malonyl-CoA, 10 μM C12-AcpP (wt) and 1 μM corresponding FabF (0 μM FabF for the control reaction) at 28 °C. 20 μL of each reaction was quenched by the addition of 10 μL of 0.3 % TFA (0.1% final TFA concentration) at 8 different time points to ensure accurate linear regression with at least 4 data points. Product formation was monitored by chromatographic separation using an Agilent 1100 series HPLC equipped with an Ascentis Express Peptide ES-18 column (15 cm* 4.6 mm, 2.7 μm) (Figure S3.2b), with a 1 mL/min flow rate and detection wavelength at 210 nm. A gradient method was used (A: ddH_2O with 0.1% (v/v) TFA; B: HPLC grade CH_3CN with 0.1% (v/v) TFA): 25% B, 0 min; 25% B, 2 min; 75% B, 12 min; 95% B, 13 min; 95% B, 15 min; 25% B, 17 min; 25% B, 20 min. *holo*-AcpP (2) concentrations were calculated from a standard curve (Figure S3.3b) and were used to determine initial reaction rates. C12-AcpP concentrations at 10 min were calculated using a standard curve (Figure S3.3a). Assays were conducted in triplicates.

FabF catalytic parameters. Approximations of K_M and k_{cat} values were determined by linear regression of Hanes-Woolf plots. Additional details are provided in the Supplementary Information (Figure S3.4).

In vivo FA profile assay. Whole cell *in vivo* Gas Chromatography Mass Spectrometry (GCMS) FA profile assays were conducted using a *fabF* knockout strain of *E. coli*, NRD23[55] graciously provided by John Cronan (UIUC) containing a chloramphenicol resistance marker to replace nucleotides 251-434. FabF was cloned into a pBAD322-kanamycin (KAN) vector[56] to afford an arabinose-inducible FabF cassette. $CaCl_2$ competent cells of NRD23 were transformed with the control plasmid, carrying wt FabF, or respective FabF mutants. Three individual colonies from each respective FabF construct were picked and grown overnight at 37° C. Individual 50 mL flasks containing Luria-Bertani broth (LB broth, Millipore-Sigma), 0.01% arabinose, and 0.05 mg/mL KAN were inoculated with 1 mL of each overnight culture, representing three biologically independent experiments for each FabF construct. Flasks were shaken at 250 rpm at 30° C until reaching an OD_{600} between 0.6 and 0.8. Three independent extractions of each 50 mL flask were performed by pelleting 6 mL of LB media in glass vials. The supernatant was removed, and the cells were resuspended in 1 mL of 1 M HCl in methanol and incubated at 55° C for 30 minutes in a Dri-block heater. Each sample was extracted using 1 mL of hexanes and analyzed on a Hewlett Packard HP6890 series GC system connected to a 5973 MSD quadrupole MS (EI) using helium as the carrier gas and a HP-5MS column. Five µl of sample were injected while the oven was held a 120 °C for three minutes followed by a gradient from 120 °C to 230 °C at 4 °C/min followed by 5 minutes at 230 °C. All compounds were verified using NIST library searches and the results were integrated using GC/MSD ChemStation software and the relative

percentages of each triplicate were averaged together (technical triplicates), to give one biologically independent reading. Three biologically independent readings were then averaged to produce the final reported values for each FabF construct.

Cy2450B fabB(Ts) ΔfabF competent cells. The *fabF* knockout Cy2450B line was originally produced by Cronan by crossing *E. coli* NRD23[55] with *fabB* temperature sensitive (Ts) using a Tn10 insertion with resistance for tetracycline. The resulting strain is a *fabF* knockout carrying a *fabB*(Ts) mutation. Therefore, Cy2450B contains only a single elongating KS, FabB(Ts), which is not functional at or above the non-permissive temperature of 42° C. $CaCl_2$ competent cells of Cy2540B were prepared by first inoculating a 5 mL overnight culture of LB broth containing 100 μM oleic acid, 0.5 % Brij58, 0.1 mg/mL streptomycin, and 0.05 mg/mL tetracycline at 27° C. Oleic acid and low temperature were used for overnight growth in order to limit the selective pressure for the formation of revertants. 100 mL of LB broth containing 100 μM oleic acid and 0.5 % Brij58 were inoculated with 1 mL of Cy2450B from the overnight culture and grown at 27° C until an OD_{600} of 0.5 was reached. Cells were then pelleted and resuspended in a cold solution of 50 mM $CaCl_2$ and 15% glycerol and incubated for 20 minutes on ice. The sample was again pelleted, supernatant was removed, and cells were resuspended in 2 mL of cold $CaCl_2$ solution and 1 mL of 80% glycerol. Competent cells were aliquoted, flash frozen in liquid nitrogen and stored at -80 °C.

Transformation of Cy2450B Cy2450B fabB(Ts) ΔfabF cells. In order to limit the number of revertants, Cy2450B cells were transformed with respective FabF constructs using a modified protocol, whereby after 42° C heat shock, cells were rescued using 500 μL LB media containing 100 μM oleic acid, 0.5 % Brij58, and incubated at 30° C for two hours.

Cells were plated on LB containing 100 μM oleic acid, 0.5 % Brij58, and 0.05 mg/mL KAN and incubated at room temperature for two days.

FabF in vivo complementation assay. Cy2450B competent cells were transformed (using the above protocol) with empty pBAD322-KAN vector (negative control), wt FabF (positive control), or FabF mutants. Cells were grown in either LB media, LB media with 100 μM oleic acid, or LB media with 100 μM oleic acid and 0.1% arabinose at both 37° C and 42° C (non-permissive temperature) for 24 hours. All cell lines grew at 37° C while growth at 42° C for FabF wt and FabF variants that complement FAB was only observed in the presence of arabinose and oleic acid. The OD_{600} of samples were taken the following day after 24 hours and compared to the OD_{600} of the pBAD322-KAN empty vector negative control. Cells that exhibited growth levels statistically different from the pBAD322-KAN negative control (p-value < 0.001) were classified as able to complement FAB.

Results

AcpP-FabF interface and mutation strategy. The x-ray structure of the AcpP-FabF covalent complex (PDB ID: 6OKG) reveals a small protein-protein interface of ~650 $Å^2$ buried surface area dominated by electrostatic interactions between a positive patch on FabF and the negatively charged AcpP (Figure 3.2).[31] The interface of the AcpP-FabF complex can be delineated into three regions based on the spatial organization and nature of the interactions (electrostatic or hydrophobic) (Figure 3.2d). We used an alanine-scanning approach, whereby we introduced one to three FabF mutations for each region in order to evaluate their individual and collective effects on FabF activity and bacterial growth. The resulting panel of FabF mutants spans all individual interacting residues, double mutants for specific regions, and triple mutants that eliminate entire regions.

FabF activity. In *E. coli* FAS, both elongating KSs, FabF and FabB, catalyze the condensation of acyl-AcpPs (donors) and malonyl-AcpPs (acceptors) to produce β-ketoacyl-AcpP intermediates (Figure 3.1).[42,57] These AcpP-based reactions ensure FA biosynthesis rather than FA oxidation, the latter of which employs acyl-CoAs. However, FabF and FabB have been shown to accept CoA-based substrates, though with K_M values larger than for the corresponding AcpP-based substrates.[57,58] Using KS substrate promiscuity for CoA-based substrates, we used an HPLC-based assay (Figure S3.2) using malonyl-CoA (acceptor) and C12-AcpP (donor) to interrogate FabF residues identified at the interface between AcpP and FabF (Figure 3.2). By monitoring the formation of *holo*-AcpP, we were able to determine the reaction rates of wt FabF and 11 FabF mutants (Figure 3.3, bar graph). C12-AcpP is fully converted to *holo*-AcpP by FabF wt after 10 min (Figure S3.2b). By analyzing the unreacted C12-AcpP at t = 10 min, we also correlated the reaction rate catalyzed by each FabF to the completion of the corresponding reaction (Figure 3.3, dots). Overall, introducing single point mutations at the FabF-AcpP interface does not significantly reduce the condensation reaction rates with one exception, as the variants K65A, R68A, K128A, S130A and F132A are at least half as fast (1.37, 1.20, 2.34, 1.69 and 2.72 min^{-1} respectively) as wt

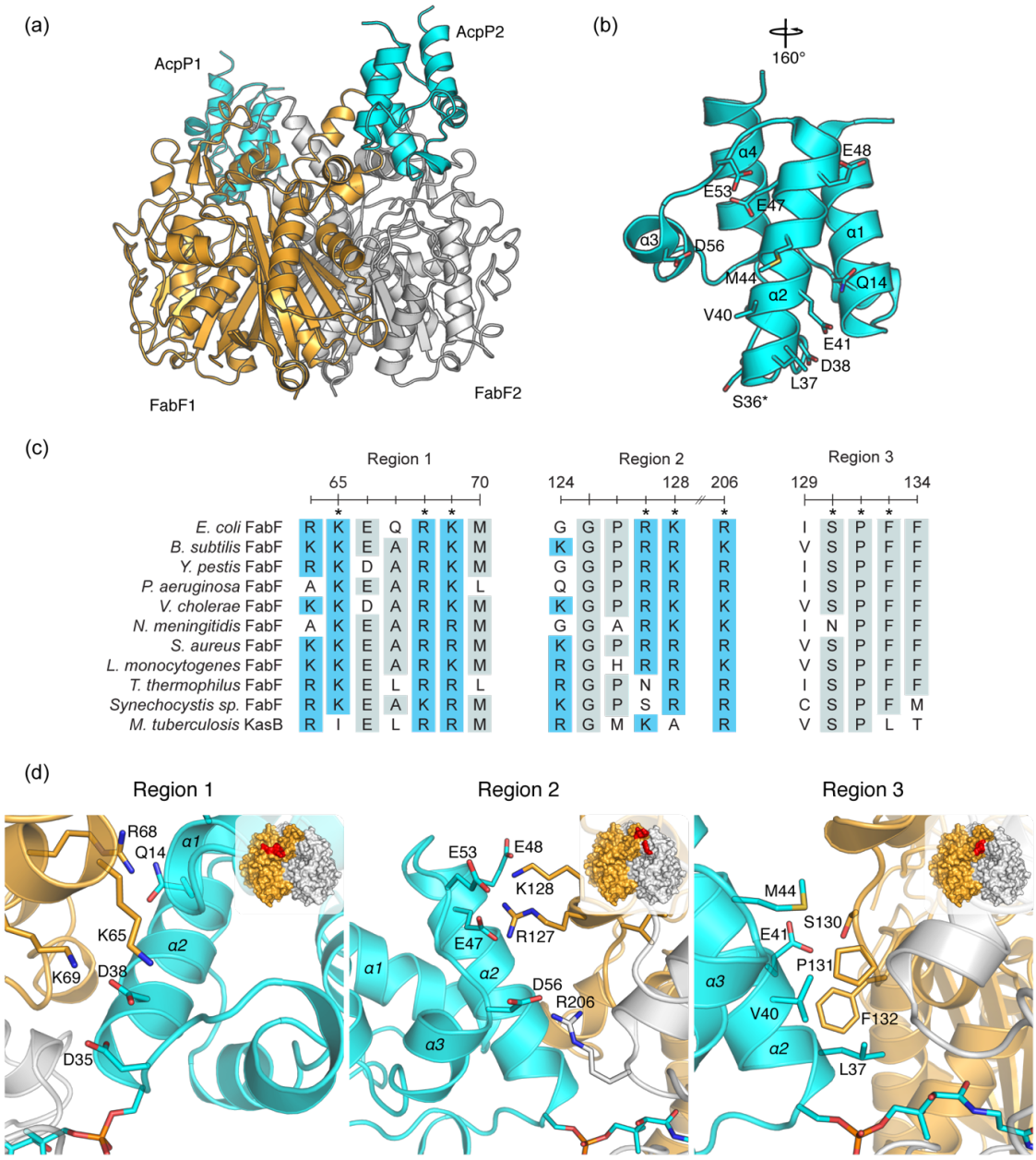

Figure 3.2: *Overview of AcpP-FabF Crosslinked complex, interface, and conservation*. **a)** Overview of AcpP-FabF crosslinked complex (PDB ID: 6OKG) showing a FabF dimer (orange and white) crosslinked to two AcpP monomers (cyan). **b)** 4-helical AcpP monomer with all residues that form interface interactions with FabF shown as sticks. The conserved serine residue that serves as the attachment site for the posttranslationally installed PPant arm is marked with an asterisk (*)**. c)** Sequence alignment of *E. coli* FabF with FabF orthologs demonstrating the conservation of regions 1, 2, and 3 of the FabF interface. Positions marked with an asterisk (*) interact with AcpP in the AcpP-FabF crosslinked structure (PDB ID: 6OKG). Residues above an identity threshold of 60% are highlighted in gray, and all positively charged residues are highlighted in blue. **d)** Interactions between AcpP and FabF shown at regions 1, 2, and 3 of the FabF interface. A cartoon inset is provided at the top right of each corner and the corresponding interface region is colored in red on the surface representation of FabF.

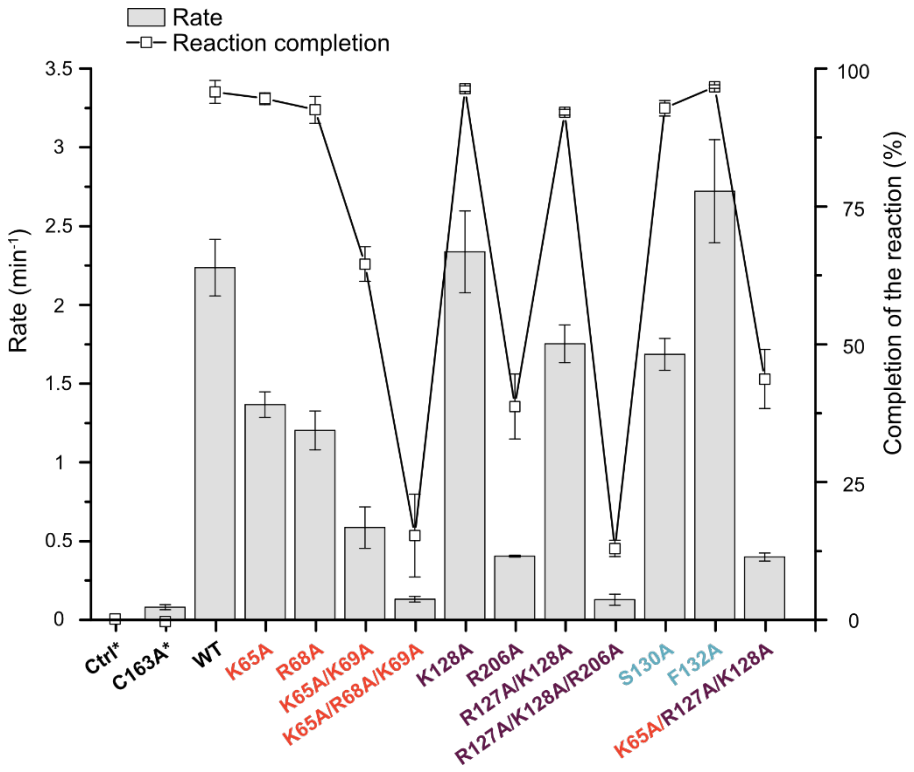

Figure 3.3: *1 FabF.* Reaction conditions: 28 °C, 50 mM phosphate pH 6.8, 50 mM NaCl, 0.5 mM TCEP, 250 µM malonyl-CoA, 10 µM C12-AcpP and 1 µM corresponding FabF ("Ctrl" corresponds to the reaction in the absence of FabF). The completion of each reaction (0-100%) was determined after 10 min reaction time by analyzing the remaining C12-AcpP (the asterisk (*) indicates that no detectable amount of C12-AcpP was consumed after 10 min). Region 1, 2, and 3 interface mutants are indicated in dark orange, deep purple, and blue, respectively. Each reaction was run in biological triplicate and the error bars indicate the standard deviation on the mean of the three measurements.

FabF (2.24 min^{-1}). However, R206A is six- and 2.72 min^{-1} respectively) as wt FabF (2.24 min^{-1}). However, R206A is six-times slower than wt (0.41min^{-1}). Both double mutants K65A/K69A (0.59 min^{-1}) and R127A/K128A (1.75 min^{-1}) are slower than the tested single mutants from the corresponding region. The region 1 and 2 delete variants, K65A/R68A/K69A and R127A/K128A/R206A, are both 17 times slower than wt (0.13 min^{-1}), while K65A/R127A/K128A , which combines mutations from both regions, is three times faster than either region delete variant (0.40 min^{-1}).The analysis of the reaction completion corroborates the kinetics results with 5 of the 6 tested single mutants (except R206A with 39% completion) and R127A/K128A fully converting C12-AcpP into *holo*-AcpP after 10 min, whereas variants K65A/K69A, K65A/R68A/K69A, R127A/K128A/R206A and K65A/R127A/K128A only partially completed the reaction (65%, 15%, 13% and 44%, respectively).

Because R206A demonstrated the largest negative effect on FabF activity of any single-point mutation, we expanded the mutational analysis of R206 to include an Asn substitution and determined the apparent catalytic parameters of the R206A/N variants and compared them to FabF wt and single variants from the electrophilic regions 1 and 2 (Table 3.1). While the decrease in catalytic efficiencies of K65A, R68A and K128A mainly results from an increase in their respective $K_{M\ app}$ values, mutating Arg206 to alanine seems to have a minimal effect on the affinity for C12-AcpP, as the $K_{M\ app}$ value is similar to that of wt FabF. Interestingly, the five-fold drop in overall catalytic efficiency of R206A is directly linked to an equivalent reduction in turnover number. This effect is observed as well when Arg206 is substituted with a polar residue. These results suggest a potential role for Arg206 in FabF catalysis rather than for AcpP recognition.

Table 3.1: *Apparent catalytic parameters of FabF wt and single variants from electrostatic regions*. Reaction conditions: 28 °C, 50 mM sodium phosphate, pH 6.8, 50 mM NaCl, 0.5 mM TCEP, 250 µM malonyl-CoA, 2.5-15 µM C12-AcpP and 1 µM corresponding FabF. Apparent catalytic parameters were determined using a linear regression from Hanes-Woolf plots (Figure S3.4). Experiments were run in triplicate, and data shown are reported as mean ± standard error. * % efficiency is in respect to kcat app/KM app of FabF wt.

FabF	$k_{cat\ app}$ (min^{-1})	$K_{M\ app}$ (µM)	$k_{cat\ app}/K_{M\ app}$ ($sec^{-1}.M^{-1}$)	efficiency (%)*
wt	2.23 ± 0.08	1.9 ± 0.3	$2.0.\ 10^4$	100
K65A	1.91 ± 0.58	7.7 ± 0.4	$4.1.\ 10^3$	21
R68A	1.26 ± 0.31	13.6 ± 2.9	$1.5.\ 10^3$	8
K128A	2.15 ± 0.15	5.2 ± 0.6	$6.9.\ 10^3$	35
R206A	0.36 ± 0.04	1.8 ± 0.8	$3.3.\ 10^3$	17
R206N	0.58 ± 0.03	2.9 ± 0.4	$3.4.\ 10^3$	17

Fatty acid profiles of FabF mutants. To determine how mutations to the FabF interface affect activity *in vivo*, we took advantage of FabF's unique capacity to elongate palmitoleoyl-AcpP (C16:1) to *cis*-vaccenoyl-AcpP (C18:1) (Figure 3.1a).[59] FabB performs all essential condensation reactions in *E. coli;* however, it does not produce appreciable quantities of C18:1. Therefore, we reasoned an *E. coli* cell line carrying a *fabF* knockout would present a FA profile with only trace C18:1 levels, allowing us to complement this cell line with wt *fabF* or *fabF* mutants and use C18:1 production as a biomarker for *in vivo* enzyme activity. To test this hypothesis, we utilized an *E. coli* Δ*fabF* cell line, NRD23[55], from John Cronan (UIUC) and benchmarked its FA profile for C18:1 production via whole cell, FA methyl ester (FAME) analyses by GCMS. The FA profile of NRD23 grown at 30 °C consisted of appreciable amounts of C16:0 and C16:1, 40.9% and 51.1% respectively, but only 2.3% C18:1 (Figure 3.4). In contrast, previous studies report a FA profile comprised of 30% C18:1 in assays conducted at 30 °C with the *E. coli* strain, CY320, carrying wt *fabF*.[46]

In order to complement the Δ*fabF* strain, we cloned *wt fabF* into pBAD322, an arabinose inducible protein expression vector designed for *E. coli* FAB complementation assays.[56] NRD23 was then transformed with either empty pBAD322 vector or pBAD322-*fabF,* and the resulting FA profiles were analyzed in the presence of arabinose to determine if an exogenously supplied *fabF* could restore C18:1 production. Indeed, our results show that induction of pBAD322-*fabF* restored the production of C18:1 and resulted in a FA profile of 35.1% C16:0, 15.8% C16:1, and 42.8% C18:1 (Figure 3.4). The C18:1 content in our FabF-induced NRD23 strain is higher than that of related wt background cell lines.[46] This result is likely due to higher FabF expression levels that result from pBAD promoter-driven expression rather than the native chromosomally regulated expression of *fabF*. The resulting

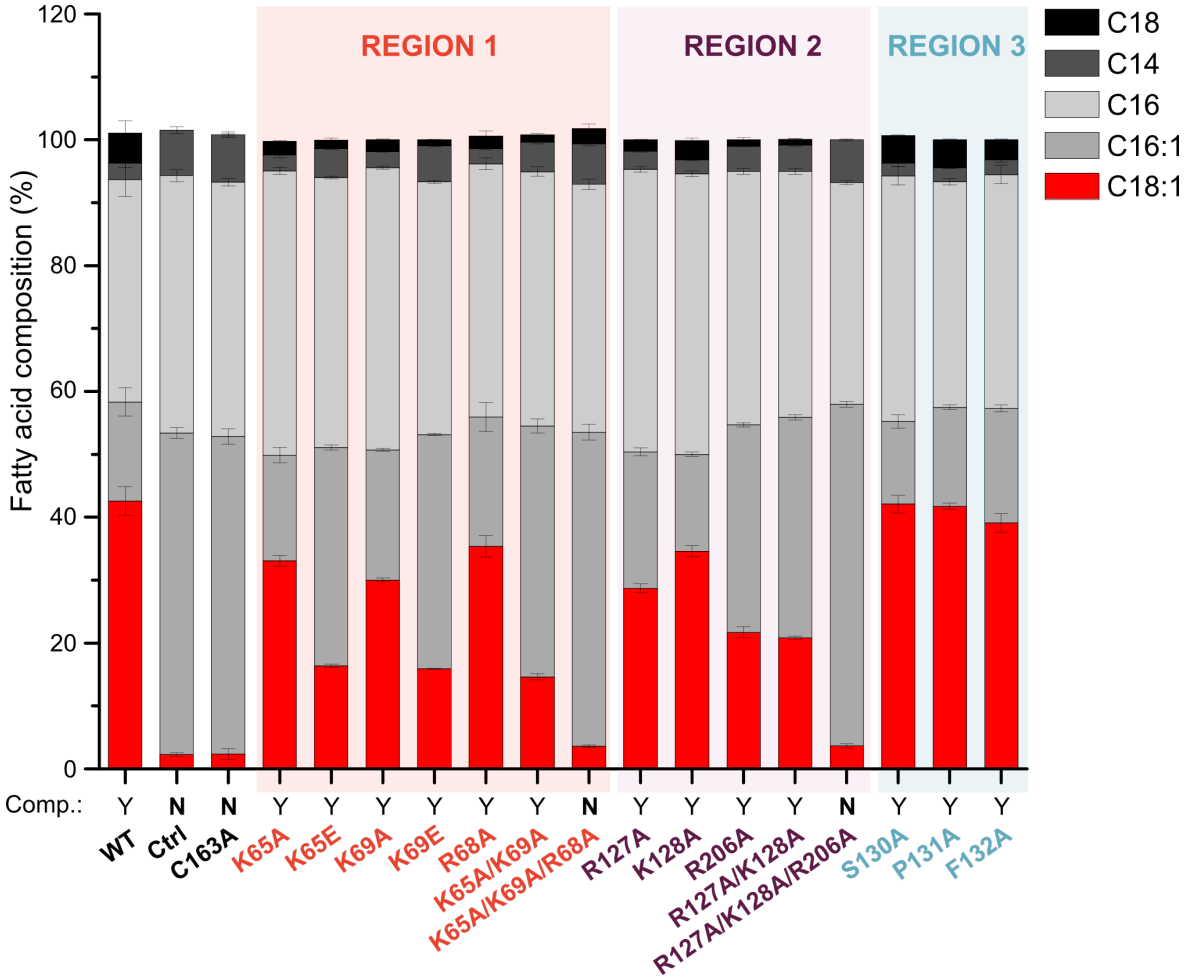

Figure 3.4: *In vivo GCMS profile and complementation assays of FabF interface mutants*. GCMS analysis of the FA profile of NRD23 Δ*fabF* strain complemented with expression of FabF interface mutants is shown in the bar chart. Total C18:1 percentage is an indicator of FabF *in vivo* activity and is shown in red. *In vivo* complementation assay results using the Cy2450B Δ*fabF*- *fabB*(Ts) cell line are shown below the corresponding FA profile for each mutant. FabF mutants that successfully complement FAB are assigned **Y** (yes) and those that do not are assigned **N** (no). See Table S3.2 for raw data and statistics. GCMS data are displayed as the average percentage of total FA content. All experiments were performed as biological independent experiments in triplicate (n=3). Error bars indicate the standard deviation on the mean.

FA profile is more similar to the *vtr* (vaccenate temperature regulation) strain of *E. coli*, CY322, which overproduces C18:1.[46] To further verify that the production of C18:1 was due to the induction of wt *fabF*, we generated a C163A catalytically inactive FabF mutant and assayed its FA profile. Results from the expression of FabF C163A mirrored that of the control vector and showed no production of C18:1.

We next analyzed the alterations in FA profiles of single, double, and triple mutants of the three FabF interface regions. Region 1 alanine mutants, K65A, K69A, and R68A, all showed similar changes in FA profiles, with C18:1 levels of 33.1%, 30.2%, and 35.4%, respectively, representing 22%, 29%, and 17% decreases in C18:1 content, respectively, as compared to wt FabF. To determine if the measured decreases in activities are related to charge loss at the interface, we prepared two charge-swapped mutants, K65E and K69E, and subjected them to the *in vivo* assay. Both K65E (16.4% C18:1) and K69E (15.9% C18:1) show significantly larger drops in C18:1 when compared to their alanine counterparts. In addition, the C18:1 levels in the charge-swapped mutants are similar to that of the double mutant K65A/K69A (14.6 % C18:1, which is a 69% drop from wt FabF levels). We next measured the FA profile of the region 1 delete mutant, K65A/R68A/K69A. The resulting FA profile is most similar to that of the negative control with 3.6% C18:1 content, representing a 92% drop from wt FabF levels.

Extending our analysis to FabF's region 2, we observed similarly modest changes to the FA profile for single point mutants, with C18:1 levels of 28.7% and 34.6% for R127A and K128A, respectively. However, the FA profile of the R206A point mutant is more significantly altered than all other single mutants tested, with C18:1 content of 21.7%, representing a 50% reduction compared to wt FabF. Analysis of the R127A/K128A (20.3%

C18:1) region 2 double mutant shows a generally comparable drop in activity as R206A. Given the retention of activity for all tested mutants of region 2, we analyzed the region 2 delete triple mutant, R127A/K128A/R206A. As seen for the region 1 delete, this mutant presents a similar FA profile to the pBAD322 negative control with a total C18:1 content of 3.7%.

We next examined the role of mutations of hydrophobic residues in region 3 of the FabF interface. Only point mutants for this region were tested and all mutants presented a FA profile similar to that of wt FabF. The FA profiles of S130A, P131A, and F132A contain 42.1%, 41.7%, and 39.1% C18:1, respectively. These results indicate that mutations of residues comprising FabF's hydrophobic patch to alanine are generally tolerated.

***In vivo* FAB complementation.** Results from both the *in vitro* and *in vivo* assays suggest that FabF can tolerate some mutational disruption of the AcpP-FabF binding surface with measurable diminutions of kinetic parameters and *in vivo* fatty acid profiles. We next asked whether the residual FabF activities of some mutants sufficiently support FAB to afford survival and proliferation. Temperature sensitive mutant strains of *E. coli* developed by Cronan and coworkers have been used extensively to genetically and biochemically evaluate the function of FAS enzymes and regulators.[41,55,60,61] John Cronan generously provided us with another *E. coli* strain (CY2450B) carrying a Δ*fabF* and temperature sensitive *fabB, fabB*(Ts). The resulting strain has only one functional elongating KS, FabB, which is incapable of performing essential FA chain extension reactions at non-permissive temperatures. CY2450 grows normally at 37 °C, but exhibits no growth at the non-permissive temperature, 42 °C. This growth arrest is due to an inadequate supply of specific FAs required for cell survival and proliferation at higher growth temperatures. Complementation of

CY2450B with an exogenously-supplied, functional KS restores normal cellular growth at 42 °C if the KS produces the necessary FAs at rates that maintain viable flux through FAB.

We developed and benchmarked our *in vivo* complementation assay by transforming CY2450B with either the empty pBAD322 or our pBAD322-*fabF* construct to determine if we could restore growth at the non-permissive temperature. This assay requires oleic acid-supplemented growth media, as FabB is essential for the *de novo* biosynthesis of UFAs, and FabF cannot perform this function (Figure 3.1).[43,44] Cell growth was restored at 42 °C in the presence of 0.1% arabinose and 100 μM oleic acid only when transformed with pBAD322-*fabF,* but not with the pBAD322 empty control vector or by expression of the catalytically inactive FabF C163A mutant gene (Figure 3.4). We then analyzed all of the interface mutants tested in our previous GCMS FA profiling studies to determine if they were capable of restoring *E. coli* growth at the non-permissive temperature. Interestingly, only the region 1 and region 2 delete mutants were incapable of maintaining cellular growth at 42 °C, while all other interface mutants were able to restore cell viability (Figure 3.4, Table S3.2). These results corroborate both the *in vitro* and *in vivo* assays and demonstrate that FabF interface mutations are relatively well tolerated and that complete removal of either region 1 or region 2 significantly compromises FabF's critical role in maintaining cell growth and division under less than ideal environmental conditions.

Discussion

A growing number of structures featuring AcpP in complex with PEs have recently become available, representing a significant advancement in our understanding of the complexity and diversity of AcpP-mediated PPIs.[19,20,28–31] Moreover, these high-resolution

structures, often accompanied by NMR studies and molecular dynamics (MD) simulations, provide a dynamic understanding of enzyme recognition of AcpP-tethered substrates. Despite these important advances, PPIs are complex mixtures of multiple points of interaction,[62,63] and only a few of these studies have evaluated the importance of specific interfacial interactions involving residues on either AcpP, the PE, or both to biosynthetic pathways *in vitro* and *in vivo*.[20,29,64]

In order to catalytically map the molecular details of AcpP-KS interactions and their importance for *E. coli* FAB, we developed a multi-tier mutational strategy to assess the importance of specific residues and regions that comprise the FabF interface and subjected these mutants to both *in vitro* and *in vivo* assays. Results from these studies demonstrate that introducing single alanine mutations at the AcpP-FabF interface often have minor effects on FabF activities. These results are generally consistent with a previous analysis of the AcpP-FabB interface showing that a single alanine mutation (D38A AcpP) only modifies the *in vivo* FA profile to a modest extent.[29] While the effects of alanine mutations are rather small, we still observe that mutations to the electrostatic regions 1 and 2 impact FabF activity more than mutations to the central hydrophobic region, emphasizing the dominant influence of electrostatics for AcpP binding. In addition, the *in vivo* activities of FabF for charge-deleted (Ala) and charge-swapped (Glu) mutants present significant differences, with the glutamate variants of region 1 producing half of the amount of C18:1 compared to their alanine counterparts. These results together indicate that the AcpP-FabF interface functions mainly through electrostatic complementarity between the acidic surface residues of AcpP and the basic residues of FabF.

However, unlike other point mutants, mutation of Arg206 to alanine resulted in a significant reduction in both *in vivo* and *in vitro* KS activity. Interestingly, Ye *et. al* have also identified Arg206 as an important residue in photo-crosslinking assays between AcpP and FabF.[65] The orientation of the guanidinium side chain of Arg206 in *apo*-FabF has been reported to inhibit CoA binding, and mutating this residue to glycine removes this steric clash and increases FabF's affinity for CoA-based substrates.[57] When we superimpose the structures of *apo*-FabF (PDB ID: 2GFW), C12-FabF (PDB ID: 2GFY) and AcpP-FabF (PDB ID: 6OKG), Arg206 undergoes a conformational change in the AcpP-FabF structure to provide an important interaction with helix III (α3) of AcpP (Figures S3.5,S3.6). AcpP's α3 is a dynamic helix that exhibits structural plasticity.[9,66–68] PPIs involving α3 have been proposed to facilitate substrate chain-flipping[49] from AcpP's hydrophobic core to the active site of PEs.[28,66,69–72] The crosslinked AcpP-FabA structure (PDB ID: 4KEH), along with NMR and MD data, suggest that chain-flipping is facilitated by FabA binding to AcpP's α3.[28] The significant drop in activity for R206A, both *in vitro* and *in vivo*, suggests a more specific function for Arg206. To test this hypothesis, we compared the effects on $k_{\text{cat app}}$ and $K_{\text{M app}}$ values of R206A/N with wt FabF and alanine variants of regions 1 and 2. We observed that, unlike for Lys65, Arg68, and Lys128, mutating Arg206 to alanine or asparagine only affects turnover number ($k_{\text{cat app}}$) and not $K_{\text{M app}}$. This result may also be due to a change in specificity for the non-natural malonyl-CoA substrate, but as noted above, replacing Arg206 with a small glycine residue results in a 10-fold decrease in K_{M} for CoA substrates instead of an increase. Taken together, these results suggest a potential role for Arg206 in catalysis rather than for AcpP binding, namely, to facilitate chain-flipping by acting as a wedge to stabilize α3 in a position suitable for substrate transfer to and from the KS active site. A close analysis

of the AcpP-FabF structure indicates that coordination between Arg206 and AcpP's α3 positions the hydrophobic portion of the arginine side chain in such a way that it could form a solvent protected path from the hydrophobic core of AcpP to the KS active site (Figure S3.6).

We analyzed the AcpP-FabF interface using combinations of double and triple mutations of FabF, focusing on the two electrophilic contact points, regions 1 and 2. Double mutants in regions 1 and 2 decrease *in vitro* FabF activity compared to single point mutants but still enable cell growth and proliferation *in vivo*. The substitution of three mutations within a region (region delete) leads to the expression of a modified FabF that cannot support FAB to levels necessary for *E. coli* growth. The activity of both FabF region delete mutants yield *in vivo* FA profiles that are similar to the profile of the catalytically inactive FabF mutant, C163A. Moreover, the *in vitro* reaction rates of these mutants are nearly 20 times slower than wt in the conditions tested. The region delete mutants result in the net removal of three interfacial interactions, leading to a net loss of three units of positive charge from the PPI. The *in vivo* and *in vitro* data indicate that there may be a correlation between charge and activity, but the triple variant K65A/R127A/K128A, which combines mutations from regions 1 and 2, remains three times more active than both region delete mutants *in vitro*. These results suggest that charge alone cannot completely explain the reduction in activity for region delete mutants. Taken together, our results suggest that the AcpP-FabF interface evolved in a modular fashion, where only the full disruption of a region leads to an inactive FabF. This concept has been previously discussed for larger protein-protein interfaces, and our study indicates that it may be applied for the small, dynamic interface between an ACP and a PE.[62,63]

To establish whether the delineation of the AcpP-FabF interface into specific regions can be broadly applied to elongating type II FAS KSs, we aligned and analyzed sequences and crystal structures from all FabF and FabB homologues currently available in the Protein Data Bank. This analysis shows that the primary sequences of type II FAS KSs, are quite conserved for regions 1, 2, and 3 (Figure 3.2c, S3.7-8). Some of these regions contain one additional or fewer positively charged residue, or their positions vary slightly in the primary sequences, but their relative placements in interaction regions appears to hold. Alignments of region 2 show that Arg127 or Lys128 can vary slightly in their respective primary sequences, but their relative placements in interaction regions appears to hold. Alignments of region 2 show that Arg127 or Lys128 can be functionally substituted into an earlier position, namely position 124 (FabF numbering), and still maintain the spatial positioning at the interface to be defined within that region (Figures 3.2c,3.5). Similarly, Arg206, which is a conserved basic residue among FabF orthologs, is not present in FabB (Figure 3.5). Instead, FabB possesses Arg45, that, while in a different position in primary sequence, maintains the same relative spatial positioning at the PPI (Figures 3.5, S3.8). In the crosslinked AcpP-FabB structure, FabB's Arg45 engages Asp56 on α3 of AcpP in a manner similar to that of Arg206 from FabF. Therefore, Arg45 likely plays an important role in AcpP mediated cargo delivery to FabB's active site.[29] Type II FAS KSs are known to be viable targets for antibiotic-based inhibition, as shown by the discovery and development of platensimycin.[36,37] The conserved nature of type II FAS KS interfaces may provide an alternative strategy for targeting the KS, namely through the development of PPI inhibitors designed to disrupt the AcpP binding site.[73–75]

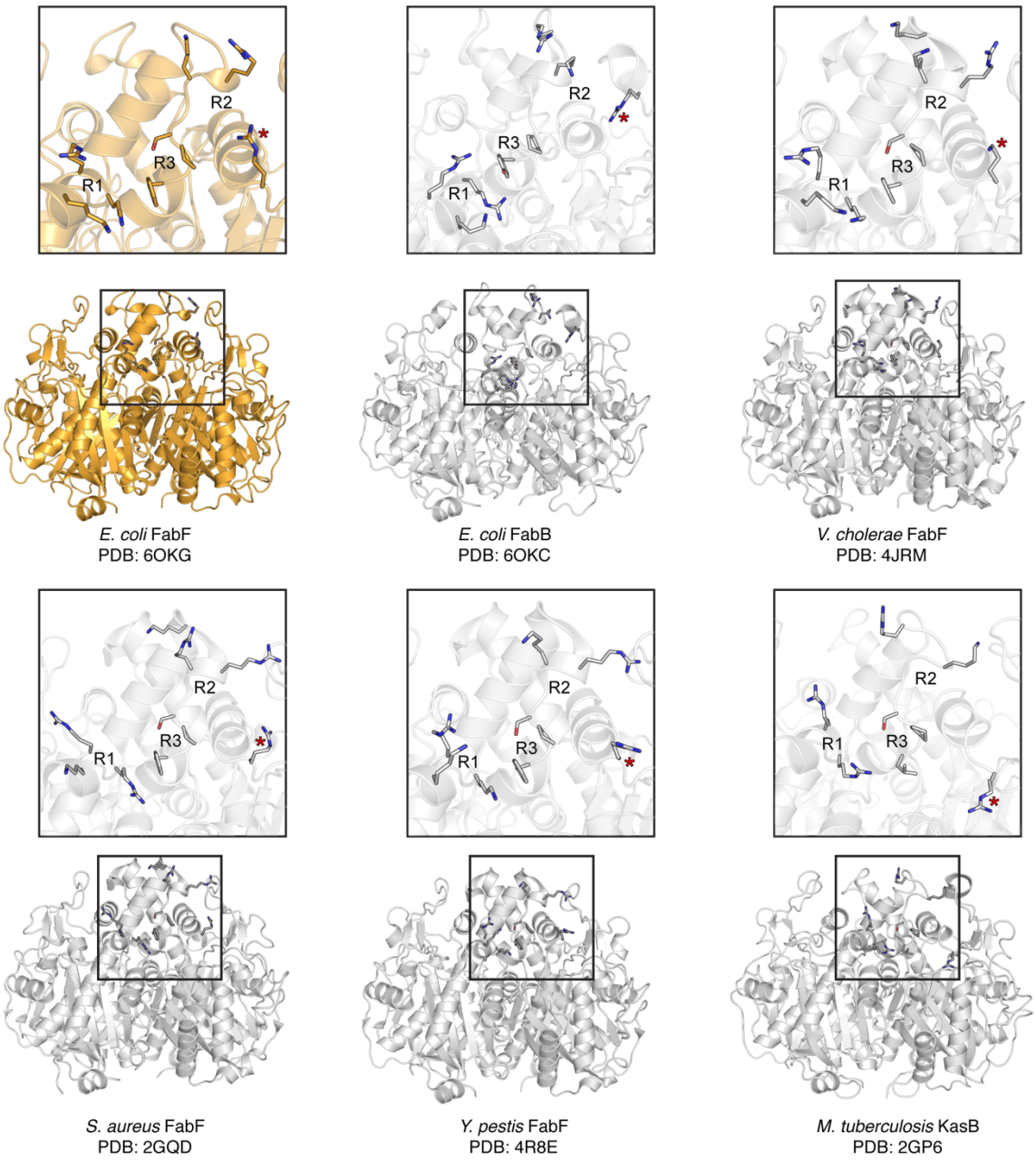

Figure 3.5: *Comparison of E. coli FabF interface residues with that of E. coli FabB and four FabF orthologs from pathogenic organisms.* The overall architecture of the elongating KS interfaces is generally conserved in sequence (Figure 3.2c) and in space with regions 1 and 2 consisting of between two and four positive residues, while region 3 is generally conserved in all FabF orthologues. Residues marked with a red asterisk (*) are found in a similar position, in space or in sequence, as Arg206 in FabF. A more complete structural comparison of the *E. coli* AcpP-FabF interface residues with other FabF orthologues, FabB homologues, and type II PKSs is provided in Figures S3.6, S3.7 and S3.10.

Given that FabF is considered the evolutionary progenitor of the KS domains found in type II PKSs,[76,77] we aligned and compared the AcpP-FabF complex to the recently published crosslinked ishigamide ACP-KS/CLF (chain length factor) complex (Iga10-Iga11/Iga12),[78] to determine what, if any, elements remain from the type II FAS PPI recognition motifs. A general overview of the two complexes shows that AcpP and Iga10 (igaACP) engage their respective KSs at the same binding interface, but igaACP is rotated with respect to AcpP in the AcpP-FabF structure (Figure S3.9). The twisted binding mode of igaACP leads to a change in the position of α2 and α3, which results in notable differences in the interfacial interactions that stabilize these two complexes. While region 1 of the ishigamide KS/CLF (igaKS/CLF) interface shares some similarities with FabF, regions 2 and 3 have diverged significantly to yield a unique set of interactions specific for igaACP (Figure S3.10). The igaKS/CLF region 2/3 interactions consist of a complex network of charged, polar, and hydrophobic residues that bury a salt bridge between Arg210 of igaKS/CLF and Glu51 of igaACP (Figure S3.10). Removal of this buried salt bridge via mutation of Arg210 to alanine results in complete loss of product formation, indicating that this interaction network is important for complex formation and specificity. Analysis of the putative ACP binding site on the aryl polyene synthase KS/CLF[79] and the ACP binding mode in the recently published antF-antD/antE ACP-KS/CLF (antACP-antKS/CLF) complex[80] from the anthraquinone biosynthetic pathway also indicates an evolutionary divergence from the conserved interface interactions seen in type II FAS KSs (Figure S3.11). Region 1 of the antKS/CLF ACP binding interface is similar to that of FabF with three positive residues (Arg61, Arg64, and Arg65) coordinating with acidic and polar residues located at the bottom and top of antF (antACP) α 1 and 2, respectively (Figure S3.12a). On the contrary, the α 3

interaction coordinated by Asp56 in AcpP is replaced by Lys58 in antACP, which docks into a polar pocket on the antKS/CLF interface found in a similar location as Arg206 in FabF (Figure S3.12b). It is not surprising to find that type II FAS and PKS KSs have different interfacial interactions with their respective ACPs, as PPIs provide an elegant way to separate primary and secondary metabolic pathways in non-compartmentalized cells by discouraging pathway crosstalk.[10] For example, the *S. coelicolor* type II FAS ACP is known to be a poor substrate for its own endogenous actinorhodin type II PKS KS/CLF.[81] The substitution of positive regions for acidic or hydrophobic regions, or for even more complex interaction networks as seen in igaKS-CLF, represents a plausible evolutionary solution to creating orthogonal pathways with internal complementarity.

There is considerable interest in manipulating PPIs as a strategy for combinatorial and metabolic engineering efforts.[82–85] The availability of both the AcpP-FabF[31] and AcpP-FabB[29,31] crosslinked structures, along with the characterization of the FabF interface reported herein, provide new insights into PPI-based engineering efforts. Grininger and coworkers have successfully shown the potential of engineering KS substrate specificity and PPIs to modify the yeast FAS profile for custom biosynthesis.[86–89] Favoring or disfavoring ACP-KS interactions by introducing mutations at the KS interface can modify chain lengths of FAs produced by the yeast FAS, although these mutants often have diminished overall enzyme activity.[89] Similarly, Milligan et *al.* showed that expression of an AcpP D38A mutant resulted in a general reduction in the total number of UFAs in *E. coli*.[29] While this study shows that mutating the AcpP interface can result in changes in the FA profile, AcpP interacts with multiple binding partners (Figure 3.1a), and any changes to the AcpP structure will likely affect associations with other PEs. The work reported herein provides an approach to

manipulating type II FAS FA profiles, similar to that implemented with the yeast FAS,[89] whereby mutation of the PE interface can selectively effect outcome of the reaction of interest. However, reductions in overall activity and flux through the FAS pathway may be a concern for implementing such a strategy. Nevertheless, mutations at the AcpP-FabF interface are well tolerated by *E. coli,* and only region delete mutations are unable to complement FAB. Therefore, KS interface mutations may serve as a viable approach to increasing the available pool of intermediate chain length acyl-ACPs for premature offloading or redirection into engineered pathways.

Conclusion

In this study we applied an *in vitro* and two *in vivo* biochemical assays to systematically interrogate all interacting residues present in the recently published AcpP-FabF crosslinked crystal structure. The *in vitro* assay provided activity relationships and apparent kinetic parameters of different FabF interface mutants, while the two *in vivo* assays took advantage of KS-mediated FAS pathway branchpoints to provide a functional readout of these FabF variants. Results from these studies reveal a robust and modular FabF interface dominated by electrostatic interactions and generally support its delineation into three interacting regions. Point mutants had a minimal effect on FabF activity both *in vitro* and *in vivo*, with the exception of Arg206, which we propose to be a catalytically relevant interface residue that stabilizes AcpP's α3 during chain-flipping events. Only the complete deletion of either electrophilic regions 1 or 2 resulted in a FabF variant that cannot sustain turnover rates capable of supporting cell survival. Sequence and structural comparison of FabF orthologs indicate that the type II FAS KS interface is generally conserved. However, the putative

interfaces of KS domains found in type II PKSs have diverged, which likely serves as an evolutionary mechanism to maintain pathway orthogonality between primary and secondary metabolism in non-compartmentalized cells. The results reported herein provide a deeper, fundamental understanding of PPIs in type II FAS and provide a general roadmap for those seeking to engineer KS interface interactions.

Supplementary Information

A. Supplementary Biological Protocols

A1. Expression and purification of FabF (wt and mutants) and AcpP wt. The genes encoding for FabF and AcpP were inserted in a pET28b vector with a cleavable N-terminal His_6-tag. The proteins (wt and variants) were expressed in *E. coli* BL21(DE3) cells. For each variant, a single colony was selected on the agar plate and grown overnight at 37 °C in 5 ml Luria-Bertani (LB) medium supplemented with 50 µg/ml kanamycin (KAN). Then, 1 L of LB medium (50 µg/mL KAN) was inoculated with the 5 mL-LB preculture and incubated at 37 °C until an optical cell density of 0.7 was reached. After induction with 0.5 mM IPTG, cells were grown for 3 h at 37 °C. Cells were harvested by centrifugation (500 RCF, 30 min) and the pellet was stored at – 20 °C. Cells were resuspended in lysis buffer (50 mM Tris pH 8.0; 300 mM NaCl; 10 % glycerol) and lysed by sonication. After centrifugation (17.400 RCF, 45 min), the supernatant was transferred to Ni-NTA-column and washed with 10 CV of lysis buffer and 2 x 10 mL lysis buffer containing 10 mM imidazole. The proteins were eluted with elution buffer (lysis buffer containing 250 mM imidazole). All FabF variants expressed with yields comparable to the wt (15 ± 5 mg of protein / L of LB). FabF wt and variants were dialyzed twice over 1 L of dialysis buffer at 4 °C (50 mM sodium phosphate pH 6.8, 150 mM NaCl, 0.5 mM TCEP and 10 % glycerol), aliquoted, frozen in liquid nitrogen and stored at -80 °C (Figure S3a). AcpP wt (expressed as a mixture of *apo*- and *holo*- forms) was subjected to His_6-tag cleavage by thrombin and the resulting His_6-tag free AcpP was purified using Ni-NTA-column supplemented with Benzamidine Separophore (bioWorld). The resulting *apo*-/*holo*-AcpP was then converted to its *holo* form.

A2. AcpP holofication. *holo*-AcpP was prepared as previously described.[50] Briefly, AcpP (*apo*/*holo*) was incubated at 37 °C overnight in the presence of the phosphopantetheinyl transferase Sfp from *Bacillus subtilis*. Final reaction concentrations were the following: 50 mM sodium phosphate pH 6.8, 50 mM NaCl, 0.5 mM TCEP, 12.5 mM $MgCl_2$, 1 mM coenzyme A, 0.05 mg/mL Sfp and 2.2 mg/mL AcpP. The completion of the reaction was determined by urea PAGE (Figure S1b).[90] The resulting *holo*-AcpP was further purified on a Superdex 75 HiLoad 16/60 size exclusion chromatography (SEC) column equilibrated with buffer (50 mM Tris pH 8, 50 mM NaCl, 5 % (v/v) glycerol, 0.5 mM TCEP). The eluted *holo*-AcpP was collected and concentrated using Amicon Ultra Centrifuge Filters (Millipore) with 3 kDa molecular weight cut off, then converted to its acyl form.

A3. *holo*-AcpP acylation. C12-AcpP was prepared as previously described.[51-53] Briefly, *holo*-AcpP was incubated for 3h at 37 °C in the presence of lauric acid and the acyl ACP-synthetase AasS from *Vibrio harveyi*. Final reaction concentrations were the following: 50 mM Tris pH 8, 50 mM NaCl, 0.5 mM TCEP, 12.5 mM $MgCl_2$, 2 mM lauric acid (prepared fresh in EtOH), 0.02 mg/mL AasS and 0.75 mg/mL *holo*-AcpP. The completion of the reaction was determined by urea PAGE (Figure S1b).[90] The resulting C12-AcpP was further purified on a Superdex 75 HiLoad 16/60 size exclusion chromatography (SEC) column equilibrated with buffer (50 mM sodium phosphate pH 6.8, 125 mM NaCl, 5 % (v/v) glycerol, 0.5 mM TCEP). The eluted C12-AcpP was collected, concentrated using Amicon Ultra Centrifuge Filters (Millipore) with 3 kDa molecular weight cut off, frozen in liquid nitrogen and stored at -80 °C.

A4. Analysis of kinetic data. Kinetic data were analyzed with Origin software. Data points from 10 s to 10 min were fitted by linear regression to give the initial velocity of substrate turnover.

A5. Hanes-Woolf plots. $1/k_{cat\ app}$ and $K_{M\ app}/k_{cat\ app}$ were determined by standard linear regression of [C12-AcpP]/rate upon [C12-AcpP] (equation 1) The standard errors (SE) for $K_{M\ app}$ and $k_{cat\ app}$ were calculated using the equations 2 and 3, respectively.

$$\frac{[\text{C12-AcpP}]}{\text{rate}} = \frac{1}{\nu_{max}}[\text{C12-AcpP}] + \frac{K_M}{\nu_{max}} \quad \text{where } \nu_{max} = k_{cat} \text{ as [FabF] = 1 } \mu\text{M} \qquad \text{eq. 1}$$

$$SE\left(\frac{K_M}{k_{cat}}\right) = \frac{K_M}{k_{cat}}\sqrt{\left(\frac{SE\,(K_M)}{K_M}\right)^2 + \left(\frac{SE\,(k_{cat})}{k_{cat}}\right)^2} \qquad \text{eq. 2}$$

$$SE\left(\frac{1}{slope}\right) = SE\left(k_{cat}\right) = \frac{1}{slope}\left(\frac{SE\,(slope)}{slope}\right) \qquad \text{eq. 3}$$

B. Supplementary Figures and Tables

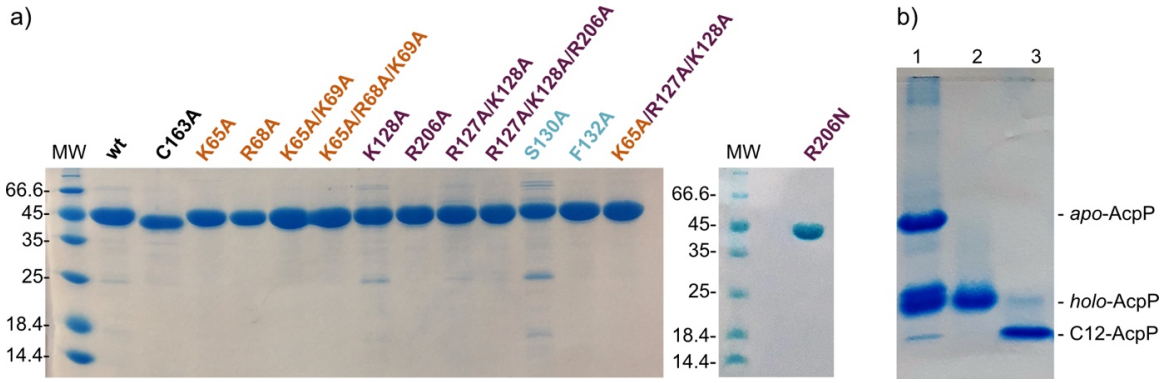

Figure S3.1: *FabF and AcpP purification and modification* **a)** 15% SDS PAGE (170 V, 1 h) of FabF wt and variants, **b)** 20 % Urea PAGE (170 V, 1h30) of AcpP after purification showing a mixture of apo- and holo-forms (1), after holofication (2) and after acylation (3)

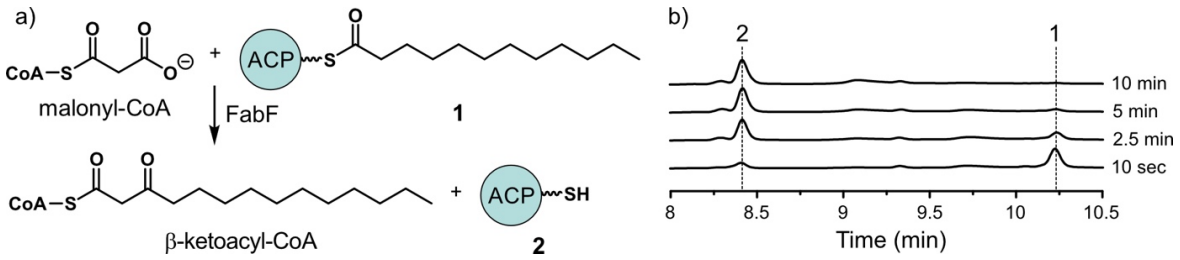

Figure S3.2: *HPLC-based ketosynthase assay.* **a)** Condensation of malonyl-CoA and C12-AcpP (1) catalyzed by FabF. β-ketoacyl-CoA (acyl-malonyl-CoA) and holo-AcpP (2) are the products of the reaction, **b)** FabF condensation reaction monitored by HPLC at λ= 210 nm. Reaction conditions for this example: 28 °C, phosphate pH 6.8 50 mM, NaCl 50 mM, TCEP 0.5 mM, malonyl-CoA 250 μM, (1) 10 μM and wt FabF 1 μM.

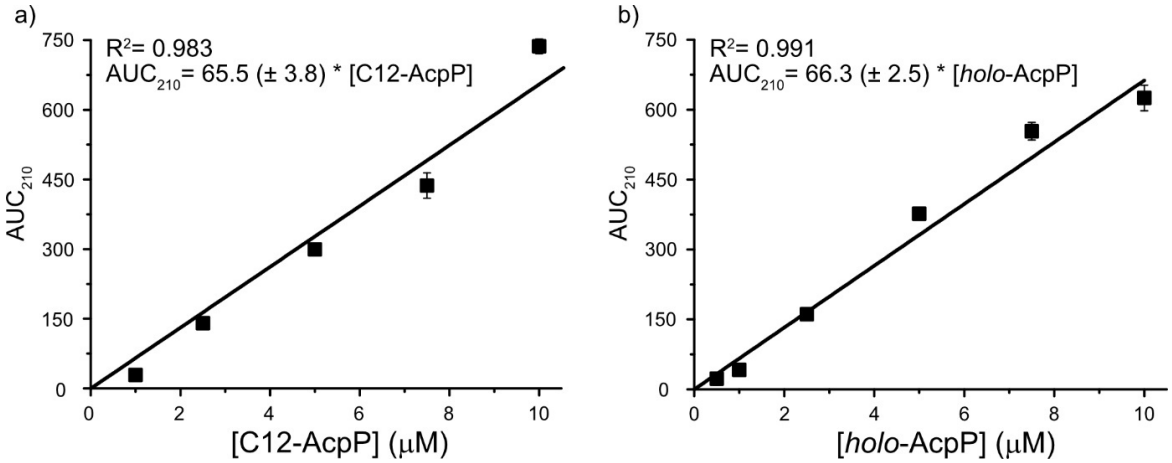

Figure S3.3: *HPLC calibration curves of C12-AcpP* (**a**) and holo-AcpP (**b**). Standards (0.5-10 μM) of C12-AcpP and holo-AcpP were injected three times and the corresponding area under the curve (AUC) at λ=210 nm were determined. The error bars represent the standard deviation of the mean of technical triplicates.

a

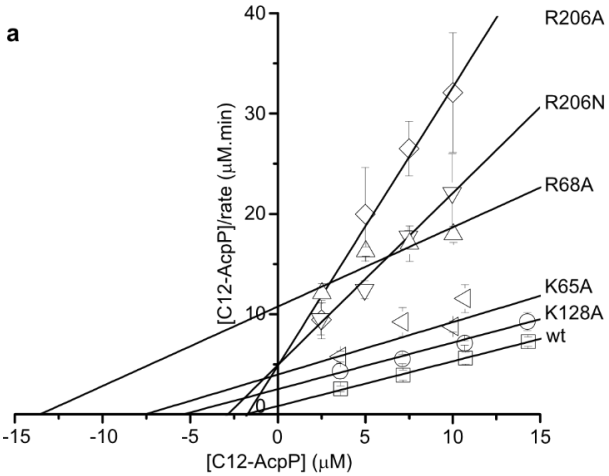

b

FabF	R^2	slope	intercept
wt	0.997	0.448 ± 0.015	0.844 ± 0.153
K128A	0.986	0.466 ± 0.032	2.404 ± 0.320
R206A	0.964	2.786 ± 0.308	5.043 ± 2.339
R206N	0.991	1.720 ± 0.090	4.956 ± 0.726
K65A	0.769	0.524 ± 0.158	4.036 ± 1.230
R68A	0.793	0.793 ± 0.196	10.775 ± 1.378

Figure S3.4: *Hanes-Woolf plots of wt FabF and single variants.* **a**) Graphical representation. The error bars represent the standard deviations of the means of biological triplicates **b**) parameters from the linear regression used to determine the k_{cat} and K_M values of each FabF. ± indicates the standard error on the parameters.

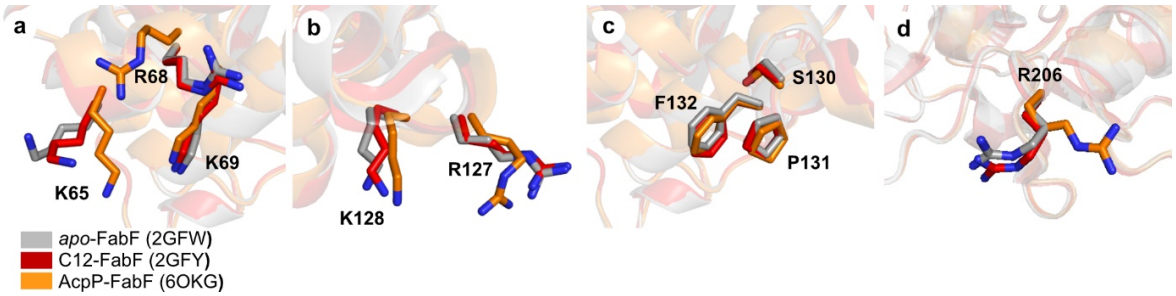

Figure S3.5: *Overlay of apo-FabF, C12-FabF and AcpP-FabF.* focusing on **a)** FabF interface residues of region 1, **b)** FabF interface residues of region 2, **c)** FabF interface residues of the hydrophobic region and **d)** R206 from region 2.

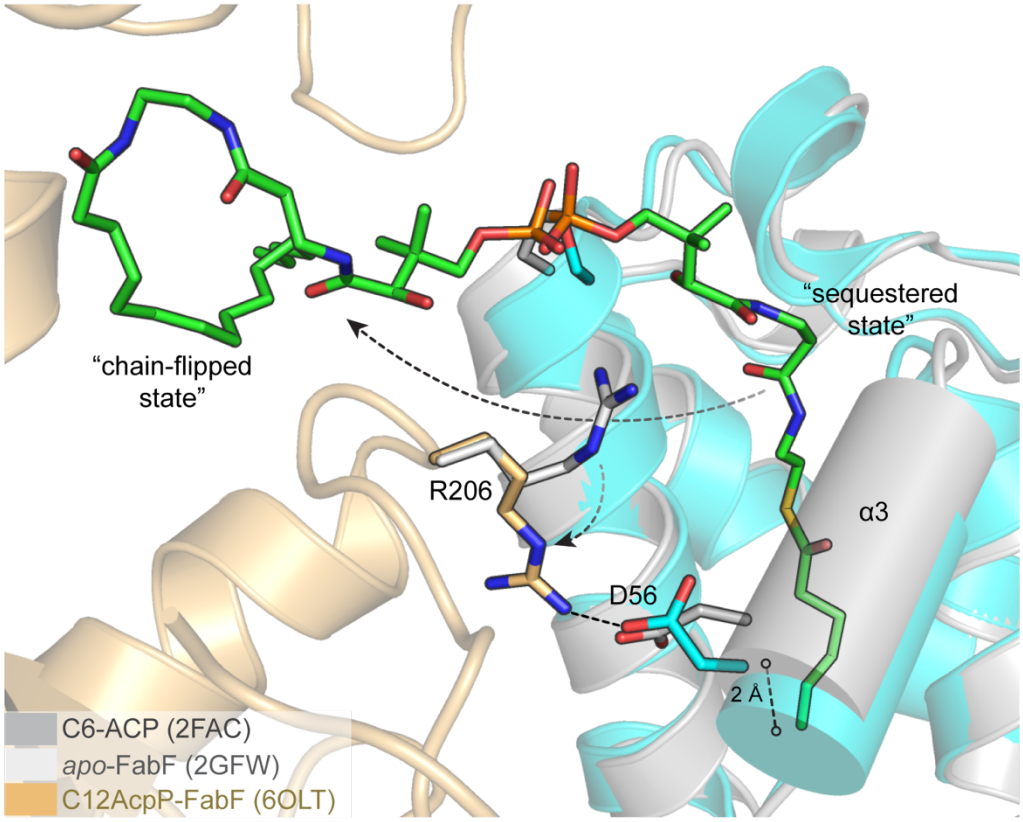

Figure S3.6: *Proposed role of Arg206 in facilitating chain-flipping*. Alignment of the C6-AcpP crystal structure (PDB ID: 2FAC) featuring a sequestered substrate with the bound ACP from AcpP-FabF (PDB ID: 6OLT) indicates that FabF's Arg206 coordinates with AcpP's Asp56 stabilizing a modest 2 to 2.5 Å shift in AcpP' s α3 positioning. The conformational rearrangement of Arg206 upon interaction with Asp56 on AcpP's α3 creates a direct pathway from the hydrophobic core (sequestered state) of AcpP to FabF active site (chain-flipped state). The hydrophobic nature of the Arg206 sidechain could therefore shield the fatty acid cargo from solvent during the chain-flipping mechanism. The "sequestered state" is derived from C6-ACP (PDB ID: 2FAC) and the "chain-flipped" state is modelled from C16ACP-FabF (PDB ID: 6OKG).

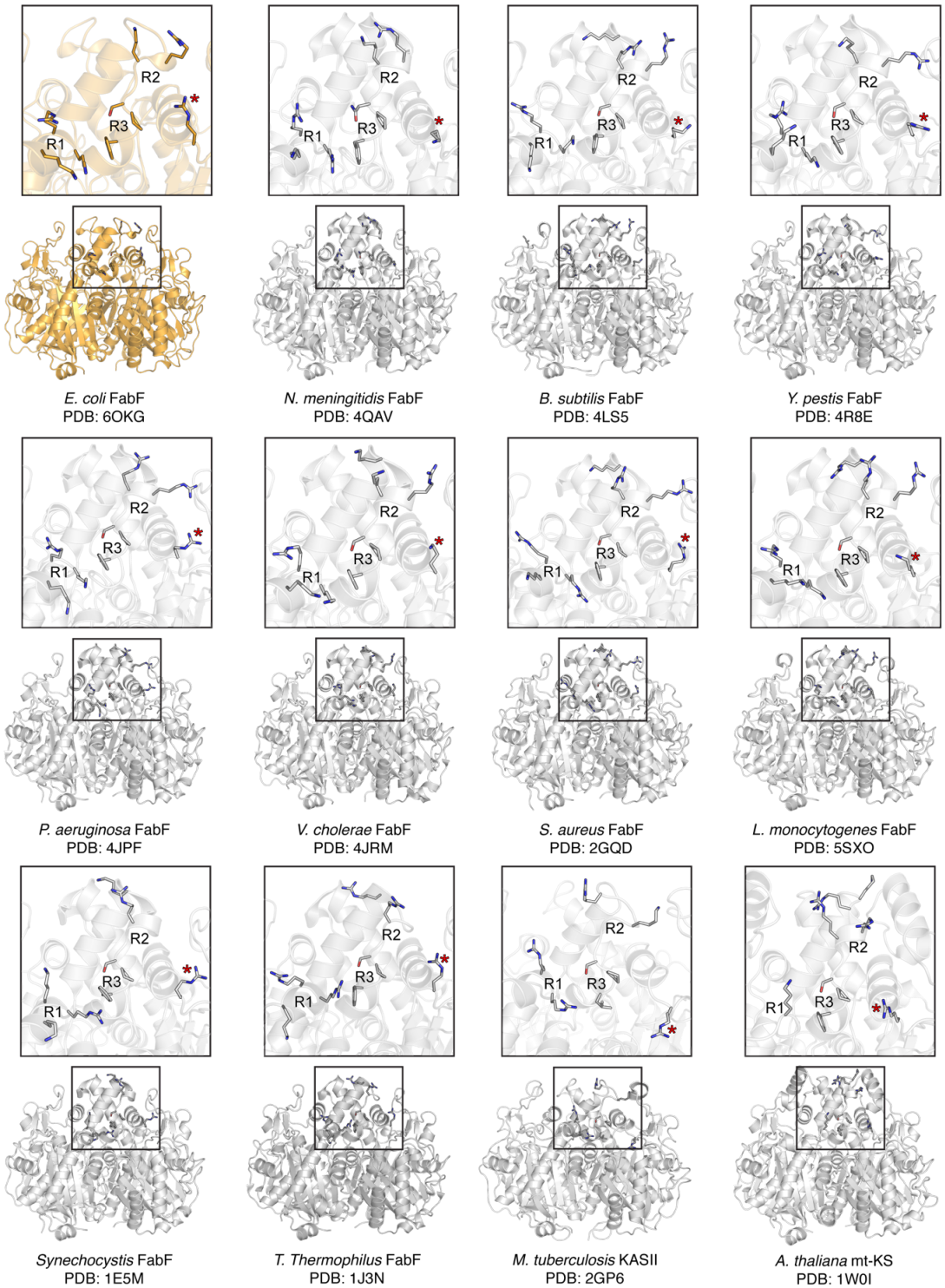

Figure S3.7: *FabF interface comparison to FabF orthologs*. The top left panel provides an overview of the interacting residues and designated interface regions of FabF while the following 11 panels show the putative AcpP binding residues from different FabF orthologs found in bacterial species and the mitochondrial KS from Arabidopsis thaliana. Residues marked with a red asterisk (*) are found in a similar position, in space or in sequence, as Arg206 in FabF.

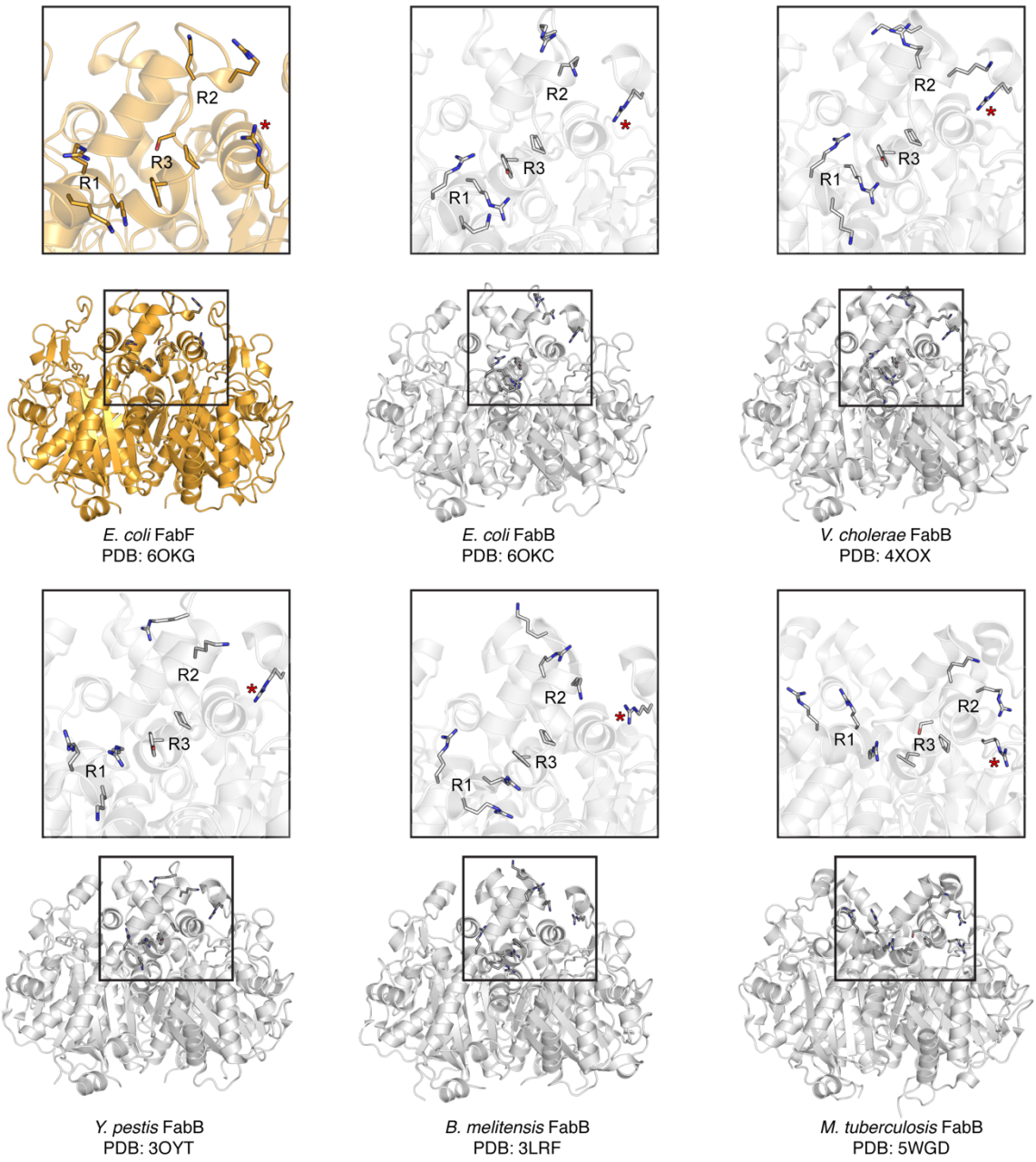

Figure S3.8: *FabF interface comparison to FabB homologs.* The top left panel provides an overview of the interacting residues and designated interface regions of FabF while the following five panels show the putative AcpP binding residues for five FabB homologs found in different bacterial species. The FabB Arg45 equivalent residue is marked with an asterisk (*) in each panel.

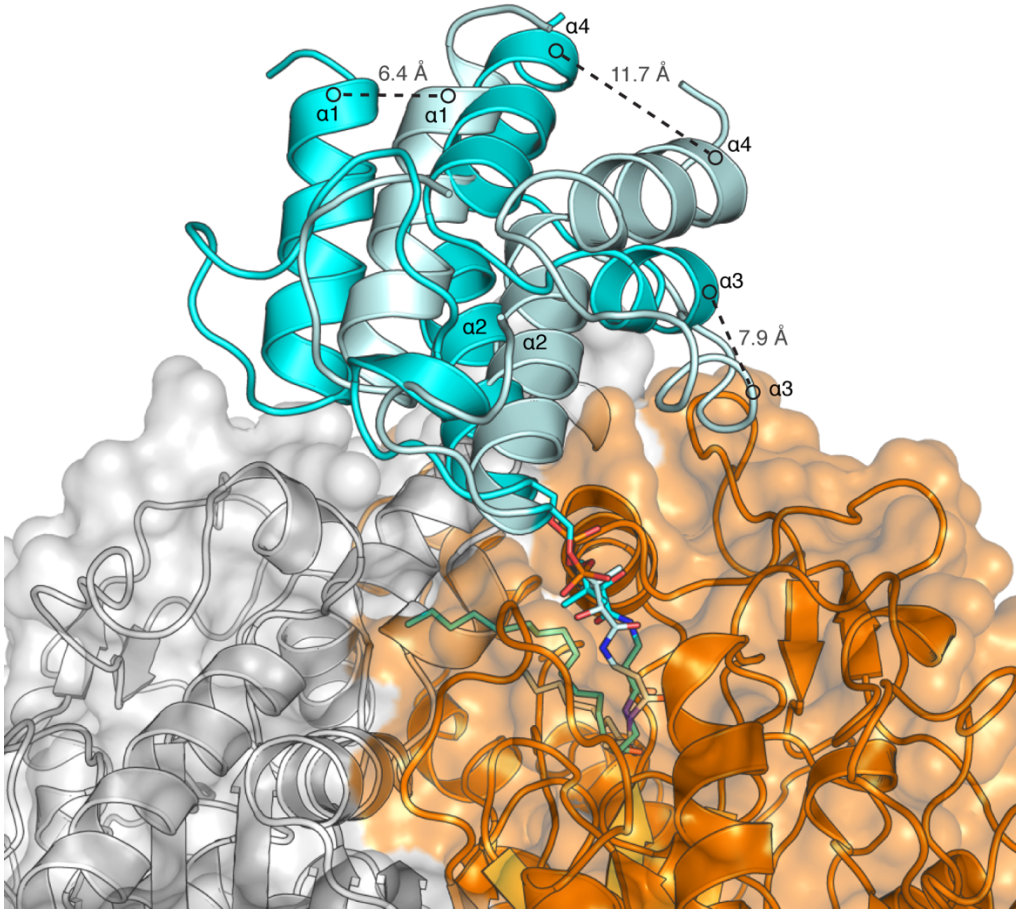

Figure S3.9: *Comparison of AcpP and igaACP binding modes.* The KS domains of FabF and *iga*KS/CLF were overlaid in order to compare the relative binding modes of AcpP (cyan) and *iga*ACP (pale cyan). The *iga*ACP is rotated and translated with respect to the binding mode of AcpP. Measurements of the displacement are shown as dots connected by dashed lines. The KS domain to which the ACPs are crosslinked is colored orange while the other KS monomer, the CLF in the case of *iga*KS/CLF, is colored white.

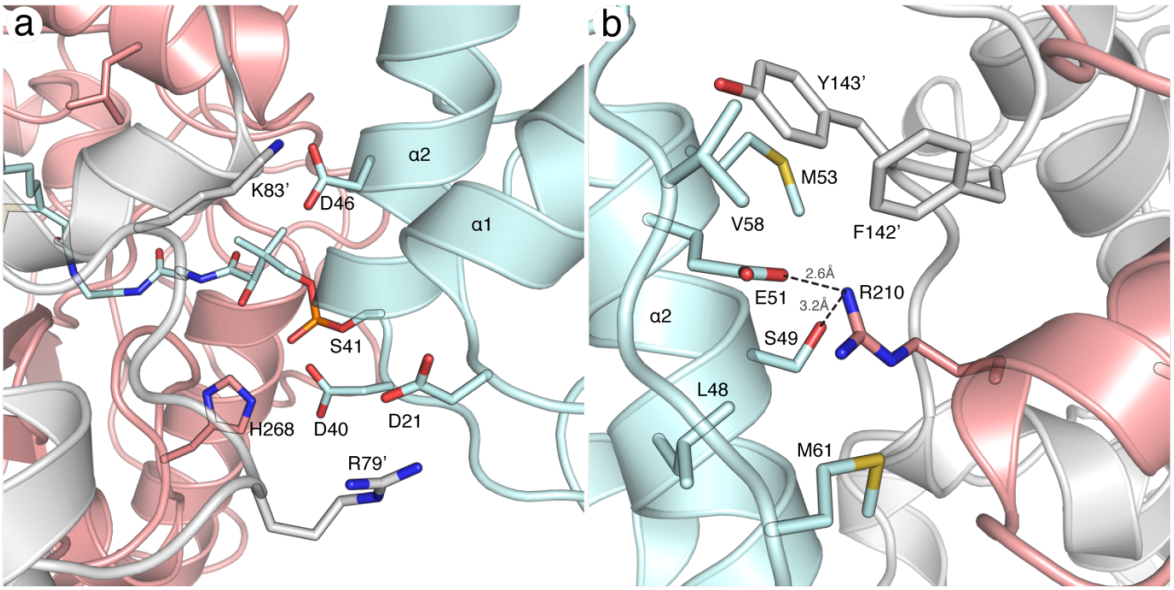

Figure S3.10: *Interface contacts between igaACP and igaKS/CLF*. **a)** The equivalent region 1 contacts found in the igaACP-KS/CLF complex. Acidic residues (Asp21, Asp40, and Asp46) at the top of helices 1 and 2 form electrostatic interactions with positively charged residues (Arg79, Lys83, His268) on *iga*KS/CLF. **b)** Coordinated interaction network that creates a buried salt bridge between Arg210 and Glu51. The *iga*ACP is colored cyan while *iga*KS is salmon and *iga*CLF is light grey. Residues from *iga*CLF are denoted with an apostrophe (').

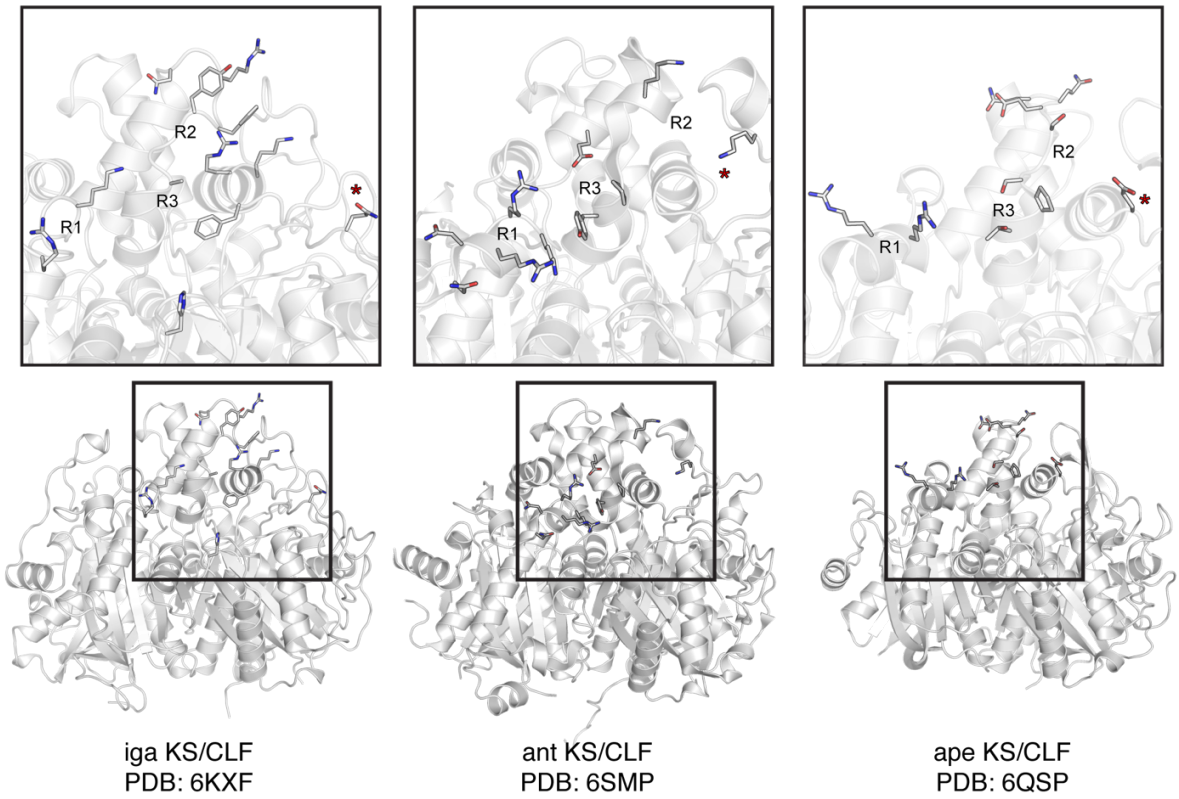

Figure S3.11: *Interface comparison of putative ACP binding sites on type II PKS KS/CLFs.* The far-left panel shows the interacting residues found at the interface of the igaACP-KS/CLF crosslinked crystal structures. The following two panels depict residues at the ACP binding site of the anthraquinone (ant) KS/CLF and the putative ACP binding site for the arylpolyene synthase (*ape*) KS/CLF, respectively. The interface regions are designated based on the AcpP-FabF crosslinked structure and the associated work reported herein. Residues marked with a red asterisk (*) are found in a similar position, in space or in sequence, as Arg206 in FabF.

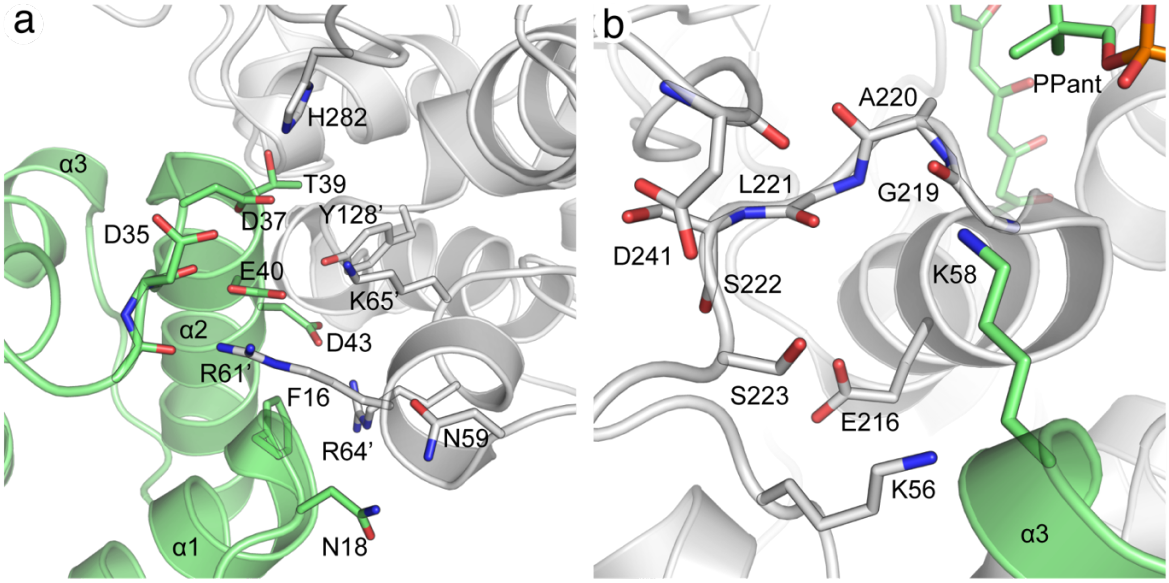

Figure S3.12: *Interface contacts between antACP and antKS/CLF.* **a)** The equivalent region 1 contacts found in the antACP-KS/CLF complex. Acidic and polar residues (Asn18, Asp35, Asp37, Thr39, Glu40, and Asp43) at the top of helices 1 and 2 form electrostatic interactions with positively charged residues (Arg61, Arg64, and Lys65) on antKS/CLF. **b)** Lys58 from antACP helix three docks into a polar pocket at the antKS/CLF interface. The antACP is colored pale green while antKS/CLF is colored light grey. Residues from the antCLF are denoted with an apostrophe (').

Table S3.1: *PCR Primers used in this study*. All mutants were confirmed by DNA sequencing.

Primer name	Primer sequence 5'-3'
LM_K65A_f	CGC GCA GAA CAG CGC AAG ATG GAT GCC TTC ATT CAA TAT GGA ATT G
LM_K65A_r	CTT GCG CTG TTC TGC GCG CGA GAT AAT GTC CTC ACA GTT AAA ATC
LM_K65E_f	CGC GAA GAA CAG CGC AAG ATG GAT GCC TTC ATT CAA TAT GGA ATT G
LM_K65E_r	CTT GCG CTG TTC TTC GCG CGA GAT AAT GTC CTC ACA GTT AAA ATC
LM_R68A_f	CAG GCG AAG ATG GAT GCC TTC ATT CAA TAT GGA ATT GTC GCT G
LM_R68A_r	CAT CTT CGC CTG TTC TTT GCG CGA GAT AAT GTC CTC AC
LM_K69A_f	CGC AAA GAA CAG CGC GCG ATG GAT GCC TTC ATT CAA TAT GGA ATT G
LM_K69A_r	CGC GCG CTG TTC TTT GCG CGA GAT AAT GTC CTC ACA GTT AAA ATC
LM_K69E_f	CGC AAA GAA CAG CGC GAG ATG GAT GCC TTC ATT CAA TAT GGA ATT G
LM_K69E_r	CTC GCG CTG TTC TTT GCG CGA GAT AAT GTC CTC ACA GTT AAA ATC
LM_K65A-K69A_f	CGC GCA GAA CAG CGC GCG ATG GAT GCC TTC ATT CAA TAT GGA ATT G
LM_K65A-K69A_r	CGC GCG CTG TTC TGC GCG CGA GAT AAT GTC CTC ACA GTT AAA ATC
LM_K128A_f	ACG TGC GAT CAG CCC ATT CTT CGT TCC GTC AAC
LM_K128A_r	TGA TCG CAC GTG GAC CAC CGT TCA TCA GAG ATG T
LM_R206A_f	GCA GCG GCA TTA TCT ACC CGC AAT GAT AAC CCG C
LM_R206A_r	GCC GCT GCC GCG CCA AAA CCA CCA AC
LM_R206N_f	GCA AAC GCA TTA TCT ACC CGC AAT GAT AAC CCG C
LM_R206N_r	ATA ATG CGT TTG CCG CGC CAA AAC CAC CAA C
LM_S130A_f	ATC GCG CCA TTC TTC GTT CCG TCA ACG ATT GTG AAC
LM_S130A_r	TGG CGC GAT CTT ACG TGG ACC ACC GTT CAT CA
LM_F132A_f	CCC AGC GTT CGT TCC GTC AAC GAT TGT GAA CAT GG
LM_F132A_r	GAA CGC TGG GCT GAT CTT ACG TGG ACC ACC GT
LM_R127A_f	GGT CCA GCG AAG ATC AGC CCA TTC TTC GTT CCG TCA
LM_R127A_r	GAT CTT CGC TGG ACC ACC GTT CAT CAG AGA TGT GTG
LM_P131A_f	ATC AGC GCG TTC TTC GTT CCG TCA ACG ATT GTG AAC ATG G
LM_P131A_r	AAC GAA GAA CGC GCT GAT CTT ACG TGG ACC ACC GTT CAT C
LM_R127A-K128A_f	GGT CCA GCA GCA ATC AGC CCA TTC TTC GTT CCG TCA
LM_R127A-K128A_r	GAT TGC TGC TGG ACC ACC GTT CAT CAG AGA TGT GTG GT
LM_C163A_f	GCG ACT GCC GCG ACT TCC GGC GTG CAC AAC ATT GG
LM_C163A_r	AGT CGC GGC AGT CGC GAT AGA GAT GCT CGG GCC AC

Table S3.2: *In vivo complementation assay results*[a]

	AVG OD600	SD +/-	P-value
FabF wt	1.017	0.120	2.733E-17
pBAD322 control	0.007	0.006	NA
FabF C163A	0.003	0.002	7.575E-02
FabF K65A	0.895	0.090	6.464E-13
FabF K65E	0.165	0.059	6.898E-07
FabF K69A	0.859	0.144	1.606E-10
FabF K69E	0.660	0.130	9.361E-10
FabF R68A	0.703	0.404	3.712E-05
FabF K65A/K69A	0.349	0.214	7.088E-05
FabF K65A/R68A/K69A	0.021	0.010	0.006*
FabF R127A	0.420	0.199	6.959E-06
FabF K128A	0.159	0.037	3.976E-09
FabF R206A	0.38	0.075	1.145E-09
FabF R127A/K128A	0.534	0.029	1.617E-15
FabF R127A/K128A/R206A	0.016	0.001	0.016*
FabF S130A	0.908	0.116	8.819E-12
FabF P131A	0.799	0.407	1.235E-05
FabF F132A	0.935	0.074	4.714E-14

[a]All assay results were calculated using an OD600 reading after 24 hours of cell growth and repeated in at least biological triplicate. P-values were calculated using the Dunnet's Test comparing all results to the negative control pBAD322 empty vector strain, which represent cells unable to grow at the non-permissible temperature of 42 °C due to defects in fatty acid biosynthesis.

*P-values marked with an asterisk represent complementation results that are not statistically significant from the pBAD322 empty vector negative control using a P-value cutoff of .001.

Table S3.3: *Molecular weight of FabF variants and C12-AcpP*. Each protein was analyzed on a LC API-SQ MS (Waters). The molecular weight of each protein (MW_{mea} ± standard error) was determined using ESIprot.[6]

FabF	MW_{calc} (Da)	MW_{mea} (Da)	**ΔMW (Da)**
WT	45288.2	45290.7 (± 5.2)	2.5
K65A	45231.1	45234.2 (± 5.9)	3.1
R68A	45203.1	45206.4 (± 6.8)	3.3
K65A/K69A	45174.0	45179.2 (± 8.4)	5.2
K65A/R68A/K69A	45121.0	45125.1 (± 6.3)	4.1
K128A	45231.1	45239.5 (± 5.9)	8.4
R206A	45203.1	45206.0 (± 5.1)	2.9
R206N	45246.1	45249.7 (± 4.7)	3.6
R127A/K128A	45178.1	45177.8 (± 5.8)	0.3
R127A/K128A/R206A	45093.0	45094.0 (±4.8)	3.3
S130A	45272.2	45277.5 (± 5.9)	5.9
F132A	45212.1	45216.3 (± 4.0)	4.2
K65A/R127A/K128A	45121.0	45121.7 (± 5.5)	0.7
AcpP	MW_{calc} (Da)	MW_{mea} (Da)	**ΔMW (Da)**
C12-AcpP*	9576.6	9575.5 (± 1.1)	1.1

*The expected molecular weight of C12-AcpP (MW_{calc}) has been calculated considering the His_6-tag cleavage and the installation of the acylated PPant arm on AcpP's catalytic serine residue.

References

(1) Beld, J., Lee, D. J., and Burkart, M. D. (2015) Fatty acid biosynthesis revisited: structure elucidation and metabolic engineering. *Mol. Biosyst. 11*, 38–59.

(2) Rock, C. O., and Cronan, J. E. (1996) *Escherichia coli* as a model for the regulation of dissociable (type II) fatty acid biosynthesis. *Biochim. Biophys. Acta - Lipids Lipid Metab. 1302*, 1–16.

(3) White, S. W., Zheng, J., Zhang, Y.-M., and Rock, C. O. (2005) The Structural Biology of Type II Fatty Acid Biosynthesis. *Annu. Rev. Biochem. 74*, 791–831.

(4) Cronan, J. E. (2014) Biotin and Lipoic Acid: Synthesis, Attachment, and Regulation. *EcoSal Plus 6*.

(5) Cronan, J. E. (2018) Advances in synthesis of biotin and assembly of lipoic acid. *Curr. Opin. Chem. Biol. 47*, 60–66.

(6) Lim, G.-H., Singhal, R., Kachroo, A., and Kachroo, P. (2017) Fatty Acid- and Lipid-Mediated Signaling in Plant Defense. *Annu. Rev. Phytopathol. 55*, 505–536.

(7) Sunshine, H., and Iruela-Arispe, M. L. (2017) Membrane lipids and cell signaling. *Curr. Opin. Lipidol. 28*, 408–413.

(8) Soto, M. J., Calatrava-Morales, N., and López-Lara, I. M. (2017) Functional Roles of Non-membrane Lipids in Bacterial Signaling BT - Biogenesis of Fatty Acids, Lipids and Membranes (Geiger, O., Ed.), pp 1–17. Springer International Publishing, Cham.

(9) Crosby, J., and Crump, M. P. (2012) The structural role of the carrier protein – active controller or passive carrier. *Nat. Prod. Rep. 29*, 1111–1137.

(10) Mindrebo, J. T., Misson, L. E., Patel, A., Kim, W. E., Davis, T. D., Ni, Q. Z., La Clair, J. J., and Burkart, M. D. (2020)Structural Basis of Acyl-Carrier Protein Interactions in Fatty Acid and Polyketide Biosynthesis, in *Comprehensive Natural Products III: Chemistry and Biology. 1, 61–122.*

(11) Beld, J., Sonnenschein, E. C., Vickery, C. R., Noel, J. P., and Burkart, M. D. (2014) The phosphopantetheinyl transferases: catalysis of a post-translational modification crucial for life. *Nat. Prod. Rep. 31*, 61–108.

(12) Blatti, J. L., Beld, J., Behnke, C. A., Mendez, M., Mayfield, S. P., and Burkart, M. D. (2012) Manipulating fatty acid biosynthesis in microalgae for biofuel through protein-protein interactions. *PLoS One 7*, 1–12.

(13) Zhu, L., and Cronan, J. E. (2015) The conserved modular elements of the acyl carrier proteins of lipid synthesis are only partially interchangeable. *J. Biol. Chem. 290*, 13791–

13799.

(14) Maier, T., Leibundgut, M., Boehringer, D., and Ban, N. (2010) Structure and function of eukaryotic fatty acid synthases. *Q. Rev. Biophys. 43*, 373–422.

(15) Maier, T., Leibundgut, M., and Ban, N. (2008) The Crystal Structure of a Mammalian Fatty Acid Synthase. *Science. 321*, 1315– 1322.

(16) Herbst, D. A., Townsend, C. A., and Maier, T. (2018) The architectures of iterative type I PKS and FAS. *Nat. Prod. Rep.* 1046–1069.

(17) Leibundgut, M., Jenni, S., Frick, C., and Ban, N. (2007) Structural basis for substrate delivery by acyl carrier protein in the yeast fatty acid synthase. *Science . 288*–290.

(18) Johansson, P., Wiltschi, B., Kumari, P., Kessler, B., Vonrhein, C., Vonck, J., Oesterhelt, D., and Grininger, M. (2008) Inhibition of the fungal fatty acid synthase type I multienzyme complex. *Proc. Natl. Acad. Sci. 105*, 12803–12808.

(19) Masoudi, A., Raetz, C. R. H., Zhou, P., and Pemble IV, C. W. (2013) Chasing acyl carrier protein through a catalytic cycle of lipid A production. *Nature 505*, 422–426.

(20) Agarwal, V., Lin, S., Lukk, T., Nair, S. K., and Cronan, J. E. (2012) Structure of the enzyme-acyl carrier protein (ACP) substrate gatekeeper complex required for biotin synthesis. *Proc. Natl. Acad. Sci. 109*, 17406–17411.

(21) Marcella, A. M., Culbertson, S. J., Shogren-Knaak, M. A., and Barb, A. W. (2017) Structure, High Affinity, and Negative Cooperativity of the *Escherichia coli* Holo-(Acyl Carrier Protein):Holo-(Acyl Carrier Protein) Synthase Complex. *J. Mol. Biol. 429*, 3763–3775.

(22) Zhang, L., Xiao, J., Xu, J., Fu, T., Cao, Z., Zhu, L., Chen, H.-Z., Shen, X., Jiang, H., and Zhang, L. (2016) Crystal structure of FabZ-ACP complex reveals a dynamic seesaw-like catalytic mechanism of dehydratase in fatty acid biosynthesis. *Cell Res. 26*, 1330–1344.

(23) Worthington, A. S., and Burkart, M. D. (2006) One-pot chemo-enzymatic synthesis of reporter-modified proteins. *Org. Biomol. Chem. 4*, 44–46.

(24) Worthington, A. S., Rivera, H., Torpey, J. W., Alexander, M. D., and Burkart, M. D. (2006) Mechanism-based protein cross-linking probes to investigate carrier protein-mediated biosynthesis. *ACS Chem. Biol. 11*, 687–691.

(25) Ishikawa, F., Haushalter, R. W., and Burkart, M. D. (2012) Dehydratase-specific probes for fatty acid and polyketide synthases. *J. Am. Chem. Soc. 134*, 769–772.

(26) Tallorin, L., Finzel, K., Nguyen, Q. G., Beld, J., La Clair, J. J., and Burkart, M. D. (2016) Trapping of the enoyl-acyl carrier protein reductase-acyl carrier protein interaction. *J. Am.*

Chem. Soc. 138, 3962–3965.

(27) Ye, Z., Bair, M., Desai, H., and Williams, G. J. (2011) A photocrosslinking assay for reporting protein interactions in polyketide and fatty acid synthases. *Mol. Biosyst. 7*, 3152–3156.

(28) Nguyen, C., Haushalter, R. W., Lee, D. J., Markwick, P. R. L., Bruegger, J., Caldara-Festin, G., Finzel, K., Jackson, D. R., Ishikawa, F., O'Dowd, B., McCammon, J. A., Opella, S. J., Tsai, S.-C., and Burkart, M. D. (2014) Trapping the dynamic acyl carrier protein in fatty acid biosynthesis. *Nature 505*, 427–431.

(29) Milligan, J. C., Lee, D. J., Jackson, D. R., Schaub, A. J., Beld, J., Barajas, J. F., Hale, J. J., Luo, R., Burkart, M. D., and Tsai, S.-C. (2019) Molecular basis for interactions between an acyl carrier protein and a ketosynthase. *Nat. Chem. Biol. 15*, 669–671.

(30) Dodge, G. J., Patel, A., Jaremko, K. L., McCammon, J. A., Smith, J. L., and Burkart, M. D. (2019) Structural and dynamical rationale for fatty acid unsaturation in *Escherichia coli. Proc. Natl. Acad. Sci. 116*, 6775 – 6783.

(31) Mindrebo, J. T., Patel, A., Kim, W. E., Davis, T. D., Chen, A., Bartholow, T. G., La Clair, J. J., McCammon, J. A., Noel, J. P., and Burkart, M. D. (2020) Gating mechanism of elongating β-ketoacyl-ACP synthases. *Nat. Commun. 11*, 1727.

(32) Misson, L. E., Mindrebo, J. T., Davis, T. D., Patel, A., McCammon, J. A., Noel, J. P., and Burkart, M. D. (2020) Structure and Dynamic Basis of Molecular Recognition Between Acyltransferase and Carrier Protein in *E. coli* Fatty Acid Synthesis. *bioRxiv* 2020.05.15.098798.

(33) Heil, C. S., Wehrheim, S. S., Paithankar, K. S., and Grininger, M. (2019) Fatty Acid Biosynthesis: Chain-Length Regulation and Control. *ChemBioChem 20*, 2298–2321.

(34) Campbell, J. W., and Cronan, J. E. (2001) Bacterial Fatty Acid Biosynthesis: Targets for Antibacterial Drug Discovery. *Annu. Rev. Microbiol. 55*, 305–332.

(35) Heath, R. J., and Rock, C. O. (2004) Fatty acid biosynthesis as a target for novel antibacterials. *Curr. Opin. Investig. Drugs 5*, 146–153.

(36) Das, M., Sakha Ghosh, P., and Manna, K. (2016) A Review on Platensimycin: A Selective FabF Inhibitor. *Int. J. Med. Chem. 2016*, 9706753.

(37) Wang, J., Soisson, S. M., Young, K., Shoop, W., Kodali, S., Galgoci, A., Painter, R., Parthasarathy, G., Tang, Y. S., Cummings, R., Ha, S., Dorso, K., Motyl, M., Jayasuriya, H., Ondeyka, J., Herath, K., Zhang, C., Hernandez, L., Allocco, J., Basilio, Á., Tormo, J. R., Genilloud, O., Vicente, F., Pelaez, F., Colwell, L., Lee, S. H., Michael, B., Felcetto, T., Gill, C., Silver, L. L., Hermes, J. D., Bartizal, K., Barrett, J., Schmatz, D., Becker, J. W., Cully, D., and Singh, S. B. (2006) Platensimycin is a selective FabF inhibitor with potent antibiotic

properties. *Nature 441*, 358–361.

(38) Martens, E., and Demain, A. L. (2011) Platensimycin and platencin: promising antibiotics for future application in human medicine. *J. Antibiot. (Tokyo). 64*, 705–710.

(39) Garwin, J., Klages, A., and Cronan, J. (1980) Structural, enzymatic, and genetic studies of beta-ketoacyl-acyl carrier protein synthases I and II of *Escherichia coli*. *J. Biol. Chem. 255*, 11949–11956.

(40) Lai, C.-Y., and Cronan, J. E. (2003) β-Ketoacyl-Acyl Carrier Protein Synthase III (FabH) Is Essential for Bacterial Fatty Acid Synthesis. *J. Biol. Chem. 278*, 51494–51503.

(41) Harder, M. E., Beacham, I. R., Cronan, J. E., Beacham, K., Honegger, J. L., and Silbert, D. F. (1972) Temperature-sensitive mutants of *Escherichia coli* requiring saturated and unsaturated fatty acids for growth: isolation and properties. *Proc. Natl. Acad. Sci. U. S. A. 69*, 3105—3109.

(42) Edwards, P., Sabo Nelsen, J., Metz, J. G., and Dehesh, K. (1997) Cloning of the *fabF* gene in an expression vector and in vitro characterization of recombinant *fabF* and *fabB* encoded enzymes from *Escherichia coli*. *FEBS Lett. 402*, 62–66.

(43) Cronan, J. E., Birge, C. H., and Vagelos, P. R. (1969) Evidence for Two Genes Specifically Involved in Unsaturated Fatty Acid Biosynthesis in *Escherichia coli*. *J. Bacteriol. 100*, 601 LP – 604.

(44) D'Agnolo, G., Rosenfeld, I. S., and Vagelos, P. R. (1975) Multiple forms of beta-ketoacyl-acyl carrier protein synthetase in *Escherichia coli*. *J. Biol. Chem. 250*, 5289–5294.

(45) de Mendoza, D., and Cronan, J. E. (1983) Thermal regulation of membrane lipid fluidity in bacteria. *Trends Biochem. Sci. 8*, 49–52.

(46) de Mendoza, D., Garwin, J. L., and Cronan, J. E. J. (1982) Overproduction of cis-vaccenic acid and altered temperature control of fatty acid synthesis in a mutant of *Escherichia coli*. *J. Bacteriol. 151*, 1608–1611.

(47) Garwin, J. L., and Cronan, J. E. (1980) Thermal modulation of fatty acid synthesis in *Escherichia coli* does not involve de novo enzyme synthesis. *J. Bacteriol. 141*, 1457–1459.

(48) Beld, J., Cang, H., and Burkart, M. D. (2014) Visualizing the chain-flipping mechanism in fatty-acid biosynthesis. *Angew. Chem. Int. Ed. Engl. 53*, 14456–14461.

(49) Cronan, J. E. (2014) The chain-flipping mechanism of ACP (acyl carrier protein)-dependent enzymes appears universal. *Biochem. J. 460*, 157– 163.

(50) Quadri, L. E., Weinreb, P. H., Lei, M., Nakano, M. M., Zuber, P., and Walsh, C. T. (1998) Characterization of Sfp, a *Bacillus subtilis* phosphopantetheinyl transferase for

peptidyl carrier protein domains in peptide synthetases. *Biochemistry 37*, 1585–1595.

(51) Jiang, Y., Chan, C. H., and Cronan, J. E. (2006) The soluble acyl-acyl carrier protein synthetase of *Vibrio harveyi* B392 is a member of the medium chain acyl-CoA synthetase family. *Biochemistry 45*, 10008–10019.

(52) Fice, D., Shen, Z., and Byers, D. M. (1993) Purification and characterization of fatty acyl-acyl carrier protein synthetase from *Vibrio harveyi*. *J. Bacteriol. 175*, 1865–1870.

(53) Beld, J., Finzel, K., and Burkart, M. D. (2014) Versatility of acyl-acyl carrier protein synthetases. *Chem. Biol. 21*, 1293–1299.

(54) Liu, H., and Naismith, J. H. (2008) An efficient one-step site-directed deletion, insertion, single and multiple-site plasmid mutagenesis protocol. *BMC Biotechnol. 8*, 91–101.

(55) De Lay, N. R., and Cronan, J. E. (2006) Gene-Specific Random Mutagenesis of *Escherichia coli In Vivo*: Isolation of Temperature-Sensitive Mutations in the Acyl Carrier Protein of Fatty Acid Synthesis. *J. Bacteriol. 188*, 287 – 296.

(56) Cronan, J. E. (2006) A family of arabinose-inducible *Escherichia coli* expression vectors having pBR322 copy control. *Plasmid 55*, 152–157.

(57) Borgaro, J. G., Chang, A., Machutta, C. A., Zhang, X., and Tonge, P. J. (2011) Substrate recognition by β-ketoacyl-ACP synthases. *Biochemistry 50*, 10678–10686.

(58) Machutta, C. A., Bommineni, G. R., Luckner, S. R., Kapilashrami, K., Ruzsicska, B., Simmerling, C., Kisker, C., and Tonge, P. J. (2010) Slow onset inhibition of bacterial beta-ketoacyl-acyl carrier protein synthases by thiolactomycin. *J. Biol. Chem. 285*, 6161–6169.

(59) Garwin, J. L., Klages, A. L., and Cronan, J. E. J. (1980) Beta-ketoacyl-acyl carrier protein synthase II of *Escherichia coli*. Evidence for function in the thermal regulation of fatty acid synthesis. *J. Biol. Chem. 255*, 3263–3265.

(60) Trajtenberg, F., Altabe, S., Larrieux, N., Ficarra, F., de Mendoza, D., Buschiazzo, A., and Schujman, G. E. (2014) Structural insights into bacterial resistance to cerulenin. *Febs J. 281*, 2324–2338.

(61) Wang, H., and Cronan, J. E. (2004) Functional replacement of the FabA and FabB proteins of *Escherichia coli* fatty acid synthesis by *Enterococcus faecalis* FabZ and FabF homologues. *J. Biol. Chem. 279*, 34489–34495.

(62) Reichmann, D., Rahat, O., Albeck, S., Meged, R., Dym, O., and Schreiber, G. (2005) The modular architecture of protein-protein binding interfaces. *Proc. Natl. Acad. Sci. U. S. A. 102*, 57–62.

(63) Reichmann, D., Rahat, O., Cohen, M., Neuvirth, H., and Schreiber, G. (2007) The

molecular architecture of protein-protein binding sites. *Curr. Opin. Struct. Biol. 17*, 67–76.

(64) Finzel, K., Nguyen, C., Jackson, D. R., Gupta, A., Tsai, S.-C., and Burkart, M. D. (2015) Probing the Substrate Specificity and Protein-Protein Interactions of the *E. coli* Fatty Acid Dehydratase, FabA. *Chem. Biol. 22*, 1453–1460.

(65) Ye, Z., and Williams, G. J. (2014) Mapping a Ketosynthase:Acyl Carrier Protein Binding Interface via Unnatural Amino Acid-Mediated Photo-Cross-Linking. *Biochemistry 53*, 7494–7502.

(66) Roujeinikova, A., Simon, W. J., Gilroy, J., Rice, D. W., Rafferty, J. B., and Slabas, A. R. (2007) Structural Studies of Fatty Acyl-(Acyl Carrier Protein) Thioesters Reveal a Hydrophobic Binding Cavity that Can Expand to Fit Longer Substrates. *J. Mol. Biol. 365*, 135–145.

(67) Mayo, K. H., and Prestegard, J. H. (1985) Acyl carrier protein from *Escherichia coli*. Structural characterization of short-chain acylated acyl carrier proteins by NMR. *Biochemistry 24*, 7834–7838.

(68) Colizzi, F., Masetti, M., Recanatini, M., and Cavalli, A. (2016, August) Atomic-Level Characterization of the Chain-Flipping Mechanism in Fatty-Acids Biosynthesis. *J. Phys. Chem. Lett.* 7, 2899–2904.

(69) Chan, D. I., Tieleman, D. P., and Vogel, H. J. (2010) Molecular dynamics simulations of beta-ketoacyl-, beta-hydroxyacyl-, and trans-2-enoyl-acyl carrier proteins of *Escherichia coli*. *Biochemistry 49*, 2860–2868.

(70) Chan, D. I., Stockner, T., Tieleman, D. P., and Vogel, H. J. (2008) Molecular dynamics simulations of the Apo-, Holo-, and acyl-forms of *Escherichia coli* acyl carrier protein. *J. Biol. Chem. 283*, 33620–33629.

(71) Płoskoń, E., Arthur, C. J., Kanari, A. L. P., Wattana-amorn, P., Williams, C., Crosby, J., Simpson, T. J., Willis, C. L., and Crump, M. P. (2010) Recognition of intermediate functionality by acyl carrier protein over a complete cycle of fatty acid biosynthesis. *Chem. Biol. 17*, 776–785.

(72) Roujeinikova, A., Baldock, C., Simon, W. J., Gilroy, J., Baker, P. J., Stuitje, A. R., Rice, D. W., Slabas, A. R., and Rafferty, J. B. (2002) X-Ray Crystallographic Studies on Butyryl-ACP Reveal Flexibility of the Structure around a Putative Acyl Chain Binding Site. *Structure 10*, 825–835.

(73) Smith, M. C., and Gestwicki, J. E. (2012) Features of protein-protein interactions that translate into potent inhibitors: topology, surface area and affinity. *Expert Rev. Mol. Med. 14*, e16.

(74) Ran, X., and Gestwicki, J. E. (2018) Inhibitors of protein-protein interactions (PPIs): an

analysis of scaffold choices and buried surface area. *Curr. Opin. Chem. Biol. 44*, 75–86.

(75) Guo, W., Wisniewski, J. A., and Ji, H. (2014) Hot spot-based design of small-molecule inhibitors for protein-protein interactions. *Bioorg. Med. Chem. Lett. 24*, 2546–2554.

(76) Ridley, C. P., Lee, H. Y., and Khosla, C. (2008) Evolution of polyketide synthases in bacteria. *Proc. Natl. Acad. Sci. U. S. A. 105*, 4595–4600.

(77) Hillenmeyer, M. E., Vandova, G. A., Berlew, E. E., and Charkoudian, L. K. (2015) Evolution of chemical diversity by coordinated gene swaps in type II polyketide gene clusters. *Proc. Natl. Acad. Sci. 112*, 13952–13957.

(78) Du, D., Katsuyama, Y., Horiuchi, M., Fushinobu, S., Chen, A., Davis, T. D., Burkart, M. D., and Ohnishi, Y. (2020) Structural basis for selectivity in a highly reducing type II polyketide synthase. *Nat. Chem. Biol. 16*, 776–1782

(79) Grammbitter, G. L. C., Schmalhofer, M., Karimi, K., Shi, Y.-M., Schöner, T. A., Tobias, N. J., Morgner, N., Groll, M., and Bode, H. B. (2019) An Uncommon Type II PKS Catalyzes Biosynthesis of Aryl Polyene Pigments. *J. Am. Chem. Soc. 141,* 16615–16623.

(80) Bräuer, A., Zhou, Q., Grammbitter, G. L. C., Schmalhofer, M., Rühl, M., Kaila, V. R. I., Bode, H. B., and Groll, M. (2020) Structural snapshots of the minimal PKS system responsible for octaketide biosynthesis. Nat. Chem. 12, 755–763. (81) Revill, W. P., Bibb, M. J., and Hopwood, D. A. (1996) Relationships between fatty acid and polyketide synthases from *Streptomyces coelicolor* A3(2): characterization of the fatty acid synthase acyl carrier protein. *J. Bacteriol. 178*, 5660–5667.

(82) Sarria, S., Bartholow, T. G., Verga, A., Burkart, M. D., and Peralta-Yahya, P. (2018) Matching Protein Interfaces for Improved Medium-Chain Fatty Acid Production. *ACS Synth. Biol. 7*, 1179–1187.

(83) Klaus, M., Ostrowski, M. P., Austerjost, J., Robbins, T., Lowry, B., Cane, D. E., and Khosla, C. (2016) Protein-protein interactions, not substrate recognition, dominate the turnover of chimeric assembly line polyketide synthases. *J. Biol. Chem. 291*, 16404–16415.

(84) Klaus, M., and Grininger, M. (2018) Engineering strategies for rational polyketide synthase design. *Nat. Prod. Rep. 35*, 1070–1081.

(85) Kosol, S., Jenner, M., Lewandowski, J. R., and Challis, G. L. (2018) Protein-protein interactions in trans-AT polyketide synthases. *Nat. Prod. Rep. 35*, 1097–1109.

(86) Zhu, Z., Zhou, Y. J., Krivoruchko, A., Grininger, M., Zhao, Z. K., and Nielsen, J. (2017) Expanding the product portfolio of fungal type I fatty acid synthases. *Nat. Chem. Biol. 13*, 360–362.

(87) Gajewski, J., Pavlovic, R., Fischer, M., Boles, E., and Grininger, M. (2017) Engineering

fungal de novo fatty acid synthesis for short chain fatty acid production. *Nat. Commun. 8*, 14650.

(88) Gajewski, J., Buelens, F., Serdjukow, S., Janßen, M., Cortina, N., Grubmüller, H., and Grininger, M. (2017) Engineering fatty acid synthases for directed polyketide production. *Nat. Chem. Biol. 13*, 363–365.

(89) Rossini, E., Gajewski, J., Klaus, M., Hummer, G., and Grininger, M. (2018) Analysis and engineering of substrate shuttling by the acyl carrier protein (ACP) in fatty acid synthases (FASs). *Chem. Commun. 2622*, 11606–11609.

(90) Rock, C. O.; Cronan, J. E.; Armitage, I. M. Molecular Properties of Acyl Carrier Protein Derivatives. J. Biol. Chem. 1981, 256 (6), 2669–2674.

Chapter 3, entitled Activity Mapping the Acyl Carrier Protein – Elongating Ketosynthase Interaction in Fatty Acid Biosynthesis, in full, is a reprint of the material as it appears: Mindrebo JT*, Misson LE*, Johnson C, Noel JP, Burkart MD. "Activity Mapping the Acyl Carrier Protein - Elongating Ketosynthase Interaction in Fatty Acid Biosynthesis". Biochemistry, 2020. The dissertation author is the primary co-author of this manuscript along with Dr. Laetitia Misson.

Chapter 4: Interfacial Plasticity Facilitates Catalysis in Type II FAS Malonyl-CoA ACP Transacylases

Abstract

Fatty acid synthases (FASs) and polyketide synthases (PKSs) iteratively elongate and often reduce two-carbon ketide units in *de novo* fatty acid and polyketide biosynthesis. Cycles of chain extensions in FAS and PKS are initiated by an acyltransferase (AT), which loads monomer units onto acyl carrier proteins (ACPs), small, flexible proteins that shuttle covalently linked intermediates between catalytic partners. Formation of productive ACP-AT interactions is required for catalysis and specificity within primary and secondary FAS and PKS pathways. Here, we use the *Escherichia coli* FAS AT, FabD, and its cognate ACP, AcpP, to interrogate type II FAS ACP-AT interactions. We utilize a covalent crosslinking probe to trap transient interactions between AcpP and FabD to elucidate the first x-ray crystal structure of a type II ACP-AT complex. Our structural data are supported using a combination of mutational, crosslinking, and kinetic analyses, and long timescale molecular dynamics (MD) simulations. Together, these complementary approaches reveal key catalytic features of FAS ACP-AT interactions. These mechanistic inferences suggest that AcpP adopts multiple, productive conformations at the AT binding interface, allowing the complex to sustain high transacylation rates. Furthermore, MD simulations support rigid body subdomain motions within the FabD structure that may play a key role in AT activity and substrate selectivity.

Introduction

Fatty acid synthases (FASs) and polyketide synthases (PKSs) iteratively condense and often reduce ketide units to assemble compounds ranging from simple fatty acids to complex bioactive molecules.[1–4] FASs and PKSs exist as either multidomain megasynthases (type I) or as discrete monofunctional enzymes (type II). They both share a common evolutionary origin,[3,5–8] and therefore, FASs and PKSs often have related enzymatic components. Both systems require small, flexible acyl carrier proteins (ACPs) that are posttranslationally modified with phosphopantetheine (PPant) arms to shuttle covalently tethered reactive intermediates in the form of thioester bonds between catalytic partners. Catalysis is initiated by an acyltransferase (AT), which selects and loads starter and/or extender units onto the ACP. In type II FAS, extender units are loaded onto ACP via a malonyl-CoA:ACP transacylase (MAT), FabD, which catalyzes the transfer of the malonyl moiety from malonyl-CoA to the PPant arm of *holo*-ACP to form malonyl-ACP (Figure 4.1). In contrast to type II FAS ATs, which only accept malonyl-CoA units, some ATs from PKSs accept a broader array of acyl-CoA units, as well as acyl-ACP units, increasing the structural diversity of their final products.[1,8–11] Interestingly, various bacterial type II PKS gene clusters lack a canonical AT to form malonyl-ACP. This activity is instead provided by the endogenous FAS MAT.[12–14] The central catalytic role of PKS and FAS MATs makes them attractive candidates for metabolic engineering and as targets for the development of new therapeutics.[15–20]

Engineering both type I and II FASs and PKSs is increasingly employed as a strategy to produce biofuels and bioactive natural products.[8,21–29] In this context, ATs are of particular interest, as they act as metabolic gatekeepers that can direct the selection of key, biosynthetic

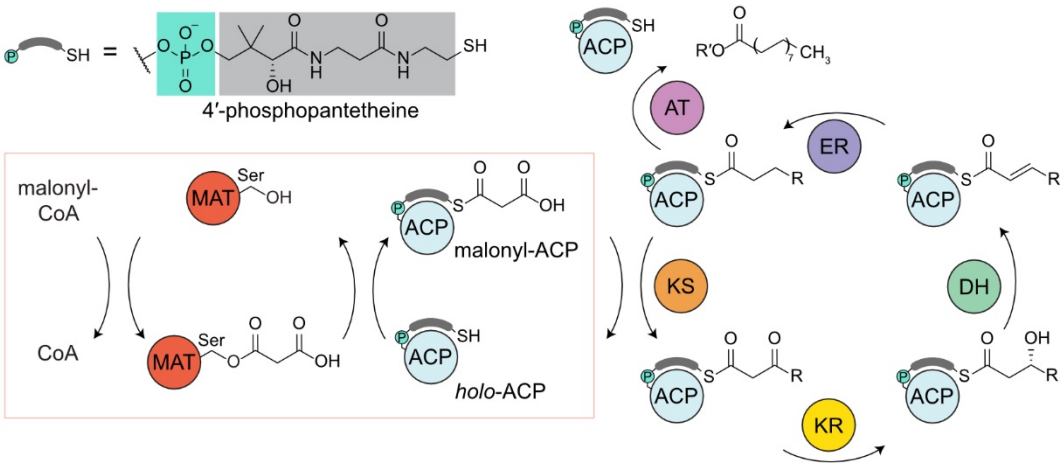

Figure 4.1: *Overview of saturated fatty acid biosynthesis from type II FAS.* highlighting the function of malonyl-CoA:ACP transacylases (MATs). The MAT (dark orange) is transiently acylated at an active site serine residue by malonyl-CoA. Then, the malonyl group is transferred to the 4′-phosphopantetheine arm of *holo*-ACP (pale blue). Additional downstream FAS enzymes catalyze chain extension, modification, and release from the synthase: the ketoacyl-ACP synthases (KS, orange), the NAD(P)H-dependent ketoacyl-ACP reductase (KR, yellow), the dehydratases (DH, aqua marine), the NAD(P)H-dependent enoylreductase (ER, purple) and the glycerol-3-phosphate acyltransferases (AT, lavender). The R and R' groups represent the omitted portion of the acyl-ACP thioester and the glycerol 3-phosphate derived backbone of a phospholipid, respectively.

building blocks. However, engineering efforts often lead to attenuated enzymatic activities[30,31] or poorly soluble chimeras,[31] likely due in part to an incomplete understanding of the transient nature of specific protein-protein interactions (PPIs) central to the iterative nature of FAS and PKS biosynthetic pathways. Interestingly, the high catalytic efficiency of FabD from *Escherichia coli*, which turns over substrate at nearly the diffusion limit (Figure S4.1, k_{cat}/K_M ~10^8 s^{-1} M^{-1}),[32,33] makes this MAT a particularly attractive target to create a diverse collection of acyl-ACPs for type II FAS and PKS engineering.[34,35]

Descriptions of type II FAS and PKS ACP-MAT interfaces have benefited by docking simulations, NMR techniques, and binding affinity assays.[14,36,37] While these studies suggest that MATs use shared binding motifs for malonyl-CoA and *holo*-ACP recognition, they often support different ACP-MAT binding interfaces. Recently, the x-ray crystal structures of two ACP-*trans*-AT covalent complexes from the vicenistatin and disorazole type I PKS pathways were elucidated.[38,39] The ACP-AT binding modes and respective interface interactions in these structures describe notable differences, and it remains unclear whether the molecular underpinnings of PKS ACP-*trans*-AT interactions are fully shared with type II ACP-MAT interactions.

To address this, we utilized active site-selective crosslinking to covalently capture *E. coli* FabD in association with its cognate ACP, AcpP, to facilitate the elucidation of the first x-ray crystal structure of a type II FAS ACP-AT complex (PDB ID: 6U0J, 1.9 Å). We conducted biochemical assays that indicate the AcpP-FabD interface tolerates mutations to residues that initially appeared to support a specific and energetically stable protein-protein complex. In addition, we computationally probed this complex using long timescale molecular dynamics (MD) simulations. These computational studies support unanticipated

plasticity at the AcpP-FabD interface, likely explaining FabD's tolerance to interface mutations with modest effects on turnover rates. A total of 32 μs of MD simulation data provides the most comprehensive sampling of AT dynamism to date, revealing rigid body subdomains motion, substrate-induced active site reorganization, and plasticity at the interface between the carrier protein and AT that likely explain the high catalytic rates of *E. coli* FabD. Our findings offer insights into the structures and dynamics of ACP-AT recognition in type II FASs. Collectively, these new results open up additional possibilities and challenges directed towards the design of protein-protein interfaces that support AT-mediated catalysis for the engineering of novel metabolic outputs.

Results and Discussion

Crystallized crosslinked complex. In order to characterize the PPIs between a type II FAS ACP and its cognate AT, we crystallized a chemoenzymatically trapped complex of *E. coli* AcpP and its cognate AT, FabD. Classically, trapping covalent complexes between an ACP and a partner enzyme (PE) has been achieved through the synthesis of pantetheinamide crosslinking probes that react selectively and uniformly with the active site residues of the PE.[40–42] These probes can be loaded onto an ACP via a one-pot chemoenzymatic method[43] to produce *crypto*-ACPs, which, when mixed with cognate PEs, form crosslinked complexes.[44–47] Despite recent successes developing active site fluorescent probes for ATs,[48] targeting the active site serine of FabD with complementary pantetheinamide probes proved challenging. To produce sufficient quantities of crosslinked complexes for x-ray crystallography, we utilized a FabD S92C mutant that reacts with thiol-reactive pantetheinamide probes.[39,48,49] Specifically, we generated C2-α-bromo-*crypto*-AcpP

from *apo*-AcpP (Figure S4.2),[43] which was subsequently incubated with FabD S92C to produce a crosslinked AcpP-FabD complex (where the "-" denotes a covalent crosslink between the two proteins). This AcpP-FabD complex yielded diffraction quality crystals, resulting in the elucidation of a refined 1.9 Å-resolution structure (Table S4.1). The complex crystallized in the C2 space group and the asymmetric unit contains one molecule of FabD crosslinked to a single AcpP.

Analysis of the 1.9 Å AcpP-FabD structure. The refined structure displays exceptional electron density for FabD, AcpP, and the synthetic crosslinker (Figures S4.3, S4.4). FabD comprises two subdomains, a larger α/β hydrolase (ABH) subdomain spanning residues 1 to 125 and 203 to 308, and a smaller ferredoxin-like (FL) subdomain spanning residues 126 to 202 (Figure 4.2a). The active site of FabD is accessed along a large groove at the interface of the two subdomains which also serves as the PPant/CoA binding site (Figure 4.2b). AcpP is bound between the two FabD subdomains abutting the aforementioned groove. In total, the AcpP-FabD interface buries 350 $Å^2$ of surface area, making it the smallest reported AcpP-PE interface to date.[42] The PPant arm extends from Ser36 of AcpP into the active site of FabD, where the α-carbon of the acetamide portion of the probe covalently attaches to the Cys92 mutant residue. The PPant arm makes a significant number of hydrophobic interactions derived almost exclusively from the FL subdomain of FabD, with the exception of Val280 from the ABH subdomain (Figure 4.2c). Asn160, Asn162 and Gln166 line the floor of the groove, forming hydrogen bonding interactions with the PPant hydroxyl and amide functional groups (Figure 4.2c). A sulfate ion from the crystallization buffer is bound in the active site and coordinates to the conserved Arg117 residue that forms a bidentate interaction with the terminal carboxylate of the malonyl substrate (Figures S4.1,

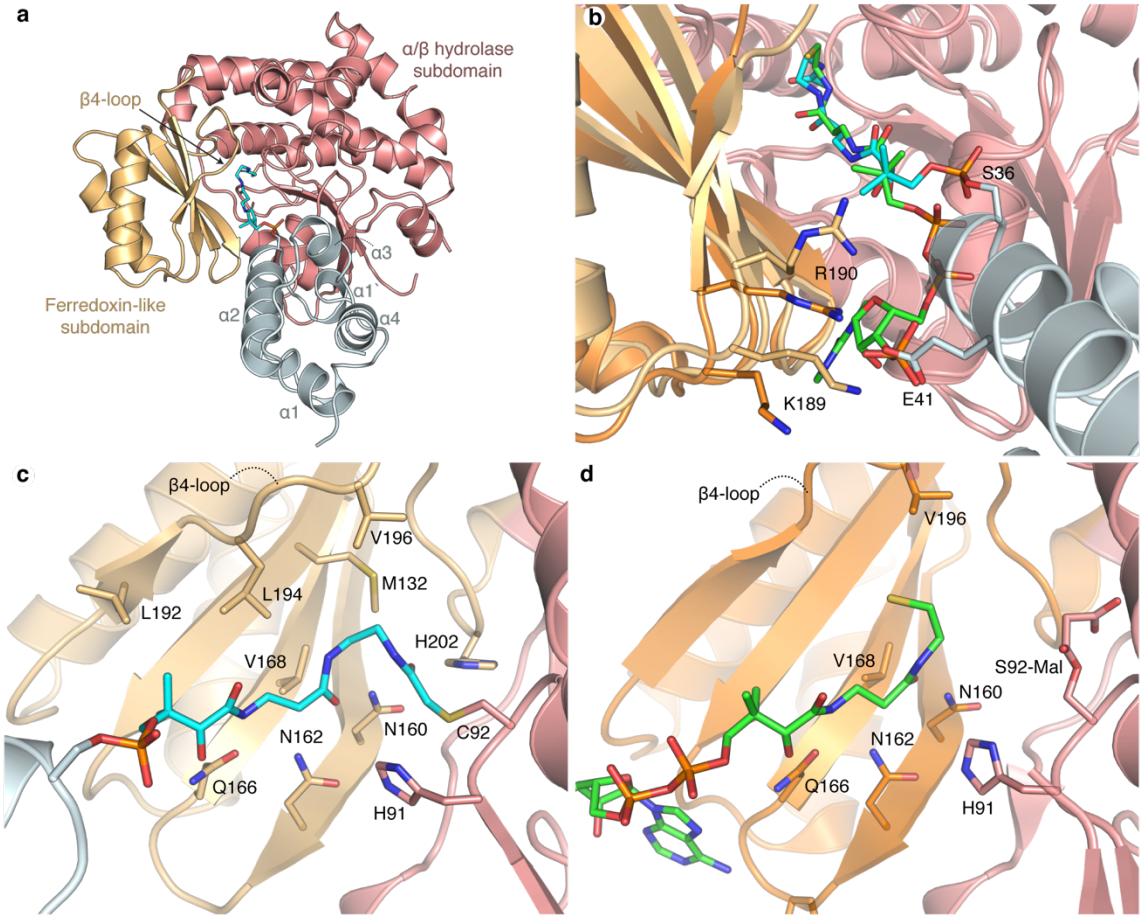

Figure 4.2: *AcpP-FabD crosslinked complex and PPant interactions.* **a**) Overall organization of the AcpP-FabD complex (PDB ID: 6U0J) **b**) Overlay of malonyl-CoA-bound FabD (orange, PDB ID: 2G2Z) and AcpP-FabD (light orange, PDB ID: 6U0J) highlighting CoA/PPant binding groove and the similarities in interactions between CoA and *holo*-AcpP. The PPant arm (carbons colored cyan) and CoA (carbons colored green) are found in similar positions and conformations, and the 3′-phosphate of the CoA ribose ring is found in the same position as Glu41 of AcpP. **c**) Interactions between the PPant arm (cyan) and FabD in AcpP-FabD structure (PDB ID: 6U0J). **d**) Interactions between CoA (green) and FabD in malonyl-CoA-bound FabD structure (PDB ID: 2G2Z). A 4 Å distance cut-off was used to display FabD interacting residues in panels **c** and **d**. Only the interactions with the FL subdomain are shown for clarity in panels **c** and **d**.

S5a).[50] The presence of the sulfate ion, the non-native thioether crosslinked bond, and the C-S bond length cause the carbonyl group of the probe to rotate away from the oxyanion hole, which is formed by the backbone amides of Gln11 and Leu93, and instead accepts two hydrogen bonds from the N_{δ} of Asn160 and the N_{ε} of His202 (Figures S4.1, S4.5b).

The FL and ABH subdomains in type I systems have been previously proposed to act as separate rigid bodies, with the FL subdomain capable of undergoing *en bloc* motions with respect to the larger ABH subdomain.[51–53] These studies suggest FL subdomain mobility may be in part responsible for the reported substrate promiscuity of the AT domain from murine FAS.[51,53] Given that FabD has undergone extensive structural characterization, we looked for potential changes in subdomain conformations induced by AcpP binding by performing a superposition using just the large ABH subdomains of *apo* FabD (PDB ID: 1MLA), malonyl-CoA-bound FabD (PDB ID: 2G2Z), and our AcpP-FabD crosslinked structure (PDB ID: 6U0J) (Figure S4.6). Indeed, these structural overlays show significant variations in the relative positioning of the two subdomains. The FL subdomain possesses a 5 Å, hinge-like displacement toward the ABH subdomain when comparing the *apo*-FabD and AcpP-FabD structures (Figure S4.6). The most notable structural changes induced by these subdomain motions are found in the loop exiting the β4 strand of the FL subdomain, referred to herein as the β4-loop. This loop translates to cover the top of the FabD active site and PPant binding tunnel and forms additional interactions between the two subdomains and the PPant moiety that are not present in either the *apo*-FabD (PDB ID: 1MLA) or the malonyl-CoA-bound FabD structures (PDB ID: 2G2Z) (Figure S4.7). Interestingly, the dihedral angles of residues in the β4-loop only differ at Ser197 and Val198 when comparing *apo*-FabD, malonyl-CoA-

bound FabD, and AcpP-FabD, suggesting that movement of this loop is largely dictated by the FL subdomain rigid body motion.

The FL subdomain, including the β4-loop, in the malonyl-CoA-bound FabD structure (PDB ID: 2G2Z) exists in an intermediate conformation between the *apo*-FabD (PDB ID: 1MLA) and AcpP-FabD structures (PDB ID: 6U0J) (Figure S4.6). This is likely due to the positioning of the free thiol from the hydrolyzed CoA moiety present in the active site that would sterically clash with Leu194 and Val196 on the β4-loop (Figure 4.2d). Despite these differences in conformation, the PPant arm of CoA and AcpP overlay almost identically in the two structures (Figure 4.2b) and form a conserved hydrogen-bonding network with Asn160, Asn162 and Gln166 along the floor of the PPant binding tunnel (Figure 4.2c,d). It is worth noting that mutation of conserved residues along the β4-loop that precede the catalytic histidine (His 201 in FabD) results in changes in substrate specificities for type I PKS ATs. This may indicate that domain motions and the repositioning of the β4-loop over the active site play key roles in determining AT substrate selectivity and activity.[11,30,54,55]

Analysis of the AcpP-FabD Interface. Here we describe the first type II FAS ACP-AT complex solved to date. Similar to all crosslinked AcpP-PE structures available (Figure S4.8),[44–47] electrostatic complementarity between AcpP and FabD facilitates molecular recognition, with the negatively charged AcpP interacting with a positive patch on FabD that likely drives initial association of AcpP and FabD (Figure 4.3a). However, the AcpP-FabD crosslinked structure also departs from canonical FAS ACP binding motifs previously reported.[42] It reveals a unique set of interfacial interactions between the two proteins involving the small helix on loop 1 of AcpP (α1') and the N-terminal portion of helix II (α2) (Figures 4.3b-d, S4.9). Additionally, unlike the dehydratases (FabA and FabZ) and

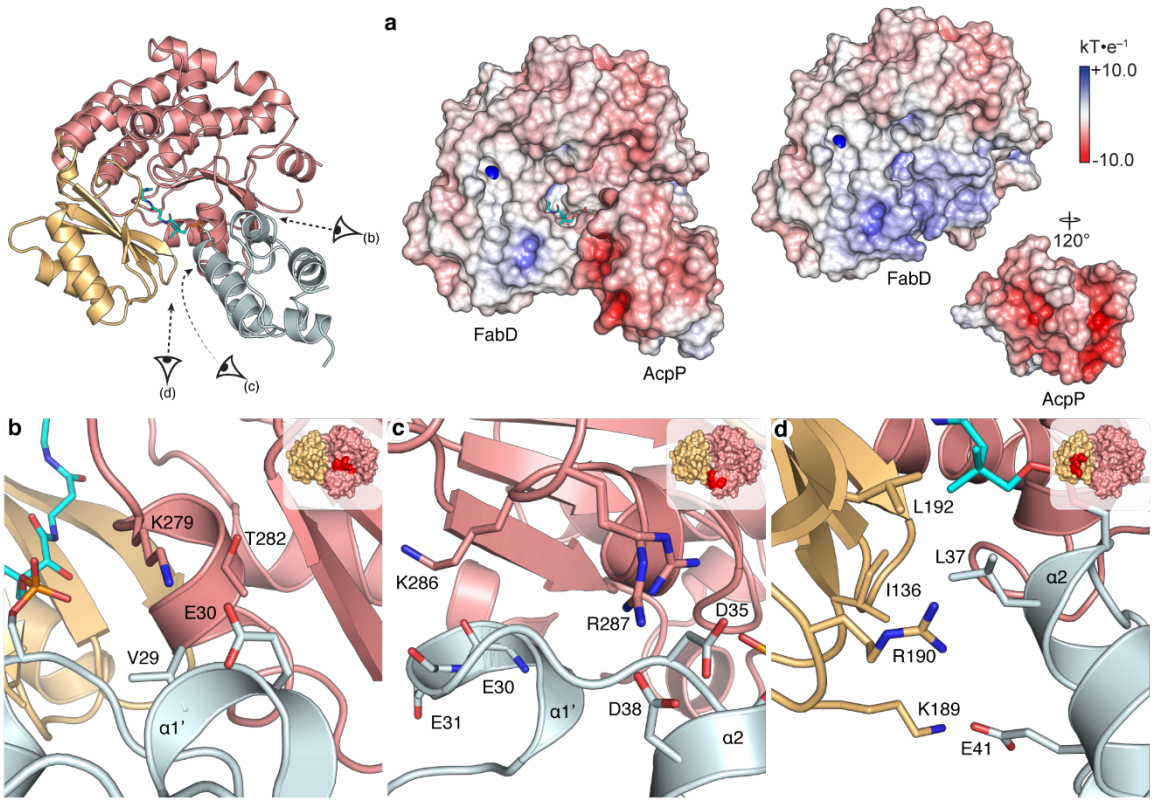

Figure 4.3: *AcpP-FabD interface* **a**). AcpP-FabD, FabD, and AcpP electrostatic potentials (ESP) mapped onto protein surface. In all cases, the ESP are mapped onto the "Connelly" surfaces of the complex and monomers using a blue to white to red color range, spanning from +10.0 kT•e^{-1} to –10.0 kT•e^{-1}. **b**) Region 1 of FabD-AcpP interface. **c**) Region 2 of FabD-AcpP interface. Arg287 was modelled in two conformations, and both are shown. **d**) Region 3 of FabD-AcpP interface. Arg190 delineates into two conformations, but only the conformation closest to AcpP is shown for clarity. A 4 Å distance cut-off was used to display AcpP-FabD interacting residues in panels **b-d**, and the location of specific regions on FabD are shown as insets in the top-right corner of each respective panel. Additionally, an overview of the AcpP-FabD complex showing perspective eyes for panels b-d is provided (top left). The ABH and FL subdomains of FabD, as well as AcpP, are shown in salmon, light orange and light blue, respectively.

elongating ketosynthases (FabB and FabF) in *E. coli* FAS, FabD makes no discernable contacts with helix III (α3) of AcpP (Figure S4.8). Notably, α3 interactions likely facilitate chain flipping[56] of AcpP-tethered cargo from the hydrophobic core of AcpP to the active sites of FabA, FabB, FabF and FabZ.[44,46,57] Since the PPant arm of FAS *holo*-ACPs does not sequester within the helical hydrophobic core (PDB IDs: 5H9H, 3GZM, 2M5R, 2FQ0), the chain flipping process required for catalysis in these latter ACP-PE complexes is likely not operative in the delivery of the PPant arm of *holo*-ACP to the FabD active site.[58–61] This may explain the lack of interfacial interactions involving α3 in the crosslinked AcpP-FabD structure.

The location of specific interactions of the AcpP-FabD interface can be delineated into three regions (Figure 4.3b-d). Region 1 comprises the C-terminal portion of the ABH subdomain, which forms interactions with α1' of AcpP. Lys279 of FabD forms a salt bridge with Glu30 of AcpP, and Val29 of AcpP fits into a hydrophobic pocket created by Lys279, Thr282, and Gly283 of FabD (Figure 4.3b).

Region 2 consists of Lys286 and Arg287, two conserved residues among bacterial type II MATs (Figure S4.10a). The key interactions in this region are between Arg287, modelled in two conformations, with both Asp35 and Asp38 at the top of AcpP's helix II flanking the PPant Ser36 (Figure 4.3c). Interestingly, the guanidinium group of Arg287 forms cation-π stacking interactions with the adenine ring in the malonyl-CoA-bound FabD structure (PDB ID: 2G2Z), demonstrating its importance for both AcpP and malonyl-CoA binding.[14,36,37,62]

Region 3 is defined by the interactions between the FL subdomain and AcpP. In this region, Leu37 of AcpP sits in a hydrophobic groove formed by Ile136 and Leu192, and Glu41

from AcpP's α2 forms a salt bridge with Lys189 of FabD (Figure 4.3d). Interestingly, overlays of AcpP-FabD and malonyl-CoA-bound FabD (PDB ID: 2G2Z) place the carboxylate side chain of Glu41 in the same location as the 3′-phosphate of the CoA ribose, indicating that CoA and AcpP form related interactions with FabD's interface region 3 (Figure 4.2b). Despite the similarity in position, the CoA 3′-phosphate coordinates with Arg190 instead of Lys189, which is rotated away in the CoA-bound structure (Figure 4.2b). Sequence alignments reveal that Lys189 is conserved among bacterial type II MATs, whereas Arg190 is conserved among both bacterial type II and eukaryotic mitochondrial MATs (Figure S4.10a). It is worth noting that the electron density for the side chains of residues Glu41, Lys189, and Arg190 is not well-defined. Glu41 and Lys189 have high B-factors and Arg190 resides in two conformations, which suggests that the side chains of these residues are dynamic. In total, these data indicate that both Lys189 and Arg190 form interactions with Glu41 of AcpP.

In accordance with literature precedent,[39,47,49,62–65] we investigated PPIs for AcpP-FabD by comparing the crosslinking efficiencies of a panel of FabD S92C interface mutants with AcpP loaded with a C2-α-bromo-pantetheinamide probe (Figures S4.10b-c, S4.11). Given that the FabD component of the interface is comprised almost exclusively of basic residues (Figure 4.3b-d), we generated three classes of FabD interface mutants: charge-neutralizing mutants (Arg to Ala or Lys to Ala), charge-conserving mutants (Arg to Lys), and charge-swapping mutants (Arg to Glu or Lys to Glu). The variants from the three regions have significantly reduced crosslinking efficiency compared to FabD S92C (Figure S4.10b-c). The results from these crosslinking studies validate the structural conclusions and support the importance of the identified interface residues for complex formation.

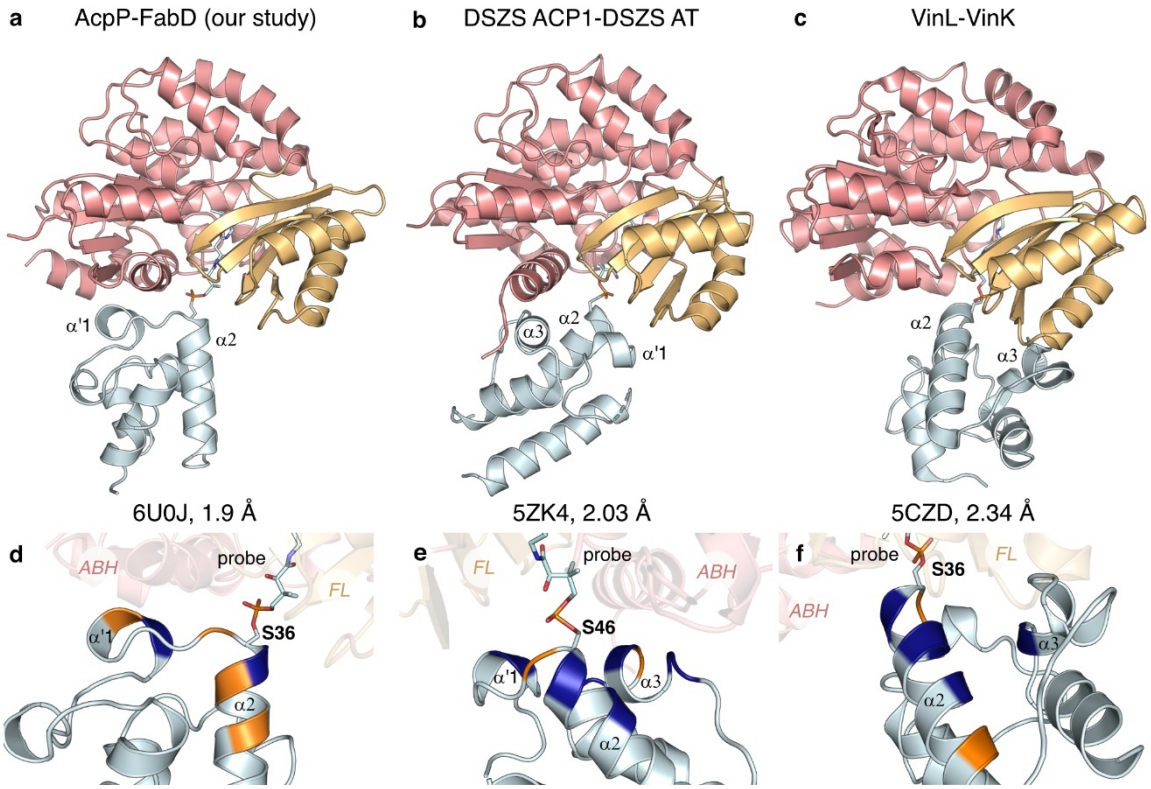

Figure 4.4: *Comparison of the AcpP-FabD complex with the ACP-trans-AT complexes DSZS ACP1-DSZS AT and VinL-VinK.* **a-c)** Cartoon representation of the AcpP-FabD, DSZS ACP1-DSZS AT and VinL-VinK complexes. The three complexes were aligned on FabD to better visualize the differences in ACP orientation. The FL and ABH subdomains of each AT are shown in light orange and salmon, respectively. The ACPs are colored in light blue. **d-f)** Close-up views at the ACP-AT interface for the three complexes displaying the nature of the interactions: blue, hydrophobic; orange: electrophilic. The interacting helices, catalytic serine and crosslinking probes are shown for each ACP. Note that e was rotated 180 ° from the above view to better visualize the interactions.

Structural comparison with *trans*-AT-ACP interfaces. To date, only two other AT-ACP covalent complexes have been reported and analyzed, namely the *trans*-AT VinK in a covalent complex with VinL,[38] and a second *trans*-AT from the disorazole synthase (DSZS) in a covalent complex with DSZS ACP1.[39] *Trans*-AT PKSs do not contain a *cis*-acting AT domain within their modules to deliver the extender units onto the ACP, but instead, standalone ATs serve this role. VinK transfers a dipeptide intermediate between two ACPs (VinL and VinP1LdACP on the loading domain of module 1) during vicenistatin biosynthesis. Disorazole synthase is initiated by its *trans*-acting AT which malonylates the ACP of module 1. Elucidation of the AcpP-FabD complex allows analyses of the common features and differences of ACP recognition between modular type I *trans*-AT PKSs and type II FAS ATs. The overall subdomain organization of the three ATs, FabD, VinK, and DSZS AT (26.3% and 39.4% sequence identity with FabD, respectively) is similar, but the orientation of the ACPs notably differ between the three complexes. (Figure 4.4a-c). As observed in the AcpP-FabD complex, electrostatic contacts are important for both ACP-*trans*-AT complexes; however, hydrophobic interactions are more prominent features at the DSZS ACP1-DSZS AT and VinL-VinK interfaces than at the AcpP-FabD interface (Figures 4.4d-f, S4.12-S4.13). The differences observed between these structures calls for a deeper look into the structural elements of the AT enzyme class.

Effect of PPIs on FabD's transacylation reaction. We performed kinetic analyses of FabD mutants by using a continuous, coupled fluorometric assay *in vitro* (Figure S4.14).[66] We assayed our panel of FabD interface mutants along with three additional AcpP mutants, E30A, D38A, and E41A. These three AcpP residues participate in salt bridges across the interface of regions 1, 2, and 3, respectively (Figure 4.3b-d). All constructs were analyzed by

SDS-PAGE and mass spectrometry (Figure S4.15, Table S4.2). The transacylation rates of the variants were measured at two concentrations of AcpP: 50 μM and 200 μM, which correspond to the concentrations of *holo*-AcpP at the K_M value and at saturation, respectively, for the wt system (Figure S4.16). The reaction rates were normalized to the transacylation rates of wt *holo*-AcpP by wt FabD at the respective concentration of AcpP. This approach enables us to compare the effect of each interface mutant on FabD's activity (Table 4.1).

At ACP_{200}, only three FabD variants show a decrease in activity compared to wt, namely K189A, K279A, and K279E. At ACP_{50}, all tested FabD mutants have reduced activity compared to wt, except for region 2 variants R287K and R287A that remain as active as wt, and R287E shows a slight loss in activity. We hypothesized that upon mutation of Arg287 to alanine, the fairly conserved Lys286 (Figure S4.10a) might have the rotational freedom to interact with Asp38 and compensate for the loss of the salt bridge between Arg287 and Asp38. We therefore tested the double mutant K286A/R287A, which remains as active as wt FabD for both AcpP concentrations. On the contrary, mutation of Lys279 in region 1 to either alanine or glutamate results in a larger decrease in relative activity as compared to FabD region 2 variants. Similarly, mutating Lys189 from region 3 also more significantly affects FabD activity, with a greater effect seen with the charge-swapped mutant, K189E, as compared to the charge-neutralized variant K189A. To determine whether Arg190 participates in AcpP recognition despite its lack of discernable interactions in our AcpP-FabD structure, we evaluated the catalytic activity of R190A and K189A/R190A mutants. The R190A variant is similar in activity to wt, while the double mutant K189A/R190A is less active than K189A but faster than K189E. These data suggest that the interactions with the FL subdomain are mediated by both Lys189 and Arg190.

Table 4.1: *Quantification of the transacylation rates of AcpP-FabD interface mutants*. Reaction conditions: 28 °C, 50 mM sodium phosphate pH 6.8, 1 mM EDTA, 0.5 mM TCEP, 2 mM α-ketoglutarate, 0.4 mM NAD^+, 0.4 mM thiamine pyrophosphate, 15 mU/100 µL α-ketoglutarate dehydrogenase, and 0.02 nM FabD. $[ACP]_{50}$ corresponds to 50 µM *holo*-AcpP and 50 µM malonyl-CoA; $[ACP]_{200}$ corresponds to 200 µM *holo*-AcpP and 200 µM malonyl-CoA. The activity of each interface mutant measured at the fixed concentration of AcpP indicated and was normalized to the corresponding activity of wt FabD, with wt AcpP for each tested condition (*see S.I. Relative activities*). Regions 1, 2 and 3 are shown in crimson, red, and orange, respectively. Experiments were run at least in triplicate, and data shown are reported as mean ± standard deviation.

FabD	AcpP	Relative activity at $[ACP]_{50}$ (%)	Relative activity at $[ACP]_{200}$ (%)
wild type	wild type	100.0	100.0
K279A	wild type	30.3 ± 6.9	23.9 ± 3.5
K279E	wild type	30.6 ± 7.6	30.2 ± 5.2
wild type	E30A	85.1 ± 7.9	99.5 ± 11.1
K279A	E30A	84.7 ± 10.3	n.a
K279E	E30A	14.2 ± 7.5	n.a
R287K	wild type	93.6 ± 3.2	102.7 ± 8.5
R287A	wild type	92.7 ± 9.4	89.0 ± 12.9
R287E	wild type	81.1 ± 7.8	99.6 ± 6.2
wild type	D38A	69.5 ± 4.8	83.2 ± 9.3
R287K	D38A	55.7 ± 5.4	n.a
R287A	D38A	77.3 ± 3.2	n.a
R287E	D38A	53.1 ± 6.9	n.a
K286A	wild type	63.1 ± 10.3	99.0 ± 10.5
K286A/R287A	wild type	96.8 ± 13.7	104.9 ± 13.9
K286A/R287A	D38A	77.9 ± 1.1	n.a
K189A	wild type	67.9 ± 7.3	77.4 ± 17.3
K189E	wild type	26.2 ± 4.8	104.0 ± 2
wild type	E41A	90.1 ± 1.9	95.8 ± 4.1
K189A	E41A	30.6 ± 2.1	n.a
K189E	E41A	10.6 ± 3.0	n.a
R190A	wild type	103.5 ± 9.5	n.a
K189A/R190A	wild type	40.1 ± 4.7	114.1 ± 8.7
K189A/R190A	E41A	15.2 ± 1.8	n.a
L192A	wild type	67.5 ± 8.2	101.0 ± 13.4

In addition to kinetically evaluating FabD interface residues, we also analyzed the transacylation rates of AcpP interface mutants, E30A, D38A, and E41A that coordinate interactions with FabD regions 1, 2, and 3, respectively. Interestingly, these mutations are less detrimental to FabD transacylation rates than their corresponding FabD interface mutants. In order to determine if the AcpP and FabD interface mutations were additive, we eliminated the three salt bridges at the interface by testing FabD interface mutants with their respective AcpP mutant counterparts. While assays of AcpP D38A and region 2 FabD mutants result in no more than a 50% drop in activity for all combinations tested, significantly slower transacylation rates were observed by combining mutant pairs from regions 1 and 3.

Results from all tested FabD and AcpP mutants demonstrate that the AcpP-FabD interface can tolerate mutations of residues that appear to be critical from the static crystal structure. We find that mutations on the FabD interface are more detrimental than their corresponding AcpP mutants, which may be due to the dynamic nature of AcpP. Our activity assays also show that mutating key residues on regions 1 and 3 of the FabD interface seem to influence the transacylation reaction more than region 2. Nevertheless, most mutations, even double mutants assayed with their corresponding AcpP mutant counterparts, do not abolish FabD's activity.

Dynamic analysis of the AcpP-FabD interface. The tolerance of the FabD interface to mutations, as indicated by our kinetic analyses, suggests flexible interactions between AcpP and FabD. Therefore, to further our understanding of the biomolecular processes that contribute to AcpP-FabD recognition, we subjected 17 protein assemblies, consisting of wt FabD and FabD mutants in the *apo*-, malonyl-CoA-, and malonyl-AcpP-bound states (Table S4.3), to MD simulations. We performed three independent 514 ns production-grade

trajectories for each wt and mutant system, resulting in a total of 32.382 μs of simulation data. General analysis of these trajectories can be found in the SI: Molecular Dynamics Simulations Protocols, as well as in the Supplementary Figures S4.17 to S4.24.

We analyzed trajectory data of the wt and mutant malonyl-AcpP•FabD complexes (where the "•" represents a non-covalent complex) in order to propose a time-resolved understanding of the noncovalent interactions most critical for AcpP•FabD recognition. To do so, we identified all pairwise AcpP and FabD interactions that form over the course of the simulations using a 3.5 Å distance cutoff criterion (Figure 4.5). This analysis generally shows that the interactions at the AcpP•FabD interface are dynamic, and a number of interactions not observed in the x-ray structure are identified during the course of the simulations. Interestingly, none of the hydrophobic interactions identified in the AcpP-FabD structure were observed computationally (Figure 4.5). In contrast, the salt bridges identified in the x-ray structure are observed over the course of the simulations; however, they are in rapid exchange with an alternate set of salt bridges that are not resolved experimentally (Figure 4.5b). For example, the most frequently sampled salt bridge interaction between AcpP and FabD is a contact between Glu41 and Arg190 not present in the x-ray structure. Simulations of the malonyl-AcpP•FabD mutant complexes show the same general trend as the wt system and indicate that there are compensatory interactions that can be formed to stabilize these complexes despite the removal of key interface residues (Figure 4.5).

Given the rotational and translational motion of AcpP at the interface, we reasoned that these conformational changes may affect substrate organization in the FabD binding pocket. Interestingly, the contact between the malonyl carboxylate of malonyl-AcpP and the FabD active site Arg117, as well as the Ser92-His201 catalytic dyad distance, are maintained

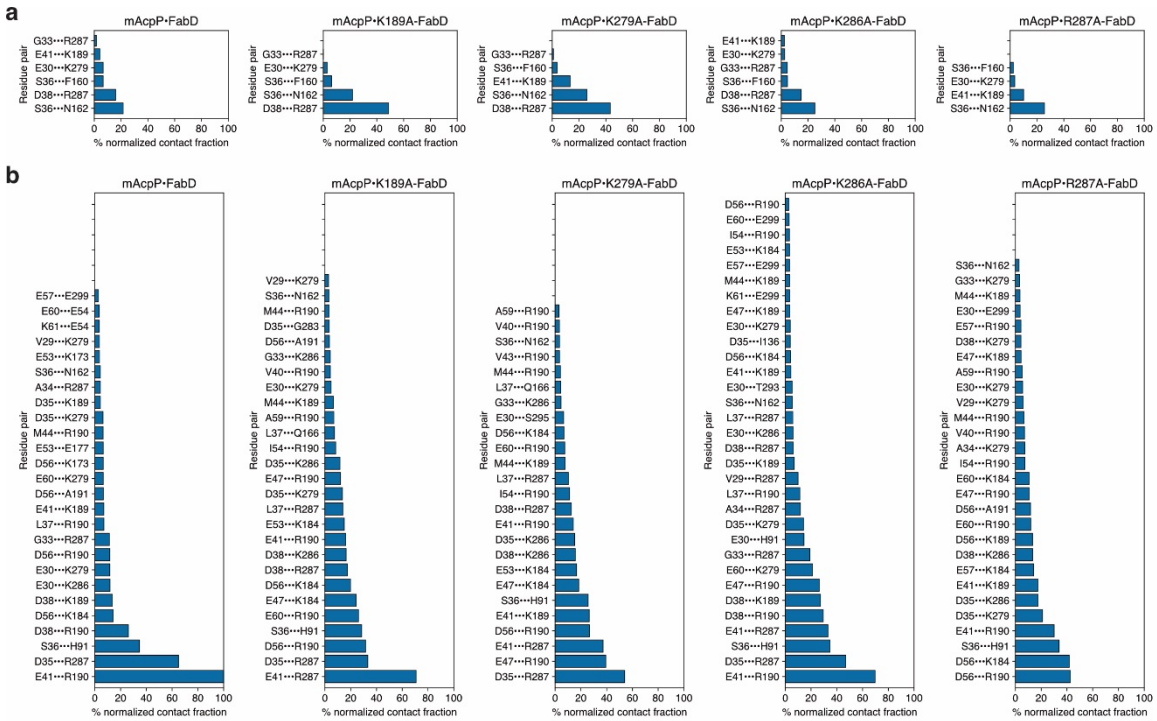

Figure 4.5:*Time-resolved analysis of the contacts formed between FabD (wt and four variants) and its binding partner malonyl-AcpP (mAcpP).* Contacts from the initial conditions and contacts formed during the course of the simulations are shown in panels **a** and **b**, respectively. The analyzed FabD (wt, K189A, K279A, K286A or R287A) is indicated on the top of each bar graph. Residues listed on the left side of the interaction pair correspond to AcpP and those on the right side of the pair correspond to FabD. The bar graphs indicate the normalized total contact fraction between FabD and malonyl-AcpP. The contact fraction is defined as the total fraction of simulation data in which a residue pair is engaged in an intermolecular contact. A distance criterion of 3.5 Å or less between a pair of heavy atoms defines such a contact. Only pairwise contacts with contact fractions (prior to normalization) greater than or equal to 0.10 are included in the plots above.

throughout the simulations despite the positional variation of AcpP (Figures S4.25-S4.26). Taken together, these data suggest significant plasticity in the AcpP•FabD interface and provide a rationale for FabD's tolerance to interface mutations, as AcpP can adopt multiple conformations at the FabD interface, while still properly positioning substrate in the active site for catalysis. In addition, our findings corroborate the smaller reduction of transacylation activity for AcpP mutations as compared to corresponding FabD mutations, as AcpP can rotate at the interface to form compensatory interactions (Figure 4.5).

Substrate-induced reorganization of FabD active site. To determine the effect of substrate binding on active site organization, we performed a time-resolved analysis of interactions involving the conserved active site residues Ser92, Arg117 and His201. The positively charged Arg117 residue has been shown to influence the preferences of ATs for α-carboxy-CoA substrates over α-descarboxy analogs. For example, the R117A mutant of FabD loads a number of α-descarboxy-CoA derivatives, including acetyl-CoA.[35] Furthermore, Rangan and Smith showed that a similar Arg to Ala mutant of the malonyl-CoA/acetyl-CoA:ACP transferase of animal FAS results in a 100-fold decrease in its malonyl-CoA transferase activity, while its acetyl-CoA transferase activity is enhanced 6.6-fold.[67] Studies by Dunn, Cane, and Khosla indicate that substrate discrimination occurs before the CoA substrate undergoes reaction at the AT active site and not by preferential hydrolysis of "misacylated" ATs after transacylation.[30]

MD simulations of *apo*-FabD suggest a possible mechanistic explanation for the broad role of Arg117 in regulating substrate selectivity in MATs. Analysis of simulation data of *apo*-FabD shows that in the absence of a substrate, the average distance between the Oγ of Ser92 and the center of geometry (COG) of Arg117's terminal guanidinium moiety is 3.68

Å (Figure 4.6a). It must be noted that measuring from the arginine, histidine, or carboxylate COG reports distances larger than are typical of non-covalent interactions.[68] Thus, simulation data show that the dyad residues, Ser92 and His201, are not preorganized for catalysis in the *apo* state because Ser92 interacts stably with Arg117 (Figure 4.6a). Interestingly, simulations of *E. coli* malonyl-CoA•FabD show that α-carboxy-CoA substrate binding disrupts the Ser92-Arg117 interaction which in turn restores the Ser-His dyad (Figures S4.25-S4.29). The average distance between the COG of Arg117 and the COG of malonyl carboxylate are 2.73 Å and 2.79 Å in simulations of wt malonyl-CoA•FabD (Figure S4.24) and wt malonyl-AcpP•FabD (Figure S4.29), respectively, suggesting a strong salt bridge interaction between substrate and enzyme in the bound state. With Arg117 engaged with the substrate, the catalytic dyad is restored, as the average distance between the Oγ of Ser92 and His201's $N_{\varepsilon}2$ sampled computationally is 3.40 Å and 2.95 Å for malonyl-AcpP•FabD and malonyl-CoA•FabD respectively, more than 1 Å shorter than what is observed over the course of simulations of *apo*-FabD (Figures 4.6a-c). These results suggest that substrate binding organizes the FabD active site for catalysis and provides an explanation for FabD's (and MATs more broadly) preference for malonyl-CoAs or malonyl-AcpP over acetyl-CoA.[35]

Rigid body subdomain motions control the disposition of substrate-recognizing residues. Recent studies on the murine FAS AT have suggested that rigid body FL and ABH subdomain motion may play a role in determining AT substrate selectivity.[51,53] Superpositions of our AcpP-FabD complex with the *apo*- and malonyl-CoA-bound FabD structures provide additional evidence for the occurrence of such motions (Figure S4.6). Moreover, biochemical and structural data implicate residues found on the β4-loop of the FL

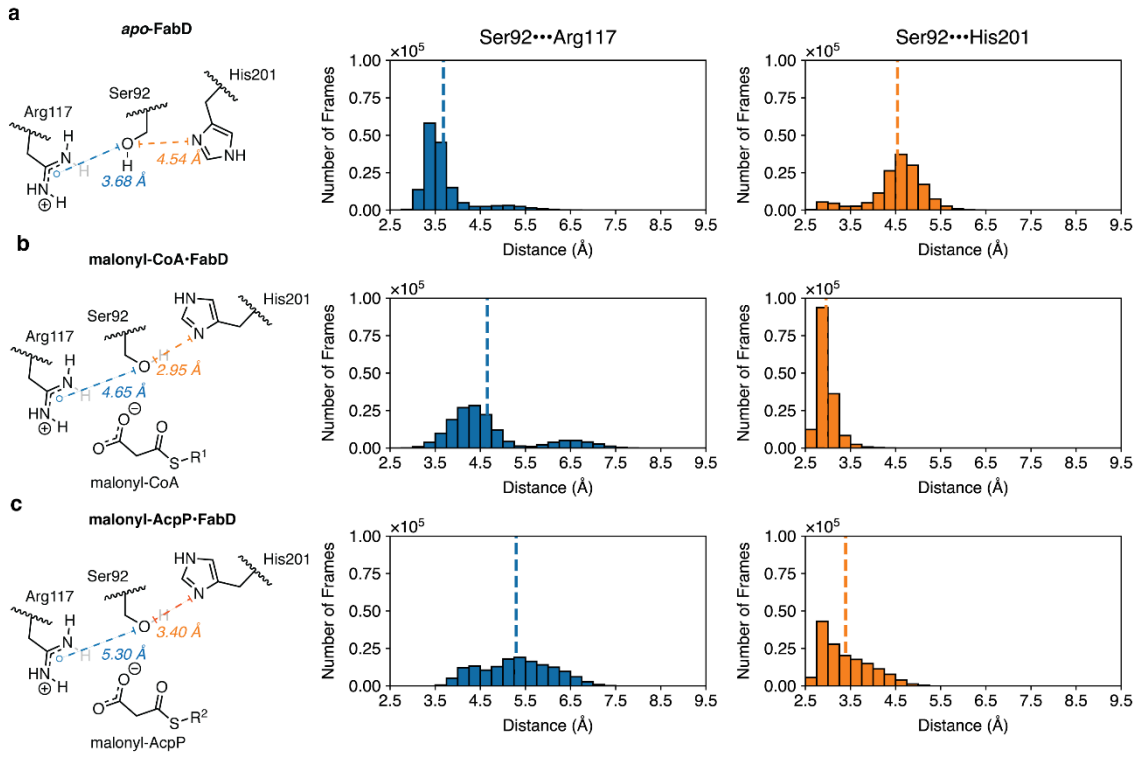

Figure 4.6: *Analysis of key active site distances sampled in the apo- and substrate-bound states of FabD.* Distribution of distances between two pairs of active site residues Ser92•••His201 and Ser92•••Arg117 sampled over the course of simulations of wt *apo*-FabD (**a**), malonyl-CoA•FabD (**b**), and malonyl-AcpP•FabD (**c**). The distance between Ser92 and His201 is measured using the Oγ of Ser92 and Nε of His 201, while the Ser92•••Arg117 distance is measured using the Oγ of Ser92 and the COG of Arg117's guanidium moiety. Simulation data written every 0.5 ps were binned to prepare histograms using a bin width of 0.25 Å.

subdomain, in particular those that immediately precede the catalytic histidine of ATs (His201 in FabD), play a role in determining AT preferences for α-branched *vs.* non-branched α-carboxy-CoA substrates.[11,30,54,55] These residues (Val198, Ser199, and Phe200 in FabD) define part of the enzyme's active site pocket and their steric bulk permits or prevents the binding of α-branched CoA substrates. We reason that rigid body motion of the FL subdomain, if present, may play a role in organizing the active site to preferentially accept either branched or non-branched CoA substrates. Therefore, we performed principal component analysis (PCA) to identify and highlight large-scale motions of the FL and ABH subdomains that may impact the activity and substrate specificity of FabD. Our analysis incorporates coordinate data from wt and mutants of *apo*-FabD (10.794 μs of simulation data), malonyl-CoA•FabD (9.252 μs of simulation data), and malonyl-AcpP•FabD (9.252 μs of simulation data).

Projections of the first principal component (determined via PCA) onto our coordinate data supports the hypothesis that the FL and ABH subdomains act as rigid bodies involving the displacement and rotation of the smaller FL subdomain away from ABH subdomain (Figure 4.7). That this motion is represented by the first principal component, the orthogonal component with the largest variance (*i.e.*, most dominant "mode" describing FabD motion), supports its role as an essential feature of FabD's function. A comparison of the first principal components generated from the dataset described above indicates that, as suggested by the comparison of x-ray structures presented in Figure S4.6, the FL subdomain moves independently of the ABH subdomain (Figure 4.7). The rigid body motions evaluated computationally disambiguate a motion of FL subdomain towards and away from the ABH domain to gate substrate access to and from the active site. In addition to active site gating,

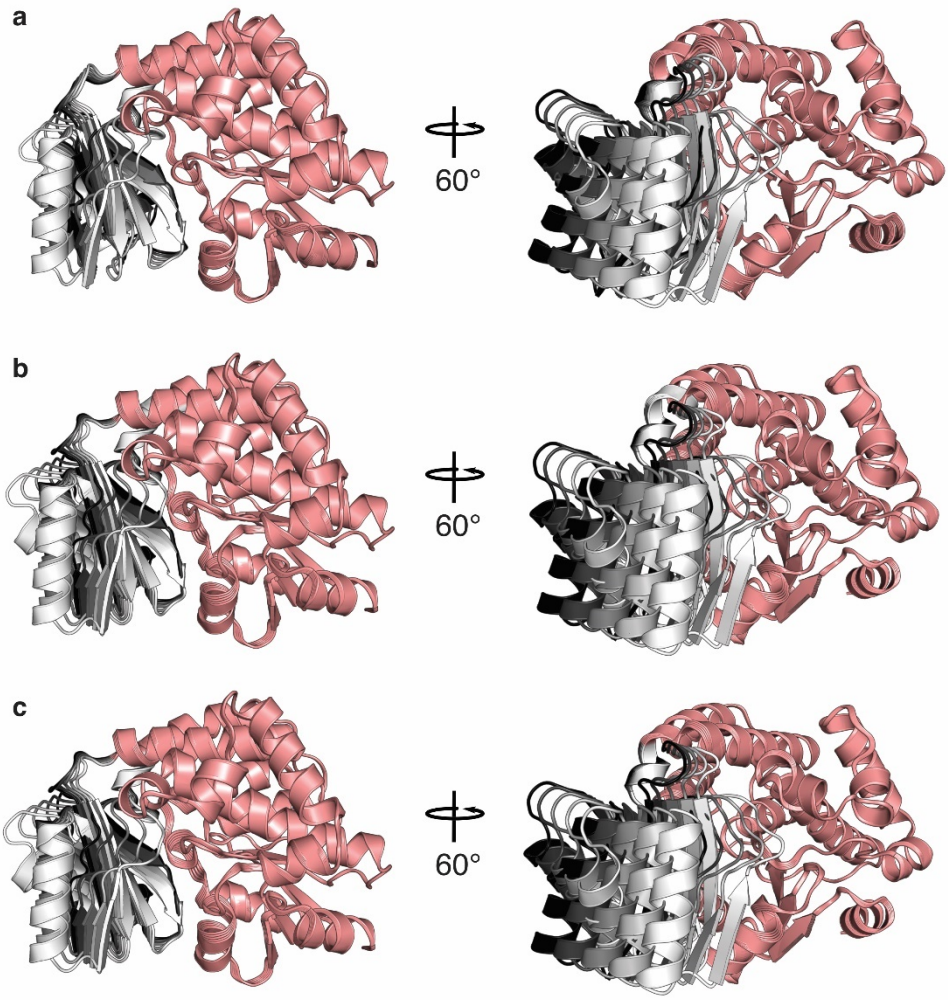

Figure 4.7: *Projection of principal component analysis data into coordinate space*. Overlaid snapshots of the pseudo-trajectories illustrating the 1st mode of motion of the FabD monomer portions of **a**) *apo*-FabD, **b**) malonyl-CoA•FabD, and **c**) malonyl-AcpP•FabD. The ABH subdomains are colored salmon while the FL subdomains are colored based upon the distance between the FL subdomain, such that more darkly colored subdomains are further from the ABH subdomain.

this rigid body motion also results in the movement of the β4-loop towards the base of the active site, not only organizing the His201 for catalysis, but also positioning the key substrate-sensing residues Val198, Ser199, and Phe200 to selectively interact with *E. coli* FabD's preferred substrate (Movies S1-S3).

Conclusion

In this study, we use *E. coli* type II FAS as a structural and mechanistic model to better understand type II ACP-AT interactions and their catalytic role in fatty acid biosynthesis. Utilizing a pantetheinamide covalent crosslinking probe, we trapped and crystallized the *E. coli* ACP, AcpP, in complex with FabD, allowing us to elucidate the first crystal structure of a type II ACP-AT complex at 1.9 Å resolution. The AcpP-FabD binding mode is different than previously described AcpP complexes and represents the smallest AcpP-PE interface reported to date. Despite the small number of experimentally determined interfacial interactions, mutation of these interface residues does not result in significant reductions in FabD transacylation activity. Long timescale MD simulations of AcpP in complex with wt FabD and FabD interface mutants demonstrate that AcpP can undergo considerable rotational and translational motion at the FabD interface while still properly positioning its PPant-tethered substrate for catalysis. These results are in line with kinetic analyses of FabD interface mutants and suggest a high-plasticity interface dominated by polar and charged interactions that are in rapid exchange. Furthermore, MD analysis of FabD in both its liganded and unliganded states corroborate the presence of *en bloc* rigid body motions of its FL and ABH subdomains and provide additional insights into Arg117's role in substrate mediated reorganization of the FabD active site. Taken together, these findings

represent a significant advancement in our understanding of type II ACP-AT interactions, AT dynamics, and AT substrate selectivity. The structural, biochemical, and computational analyses of these systems reported herein represent another necessary step toward a broader and more complete understanding of PPIs in type II FAS and natural product biosynthesis.

Supplementary Information

A. Biological Protocols

A1. Expression and purification of FabD and AcpP wt and mutants. The genes encoding for FabD and AcpP were inserted in a pET28b vector with a cleavable N-terminal His_6-tag. The proteins (wt and variants) were expressed in *E. coli* BL21(DE3) cells. For each variant, a single colony was selected on the agar plate and grown overnight at 37 °C in 5 ml Luria-Bertani (LB) medium supplemented with 50 µg/ml kanamycin (KAN). Then, 1 L of LB medium (50 µg/mL KAN) was inoculated with the 5 mL-LB preculture and incubated at 37 °C until an optical cell density at 600 nm of 0.7 was reached. After induction with 0.5 mM IPTG, cells were grown for 3 h at 37 °C. Cells were harvested by centrifugation (500 RCF, 30 min) and the pellet was stored at – 20 °C. Cells were resuspended in lysis buffer (50 mM Tris pH 8.0; 300 mM NaCl; 10 % glycerol) and lysed by sonication. After centrifugation (17.400 RCF, 45 min), the supernatant was transferred to Ni-NTA-column and washed with 10 CV of lysis buffer and 2 x 10 mL lysis buffer containing 10 mM imidazole. The proteins were eluted with elution buffer (lysis buffer containing 250 mM imidazole). All FabD and AcpP mutants expressed with yields comparable to the wt proteins, ranging from 25 ± 5 and 15 ± 5 mg of protein / L of LB, respectively. FabD wt and variants were dialyzed twice over 1 L of dialysis buffer at 4 °C (50 mM phosphate pH 6.8, 150 mM NaCl, 0.5 mM TCEP and 10 % glycerol), aliquoted, frozen in liquid nitrogen and stored at -80 °C. AcpP wt and variants (expressed as a mixture of *apo* and *holo* forms) were subjected to His_6-tag cleavage by thrombin and the resulting His_6-tag free AcpPs were purified using Ni-NTA-column

supplemented with Benzamidine Separophore (bioWorld). The resulting *apo*-/*holo*-AcpPs were then converted to their *holo* form.

A2. FabD S92C thrombin His_6-tag cleavage. The His_6-tag of FabD S92C (purified as reported above) was cleaved using bovine thrombin (2 U per 1 mg protein) overnight at 6 °C while dialyzing against dialysis buffer (50 mM Tris, 150 mM NaCl, 10% glycerol, pH 8.0). Resulting solutions were re-purified using Ni-NTA resin (Thermo Fisher Scientific) to remove un-cleaved proteins. The resulting His_6-tag free FabD was further purified by FPLC using the HiLoad Superdex 200 (GE Biosciences) size exclusion column. The eluted protein was collected and concentrated to 2-4 mg/mL using Amicon Ultra Centrifuge Filters (MilliporeSigma) with 10 kDa molecular weight cut off.

A3. *Apo*-AcpP loading and C2-α-bromo-*crypto*-AcpP purification. C2-α-bromo-pantetheinamide crosslinkers were loaded onto *apo*-AcpP using a "one-pot" chemoenzymatic method.[69] This method utilizes the CoA biosynthetic enzymes (CoaA, CoaD, CoaE) to form CoA analogues and a phosphopantetheinyl transferase (PPTase, Sfp) to load them onto *apo*-AcpP, resulting in *crypto*-AcpP. Final reaction concentrations: 1 mg/mL *apo*-AcpP, 0.04 mg/mL Sfp, 0.01 mg/mL CoaA, 0.01 mg/mL CoaD, 0.01 mg/mL CoaE, 50 mM potassium phosphate pH 7.2, 12.5 mM $MgCl_2$, 1 mM DTT, 0.2 mM C2-α-bromo-pantetheinamide, and 8 mM ATP. The stock solution of C2-α-bromo-pantetheinamide crosslinking probe was prepared in DMSO at a final concentration of 50 mM. Reactions were incubated at 37 °C for 16 h and then purified by HiLoad Superdex 75 (GE Biosciences) size exclusion column. The eluted protein was collected and concentrated

using Amicon Ultra Centrifuge Filters (Millipore Sigma) with 3 kDa molecular weight cut off up to a concentration at 1-3 mg/mL.

A4. Production and purification of AcpP-FabD complex for crystal trials. The crosslinking reaction was carried out by mixing C2-α-bromo-*crypto*-AcpP with His_6-tag free FabD S92C at 2:1 (C2-α-Bromo-*crypto*-AcpP:FabD S92C) ratio at 37 °C for 16 h. Reactions were analyzed by 12 % SDS PAGE. Crosslinked AcpP-FabD complex was purified by a Ni-NTA resin (Thermo Fisher Scientific), allowing the removal of uncrosslinked His_6-tag cleaved FabD S92C from the reaction mixture. The bound AcpP-FabD complex and was eluted from the column using 250mM imidazole. The resulting fractions containing the AcpP-FabD complex were purified on a HiLoad 16/600 Superdex 200 PG (GE Biosciences) size exclusion column using minimal buffer (12.5 mM Tris, 100 mM NaCl, pH 8.0). The resulting protein complex was greater than 95 % in purity, determined by SDS PAGE, and was concentrated to 8 mg/mL using Amicon Ultra Centrifuge Filters (MilliporeSigma) with 10 kDa molecular weight cut off. The concentrated crosslinked complex was immediately used for protein crystallization or flash-frozen and stored in –80 °C freezer for later use.

A5. Crystallization, data collection, and refinement. The crystals of the AcpP-FabD crosslinked complex were grown by vapor diffusion using the hanging drop method at 6 °C. In detail, 1 μL of crosslinked complex (8 mg/mL) was mixed with 1 μL of corresponding mother liquor and the mixture was placed inverted over 500 μL of the well solution (hanging-drop method). The AcpP-FabD complex crystallized in 2.3-2.7 M $AmSO_4$, 1% PEG 400, and 0.1 M sodium cacodylate pH 6-7. These conditions initially yielded

multiple yellow spherulites that eventually resulted in numerous small needle-like crystals in 1-2 weeks. The best well condition (2.5M $AmSO_4$, 1% PEG 400, pH 7.0) resulted in a few small ovular plates (diffracted to 1.9 Å). All data were collected at the Advanced Light Source (ALS) synchrotron at Berkeley. Data were indexed using iMosflm[70] then scaled and merged using the aimless program from the CCP4 software suite.[71] Scaled and merged reflection output data was used for molecular replacement and model building in PHENIX.[72] Phases were solved using molecular replacement using FabD (PDB ID: 1MLA) as a search model with program Phaser from the PHENIX software suite. AcpP (PDB ID: 2FAC) was manually placed and rebuilt in the residual electron density using Coot.[73] The parameter file for the covalently bonded 4'-phosphopantetheine was generated using eLBOW in the PHENIX software suite.[74] Manually programmed parameter restraints using values provided by Jligand (CCP4)[75] were used to create the associated covalent bonds between 4'-phosphopantetheine to Ser36 and Cys92 during refinement.

A6. AcpP holofication for kinetic assay. *holo*-AcpP (wt or mutants) was prepared as previously described.[76] Briefly, AcpP (*apo*/*holo*) was incubated at 37 °C overnight in the presence of the phosphopantetheinyl transferase Sfp from *Bacillus subtilis*. Final reaction concentrations were the following: 50 mM phosphate pH 6.8, 50 mM NaCl, 0.5 mM TCEP, 12.5 mM $MgCl_2$, 1 mM coenzyme A, 0.05 mg/mL Sfp and 2.2 mg/mL AcpP. The completion of the reaction was determined by urea PAGE (Figure S4.15, 4.2b) and mass spectrometry (Table S4.2). The resulting *holo*-AcpP was further purified on a Superdex 75 HiLoad 16/60 size exclusion chromatography (SEC) column equilibrated with buffer (50 mM sodium phosphate pH 6.8, 125 mM NaCl, 5 % (v/v) glycerol, 0.5 mM TCEP). The eluted AcpP was

collected, concentrated using Amicon Ultra Centrifuge Filters (Millipore) with 3 kDa molecular weight cut off, frozen in liquid nitrogen and stored at -80 °C.

A7. Site-directed mutagenesis. FabD and AcpP mutants (except FabD S92C and AcpP D38A) were generated by polymerase chain reaction (PCR) amplification process using the primers listed in Table S4.4. FabD S92C and AcpP D38A constructs were provided from previous studies.[44,48] While D35 interacts with R287 on our structure (Figure 4.3), it is part of the highly conserved DSL motif at the N-terminus of helix II that serves as a recognition sequence and the site of PPant modification by ACPS, the holo-AcpP synthase in *E. coli*.[77] Mutating Asp35 would result in the apo form of any AcpP variant and was therefore not further investigated.

A8. α-Ketoglutarate dehydrogenase (KDH) coupled activity assay. The KDH coupled assay (Figure S4.14) used in this study was adapted from previous work. [51,66,78] Briefly, all enzymatic reactions were in a final volume of 100 µl and performed in 96-well half-area plates (Corning, Fisher Scientific). NADH fluorescence was monitored using a Varioskan Lux microplate reader (Thermo Scientific) at the excitation and emission wavelengths of 340 and 460 nm, respectively. The background reaction rate of this assay was determined in the absence of FabD and subtracted to each of the reactions performed in the presence of FabD. Equidistant kinetic measurements were taken every 5 s for 5 min at 28 °C.

A9. Analysis of kinetic data. Kinetic data were analyzed with Origin software. Data points from 20–120 s were fitted by linear regression to give the initial velocity of substrate

turnover. The averages of triplicates were calculated, and the background reaction rate subtracted. Relative fluorescence units (RFU) were converted into concentrations (μM) using a calibration curve (Figure S4.14).

A10. Michaelis-Menten kinetics. The Michaelis-Menten parameters of FabD transacylation reaction have been previously reported.[32,33,66] However, to ensure that we would perform our mutagenesis analysis at the expected AcpP concentrations (1x K_M (wt AcpP) and 4x K_M (wt AcpP)), we determined those parameters as well. The final concentrations of all reagents to determine K_M (AcpP) and K_M (malCoA) were: 50 mM sodium phosphate pH 6.8, 0.5 mM TCEP, 1 mM EDTA, 2 mM α-ketoglutaric acid, 0.4 mM NAD^+, 0.4 mM TPP, 15 mU/100 μL KDH, 0.025 mg/mL BSA, 10-250 μM *holo*-AcpP wt and 200 μM malCoA or 200 μM *holo*-AcpP wt and 1-100 μM malCoA, 0.02 nM FabD wt. The data obtained by the KDH assay were fitted to the function:

$$\nu = kcat \cdot [substrate] / (K_M + [substrate]) \qquad \text{eq.1}$$

The corresponding k_{cat} and K_M parameters are indicated on each graph (Figure S4.16).

A11. Relative activities of FabD and AcpP mutants. To most accurately report the effect of each mutation on FabD activity, each rate of transacylation reaction catalyzed by a FabD variant, or with AcpP variant as substrate, or both, was normalized to the reaction rate catalyzed by wt FabD with wt AcpP at the corresponding concentration of substrate for each replicate. Therefore, the relative rate of wt *holo*-AcpP malonylation catalyzed by wt FabD is set to 100 %. The final concentrations of all reagents were: 50 mM sodium phosphate pH 6.8, 0.5 mM TCEP, 1 mM EDTA, 2 mM α-ketoglutarate, 0.4 mM NAD^+, 0.4 mM TPP, 15

mU/100 μL KDH, 0.025 mg mL^{-1} BSA, 50 (1x K_M) or 200 (4x K_M) μM AcpP (wt or mutants), 50 or 200 μM malonyl-CoA (malCoA) and 0.02 nM FabD (wt or mutants).

A12. Preparation of C2-α-bromo-*crypto*-AcpP for analytical crosslinking efficiency assays. *apo*-AcpP (1.5 mg/mL) was treated with CoaA (0.20 mg/mL), CoaD (0.20 mg/mL), CoaE (0.20 mg/mL), Sfp (0.10 mg/mL), and C2-α-bromo-pantetheine (**1**) (1.0 mM) in 50 mM Tris, pH 8.0 containing NaCl (50 mM), $MgCl_2$ (25 mM), ATP (30 mM), TCEP (1.0 mM), and TritonX (0.02%) at 37 °C until no *apo*-AcpP remained, as determined by 20% urea-PAGE (~22 h). The resulting *crypto*-AcpP was purified by size-exclusion chromatography on a Superdex 75 pg (S75) column in 50 mM Tris, pH 7.4, 150 mM NaCl, 0.5 mM TCEP, and 10% glycerol.

A13. Analytical crosslinking assays. 5 μM FabD S92C (or 5 μM FabD S92C interface mutant) and 25 μM C2-α-bromo-*crypto*-AcpP were incubated in 50 mM Tris, pH 8.0 containing 0.5 mM TCEP for 26 h at 37 °C. Negative control reactions were performed simultaneously with FabD S92C (or FabD S92C interface mutant) in the absence of AcpP. Positive control reactions were performed with 5 μM FabF and 25 μM C2-α-bromo-*crypto*-AcpP. Reactions were quenched with 5x SDS loading buffer, heated at 95 °C for 5 min, and subjected to 12% SDS-PAGE, 160 V, 1 h. Gels were stained with Coomassie Brilliant Blue and scanned at 600 dpi using and EPSON Perfection V19 scanner. Coomassie staining was measured using Image Studio Lite Version 5.2 (Li-Cor Biosciences). Crosslinking efficiencies were calculated by dividing the intensity of the AcpP-FabD crosslinked band by the sum of the intensities of the AcpP-FabD crosslinked and FabD bands. Crosslinking

efficiencies of each FabD S92C interface mutant were normalized to the crosslinking efficiency of FabD S92C.

While crosslinking results indicate that nearly all of the interactions identified in the AcpP-FabD structure are important for complex formation (Figure S4.10c), the kinetic results demonstrate that the AcpP-FabD interface can tolerate variations. We believe this difference can be explained by the relative rates of these two different reactions. The reported k_{cat} values of FabD for *holo*-ACP transacylation range between 1500 and 2500 s^{-1} (Figure S4.16),[32,33] while the crosslinking reaction between C2-α-bromo-*crypto*-AcpP and FabD S92C requires several hours to form appreciable amounts of product (Figure S4.30). We therefore conclude that the formation of crosslinked complex via S_N2 displacement of bromine by the non-natural Cys92 residue relies more upon longer-lived PPIs than the native transacylation reaction.

A14. Time-dependent crosslinking. 10 μM FabD S92C and 50 μM C2-α-bromo-*crypto*-AcpP were incubated in PBS, pH 7.0 for 1–48 h at 37 °C. A control was performed by incubating 10 μM FabD S92C with 50 μM *apo*-AcpP for 48 h. Reactions were quenched with 5x SDS loading buffer, heated at 95 °C for 5 min, and subjected to 12% SDS-PAGE, 160 V, 1 h. Gels were visualized with Coomassie Brilliant Blue and scanned.

B. Synthetic Protocols

B1. General synthetic methods. Chemical reagents were purchased from Acros, Fluka, Sigma-Aldrich, or TCI. Deuterated NMR solvents were purchased from Cambridge

Isotope Laboratories. When necessary, reactions were conducted with vigorously dried anhydrous solvents that were obtained by passing through a solvent column exposed of activated A2 alumina. Air and moisture-sensitive reactions were performed under positive pressure of argon in flame-dried glassware sealed with septa and stirred with Teflon coated stir bars using an IKAMAG TCT-basic mechanical stirrer (IKA GmbH). Analytical Thin Layer Chromatograpy (TLC) was performed on Silica Gel 60 F254 precoated glass plates (EM Sciences). Visualization was achieved with UV light and/or appropriate stain (I_2 on SiO_2, $KMnO_4$, bromocresol green, dinitrophenylhydrazine, ninhydrin, or ceric ammonium molybdate). Flash column chromatography was carried out with Geduran Silica Gel 60 (40–63 mesh) from EM Biosciences. Yield and characterization data correspond to isolated, chromatographically, and spectroscopically homogeneous materials. ^{1}H NMR spectra were recorded on Varian Mercury 400, Varian Mercury Plus 400, or JEOL ECA500 spectrometers. ^{13}C NMR spectra were recorded at 100 MHz on Varian Mercury 400 or Varian Mercury Plus 400 spectrometers, or at 125 MHz on a JEOL ECA500 spectrometer. Chemical shifts for ^{1}H NMR and ^{13}C NMR analyses were referenced to the reported values of Gottlieb[79] using the signal from the residual solvent for ^{1}H spectra, or to the ^{13}C signal from the deuterated solvent. Chemical shift δ values for the ^{1}H and ^{13}C spectra are reported in parts per millions (ppm) relative to these referenced values, and multiplicities are abbreviated as s=singlet, d=doublet, t=triplet, q-quartet, m=multiplet, b=broad. All ^{13}C NMR spectra were recorded with complete proton decoupling. FID files were processed using MestreNova 10.0 (MestreLab Research). Electrospray ionization (ESI) mass spectrometric analyses were preformed using a ThermoFinnigan LCQ Deca spectrometer. Spectral data and procedures are provided for all new compounds and copies of spectra have been provided.

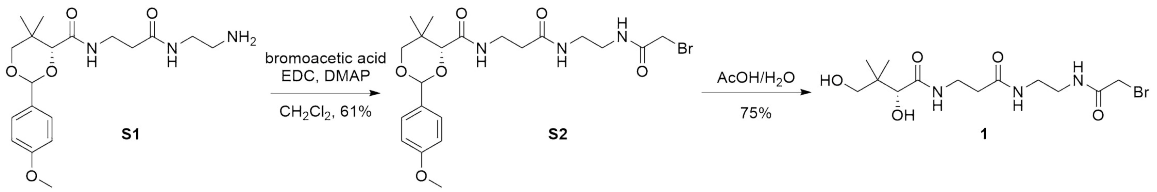

Scheme S1. Synthesis of C2-α-bromo-pantetheineamide (1). EDC=1-Ethyl-3-(3-dimethylaminopropyl)carbodiimide); DMAP=4-(dimethylamino)-pyridine; AcOH=acetic acid.

(4*R*)-*N*-(3-((2-aminoethyl)amino)-3-oxopropyl)-2-(4-methoxyphenyl)-5,5-dimethyl-1,3-dioxane-4-carboxamide (S2). In a 10 mL pear-shaped flask, (4*R*)-*N*-(3-((2-aminoethyl)amino)-3-oxopropyl)-2-(4-methoxyphenyl)-5,5-dimethyl-1,3-dioxane-4-carboxamide **S1**[80] (102.0 mg, 0.2688 mmol, 1.0 equiv.), bromoacetic acid (58.6 mg, 0.422 mmol, 1.6 equiv.), and 3 mL CH_2Cl_2 were added. To the solution was added EDC•HCl (81.6 mg, 0.426 mmol, 1.6 equiv.) and DMAP (9.7 mg, 0.0794 mmol, 0.30 equiv.). After 21 h, the reaction was dissolved in 100 mL CH_2Cl_2 and washed with deionized water (10 mL). The organic phase was dried over $MgSO_4$, filtered, and concentrated by rotary evaporation. Purification by silica flash chromatography (39:1 → 9:1 CH_2Cl_2/MeOH) afforded **S2** (81.6 mg, 60.7%) as a white solid.

TLC: R_f 0.14 (19:1 CH_2Cl_2/MeOH). **^{1}H-NMR** (500 MHz, $CDCl_3$): δ 7.40 (d, *J* = 10.8 Hz, 2H), 7.06–6.99 (m, 2H), 6.88 (d, *J* = 8.8 Hz, 1H), 5.43 (s, 1H), 4.04 (s, 1H), 3.94 (s, 1H), 3.78 (s, 3H), 3.75 (s, 1H), 3.70–3.59 (m, 2H), 3.49 (s, 2H), 3.32 (s, 4H), 2.46–2.34 (m, 2H), 1.05 (d, *J* = 12.2 Hz, 6H).**^{13}C-NMR** (125 MHz, $CDCl_3$): δ 172.17, 169.79, 167.17, 160.33, 130.17, 127.63, 113.81, 101.42, 83.91, 78.48, 55.44, 42.59, 40.45, 39.23, 36.11, 35.16, 33.15, 28.92, 21.94, 19.22. **HR-ESI-MS** *m/z* calcd. $[C_{21}H_{30}BrN_3O_6Na]^+$: 522.1210, found 522.1206.

(R)-N-(3-((2-(2-bromoacetamido)ethyl)amino)-3-oxopropyl)-2,4-dihydroxy-3,3-dimethylbutanamide (C2-α-bromo-pantetheineamide, 1). In a 20 mL vial, **S2** (81.6 mg, 0.163 mmol, 1.0 equiv.) and1.0 mL 4:1 AcOH/H_2O were added. After 7 h, the mixture was concentrated by rotary evaporation, then azeotroped from cyclohexane (5x10 mL) and benzene (3x10 mL). Purification by silica flash chromatography (19:1 → 3:1 CH_2Cl_2/MeOH) afforded **1** (47.0 mg, 75.4%) as a clear oil. Analytical data were consistent with previous reports.[39]

TLC: R_f 0.22 (9:1 CH_2Cl_2/MeOH). **^{1}H-NMR** (400 MHz, CD_3OD): δ 4.06 (s, 2H), 3.87 (d, *J* = 16.4 Hz, 2H), 3.54–3.42 (m, 4H), 3.42–3.28 (m, 5H), 2.42 (t, *J*=6.6 Hz, 2H), 0.91 (s, 6H).**^{13}C-NMR** (100 MHz, CD_3OD): δ 174.87, 173.09, 168.50, 76.20, 69.11, 42.04, 39.37, 39.19, 38.60, 35.44, 35.23, 20.28, 19.68. **HR-ESI-MS** *m/z* calcd. $[C_{13}H_{24}BrN_3O_5Na]^+$: 404.0792, found 404.0793.

C. Molecular Dynamics Simulations Protocols

C1. Structure preparation. As shown in Table 4.3, a total of 17 systems were subjected to computer simulations. For simulation work, the coordinates of the wildtype and mutant *apo*-FabD, malonyl-CoA•FabD, and malonyl-AcpP•FabD structures were generated using x-ray crystal structures of *apo*-FabD (PDB ID: 1MLA, 2G1H)[50,81] malonyl-CoA-bound FabD (PDB ID: 2G2Z)[50], and the crosslinked AcpP-FabD (reported herein), respectively. Mutants of the enzymes and enzyme complexes were generated using Pymol v.2.3[82] (https://pymol.org/2/support.html) and Schrodinger's Protein Preparation Wizard[82–84] (https://www.schrodinger.com/protein-preparation-wizard[85,86]) and

https://www.schrodinger.com/prime were used to add missing C-, N-terminal residues and missing side chains not resolvable from the experimental density, and hydrogen atoms were added all heavy atoms to cap all open valences. To predict the protonation states of the titratable residues in each structure assuming a pH of 7.4, and to optimize the orientation, all waters resolved crystallographically. Note that in the preparation of all protein structures the active site S92C mutation of the FabD was "reversed" in order to restore the active site serine found in the wildtype enzyme. Histidine protonation states were inspected by hand.

C2. Simulation preparation. TLEAP (https://ambermd.org/CiteAmber.php) were used to generate AMBER (ff14SB/GAFF2) topology and the parameters files for the simulation cell of all 17 systems of interest. Parameterization of the malonyl-CoA and malonyl-AcpP's nonstandard residue was performed using ANTECHAMBER and GAFF2 force field (https://ambermd.org/CiteAmber.php).[87,88] Subsequently topology and parameter files were prepared using TLEAP. TLEAP was used to prepare the simulation cell/ All simulation cells were prepared using TIP3P water molecules[89] to generate isometric cell to ensure that the cell walls are 10 Å away from the closet portion of the coordinates derived from experimental data in either data. The restrained electrostatic potential (RESP) method[90] was used to determined partial atomic charges for the ANTECHAMBER parameterization of the malonyl-containing nonstandard residue.[87] The potential was computed at the HF/6-31G(d) level of theory using Gaussian 09 (https://gaussian.com/g09citation/).

C3. Simulation methodology. Simulations were performed using GPU-accelerated Amber 2016 and Amber 2018 (https://ambermd.org/CiteAmber.php).[91,92] A 2 fs time-step

was utilized via the SHAKE algorithm, which constrains all nonpolar bonds involving hydrogen atoms.[93] Long-range electrostatic interactions were treated using the Particle Mesh Ewald (PME) method with a 10 Å cutoff for all non-bonded interactions.[94] Both solvated protein complexes were energy minimized in a two-step fashion. In a first step, solvent molecules and counterions were allowed to relax, while all protein atoms were restrained using a harmonic potential ($k = 500$ kcal mol^{-1} $Å^{-2}$). This geometry optimization was followed by an unrestrained energy minimization of the entire system. The thermal energy available at a physiological temperature of 310 K was slowly added to each system over the course of a 2 ns NVT ensemble simulation. The solvated complexes were then subjected to unbiased isobaric-isothermal (NPT) simulations for 10 ns in order to equilibrate the heated structures. Three independent 512 ns production MD (NPT ensemble) of each system were performed with different initial velocities. For both NVT and NPT simulations, the Langevin thermostat ($\lambda = 5.0$ ps^{-1}) was used to maintain temperature control.[95–97] Pressure regulation in NPT simulations (target pressure of 1 atm) was achieved by isotropic position scaling of the simulation cell volume using a Berendsen barostat.[98] Coordinate data was written to disk every 10 ps.

C4. Analysis and visualization of simulation data: Analysis was performed using CPPTRAJ,[99] PYTRAJ, a Python front-end for the CPPTRAJ analysis code (https://amber-md.github.io/pytraj/latest/overview.html#citations). Trajectories were visualized using NGLview[100–102] and Pymol v2.3 (https://gaussian.com/g09citation/). All data was plotted using matplotlib library of Python.

The process of modifying the experimental structure through structure and simulation preparation modifies its geometry such that there is a modest difference between the experiment and initial coordinates (for simulation). Furthermore, because the crosslinker used to trap the experimental AcpP-FabD complex was replaced with malonyl moiety in the structures prepared for simulation, some analysis including native contact analyses were performed using the initial coordinates instead of the experimental ones.

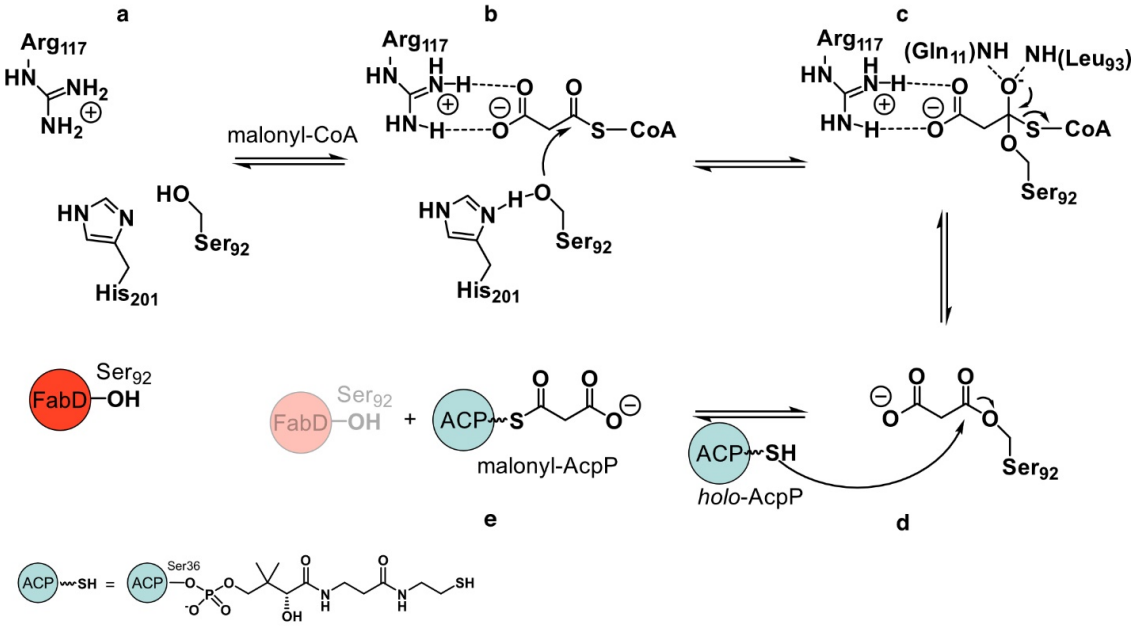

Figure S4.1: *Reaction catalyzed by FabD (adapted from references [69,103,104]).* **a**) FabD active site residues. **b**) FabD-catalyzed incorporation of malonyl-CoA occurs via a ping–pong bi–bi mechanism involving the malonylation of FabD catalytic serine (Ser92) in the first step. **c**) The tetrahedral intermediate is stabilized by an oxyanion hole formed with the backbone amides from Gln11 and Leu93. **d**) The acyl-FabD intermediate is then subject to a nucleophilic attack by the thiol of the phosphopantetheine arm of holo-AcpP, **e**) which results in the formation of malonyl-AcpP.

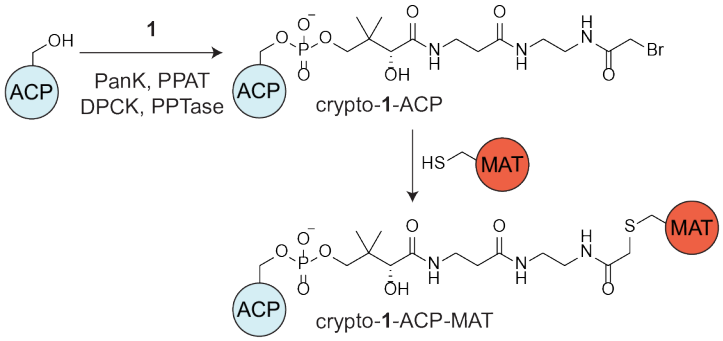

Figure S4.2: *Chemoenzymatic modification of apo-AcpP with C2-α-bromo-pantetheine (1) and subsequent FabD S92C crosslinking. apo*-ACP is modified with 1 to form *crypto*-1-ACP, followed by nucleophilic attack by the active site cysteine from the MAT to form crosslinked ACP-MAT complex. In situ conversion of pantetheine analog 1 is converted into a coenzyme A analog using pantothenate kinase (PanK), 4′-phosphopantetheine adenyltransferase (PPAT), and dephospho-coenzymeA kinase (DPCK), followed by *B. subtilis* phosphopantetheinyl transferase (PPTase)-catalyzed loading of phosphopantetheine analog onto *apo*-ACP.

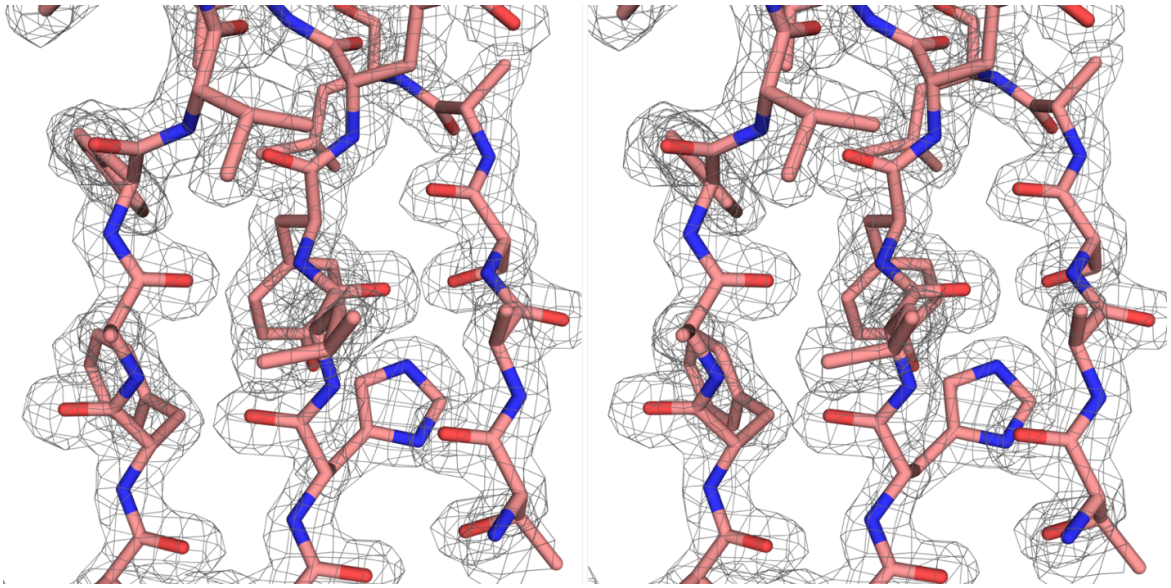

Figure S4.3: *Stereo images of AcpP-FabD electron density map.* Stereo images of 2Fo-Fc electron density maps for AcpP-FabD complex (PDB ID: 6U0J) contoured at 1.0 σ and rendered using a carve radius of 1.6 Å. Beta sheets shown (from left to right) consist of residues Gln3-Val7, Glu270-Glu274, and Thr293-Ala296.

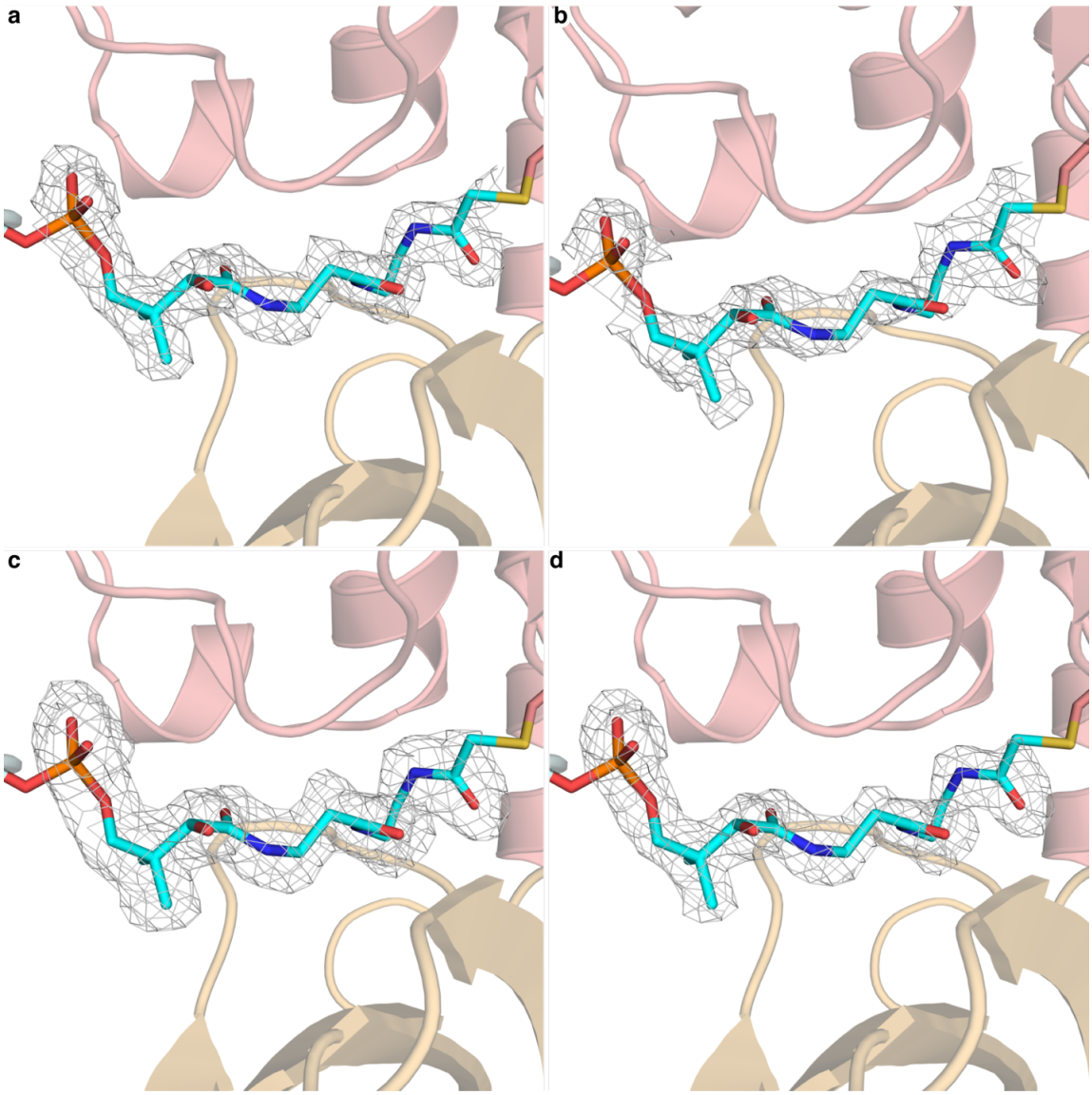

Figure S4.4: *Electron density maps of PPant crosslinker*. **a)** 2Fo-Fc electron density map show density for the PPant crosslinker (PDB ID: 6U0J) contoured at 1.0 σ and rendered using a carve radius of 1.6 Å. **b)** A 2mFo-dFc composite 'iterative build" OMIT105 electron density map showing unbiased density for the PPant crosslinker contoured at 1.0 σ and rendered using a carve radius of 1.6 Å. Composite OMIT maps were calculated using PHENIX's composite omit map function with simulated annealing (torsion angle) performed in between each iteration. **c)** Fo-Fc polder omit map calculated by omitting PPant crosslinker and bulk solvent from the region defined by a 5 Å solvent exclusion radius. The Fo-Fc polder map is contoured at 3.0 σ and rendered using a carve radius of 1.6 Å. **d)** Standard Fo-Fc omit map (no bulk solvent exclusion from omitted region) contoured at 3.0 σ and rendered using a carve radius of 1.6 Å.

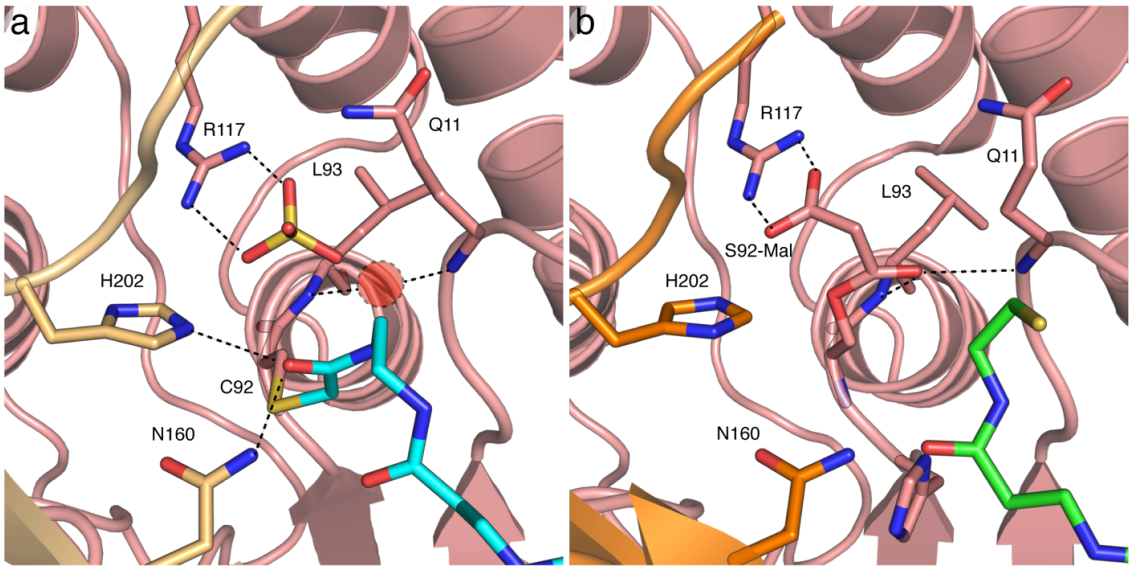

Figure S4.5: *Comparison of AcpP-FabD and malonyl-CoA-bound FabD active site interactions.* **a)** Active site of FabD from AcpP-FabD structure (PDB ID: 6U0J) highlighting interactions between the acetamide portion of the PPant crosslinking probe (carbon colored cyan) and the bound sulfate ion in the active site. The acetamide carbonyl group is found rotated away from the oxyanion hole and instead engages in hydrogen-bonding interactions with Asn160 and His202. The oxyanion hole, formed by backbone amides of Gln11 and Leu93, is shown as red transparent circle with a dotted outline. Residues from the FL subdomain have light-orange colored carbon atoms and residues from the ABH subdomain have salmon colored carbon atoms. **b)** Active site of FabD from malonyl-CoA-bound FabD (PDB ID: 2G2Z) showing the carbonyl group of bound malonyl-Ser92 coordinated in the active site oxyanion hole and bidentate salt-bridge interaction between the carboxylate of malonyl-Ser92 with Arg117. The bound hydrolyzed CoA moiety (carbon colored green) is also shown in the active site. Important interactions within a hydrogen bonding distance cutoff of 3.5 Å are shown by dotted lines. Residues from the FL subdomain have orange colored carbon atoms and residues from the ABH subdomain have salmon colored carbon atoms.

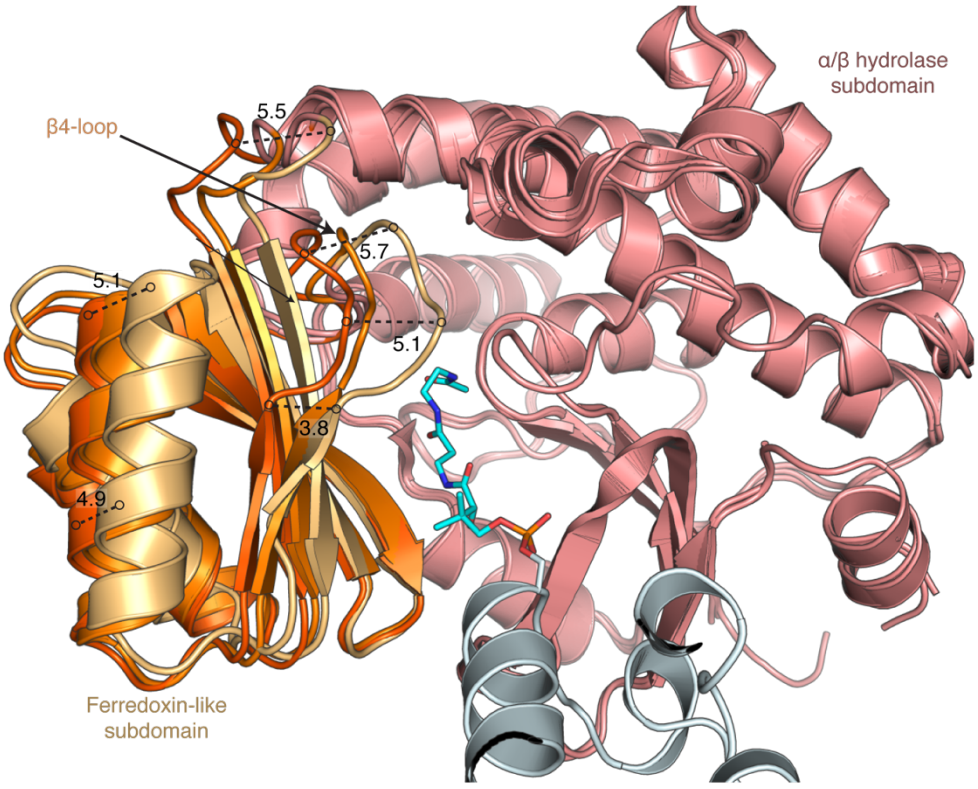

Figure S4.6: *Measurement of FL subdomain rigid body motions*. Measurements (Å) of the rigid body domain motions of the FL subdomain with respect to the ABH subdomain in the *apo*-FabD (PDB ID: 1MLA, dark orange) and AcpP-FabD (PDB ID: 6U0J, light orange) structures (distance given in Å). The malonyl-CoA-bound FabD complex (PDB ID: 2G2Z, orange) is also displayed for consistency with the main text figures.

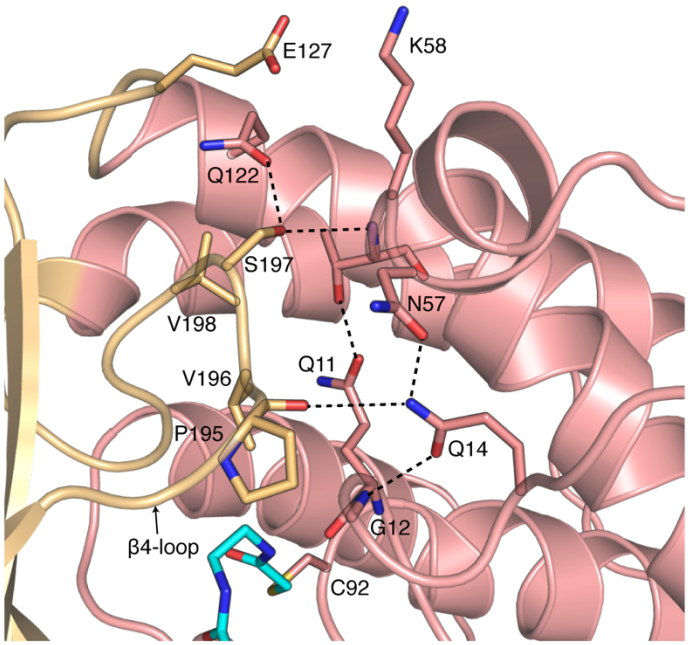

Figure S4.7: *Interaction networks formed between FL and ABH subdomains in AcpP-FabD structure.* Rigid body subdomain motion of the FL subdomain results in new contacts formed between the ABH and FL subdomain in the AcpP-FabD structure (PDB ID: 6U0J). Residues along the β4-loop form a new network of contacts and important interactions within a hydrogen bonding distance cutoff of 3.5 Å are shown by dotted lines. Residues from the FL subdomain have light-orange colored carbon atoms and residues from the ABH subdomain have salmon colored carbon atoms. The PPant arm is shown crosslinked to the active site Cys92 residue and carbons are colored cyan.

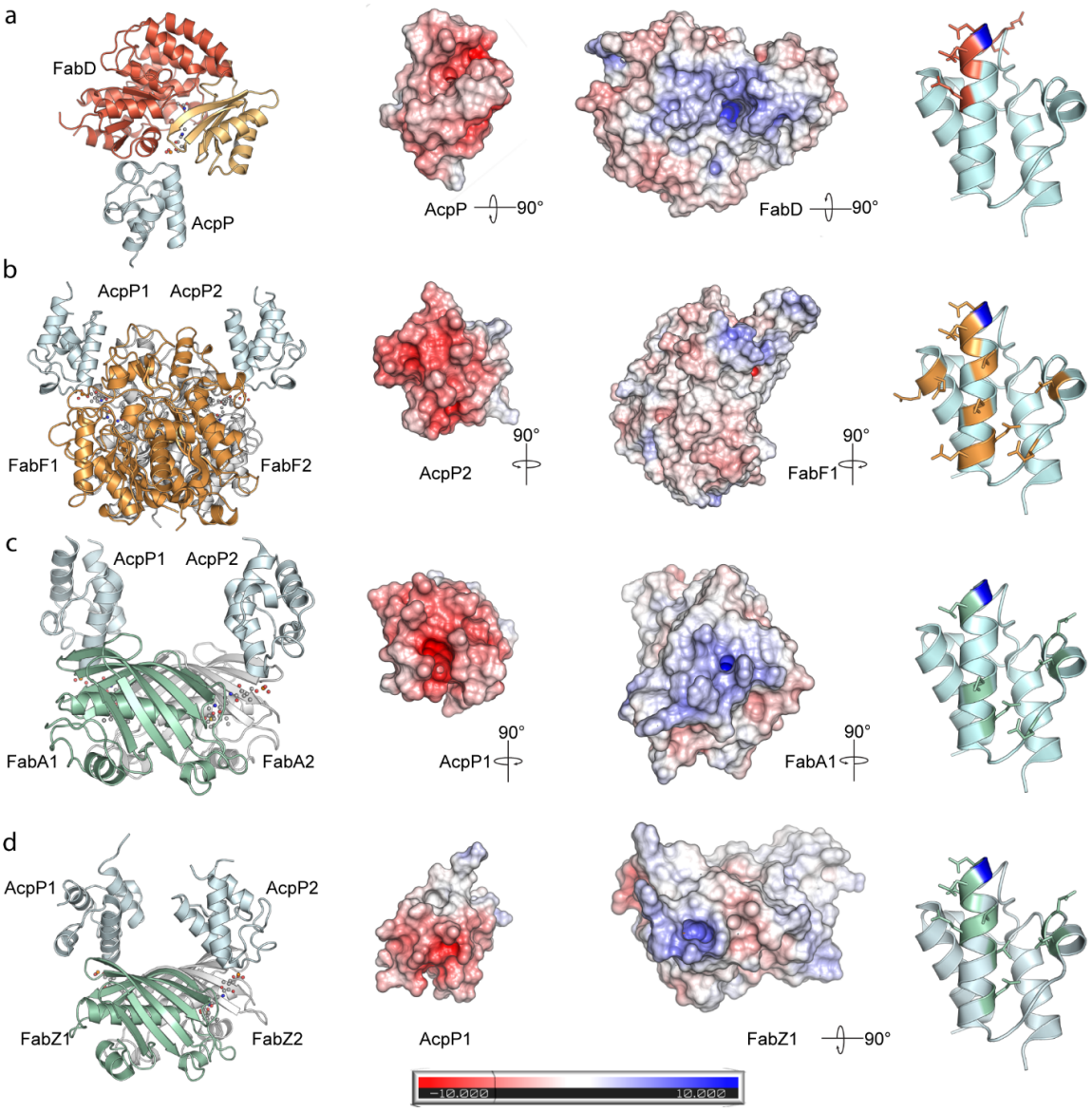

Figure S4.8: *AcpP Interactome.* Structural comparison of the *E. coli* **a)** AcpP-FabD (PDB ID: 6U0J), **b)** AcpP-FabF (PDB ID: 6OKG) **c)** AcpP-FabA (PDB ID: 4KEH), and **d**) AcpP-FabZ dimer (PDB ID: 6N3P) crosslinked complexes, depicting the overall structural architecture (left), electrostatic potential (ESP) maps of the partner protein and AcpP monomers (middle), and *apo*-AcpP structure (PDB ID: 1T8K), illustrating contacts that each partner protein makes with the AcpP (right), with the phosphopantetheinylation site (Ser36) depicted in blue. In all cases, the ESP is mapped onto the solvent-excluded surface (Connolly surface) of the partner protein and AcpP monomers using a blue to white to red color scheme spanning from –10.0 kTe^{-1} to +10.0 kTe^{-1}. Note that AcpP-FabZ structure is a hexamer consisting of three dimers. Here, one of those dimers is depicted in panel **d**.

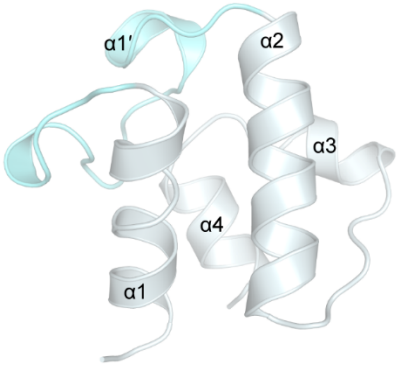

Figure S4.9: *Overall topology of AcpP in the AcpP-FabD structure (PDB ID: 6U0J).* AcpP forms contacts with FabD through a small helix in loop 1 (α1′) and the N-terminal region of helix II (α2). The loop 1 region is colored aquamarine.

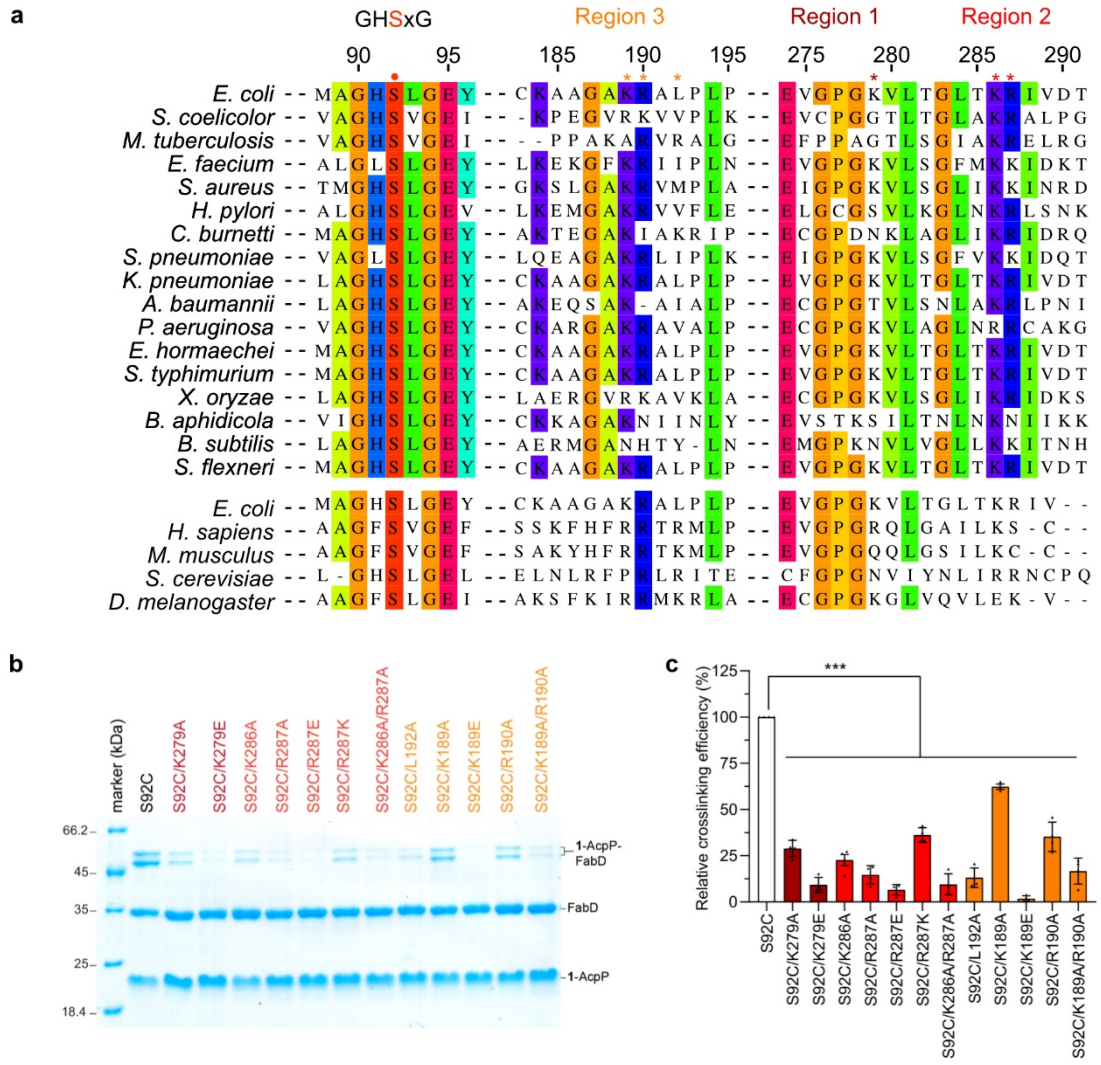

Figure S4.10: *Validation of FabD-AcpP interface via mutagenesis and crosslinking.* **a)** Sequence alignment of MATs from type II FAS (top) and type II eukaryotic mitochondrial MATs (bottom). The catalytic serine of FabD, part of the highly conserved GHSxG motif in ATs active site, is denoted by a red circle. Residues that were mutated for crosslinking and kinetics studies are denoted by asterisks. Residues are colored based on sequence identity (threshold set at 70%). **b)** SDS-PAGE analysis depicting crosslinking between 5 µM FabD S92C interface mutants and 25 µM C2-α-bromo-crypto-AcpP in 50 mM Tris, pH 8.0 containing 0.5 mM TCEP at 37 °C for 26 h. **c)** Semi-quantitative densitometric analysis of SDS-PAGE data, showcasing FabD interface residues from region 1 (crimson), region 2 (red), and region 3 (orange). The mutants were subjected to a crosslinking assay using C2-α-bromo-crypto-AcpP and all reported data were normalized to FabD S92C crosslinking efficiency. Data is reported as the mean ± standard deviation from 4 replicates. Statistical significance was compared using one-way ANOVA and Dunnett's multiple comparison test. ***p<0.001.

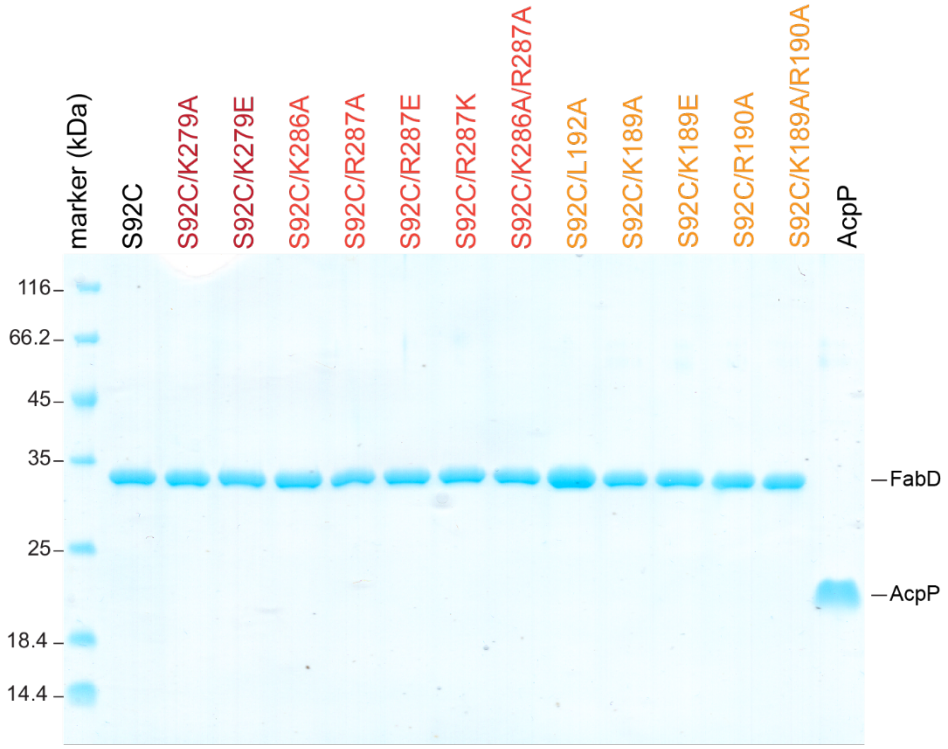

Figure S4.11: *Purified FabD S92C interface mutants for crosslinking validation*. Coomassie-stained 12% SDS-PAGE gel of FabD S92C interface mutants and C2-α-Br-pantetheinamide-AcpP.

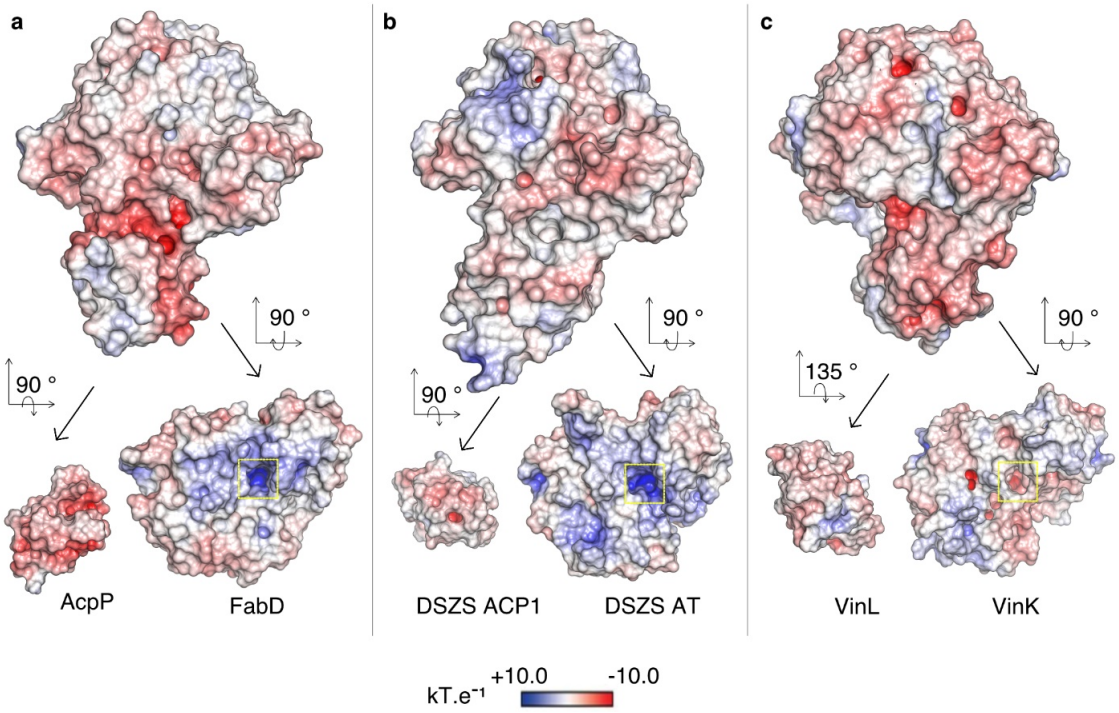

Figure S4.12: *ACP-AT electrostatic potentials (ESP) maps of ACP-AT complexes and respective monomers*. **a)** AcpP-FabD (PDB ID: 6U0J), **b)** DSZS ACP1-DSZS AT (PDB ID: 5ZK4), **c)** VinL-VinK (PDB ID: 5CZD). In all cases, the ESP are mapped onto the "Connelly" surfaces of the AT and ACP monomers using a blue to white to red color range, spanning from +10.0 kT•e−1 to –10.0 kT•e−1. The entrance of the AT active site is indicated by the yellow box.

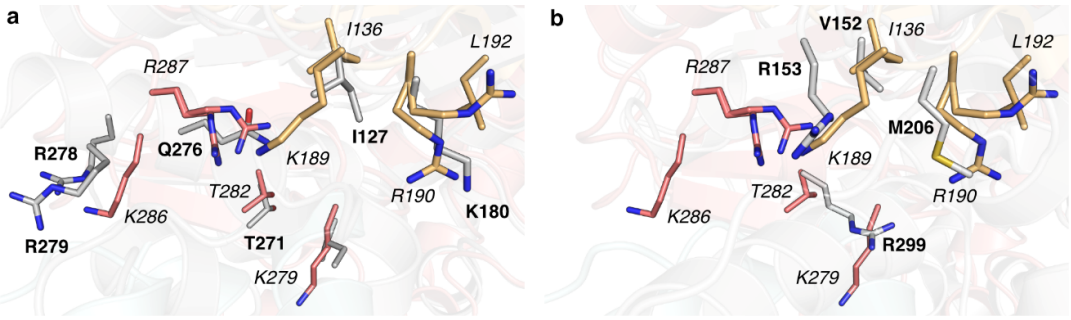

Figure S4.13: *Interfaces residues of trans-ATs compared to FabD*. **a)** AcpP-FabD (PDB ID: 6U0J) overlaid with DSZS ACP1-DSZS AT (PDB ID: 5ZK4). **b)** AcpP-FabD overlaid with VinL-VinK (PDB ID: 5CZD). Only AT interface residues are shown for clarity. Interface residues from the trans-ATs (grey) and from FabD (colored) are shown in bold and in italic, respectively.

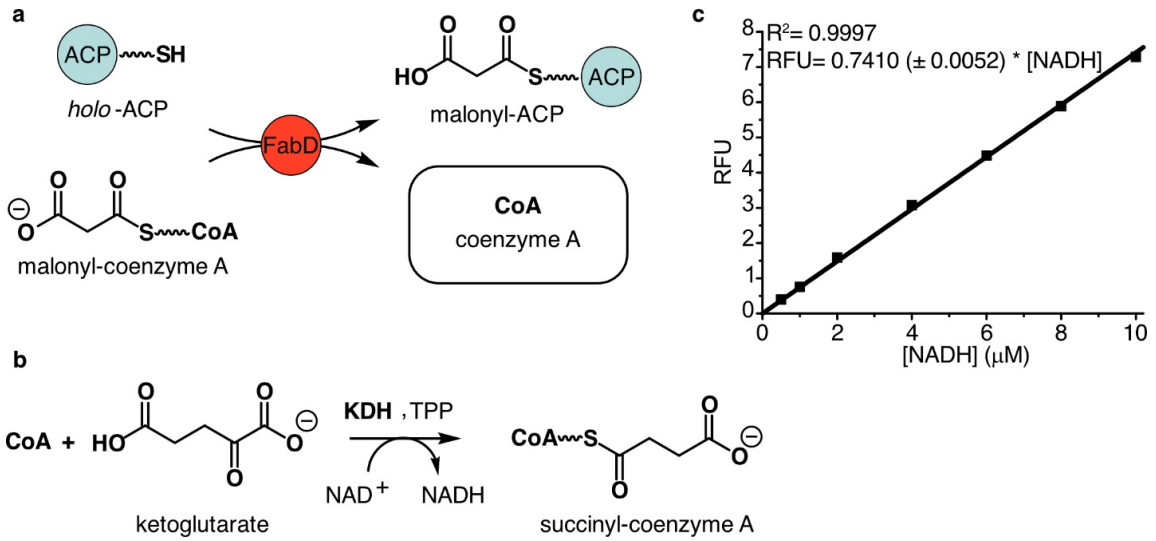

Figure S4.14: *FabD continuous coupled assay using α-ketoglutarate dehydrogenase (KDH).* **a)** KDH is a nicotinamide adenine dinucleotide (NAD+)- and thiamine pyrophosphate- (TPP) dependent enzyme which reacts with the free coenzyme A (CoA) generated by FabD. **b)** This reaction is accompanied with a reduction of NAD+ to NADH which can be monitored by fluorescence. **c)** NADH calibration curve (each point was repeated in triplicate).

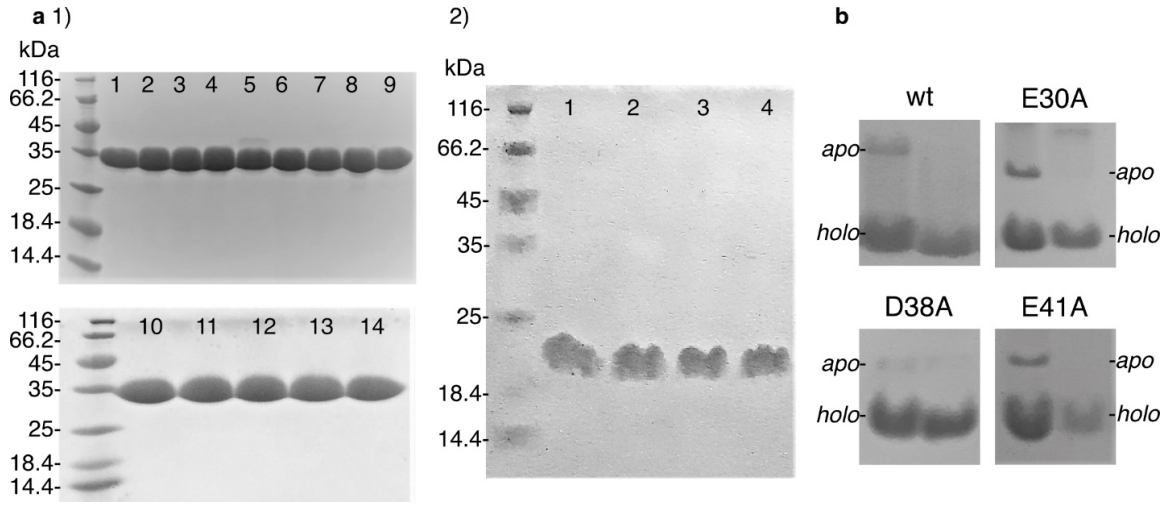

Figure S4.15: *SDS Page Gels of FabD and AcpP* **a)** Coomassie-stained SDS-PAGE gels (15 % acrylamide, 170 V, 60 min) of FabD wt and mutants (1): FabD wt (1), K279E (2), R287A (3), R287E (4), R287K (5), S295A (6), K279A (7), K286A (8), L192A (9), K189A (10), K189E (11), R190A (12), K189A R190A (13), K286A R287A (14), and of AcpP wt and mutants (2): AcpP wt (1), E30A (2), D38A (3), E41A (4). **b)** Coomassie-stained urea-PAGE gels (20 % acrylamide, 170 V, 90 min) of AcpP wt and mutants. AcpP is expressed in both apo and holo form (left lane) and is fully converted to its holo form after reaction with Sfp (right lane).

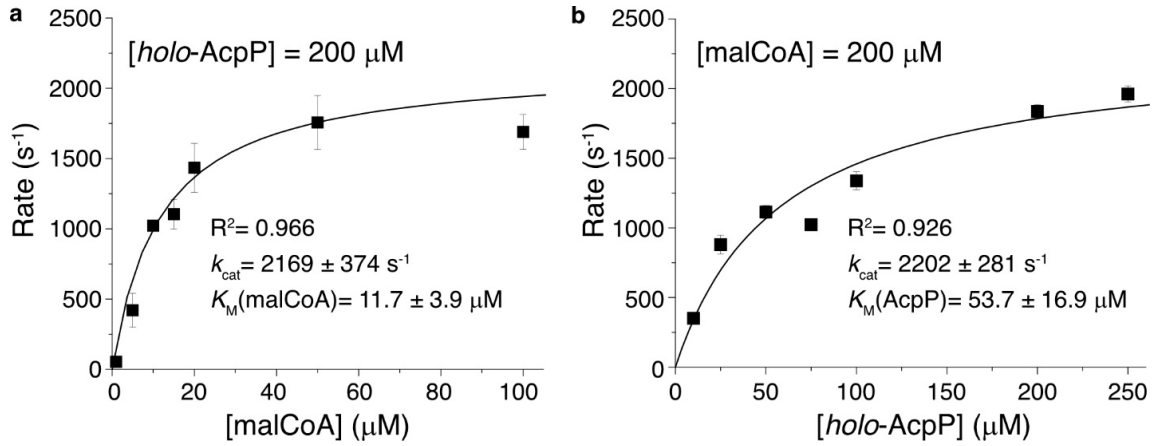

Figure S4.16: *Michaelis-Menten curves of FabD wt.* **a)** The concentration of holo-AcpP is kept constant (200 μM or 4 x KM(AcpP)) to determine KM(malCoA). **b)** The concentration of malCoA is kept constant (200 μM or > 4x KM(malCoA)) to determine KM(AcpP). Each reaction was run in biological triplicate and the error bars indicate the standard deviation on the mean of the three measurements.

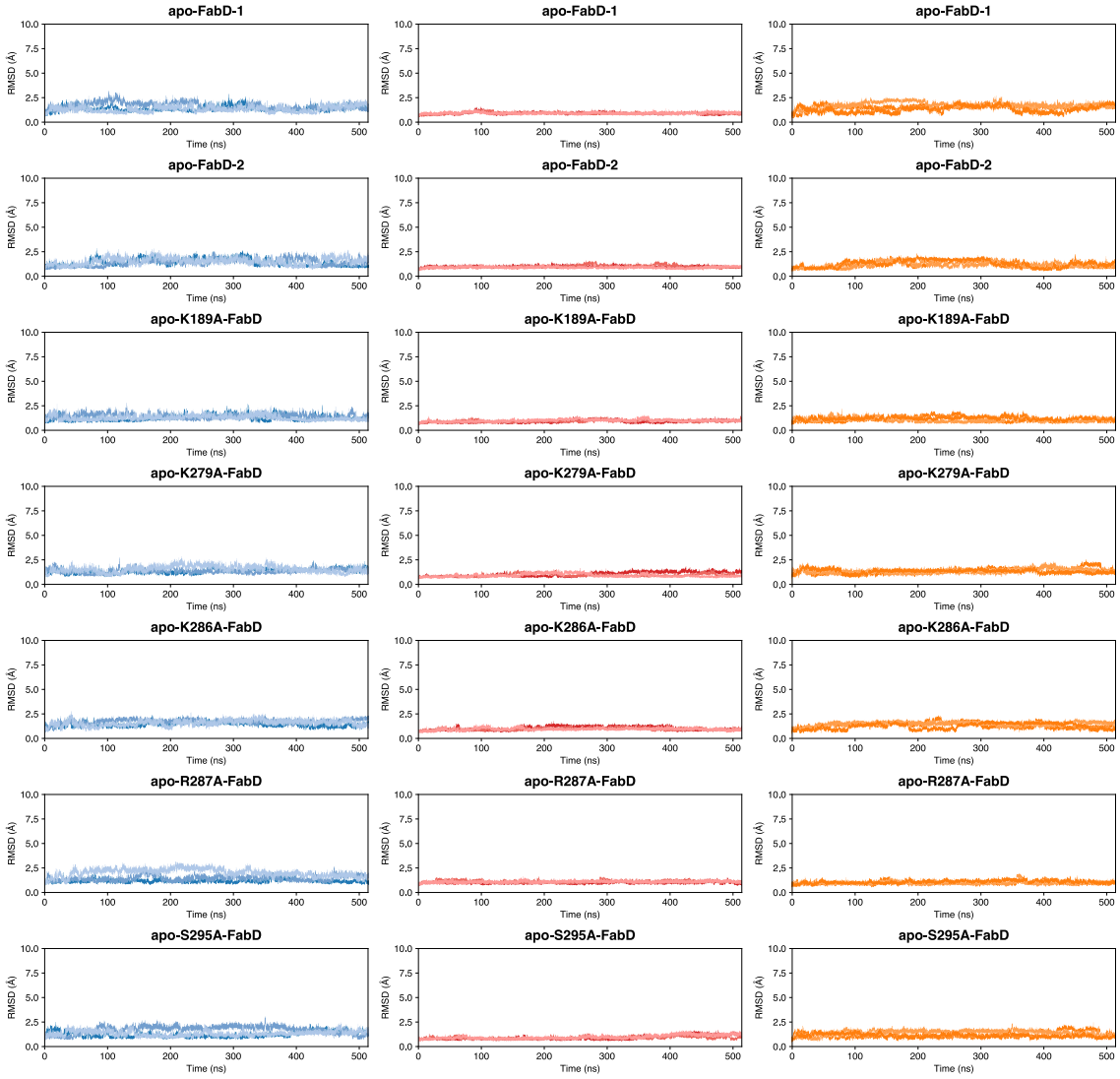

Figure S4.17: *C_α root mean square analysis (RMSD) in Ångstroms (Å) of the simulations of wildtype (wt) apo-FabD and five FabD mutants.* Analysis was performed on 3 independent 524 ns molecular dynamics (MD) simulations. Each plot is labeled to indicate the FabD system analyzed. The RMSDs of the entire FabD domain (left, blue curves), the ABH (large) subdomain (center, red curves), and FL (small) subdomain (right, orange curves) of FabD simulations.

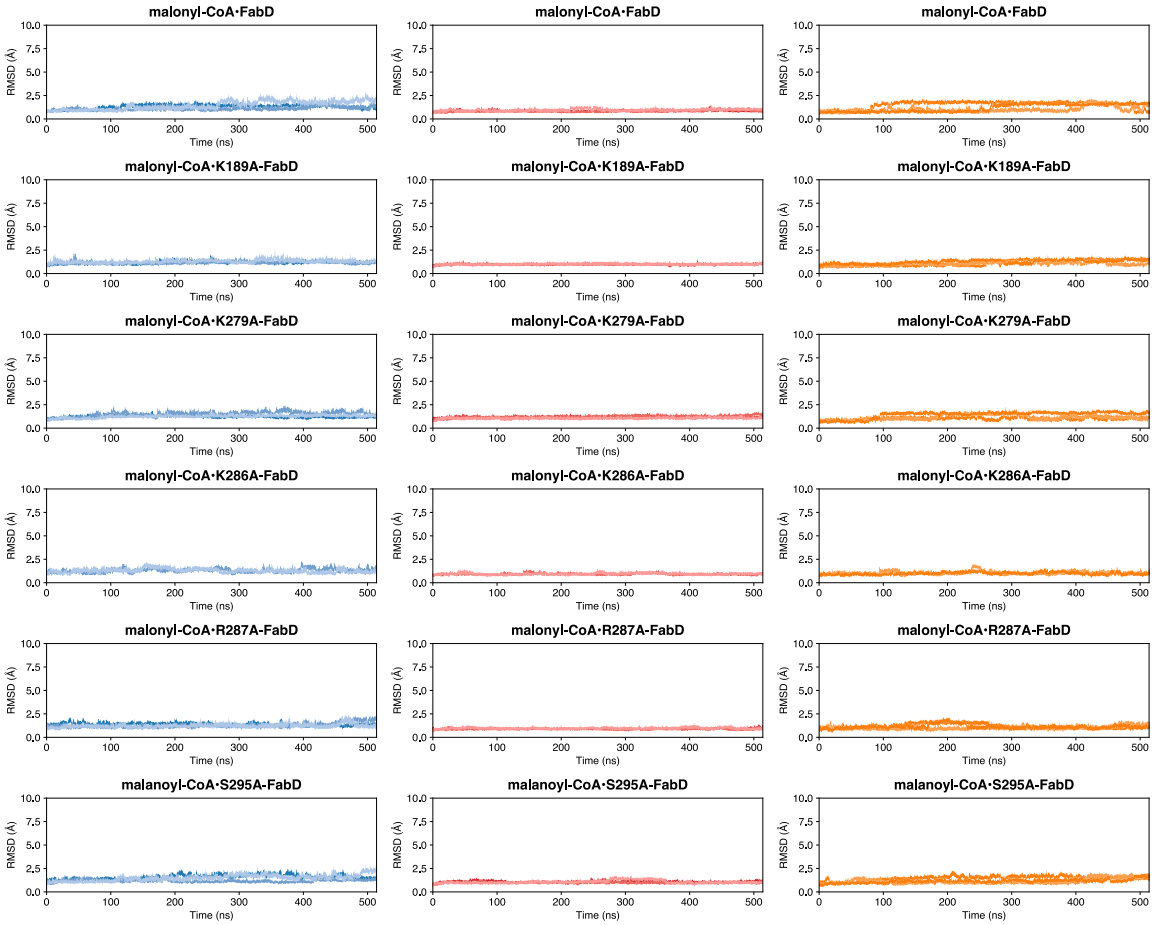

Figure S4.18: *C_α root mean square analysis (RMSD) in Ångstroms (Å) of the simulations of wildtype (wt) FabD and apo-FabD bound with malonyl-CoA performed using ff14SB/GAFF2 force field parameter*. Analysis was performed on 3 independent 524 ns molecular dynamics (MD) simulations. Each plot is labeled to indicate the FabD system analyzed. The RMSDs of the entire FabD domain (left, blue curves), the ABH (large) subdomain (center, red curves), and FL (small) subdomain (right, orange curves) of FabD. Analysis was performed on 3 independent 524 ns molecular dynamics (MD) simulations. Each plot is labeled to indicate the FabD system analyzed and show the change in protein RMSD over the course of each 524 ns simulation (shown in a blue, red, or orange hue).

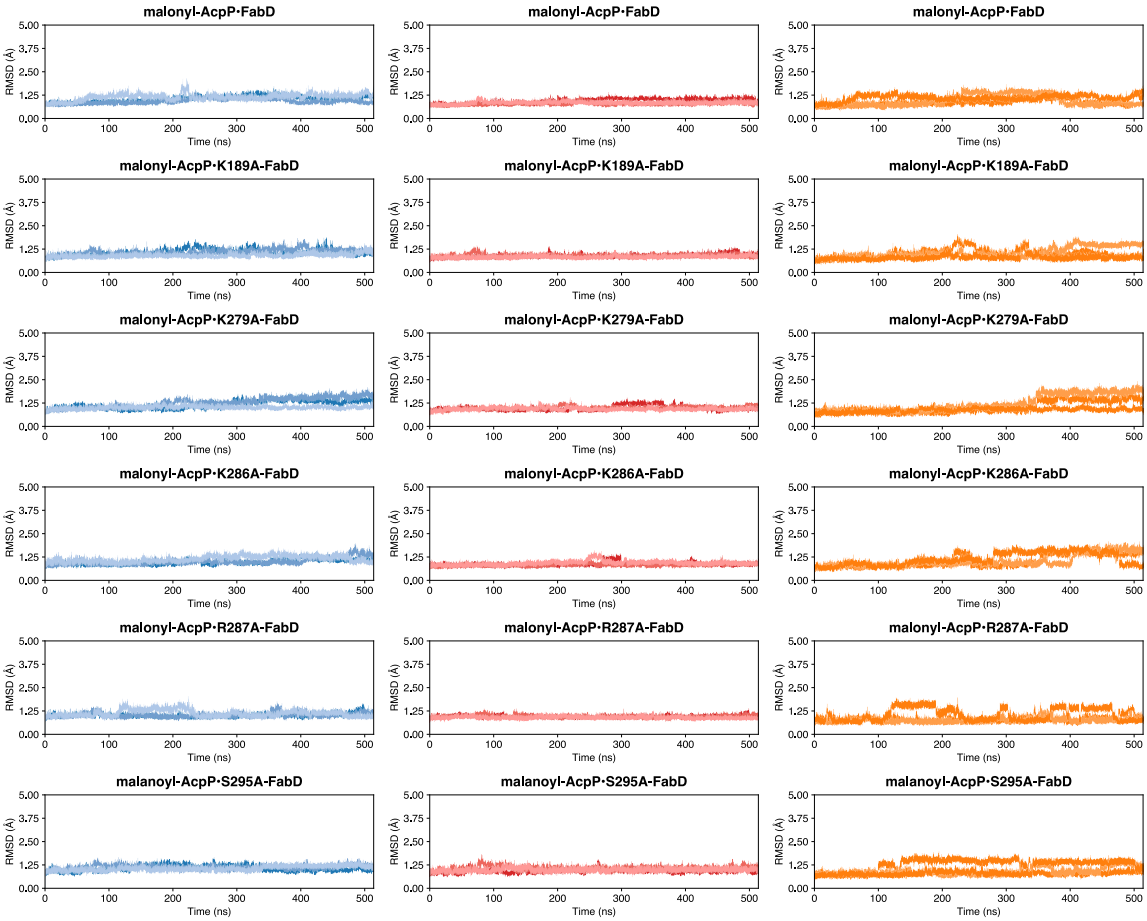

Figure S4.19: *C_α root mean square analysis (RMSD) in Ångstroms (Å) of the simulations of malonyl-AcpP-bound wildtype (wt) FabD and apo-FabD.* Analysis was performed on 3 independent 524 ns molecular dynamics (MD) simulations. Each plot is labeled to indicate the FabD system analyzed. The RMSDs of the entire FabD domain (left, blue curves), the ABH (large) subdomain (center, red curves), and FL (small) subdomain (right, orange curves) of FabD. Analysis was performed on 3 independent 524 ns molecular dynamics (MD) simulations. Each plot is labeled to indicate the FabD system analyzed and show the change in protein RMSD over the course of each 524 ns simulation (shown in a blue, red, or orange hue).

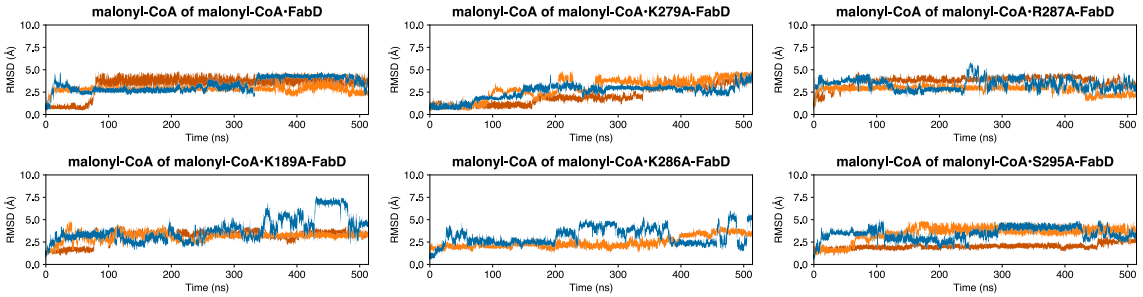

Figure S4.20: *Heavy atom root mean square deviation analysis (RMSD) in Ångstroms (Å) of the malonyl-CoA substrate of the wt and mutant malonyl-CoA•FabD complexes.* Analysis was performed on 3 independent 524 ns molecular dynamics (MD) simulations. Each plot is labeled to indicate the FabD system analyzed. The nonstandard MPS residues includes the conserved Ser36 of AcpP, the phosphopantetheine prosthetic arm, and the ligated malonyl moiety.

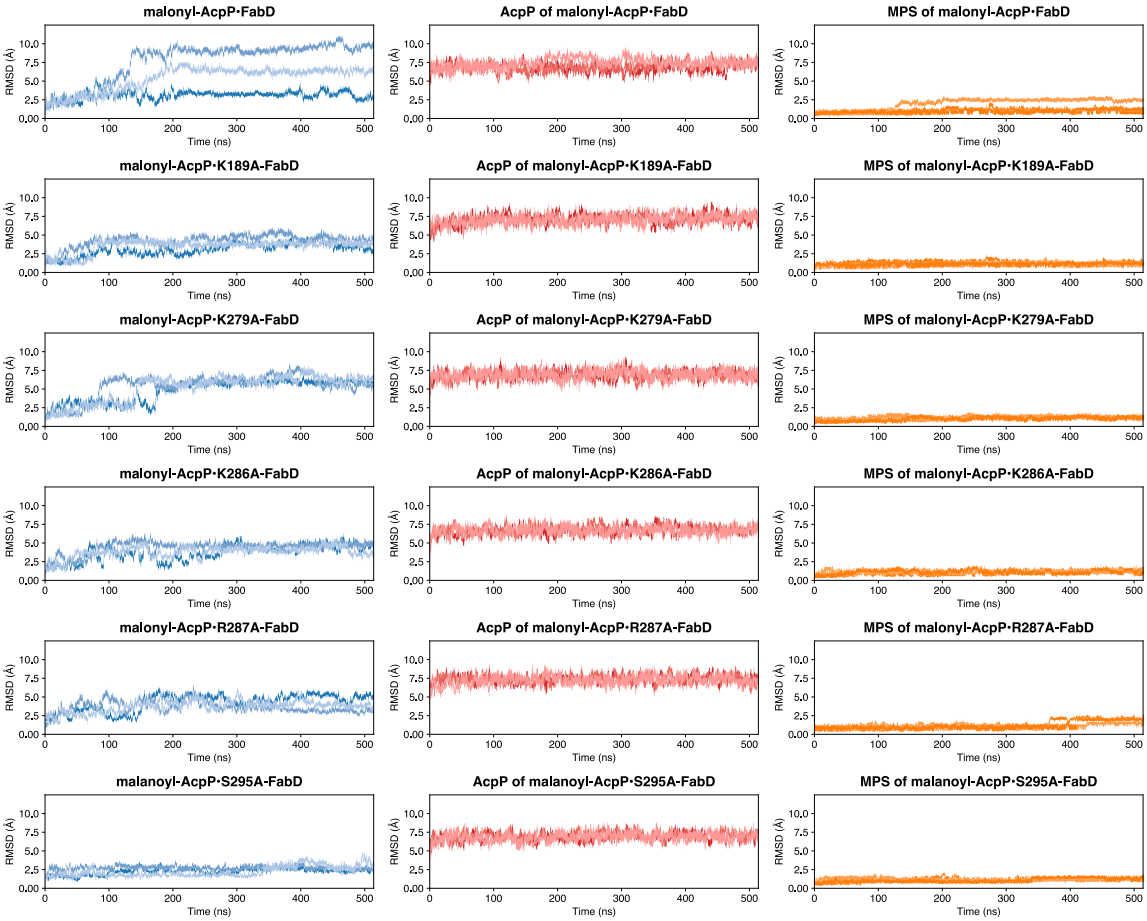

Figure S4.21: *Heavy atom root mean square analysis (RMSD) in Ångstroms (Å) of the wt and mutant malonyl-AcpP•FabD complexes*. Analysis was performed on 3 independent 524 ns molecular dynamics (MD) simulations. Each plot is labeled to indicate the malonyl-AcpP•FabD system analyzed. The RMSDs of the entire AcpP•FabD complex (left, blue curves), the AcpP monomer (center, red curves), and nonstandard residue (right, orange curves). Each plot is labeled to indicate the FabD system analyzed and show the change in protein RMSD over the course of each 524 ns simulation (shown in a blue, red, or orange hue). The nonstandard MPS residues includes the conserved Ser36 of AcpP, the phosphopantetheine prosthetic arm, and the ligated malonyl moiety. Simulation data was superimposed over entire AcpP•FabD complex.

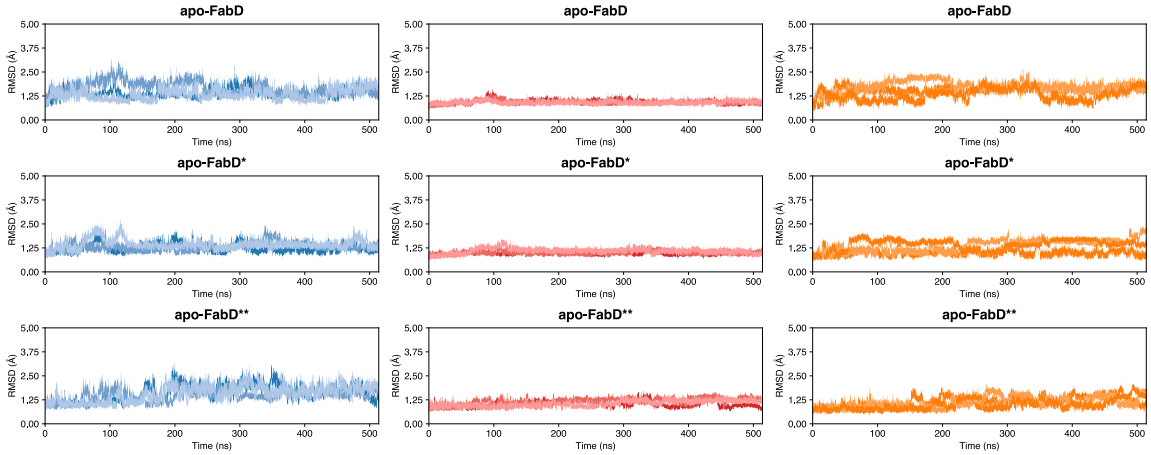

Figure S4.22: *C_α root mean square analysis (RMSD) in Ångstroms (Å) of the simulations of wildtype (wt) apo-FabD*(apo-FabD derived from malonyl-AcpP•FabD) and apo-FabD**(apo-FabD derived from malonyl-CoA•FabD).* Analysis was performed on 3 independent 524 ns molecular dynamics (MD) simulations. Each plot is labeled to indicate the FabD system analyzed. The RMSDs of the entire FabD domain (left, blue curves), the ABH (large) subdomain (center, red curves), and FL (small) subdomain (right, orange curves) of FabD.

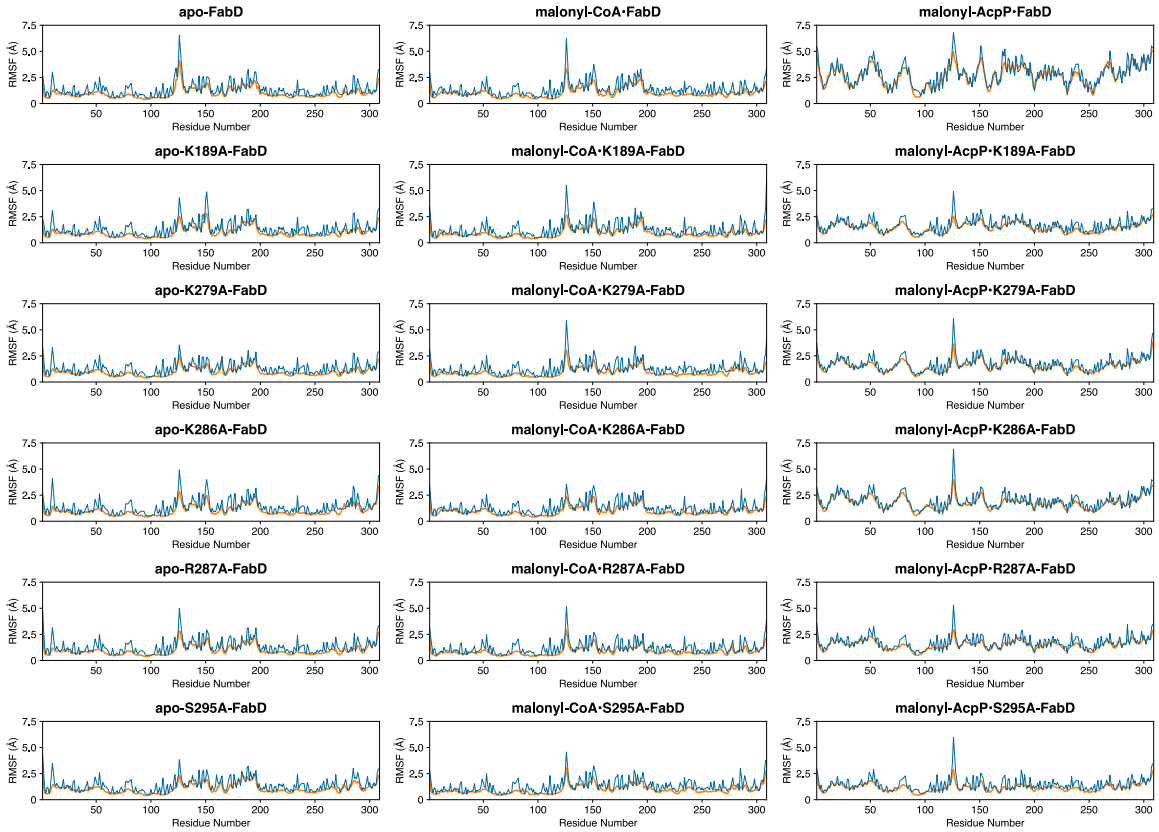

Figure S4.23: *Root mean square fluctuations (RMSFs) of each residue of FabD of the variants of the apo-FabD, malonyl-CoA•FabD, and malonyl-AcpP•FabD systems subjected to MD simulation.* The blue curve shows the RMS fluctuations of the backbone – measured using backbone heavy (non-hydrogenic) atoms – of each residue, whereas the orange curve shows the RMS fluctuation of sidechains measured using each residue's sidechain heavy (non-hydrogen) atoms. Coordinate data was superimposed overall all backbone atoms.

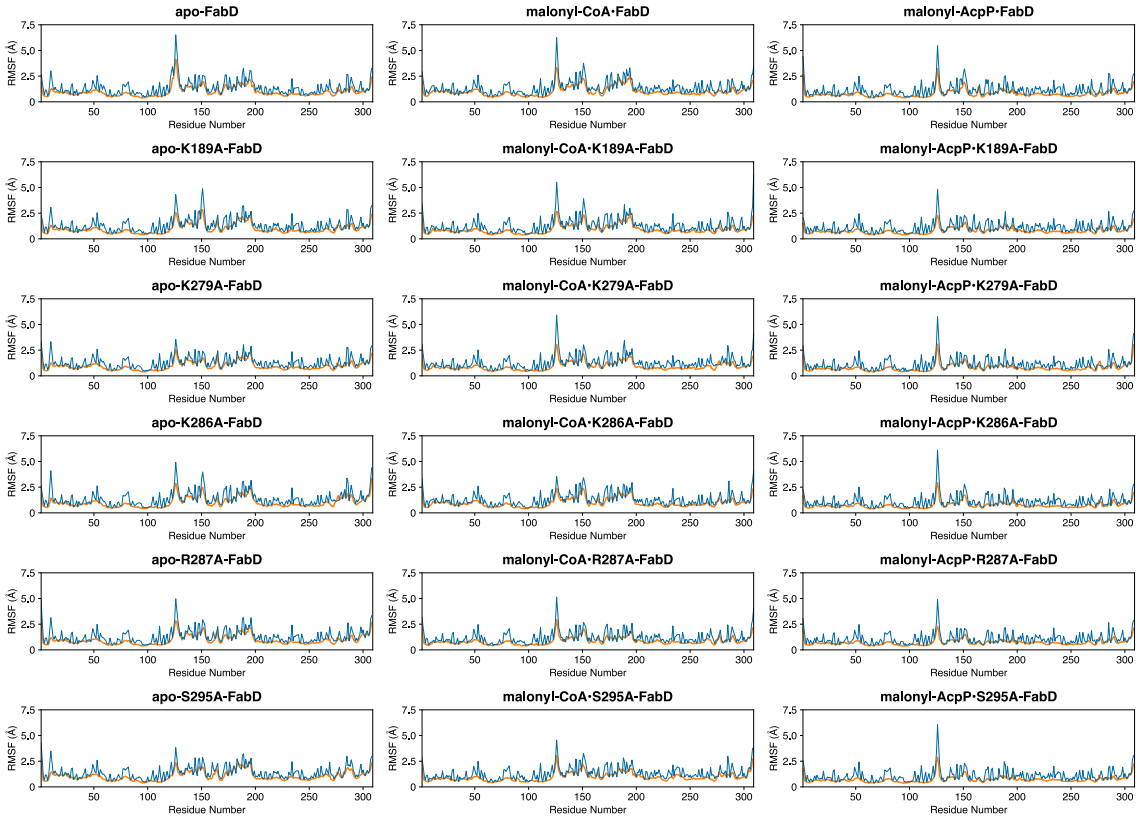

Figure S4.24: *Root mean square fluctuations (RMSFs) of each residue of FabD of the variants of the apo-FabD, malonyl-CoA•FabD, and malonyl-AcpP•FabD systems subjected to MD simulation*. The blue curve shows the RMS fluctuations of the backbone – measured using backbone heavy (non-hydrogenic) atoms – of each residue, whereas the orange curve shows the RMS fluctuation of sidechains measured using each residue's sidechain heavy (non-hydrogen) atoms. Coordinate data was superimposed overall backbone atoms of the FabD components of each system.

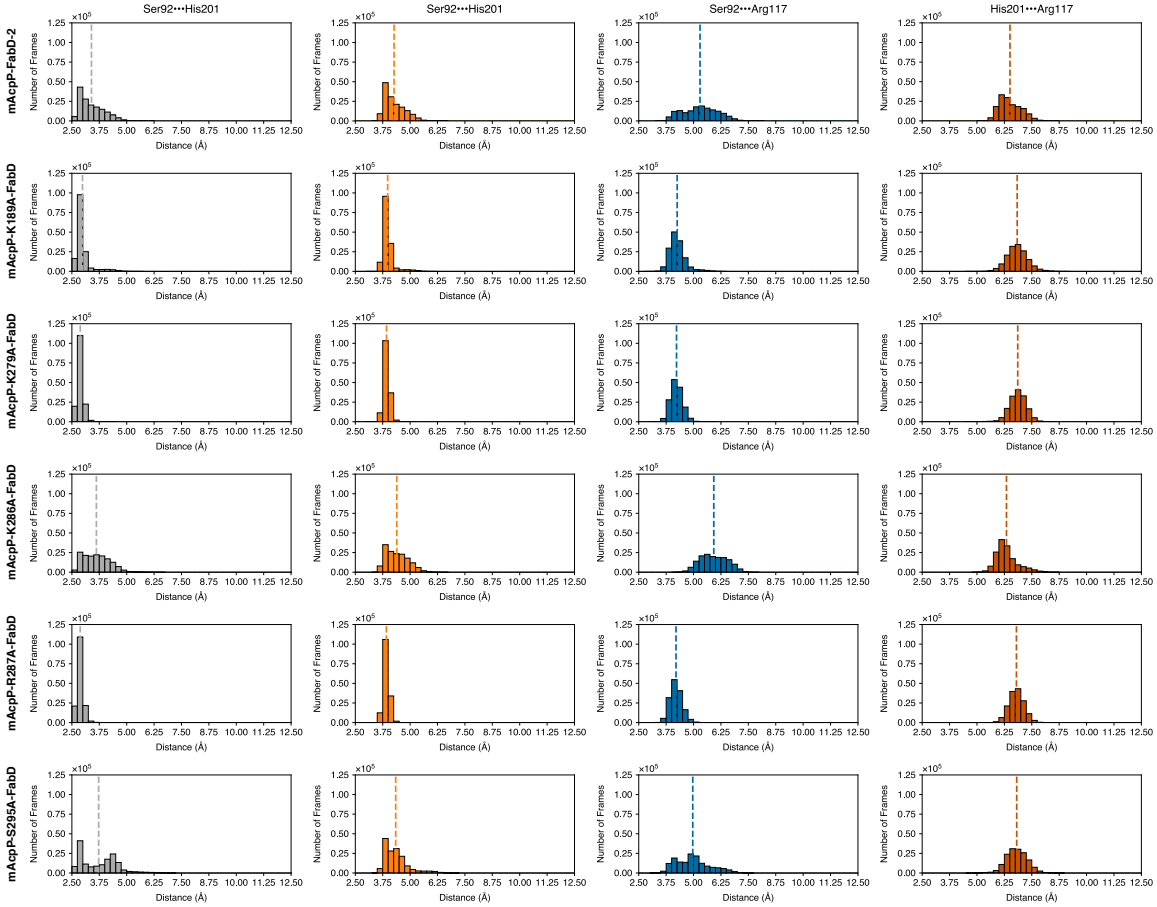

Figure S4.25: *Distribution of distances between key active site residues sampled throughout the course of MD simulations of malonyl-AcpP•FabD variants.* From left to right the distribution of distances between Ser92 and His201 (measured in two different ways in the 1st and 2nd columns), Ser92 and Arg117, and His201 and Arg 117 (from left to right). The distances between Ser92 and His201 were measured as distance between Oγ of Ser92 and His92's Nε2 (1st column) or as the distance between Oγ of Ser and the center of geometry of His201's imidazole ring. The Ser92-Arg117 is measured between Oγ of Ser and the center of geometry of Arg117's guanidinium moiety. Lastly, the distance between His201 and Arg117 is determined the centers of geometry of the imidazole and guanidinium moiety of His201 and Argy117, respectively. The dotted vertical line indicates the average distance. Distances are measured in Å. 1D histograms was generated using a bin width of 0.25 Å.

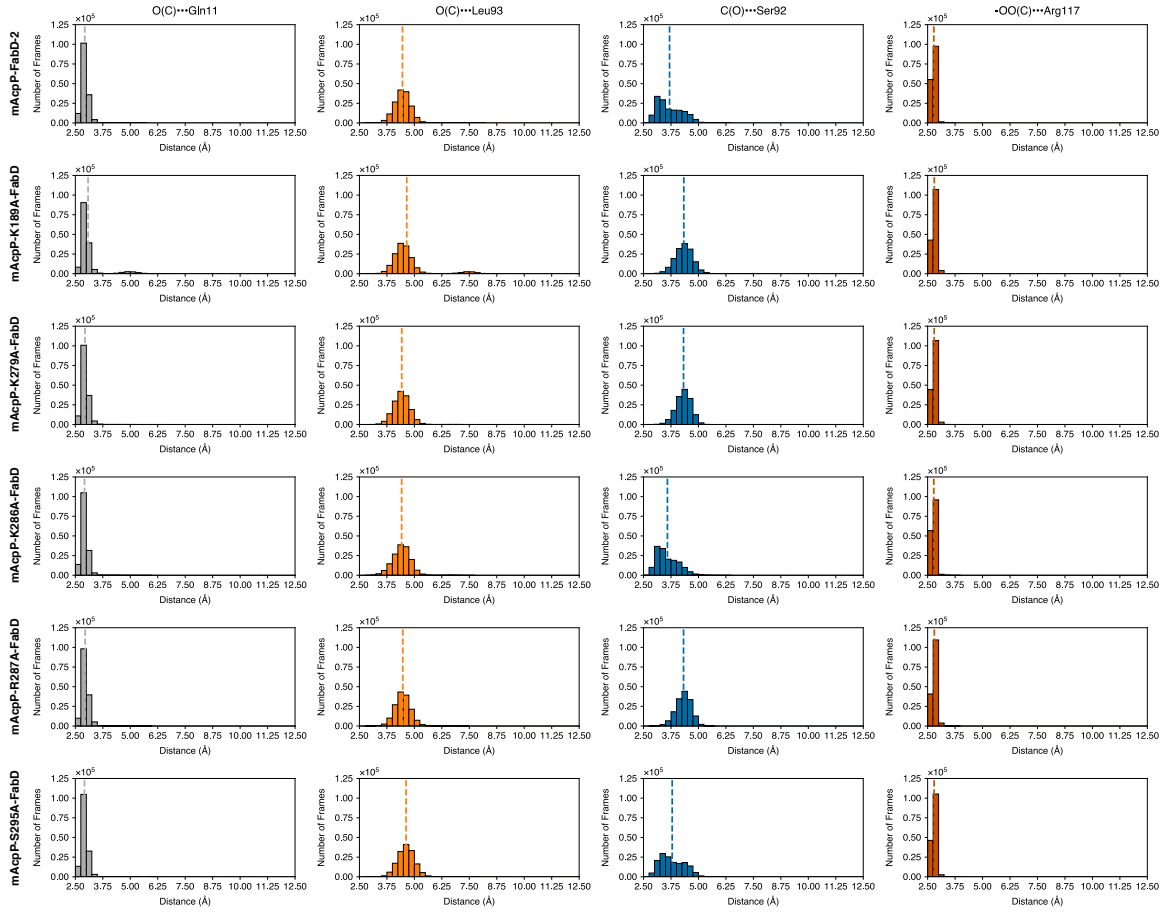

Figure S4.26: *Distribution of distances between key active site residues and malonyl portion of malonyl-AcpP sampled throughout the course of MD simulations of malonyl-AcpP•FabD variants.* From left to right, the distribution of distances between the backbone amide or Gln11 and the carbonyl oxygen of the thioester group of malonyl-CoA, the distribution of distances between the backbone amide or Leu93 and the carbonyl oxygen of the thioester group of malonyl-CoA, the distribution of distances of Ser92's Oγ and the carbonyl carbon of thioester, the distribution of distances of Arg117, and the centers of geometry of α-carboxylate moiety of malonyl-CoA and Arg117's guanidinium function. The dotted vertical line indicates the average distance. Distances are measured in Å. 1D histograms was generated using a bin width of 0.25 Å.

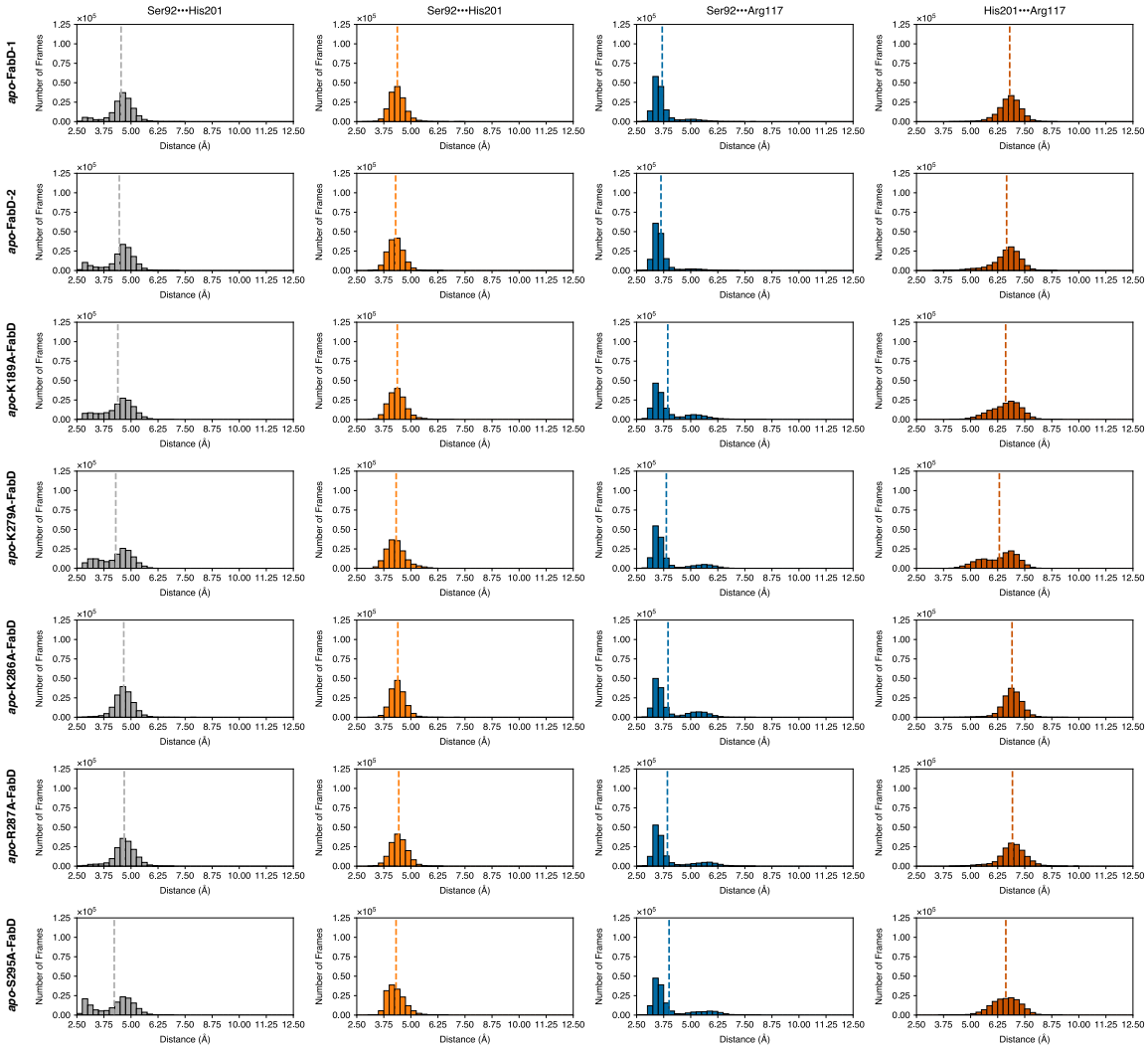

Figure S4.27: *Distribution of distances between key active site residues sampled throughout the course of MD simulations of apo-FabD variants.* From left to right the distribution of distances between Ser92 and His201 (measured in two different ways in the 1st and 2nd columns), Ser92 and Arg117, and His201 and Arg 117 (from left to right). The distances between Ser92 and His201 were measured as distance between Oγ of Ser92 and His92's Nε2 (1st column) or as the distance between Oγ of Ser and the center of geometry of His201's imidazole ring. The Ser92-Arg117 is measured between Oγ of Ser and the center of geometry of Arg117's guanidinium moiety. Lastly, the distance between His201 and Arg117 is determined the centers of geometry of the imidazole and guanidinium moiety of His201 and Argy117, respectively. The dotted vertical line indicates the average distance. Distances are measured in Å. 1D histograms was generated using a bin width of 0.25 Å.

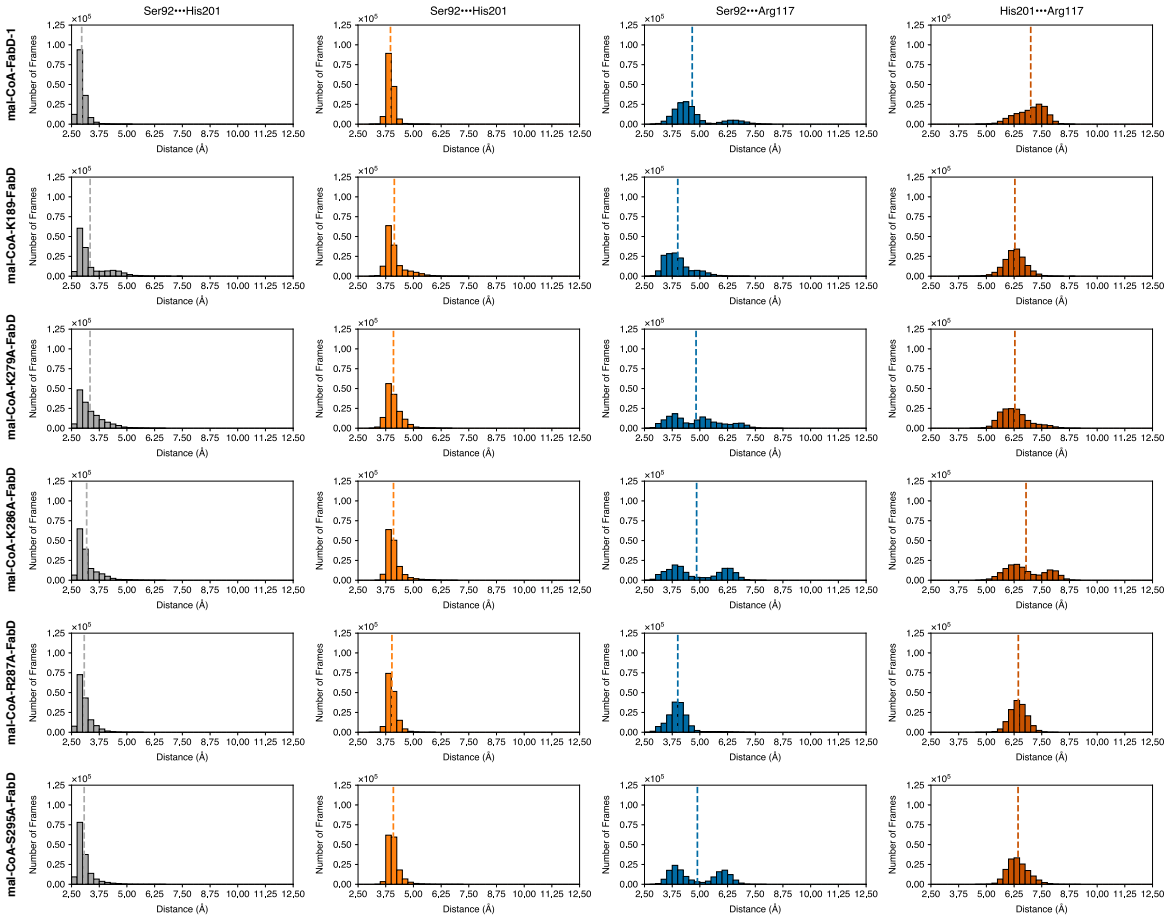

Figure S4.28: *Distribution of distances between key active site residues sampled throughout the course of MD simulations of malonyl-CoA•FabD variants.* From left to right the distribution of distances between Ser92 and His201 (measured in two different ways in the 1st and 2nd columns), Ser92 and Arg117, and His201 and Arg 117 (from left to right). The distances between Ser92 and His201 were measured as distance between Oγ of Ser92 and His92's Nε2 (1st column) or as the distance between Oγ of Ser and the center of geometry of His201's imidazole ring. The Ser92-Arg117 is measured between Oγ of Ser and the center of geometry of Arg117's guanidinium moiety. Lastly, the distance between His201 and Arg117 is determined the centers of geometry of the imidazole and guanidinium moiety of His201 and Argy117, respectively. The dotted vertical line indicates the average distance. Distances are measured in Å. 1D histograms was generated using a bin width of 0.25 Å.

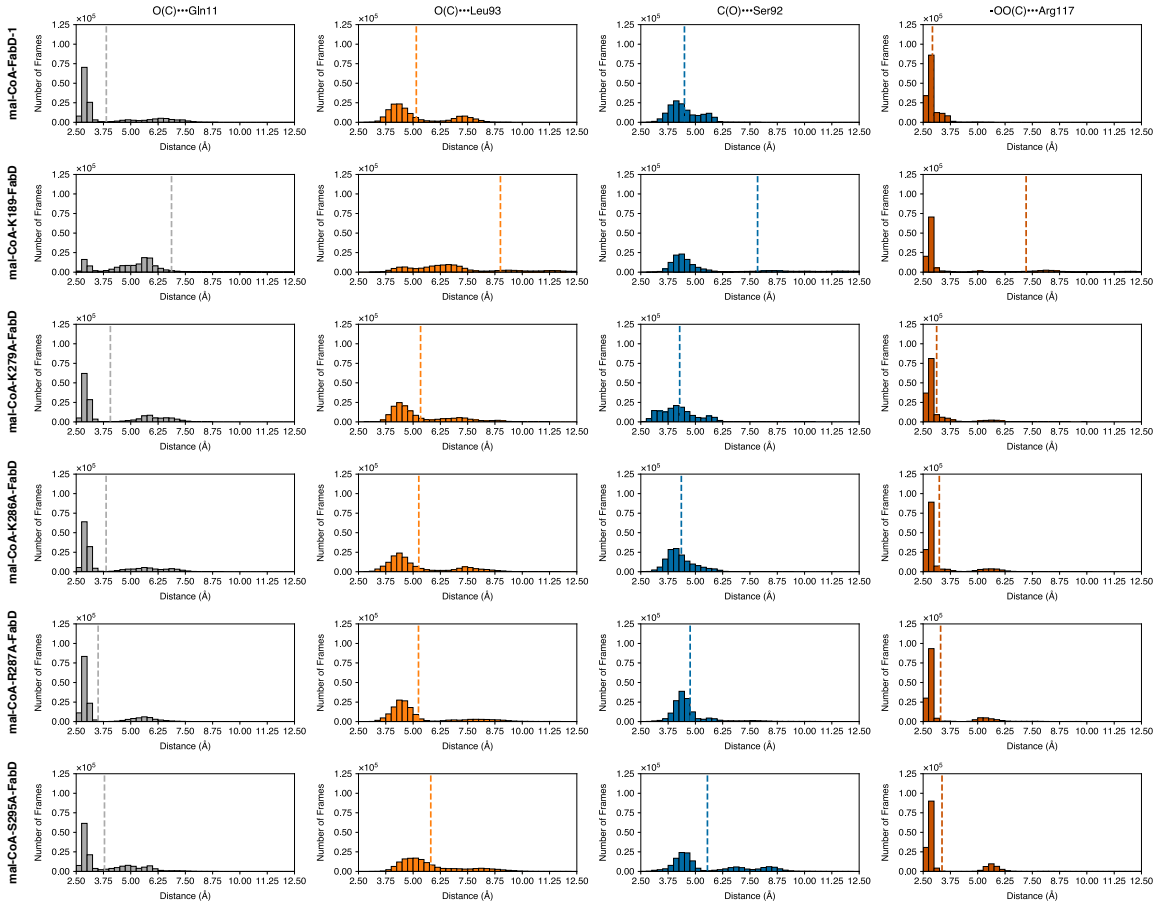

Figure S4.29: *Distribution of distances between key active site residues and malonyl portion of malonyl-AcpP sampled throughout the course of MD simulations of malonyl-CoA•FabD variants.* From left to right, the distribution of distances between the backbone amide or Gln11 and the carbonyl oxygen of the thioester group of malonyl-CoA, the distribution of distances between the backbone amide or Leu93 and the carbonyl oxygen of the thioester group of malonyl-CoA, the distribution of distances of Ser92's Oγ and the carbonyl carbon of thioester, the distribution of distances of Arg117, and the centers of geometry of α-carboxylate moiety of malonyl-CoA and Arg117's guanidinium function. The dotted vertical line indicates the average distance. Distances are measured in Å. 1D histograms was generated using a bin width of 0.25 Å.

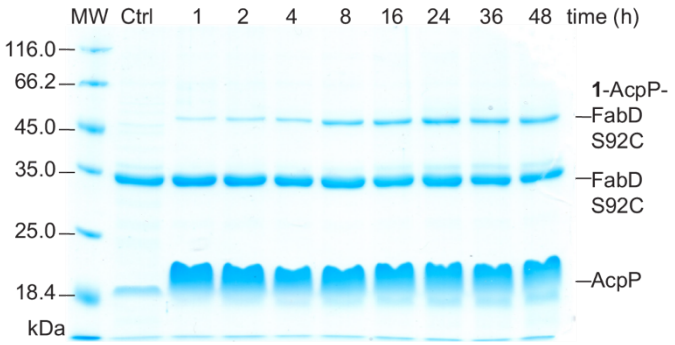

Figure S4.30: *Time-dependent C2α-bromo-crypto-AcpP-FabD S92C crosslinking.* SDS-PAGE analysis depicting crosslinking between 10 μM FabD S92C and 50 μM C2-α-bromo-crypto-AcpP in PBS, pH 7.0 at 37 °C for 1–48 h. The lane denoted as Ctrl is a control reaction between 10 μM FabD and 20 μM apo-AcpP.

Table S4.1: *Table 1 X-ray crystallography data collection and refinement statistics*

Primer name	Primer sequence
Complex	C2AcpP-FabD
Wavelength	1
Resolution range	44.73 - 1.9 (1.968 - 1.9)
Space group	C 1 2 1
Unit cell	73.15 56.846 99.874 90 97.838 90
Total reflections	231636 (22001)
Unique reflections	32206 (3205)
Multiplicity	7.2 (6.9)
Completeness (%)	99.87 (99.78)
Mean I/sigma(I)	7.16 (1.53)
Wilson B-factor	15.77
R-merge	0.286 (1.691)
R-meas	0.335 (1.997)
R-pim	0.173 (1.053)
CC1/2	0.987 (0.468)
CC*	0.997 (0.805)
Reflections used in refinement	32190 (3203)
Reflections used for R-free	1704 (170)
R-work	0.1846(0.3373)
R-free	0.2213 (0.3647)
CC(work)	0.959 (0.758)
CC(free)	0.963 (0.712)
Number of non-hydrogen atoms	3281
macromolecules	2874
ligands	57
solvent	350
Protein residues	385
RMS(bonds)	0.008

Table S4.2: *Molecular weight of FabD and holo-AcpP variants.* The molecular weight of each protein (MWmea) was determined by LC ESI-TOF MS (Agilent 6230). The expected molecular weight of holo-AcpPs (MWcalc) have been calculated considering the His6-tag cleavage and the installation of the PPant arm on AcpP's catalytic Ser36.

FabD	MW_{calc} (Da)	MW_{mea} (Da)	**ΔMW (Da)**
WT	34449.33	34449.00	0.33
K189A	34392.23	34391.70	0.53
K189E	34450.27	34449.90	0.37
R190A	34364.22	34364.20	0.02
L192A	34407.25	34407.20	0.05
K279A	34392.23	34392.20	0.03
K279E	34450.27	34450.00	0.27
K286A	34392.23	34391.80	0.43
R287A	34364.22	34364.00	0.22
R287E	34422.25	34421.80	0.45
R287K	34421.31	34421.20	0.11
K189A R190A	34307.12	34307.10	0.02
K286A R287A	34307.12	34306.50	0.62
***holo*-AcpP**	MW_{calc} (Da)	MW_{mea} (Da)	**ΔMW (Da)**
WT	9392.33	9392.36	0.03
E30A	9334.30	9333.41	1.11
D38A	9348.32	9347.39	0.93
E41A	9334.30	9333.35	0.95

Table S4.3: *FabD systems subjected to molecular dynamics simulations*

System	ff14SB/GAFF2
apo-FabD-1	Yes
apo-FabD-2	Yes
apo-K189A-FabD	Yes
apo-K279A-FabD	Yes
apo-K286A-FabD	Yes
apo-R276A-FabD	Yes
apo-S295A-FabD	Yes
malonyl-CoA•wt FabD	Yes
malonyl-CoA•K189A-FabD	Yes
malonyl-CoA•K279A-FabD	Yes
malonyl-CoA•K286A-FabD	Yes
malonyl-CoA•R276A-FabD	Yes
malonyl-CoA•S295A-FabD*	Yes
malonyl-AcpP•FabD	Yes
malonyl-AcpP•K189A•FabD	Yes
malonyl-AcpP•K279A-FabD	Yes
malonyl-AcpP•K286A-FabD	Yes
malonyl-AcpP•R276A-FabD	Yes
malonyl-AcpP•S295A-FabD*	Yes
(malonyl-CoA•)FabD	Yes
(malonyl-AcpP•)FabD	Yes

*S295 was a residue initially selected for mutation but ultimately not investigated experimentally. Nonetheless, MD simulations of the *apo*- and substrate-bound S295A-FabD systems were in progress and provide a considerable amount of additional data (2.286 μs). Because these data, in principle, improves sampling it was included in our computational analysis.

Table S4.4: *PCR primers used in this study.*

Primer name	Primer sequence
LM_E30Af	5'- CGT TGC GGA CCT GGG CGC GGA TTC -3'
LM_E30Ar	5'- GTC CGC AAC GAA AGA AGC ATT GTT GGT AAC TTC TTC CTG CTT AAC GCC -3'
LM_E41Af	5'- CGT TGC GCT GGT AAT GGC TCT GGA AGA AGA GTT TGA TAC TGA GAT TCC -3'
LM_E41Ar	5'- CAG CGC AAC GGT GTC AAG AGA ATC CGC GC -3'
LM_R287Kf	5'- CGA AAA AAA TTG TCG ACA CCC TGA CCG CCT CG -3'
LM_R287Kr	5'- CGA CAA TTT TTT TCG TCA GGC CAG TAA GCA CTT TGC C -3'
LM_R287Af	5'- CGA AAG CGA TTG TCG ACA CCC TGA CCG CC -3'
LM_R287Ar	5'- ACA ATC GCT TTC GTC AGG CCA GTA AGC ACT TTG CC -3'
LM_R287Ef	5'- CGA AAG AAA TTG TCG ACA CCC TGA CCG CCT CG -3'
LM_R287Er	5'- CGA CAA TTT CTT TCG TCA GGC CAG TAA GCA CTT TGC C -3'
LM_K279Af	5'- GGC GCG GTG CTT ACT GGC CTG ACG AAA C -3'
LM_K279Ar	5'- ACC GCG CCC GGG CCG ACT TCA TAG AGA TGT TC -3'
LM_K279Ef	5'- GGG CGA AGT GCT TAC TGG CCT GAC GAA ACG C -3'
LM_K279Er	5'- CAC TTC GCC CGG GCC GAC TTC ATA GAG ATG TTC TAC G -3'
LM_K286Af	5'- CTG ACG GCG CGC ATT GTC GAC ACC CTG -3'
LM_K286Ar	5'- GAC AAT GCG CGC CGT CAG GCC AGT AAG CAC -3'
LM_L192Af	5'- CGC GGC GCC GTT ACC AGT GAG CGT AC- 3'
LM_L192Ar	5'- GTA ACG GCG CCG CGC GTT TTG CG -3'
LM_K189Af	5'- GCA GCA CGC GCG CTG CCG TTA CCA G- 3'
LM_K189Ar	5'- GCG TGC TGC GCC CGC CGC TTT ACA G -3'
LM_K189Ef	5'- GCA GAA CGC GCG CTG CCG TTA CCA G- 3'
LM_K189Er	5'- GCG TTC TGC GCC CGC CGC TTT ACA G -3'
LM_R190Af	5'- GCA AAA GCG GCG CTG CCG TTA CCA GTG AGC -3'
LM_R190Ar	5'- GCC GCT TTT GCG CCC GCC GCT TTA CAG G -3'
LM_K189AR190Af	5'- GCA GCA GCA GCG CTG CCG TTA CCA GTG AG -3'
LM_K189AR190Ar	5'- GCT GCT GCT GCG CCC GCC GCT TTA C -3'
LM_K286AR287Af	5'- ACG GCG GCG ATT GTC GAC ACC CTG ACC -3'
LM_K286AR287Ar	5'- CGC CGC CGT CAG GCC AGT AAG CAC TTT G -3'

E. ^{1}H and ^{13}C NMR Spectra

1H-NMR (500 MHz) of PMB-protected pantetheineamide S2 in CDCl3

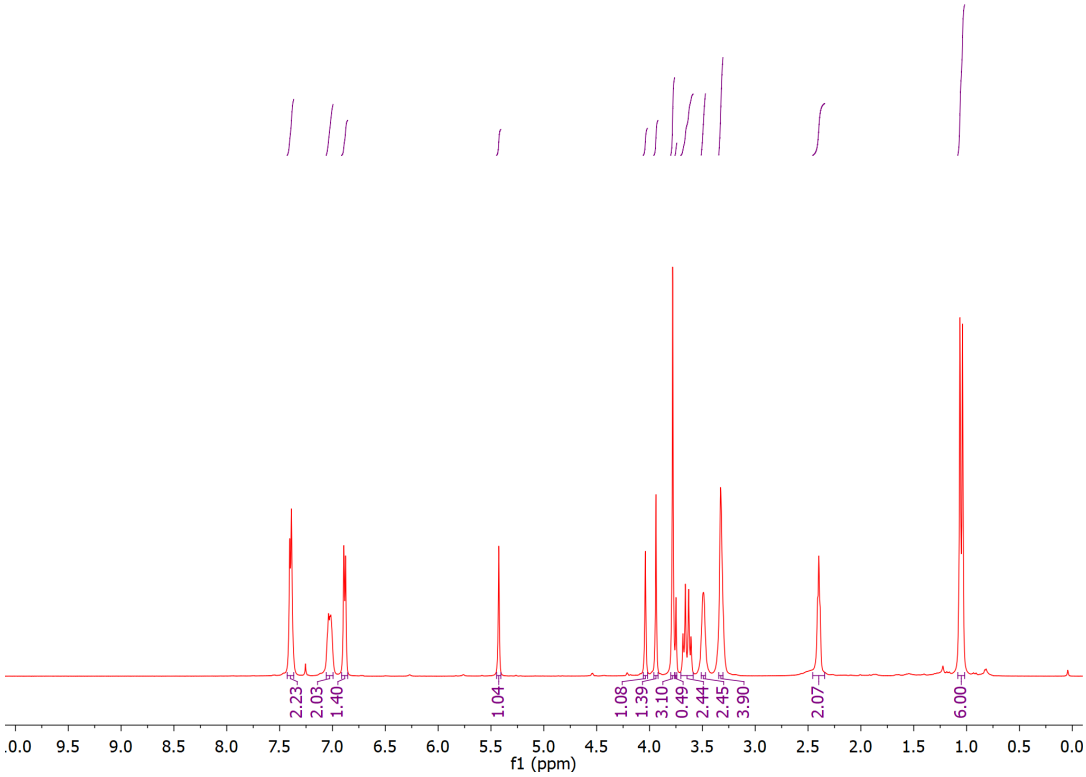

13C-NMR (125 MHz) of PMB-protected pantetheineamide S2 in CDCl3

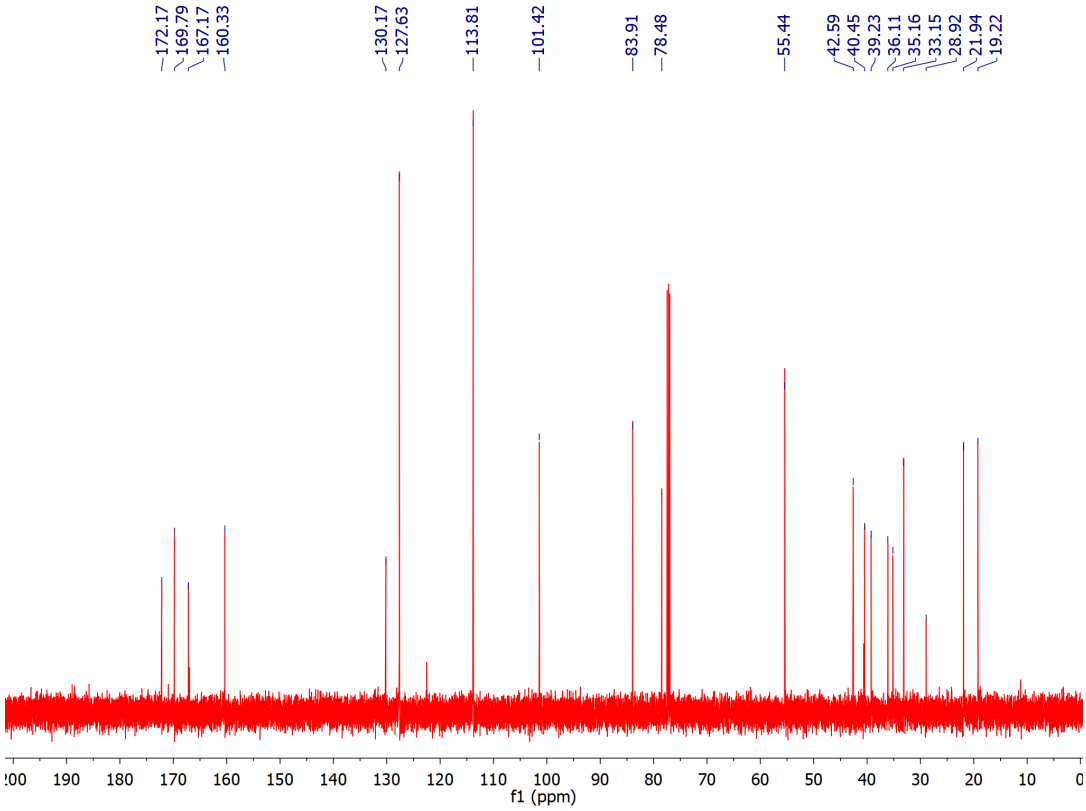

1H-NMR (400 MHz) of pantetheineamide 1 in CD3OD

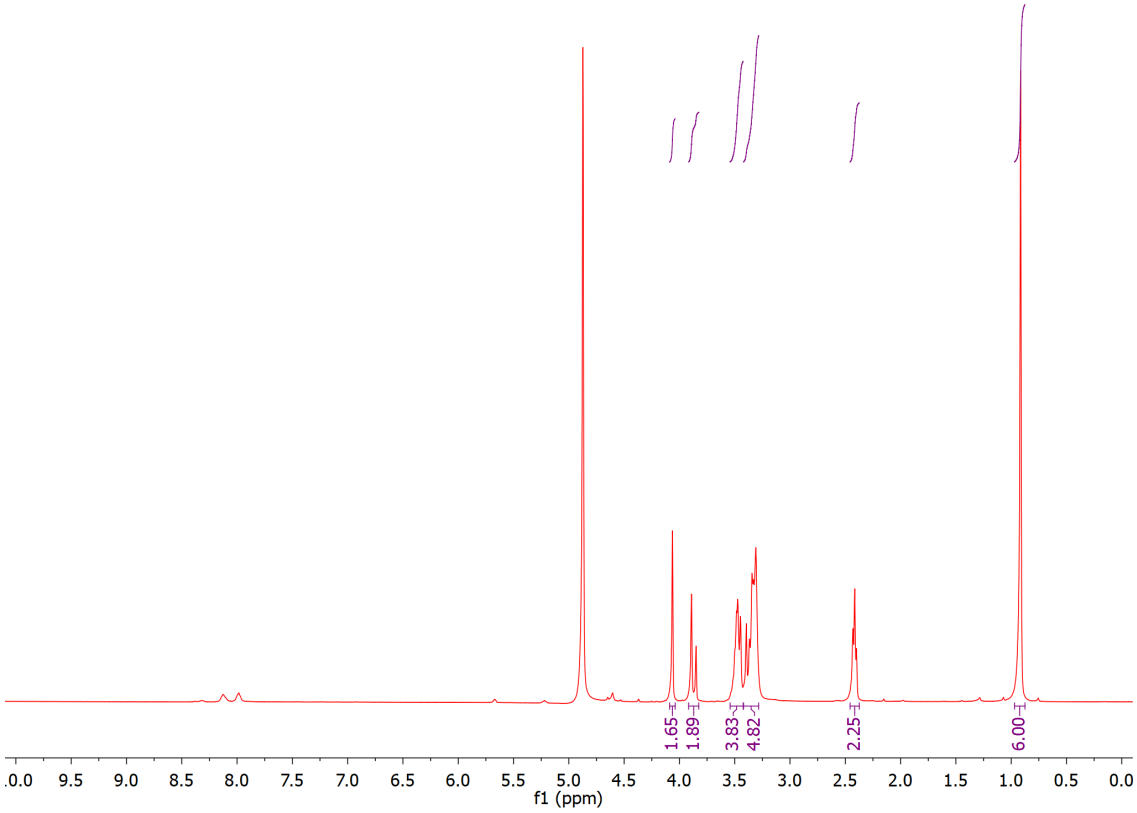

13C-NMR (100 MHz) of pantetheineamide 1 in CD3OD

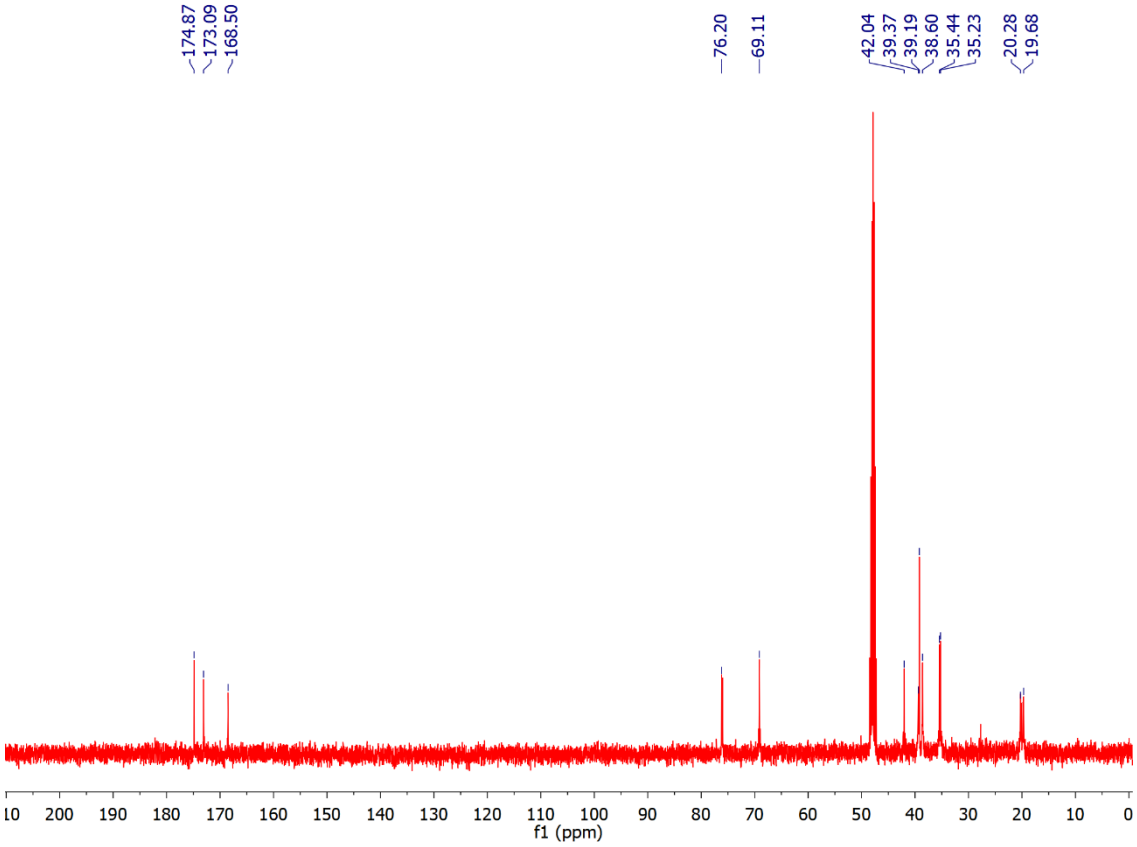

References

(1) Hertweck, C. (2009) The Biosynthetic Logic of Polyketide Diversity. *Angew. Chemie Int. Ed. 48*, 4688–4716.

(2) Maier, T., Leibundgut, M., Boehringer, D., and Ban, N. (2010) Structure and function of eukaryotic fatty acid synthases. *Q. Rev. Biophys. 43*, 373–422.

(3) Herbst, D. A., Townsend, C. A., and Maier, T. (2018) The architectures of iterative type I PKS and FAS. *Nat. Prod. Rep.* 1046–1069.

(4) Cronan, J. E., and Thomas, J. B. T.-M. in E. (2009) Chapter 17 Bacterial Fatty Acid Synthesis and its Relationships with Polyketide Synthetic Pathways, in *Complex Enzymes in Microbial Natural Product Biosynthesis, Part B: Polyketides, Aminocoumarins and Carbohydrates*, pp 395–433. Academic Press.

(5) Kohli, G. S., John, U., Van Dolah, F. M., and Murray, S. A. (2016) Evolutionary distinctiveness of fatty acid and polyketide synthesis in eukaryotes. *ISME J. 10*, 1877–1890.

(6) Hillenmeyer, M. E., Vandova, G. A., Berlew, E. E., and Charkoudian, L. K. (2015) Evolution of chemical diversity by coordinated gene swaps in type II polyketide gene clusters. *Proc. Natl. Acad. Sci. 112*, 13952–13957.

(7) Grininger, M. (2014) Perspectives on the evolution, assembly and conformational dynamics of fatty acid synthase type I (FAS I) systems. *Curr. Opin. Struct. Biol. 25*, 49–56.

(8) Ray, L., and Moore, B. S. (2016) Recent advances in the biosynthesis of unusual polyketide synthase substrates. *Nat. Prod. Rep. 33*, 150—161.

(9) Dunn, B. J., and Khosla, C. (2013) Engineering the acyltransferase substrate specificity of assembly line polyketide synthases. *J. R. Soc. Interface 10*, 20130297.

(10) Winter, J. M., Cascio, D., Dietrich, D., Sato, M., Watanabe, K., Sawaya, M. R., Vederas, J. C., and Tang, Y. (2015) Biochemical and Structural Basis for Controlling Chemical Modularity in Fungal Polyketide Biosynthesis. *J. Am. Chem. Soc. 137*, 9885–9893.

(11) Park, H., Kevany, B. M., Dyer, D. H., Thomas, M. G., and Forest, K. T. (2014) A polyketide synthase acyltransferase domain structure suggests a recognition mechanism for its hydroxymalonyl-acyl carrier protein substrate. *PLoS One 9*, e110965.

(12) Ishikawa, F., Sugimoto, H., and Kakeya, H. (2016) In Vitro Investigation of Crosstalk between Fatty Acid and Polyketide Synthases in the Andrimid Biosynthetic Assembly Line. *ChemBioChem 17*, 2137–2142.

(13) J. Rawlings, B. (1999) Biosynthesis of polyketides (other than actinomycete macrolides). *Nat. Prod. Rep. 16*, 425–484.

(14) Arthur, C. J., Williams, C., Pottage, K., Płoskoń, E., Findlow, S. C., Burston, S. G., Simpson, T. J., Crump, M. P., and Crosby, J. (2009) Structure and Malonyl CoA-ACP Transacylase Binding of Streptomyces coelicolor Fatty Acid Synthase Acyl Carrier Protein. *ACS Chem. Biol. 4*, 625–636.

(15) Liu, W., Han, C., Hu, L., Chen, K., Shen, X., and Jiang, H. (2006) Characterization and inhibitor discovery of one novel malonyl-CoA: Acyl carrier protein transacylase (MCAT) from Helicobacter pylori. *FEBS Lett. 580*, 697–702.

(16) Kumar, V., Sharma, A., Pratap, S., and Kumar, P. (2018) Biochemical and biophysical characterization of 1,4-naphthoquinone as a dual inhibitor of two key enzymes of type II fatty acid biosynthesis from Moraxella catarrhalis. *Biochim. Biophys. Acta - Proteins Proteomics 1866*, 1131–1142.

(17) Lee, W. C., Park, J., Balasubramanian, P. K., and Kim, Y. (2018) Elucidation of the crystal structure of FabD from the multidrug-resistant bacterium Acinetobacter baumannii. *Biochem. Biophys. Res. Commun. 505*, 208–214.

(18) Kumar, V., Sharma, A., Pratap, S., and Kumar, P. (2018) Biophysical and in silico interaction studies of aporphine alkaloids with Malonyl-CoA: ACP transacylase (FabD) from drug resistant Moraxella catarrhalis. *Biochimie 149*, 18—33.

(19) Zhang, X., Agrawal, A., and San, K. Y. (2012) Improving fatty acid production in *Escherichia coli* through the overexpression of malonyl coA-Acyl carrier protein transacylase. *Biotechnol. Prog. 28*, 60–65.

(20) Ghadbane, H., Brown, A. K., Kremer, L., Besra, G. S., and Fütterer, K. (2007) Structure of Mycobacterium tuberculosis mtFabD, a malonyl-CoA:acyl carrier protein transacylase (MCAT). *Acta Crystallogr. Sect. F. Struct. Biol. Cryst. Commun. 63*, 831–835.

(21) Gajewski, J., Pavlovic, R., Fischer, M., Boles, E., and Grininger, M. (2017) Engineering fungal de novo fatty acid synthesis for short chain fatty acid production. *Nat. Commun. 8*, 14650.

(22) Zhang, X., Li, M., Agrawal, A., and San, K. Y. (2011) Efficient free fatty acid production in *Escherichia coli* using plant acyl-ACP thioesterases. *Metab. Eng. 13*, 713–722.

(23) Rahman, Z., Sung, B. H., Nawab, J., Siddiqui, M. F., Ali, A., Geraldi, A., and Kim, S. C. (2019) Enhanced Production of Fatty Acid Ethyl Ester with Engineered fabHDG Operon in *Escherichia coli*. *Microorganisms 7*.

(24) Wu, J., Zhou, P., Zhang, X., and Dong, M. (2017) Efficient de novo synthesis of resveratrol by metabolically engineered *Escherichia coli*. *J. Ind. Microbiol. Biotechnol. 44*, 1083–1095.

(25) Klaus, M., D'Souza, A. D., Nivina, A., Khosla, C., and Grininger, M. (2019)

Engineering of Chimeric Polyketide Synthases Using SYNZIP Docking Domains. *ACS Chem. Biol. 14*, 426–433.

(26) Rossini, E., Gajewski, J., Klaus, M., Hummer, G., and Grininger, M. (2018) Analysis and engineering of substrate shuttling by the acyl carrier protein (ACP) in fatty acid synthases (FASs). *Chem. Commun. 2622*, 11606–11609.

(27) Gajewski, J., Buelens, F., Serdjukow, S., Janßen, M., Cortina, N., Grubmüller, H., and Grininger, M. (2017) Engineering fatty acid synthases for directed polyketide production. *Nat. Chem. Biol. 13*, 363.

(28) Murli, S., MacMillan, K. S., Hu, Z., Ashley, G. W., Dong, S. D., Kealey, J. T., Reeves, C. D., and Kennedy, J. (2005) Chemobiosynthesis of novel 6-deoxyerythronolide B analogues by mutation of the loading module of 6-deoxyerythronolide B synthase 1. *Appl. Environ. Microbiol. 71*, 4503—4509.

(29) Walker, M. C., Thuronyi, B. W., Charkoudian, L. K., Lowry, B., Khosla, C., and Chang, M. C. Y. (2013) Expanding the Fluorine Chemistry of Living Systems Using Engineered Polyketide Synthase Pathways. *Science (80-.). 341*, 1089 LP – 1094.

(30) Dunn, B. J., Cane, D. E., and Khosla, C. (2013) Mechanism and specificity of an acyltransferase domain from a modular polyketide synthase. *Biochemistry 52*, 1839—1841.

(31) Weissman, K. J. (2016) Genetic engineering of modular PKSs: From combinatorial biosynthesis to synthetic biology. *Nat. Prod. Rep. 33*, 203–230.

(32) Marcella, A. M., and Barb, A. W. (2016) A rapid fluorometric assay for the S-malonyltransacylase FabD and other sulfhydryl utilizing enzymes. *J. Biol. methods 3*, 1–10.

(33) Szafranska, A. E., Hitchman, T. S., Cox, R. J., Crosby, J., and Simpson, T. J. (2002) Kinetic and Mechanistic Analysis of the Malonyl CoA:ACP Transacylase from Streptomyces coelicolor Indicates a Single Catalytically Competent Serine Nucleophile at the Active Site. *Biochemistry 41*, 1421–1427.

(34) Marcella, A. M., and Barb, A. W. (2018) Acyl-coenzyme A:(holo-acyl carrier protein) transacylase enzymes as templates for engineering. *Appl. Microbiol. Biotechnol. 102*, 6333–6341.

(35) Marcella, A. M., and Barb, A. W. (2017) The R117A variant of the *Escherichia coli* transacylase FabD synthesizes novel acyl-(acyl carrier proteins). *Appl. Microbiol. Biotechnol. 101*, 8431–8441.

(36) Keatinge-Clay, A. T., Shelat, A. A., Savage, D. F., Tsai, S.-C., Miercke, L. J. W., O'Connell, J. D., Khosla, C., and Stroud, R. M. (2003) Catalysis, Specificity, and ACP Docking Site of Streptomyces coelicolor Malonyl-CoA:ACP Transacylase. *Structure 11*, 147–154.

(37) Zhang, L., Liu, W., Xiao, J., Hu, T., Chen, J., Chen, K., Jiang, H., and Shen, X. (2007) Malonyl-CoA: acyl carrier protein transacylase from Helicobacter pylori: Crystal structure and its interaction with acyl carrier protein. *Protein Sci. 16*, 1184–1192.

(38) Miyanaga, A., Iwasawa, S., Shinohara, Y., Kudo, F., and Eguchi, T. (2016) Structure-based analysis of the molecular interactions between acyltransferase and acyl carrier protein in vicenistatin biosynthesis. *Proc. Natl. Acad. Sci. U. S. A. 113*, 1802–7.

(39) Miyanaga, A., Ouchi, R., Ishikawa, F., Goto, E., Tanabe, G., Kudo, F., and Eguchi, T. (2018) Structural Basis of Protein-Protein Interactions between a trans-Acting Acyltransferase and Acyl Carrier Protein in Polyketide Disorazole Biosynthesis. *J. Am. Chem. Soc. 140*, 7970–7978.

(40) Gulick, A. M., and Aldrich, C. C. (2018) Trapping interactions between catalytic domains and carrier proteins of modular biosynthetic enzymes with chemical probes. *Nat. Prod. Rep. 35*, 1156—1184.

(41) Finzel, K., Lee, D. J., and Burkart, M. D. (2015) Using Modern Tools To Probe the Structure–Function Relationship of Fatty Acid Synthases. *ChemBioChem 16*, 528–547.

(42) Mindrebo, J. T., Patel, A., Misson, L. E., Kim, W. E., Davis, T. D., Ni, Q. Z., La Clair, J. J., and Burkart, M. D. (2020) Structural Basis of Acyl-Carrier Protein Interactions in Fatty Acid and Polyketide Biosynthesis, in *Comprehensive Natural Products III: Chemistry and Biology.* (Liu, H.-W. (Ben), and Begley, T. P. B. T.-C. N. P. I. I. I., Eds.), pp 61–122. Elsevier, Oxford.

(43) Worthington, A. S., and Burkart, M. D. (2006) One-pot chemo-enzymatic synthesis of reporter-modified proteins. *Org. Biomol. Chem. 4*, 44–46.

(44) Milligan, J. C., Lee, D. J., Jackson, D. R., Schaub, A. J., Beld, J., Barajas, J. F., Hale, J. J., Luo, R., Burkart, M. D., and Tsai, S.-C. (2019) Molecular basis for interactions between an acyl carrier protein and a ketosynthase. *Nat. Chem. Biol. 15*, 669–671.

(45) Dodge, G. J., Patel, A., Jaremko, K. L., McCammon, J. A., Smith, J. L., and Burkart, M. D. (2019) Structural and dynamical rationale for fatty acid unsaturation in *Escherichia coli*. *Proc. Natl. Acad. Sci. U. S. A. 116*, 6775–6783.

(46) Nguyen, C., Haushalter, R. W., Lee, D. J., Markwick, P. R., Bruegger, J., Caldara-Festin, G., Finzel, K., Jackson, D. R., Ishikawa, F., O'Dowd, B., McCammon, J. A., Opella, S. J., Tsai, S. C., and Burkart, M. D. (2014) Trapping the dynamic acyl carrier protein in fatty acid biosynthesis. *Nature 505*, 427–431.

(47) Mindrebo, J. T., Patel, A., Kim, W. E., Davis, T. D., Chen, A., Bartholow, T. G., La Clair, J. J., McCammon, J. A., Noel, J. P., and Burkart, M. D. (2020) Gating mechanism of elongating β-ketoacyl-ACP synthases. *Nat. Commun. 11*, 1727.

(48) Davis, T. D., Michaud, J. M., and Burkart, M. D. (2019) Active site labeling of fatty acid and polyketide acyl-carrier protein transacylases. *Org. Biomol. Chem. 17*, 4720–4724.

(49) Wong, F. T., Jin, X., Mathews, I. I., Cane, D. E., and Khosla, C. (2011) Structure and mechanism of the trans-acting acyltransferase from the disorazole synthase. *Biochemistry 50*, 6539–6548.

(50) Oefner, C., Schulz, H., D'Arcy, A., and Dale, G. E. (2006) Mapping the active site of *Escherichia coli* malonyl-CoA acyl carrier protein transacylase (FabD) by protein crystallography. *Acta Crystallogr. Sect. D 62*, 613–618.

(51) Rittner, A., Paithankar, K. S., Huu, K. V., and Grininger, M. (2018) Characterization of the Polyspecific Transferase of Murine Type i Fatty Acid Synthase (FAS) and Implications for Polyketide Synthase (PKS) Engineering. *ACS Chem. Biol. 13*, 723–732.

(52) Pappenberger, G., Benz, J., Gsell, B., Hennig, M., Ruf, A., Stihle, M., Thoma, R., and Rudolph, M. G. (2010) Structure of the human fatty acid synthase KS-MAT didomain as a framework for inhibitor design. *J. Mol. Biol. 397*, 508–519.

(53) Rittner, A., Paithankar, K. S., Himmler, A., and Grininger, M. (2020) Type I fatty acid synthase trapped in the octanoyl-bound state. *Protein Sci. 29*, 589–605.

(54) Zhang, F., Shi, T., Ji, H., Ali, I., Huang, S., Deng, Z., Min, Q., Bai, L., Zhao, Y., and Zheng, J. (2019) Structural Insights into the Substrate Specificity of Acyltransferases from Salinomycin Polyketide Synthase. *Biochemistry 58*, 2978–2986.

(55) Reeves, C. D., Murli, S., Ashley, G. W., Piagentini, M., Hutchinson, C. R., and McDaniel, R. (2001) Alteration of the Substrate Specificity of a Modular Polyketide Synthase Acyltransferase Domain through Site-Specific Mutations. *Biochemistry 40*, 15464–15470.

(56) Cronan, J. E. (2014) The chain-flipping mechanism of ACP (acyl carrier protein)-dependent enzymes appears universal. *Biochem. J. 460*, 157–163.

(57) Colizzi, F., Masetti, M., Recanatini, M., and Cavalli, A. (2016, August) Atomic-Level Characterization of the Chain-Flipping Mechanism in Fatty-Acids Biosynthesis. *J. Phys. Chem. Lett.* United States.

(58) Gallagher, J. R., and Prigge, S. T. (2010) Plasmodium falciparum acyl carrier protein crystal structures in disulfide-linked and reduced states and their prevalence during blood stage growth. *Proteins 78*, 575–588.

(59) Sharma, A. K., Sharma, S. K., Surolia, A., Surolia, N., and Sarma, S. P. (2006) Solution Structures of Conformationally Equilibrium Forms of Holo-Acyl Carrier Protein (PfACP) from Plasmodium falciparum Provides Insight into the Mechanism of Activation of ACPs,. *Biochemistry 45*, 6904–6916.

(60) Evans, S. E., Williams, C., Arthur, C. J., Burston, S. G., Simpson, T. J., Crosby, J., and Crump, M. P. (2008) An ACP structural switch: Conformational differences between the apo and holo forms of the actinorhodin polyketide synthase acyl carrier protein. *ChemBioChem 9*, 2424–2432.

(61) Chan, D. I., Stockner, T., Tieleman, D. P., and Vogel, H. J. (2008) Molecular dynamics simulations of the Apo-, Holo-, and acyl-forms of Escherichia coli acyl carrier protein. *J. Biol. Chem. 283*, 33620–33629.

(62) Worthington, A. S., Porter, D. F., and Burkart, M. D. (2010) Mechanism-based crosslinking as a gauge for functional interaction of modular synthases. *Org. Biomol. Chem. 8*, 1769–1772.

(63) Worthington, A. S., Hur, G. H., Meier, J. L., Cheng, Q., Moore, B. S., and Burkart, M. D. (2008) Probing the compatibility of type II ketosynthase-carrier protein partners. *Chembiochem 9*, 2096–2103.

(64) Finzel, K., Nguyen, C., Jackson, D. R., Gupta, A., Tsai, S.-C., and Burkart, M. D. (2015) Probing the Substrate Specificity and Protein-Protein Interactions of the *E. coli* Fatty Acid Dehydratase, FabA. *Chem. Biol. 22*, 1453–1460.

(65) Barajas, J. F., Finzel, K., Valentic, T. R., Shakya, G., Gamarra, N., Martinez, D., Meier, J. L., Vagstad, A. L., Newman, A. G., Townsend, C. A., Burkart, M. D., and Tsai, S.-C. (2016) Structural and Biochemical Analysis of Protein-Protein Interactions Between the Acyl-Carrier Protein and Product Template Domain. *Angew. Chem. Int. Ed. Engl. 55*, 13005–13009.

(66) Molnos, J., Gardiner, R., Dale, G. E., and Lange, R. (2003) A continuous coupled enzyme assay for bacterial malonyl-CoA:acyl carrier protein transacylase (FabD). *Anal. Biochem. 319*, 171–176.

(67) Rangan, V. S., and Smith, S. (1997) Alteration of the substrate specificity of the malonyl-CoA/acetyl- CoA:acyl carrier protein S-acyltransferase domain of the multifunctional fatty acid synthase by mutation of a single arginine residue. *J. Biol. Chem. 272*, 11975–11978.

(68) Malinska, M., Dauter, M., and Dauter, Z. (2016) Geometry of guanidinium groups in arginines. *Protein Sci. 25*, 1753–1756.

(69) Joshi, V. C., and Wakil, S. J. (1971) Studies on the mechanism of fatty acid synthesis: XXVI. Purification and properties of malonyl-coenzyme A—Acyl carrier protein transacylase of *Escherichia coli*. *Arch. Biochem. Biophys. 143*, 493–505.

(70) Battye, T. G. G., Kontogiannis, L., Johnson, O., Powell, H. R., and Leslie, A. G. W. (2011) iMOSFLM: a new graphical interface for diffraction-image processing with MOSFLM. *Acta Crystallogr. D. Biol. Crystallogr. 67*, 271–281.

(71) Winn, M. D., Ballard, C. C., Cowtan, K. D., Dodson, E. J., Emsley, P., Evans, P. R., Keegan, R. M., Krissinel, E. B., Leslie, A. G. W., McCoy, A., McNicholas, S. J., Murshudov, G. N., Pannu, N. S., Potterton, E. A., Powell, H. R., Read, R. J., Vagin, A., and Wilson, K. S. (2011) Overview of the CCP4 suite and current developments. *Acta Crystallogr. D. Biol. Crystallogr. 67*, 235–242.

(72) Adams, P. D., Afonine, P. V, Bunkóczi, G., Chen, V. B., Davis, I. W., Echols, N., Headd, J. J., Hung, L.-W., Kapral, G. J., Grosse-Kunstleve, R. W., McCoy, A. J., Moriarty, N. W., Oeffner, R., Read, R. J., Richardson, D. C., Richardson, J. S., Terwilliger, T. C., and Zwart, P. H. (2010) PHENIX: a comprehensive Python-based system for macromolecular structure solution. *Acta Crystallogr. D. Biol. Crystallogr. 66*, 213–221.

(73) Emsley, P., Lohkamp, B., Scott, W. G., and Cowtan, K. (2010) Features and development of Coot. *Acta Crystallogr. D. Biol. Crystallogr. 66*, 486–501.

(74) Moriarty, N. W., Grosse-Kunstleve, R. W., and Adams, P. D. (2009) electronic Ligand Builder and Optimization Workbench (eLBOW): a tool for ligand coordinate and restraint generation. *Acta Crystallogr. D. Biol. Crystallogr. 65*, 1074–80.

(75) Lebedev, A. A., Young, P., Isupov, M. N., Moroz, O. V, Vagin, A. A., and Murshudov, G. N. (2012) JLigand: a graphical tool for the CCP4 template-restraint library. *Acta Crystallogr. D. Biol. Crystallogr. 68*, 431–440.

(76) Quadri, L. E., Weinreb, P. H., Lei, M., Nakano, M. M., Zuber, P., and Walsh, C. T. (1998) Characterization of Sfp, a Bacillus subtilis phosphopantetheinyl transferase for peptidyl carrier protein domains in peptide synthetases. *Biochemistry 37*, 1585–1595.

(77) Beld, J., Sonnenschein, E. C., Vickery, C. R., Noel, J. P., and Burkart, M. D. (2014) The phosphopantetheinyl transferases: catalysis of a post-translational modification crucial for life. *Nat. Prod. Rep. 31*, 61–108.

(78) Dunn, B. J., Watts, K. R., Robbins, T., Cane, D. E., and Khosla, C. (2014) Comparative Analysis of the Substrate Specificity of trans- versus cis-Acyltransferases of Assembly Line Polyketide Synthases. *Biochemistry 53*, 3796–3806.

(79) Gottlieb, H. E., Kotlyar, V., and Nudelman, A. (1997) NMR Chemical Shifts of Common Laboratory Solvents as Trace Impurities. *J. Org. Chem. 62*, 7512–7515.

(80) Meier, J. L., and Burkart, M. D. (2009) Chapter 9. Synthetic probes for polyketide and nonribosomal peptide biosynthetic enzymes. *Methods Enzymol. 458*, 219–254.

(81) Serre, L., Verbree, E. C., Dauter, Z., Stuitje, A. R., and Derewenda, Z. S. (1995) The *Escherichia coli* Malonyl-CoA:Acyl Carrier Protein Transacylase at 1.5-Å Resolution.: Crystsal Structure of A Fatty Acid Synthase Component. *J. Biol. Chem. 270*, 12961–12964.

(82) Sastry, G. M., Adzhigirey, M., Day, T., Annabhimoju, R., and Sherman, W. (2013)

Protein and ligand preparation: parameters, protocols, and influence on virtual screening enrichments. *J. Comput. Aided. Mol. Des. 27*, 221—234.

(83) Shelley, J. C., Cholleti, A., Frye, L. L., Greenwood, J. R., Timlin, M. R., and Uchimaya, M. (2007) Epik: a software program for pK(a) prediction and protonation state generation for drug-like molecules. *J. Comput. Aided. Mol. Des. 21*, 681—691.

(84) Greenwood, J. R., Calkins, D., Sullivan, A. P., and Shelley, J. C. (2010) Towards the comprehensive, rapid, and accurate prediction of the favorable tautomeric states of drug-like molecules in aqueous solution. *J. Comput. Aided. Mol. Des. 24*, 591—604.

(85) Jacobson, M. P., Pincus, D. L., Rapp, C. S., Day, T. J. F., Honig, B., Shaw, D. E., and Friesner, R. A. (2004) A hierarchical approach to all-atom protein loop prediction. *Proteins 55*, 351–67.

(86) Jacobson, M. P., Friesner, R. A., Xiang, Z., and Honig, B. (2002) On the role of the crystal environment in determining protein side-chain conformations. *J. Mol. Biol. 320*, 597—608.

(87) Wang, J., Wang, W., Kollman, P. A., and Case, D. A. (2006) Automatic atom type and bond type perception in molecular mechanical calculations. *J. Mol. Graph. Model. 25*, 247–260.

(88) Maier, J. A., Martinez, C., Kasavajhala, K., Wickstrom, L., Hauser, K. E., and Simmerling, C. (2015) ff14SB: Improving the Accuracy of Protein Side Chain and Backbone Parameters from ff99SB. *J. Chem. Theory Comput. 11*, 3696–3713.

(89) Price, D. J., and Brooks, C. L. (2004) A modified TIP3P water potential for simulation with Ewald summation. *J. Chem. Phys. 121*, 10096–103.

(90) Bayly, C. I., Cieplak, P., Cornell, W., and Kollman, P. A. (1993) A well-behaved electrostatic potential based method using charge restraints for deriving atomic charges: the RESP model. *J. Phys. Chem. 97*, 10269–10280.

(91) Götz, A. W., Williamson, M. J., Xu, D., Poole, D., Le Grand, S., and Walker, R. C. (2012) Routine Microsecond Molecular Dynamics Simulations with AMBER on GPUs. 1. Generalized Born. *J. Chem. Theory Comput. 8*, 1542–1555.

(92) Salomon-Ferrer, R., Götz, A. W., Poole, D., Le Grand, S., and Walker, R. C. (2013) Routine Microsecond Molecular Dynamics Simulations with AMBER on GPUs. 2. Explicit Solvent Particle Mesh Ewald. *J. Chem. Theory Comput. 9*, 3878–88.

(93) Ryckaert, J.-P., Ciccotti, G., and Berendsen, H. J. C. (1977) Numerical integration of the cartesian equations of motion of a system with constraints: molecular dynamics of n-alkanes. *J. Comput. Phys. 23*, 327–341.

(94) Darden, T., York, D., and Pedersen, L. (1993) Particle mesh Ewald: An N·log(N) method for Ewald sums in large systems. *J. Chem. Phys. 98*, 10089–10092.

(95) Larini, L., Mannella, R., and Leporini, D. (2007) Langevin stabilization of molecular-dynamics simulations of polymers by means of quasisymplectic algorithms. *J. Chem. Phys. 126*, 104101.

(96) Liu, J., Li, D., and Liu, X. (2016) A simple and accurate algorithm for path integral molecular dynamics with the Langevin thermostat. *J. Chem. Phys. 145*, 24103.

(97) Loncharich, R. J., Brooks, B. R., and Pastor, R. W. (1992) Langevin dynamics of peptides: The frictional dependence of isomerization rates of N-acetylalanyl-N′-methylamide. *Biopolymers 32*, 523–535.

(98) Berendsen, H. J. C., Postma, J. P. M., van Gunsteren, W. F., DiNola, A., and Haak, J. R. (1984) Molecular dynamics with coupling to an external bath. *J. Chem. Phys. 81*, 3684–3690.

(99) Roe, D. R., and Cheatham, T. E. (2013) PTRAJ and CPPTRAJ: Software for Processing and Analysis of Molecular Dynamics Trajectory Data. *J. Chem. Theory Comput. 9*, 3084–95.

(100) Rose, A. S., and Hildebrand, P. W. (2015) NGL Viewer: a web application for molecular visualization. *Nucleic Acids Res. 43*, W576-9.

(101) Nguyen, H., Case, D. A., and Rose, A. S. (2018) NGLview-interactive molecular graphics for Jupyter notebooks. *Bioinformatics 34*, 1241–1242.

(102) Tiemann, J. K. S., Guixà-González, R., Hildebrand, P. W., and Rose, A. S. (2017) MDsrv: viewing and sharing molecular dynamics simulations on the web. *Nat. Methods 14*, 1123–1124.

(103) Oefner, C., Schulz, H., D'Arcy, A., and Dale, G. E. (2006) Mapping the active site of *Escherichia coli* malonyl-CoA-acyl carrier protein transacylase (FabD) by protein crystallography. *Acta Crystallogr.,Sect.D 62*, 613–618.

(104) Ruch, F. E., and Vagelos, P. R. (1973) The isolation and general properties of *Escherichia coli* malonyl coenzyme A-acyl carrier protein transacylase. *J. Biol. Chem. 248*, 8086–8094.

(105) Terwilliger, T. C., Grosse-Kunstleve, R. W., Afonine, P. V, Moriarty, N. W., Adams, P. D., Read, R. J., Zwart, P. H., and Hung, L.-W. (2008) Iterative-build OMIT maps: map improvement by iterative model building and refinement without model bias. *Acta Crystallogr. D. Biol. Crystallogr. 64*, 515—524.

Chapter 4, entitled Interfacial Plasticity Facilitates Catalysis in Type II FAS Malonyl-CoA ACP Transacylases, in full, , is a reprint of the material as it appears: Misson LE*, Mindrebo JT*, Davis TD*, Patel A*, McCammon JA, Noel JP, Burkart MD. "Interfacial Plasticity Facilitates High Reaction Rates of *E. coli* FAS Malonyl-CoA:ACP Transacylase, FabD" Proceedings of the National Academy of Sciences, 2020. The dissertation author is the primary author of this manuscript along with Dr. Laetitia Misson, Dr. Tony D. Davis, and Dr. Ashay Patel.